



DEVELOPMENT AND MECHANISTIC STUDY OF SINGLE SITES IN 2D-COVALENT ORGANIC FRAMEWORKS FOR CO₂ ELECTROREDUCTION

Geyla Caridad Dubed Bandomo

ADVERTIMENT. L'accés als continguts d'aquesta tesi doctoral i la seva utilització ha de respectar els drets de la persona autora. Pot ser utilitzada per a consulta o estudi personal, així com en activitats o materials d'investigació i docència en els termes establerts a l'art. 32 del Text Refós de la Llei de Propietat Intel·lectual (RDL 1/1996). Per altres utilitzacions es requereix l'autorització prèvia i expressa de la persona autora. En qualsevol cas, en la utilització dels seus continguts caldrà indicar de forma clara el nom i cognoms de la persona autora i el títol de la tesi doctoral. No s'autoritza la seva reproducció o altres formes d'explotació efectuades amb finalitats de lucre ni la seva comunicació pública des d'un lloc aliè al servei TDX. Tampoc s'autoritza la presentació del seu contingut en una finestra o marc aliè a TDX (framing). Aquesta reserva de drets afecta tant als continguts de la tesi com als seus resums i índexs.

ADVERTENCIA. El acceso a los contenidos de esta tesis doctoral y su utilización debe respetar los derechos de la persona autora. Puede ser utilizada para consulta o estudio personal, así como en actividades o materiales de investigación y docencia en los términos establecidos en el art. 32 del Texto Refundido de la Ley de Propiedad Intelectual (RDL 1/1996). Para otros usos se requiere la autorización previa y expresa de la persona autora. En cualquier caso, en la utilización de sus contenidos se deberá indicar de forma clara el nombre y apellidos de la persona autora y el título de la tesis doctoral. No se autoriza su reproducción u otras formas de explotación efectuadas con fines lucrativos ni su comunicación pública desde un sitio ajeno al servicio TDR. Tampoco se autoriza la presentación de su contenido en una ventana o marco ajeno a TDR (framing). Esta reserva de derechos afecta tanto al contenido de la tesis como a sus resúmenes e índices.

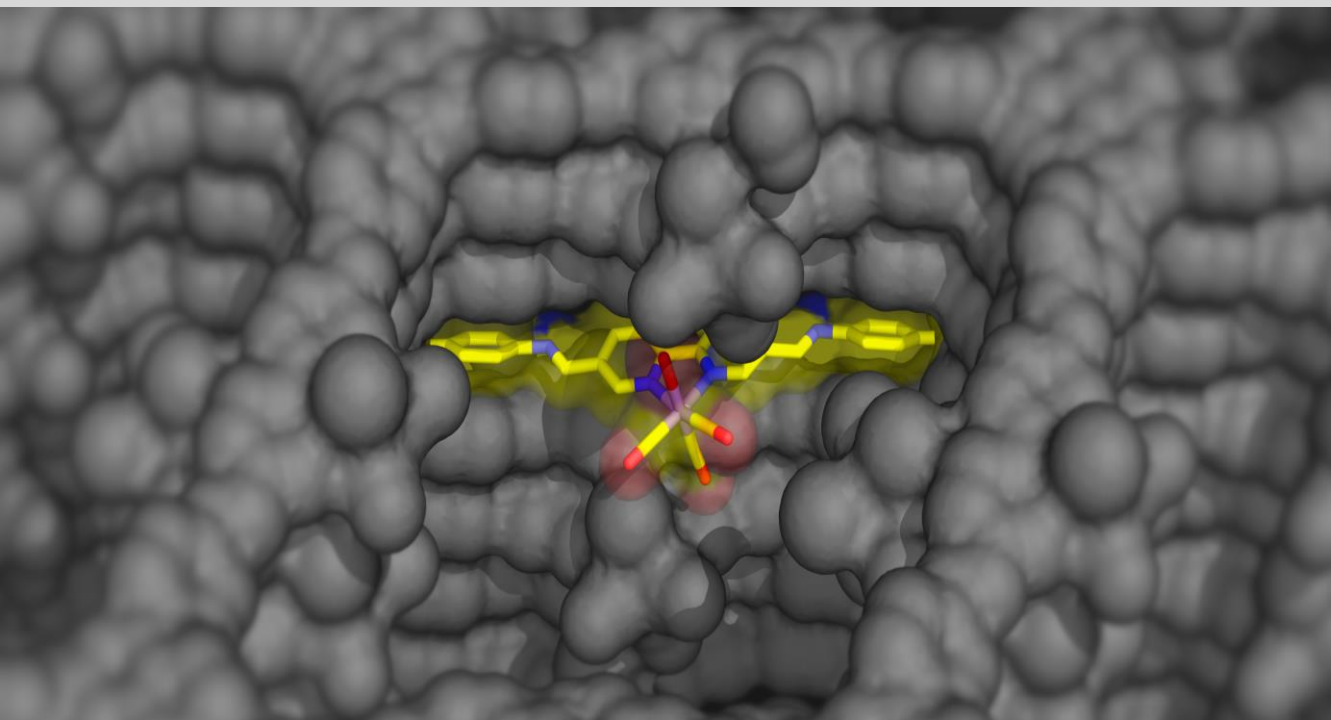
WARNING. Access to the contents of this doctoral thesis and its use must respect the rights of the author. It can be used for reference or private study, as well as research and learning activities or materials in the terms established by the 32nd article of the Spanish Consolidated Copyright Act (RDL 1/1996). Express and previous authorization of the author is required for any other uses. In any case, when using its content, full name of the author and title of the thesis must be clearly indicated. Reproduction or other forms of for profit use or public communication from outside TDX service is not allowed. Presentation of its content in a window or frame external to TDX (framing) is not authorized either. These rights affect both the content of the thesis and its abstracts and indexes.



UNIVERSITAT
ROVIRA I VIRGILI

Development and Mechanistic Study of Single Sites in 2D-Covalent Organic Frameworks for CO₂ Electroreduction

GEYLA CARIDAD DUBED BANDOMO



DOCTORAL THESIS
2022

Geyla Caridad Dubed Bandomo

Development and Mechanistic Study of Single Sites in 2D-Covalent Organic Frameworks for CO₂ Electroreduction

DOCTORAL THESIS

Supervised by Prof. Dr. Julio Lloret Fillol
Institute of Chemical Research of Catalonia



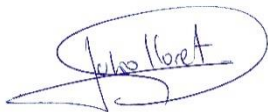
Tarragona, Catalunya 2022



Prof. Dr. Julio Lloret Fillol, Research Professor of the Catalan Institution for Research and Advanced Studies (ICREA) and Group Leader at the Institute of Chemical Research of Catalonia (ICIQ).

I STATE that the present study, entitled “Development and Mechanistic Study of Single Sites in 2D-Covalent Organic Frameworks for CO₂ Electroreduction”, presented by Geyla Caridad Dubed Bandomo for the award of the degree of Doctor, has been carried out under my supervision in my group at the Institute of Chemical Research of Catalonia (ICIQ) and fulfills all the requirements for the International Doctor Distinction.

Tarragona, August 30th, 2022



Doctoral Thesis Supervisor

Prof. Dr. Julio Lloret Fillol

“What we know is a drop, what we don't know is an ocean.”

Isaac Newton

Dedicated to my family

ACKNOWLEDGEMENTS

I would like to acknowledge all the people that have made this thesis possible.

First, I would like to express my sincere gratitude to my supervisor Prof. Dr. Julio Lloret, for accepting me to do my PhD study at ICIQ, for his guidance, his academic and scientific suggestions. Over the past years, you have offered me tremendous guidance to upgrade my research works and to shape my way of thinking logically, which paves me the way to a successful PhD study and will benefit me in future career. Thanks for all your positive, constructive comments and suggestions during my formation. I am very grateful to have the chance to learn from you to be rigorous, serious and reliable for research.

I have to thank Prof. Dr. Nuria López and Dr. Manuel Ortuño for helping me in our project with the DFT calculations.

I am as well grateful to Prof. Dr. Olaf Rüdiger and Prof. Dr. Serena DeBeer for welcoming me in their laboratory during my stay at the IMP of Chemical Energy Conversion y for all the support with the SEIRA and EPR analysis. Without a doubt, it was an enriching personal and professional experience.

This dissertation would not have been possible without the contributions of my highly talented colleagues and the support of friends and family.

I am deeply grateful to all the members of the former and the current Lloret group team for sharing their knowledge with me. I would like to thank Suvendu, Vlad, Noufal, Fèlix, Katia, Alberto, Gonell, Fabio, Klaudia, David, Luis, Changwei, Suyun Sun, Ahmed, Jingjing... for their questions, suggestions, and for their scientific support.

Y siempre hay personas que con un agradecimiento no es suficiente. Sergicito, a ti te podría decir tantas cosas! Amigo, no podría estar más agradecida de haberte conocido y vivir juntos esta aventura. Jamás olvidaré las risas, los consejos, la música (mención especial a esa canción mítica que nos representa)... Aragón (Jordi), visca Barça visca Catalunya!!! moltes gràcies pels moments compartit, per ensenyar-me de ciència, de futbol i de música, et prometo que queden pendents les meves classes de català, hi treballaré. Fede, mil gracias por todo lo que me has enseñado, por ser una pieza fundamental durante mi formación, de ti he aprendido muchísimo y también me llevo muchos buenos recuerdos. Carla, nena, muchas gracias por todos los consejos, por apoyarme y animarme, y demostrarme que con trabajo se logran los sueños. Thanks to all of you for being like my group therapy.

Pero hay personas a las que les debo todo lo que soy y lo que seré. Mis padres, mis fuerzas, gracias por haberme enseñado a superarme constantemente, por todo el apoyo, por toda la energía, porque estando lejos están a mi lado constantemente, no puedo ser más afortunada y estar más agradecida de tener una familia como la que tengo. A mi abuelo y mi abuela, mi ángel que me cuida, gracias por tanto. Un agradecimiento muy especial a mi increíble esposo, mi “coquí”. De ti he aprendido mucho, no imaginas lo afortunada que me siento de compartir mi vida a tu lado, gracias por motivarme, apoyarme e impulsarme. A mis padres y a mi esposo gracias por estar a mi lado, sin su apoyo incondicional no hubiera sido posible.

I also want to acknowledge the ICIQ Research Support Area, specially José León and Xavi, because without them some of the experiments would not have been possible.

I also would like to thank the European Commission for the ERCCG-2014- 648304 (J. Ll.-F.) project. The financial support from the ICIQ Foundation and the Canonja through the Canonja-ICIQ for the Grant "La Canonja Green Educational and Scientific Project". I also thank the

CERCA Programme (Generalitat de Catalunya) for financial support and
MINECO (CTQ2016-80038-R, Severo Ochoa Excellence Accreditation
2014– 2018; SEV-2013-0319).



LIST OF PUBLICATIONS

-“Mechanically Constrained Catalytic Mn(CO)₃Br Single Sites in a Two-Dimensional Covalent Organic Framework for CO₂ Electroreduction in H₂O”. *ACS Catal.* **2021**, 7210-7222. *Cover feature.*

Geyla C. Dubed Bandomo, Suvendu Sekhar Mondal, Federico Franco, Alberto Bucci, Vlad Martin-Diaconescu, Manuel A. Ortuño, Phebe H. van Langevelde, Alexandr Shafir, Núria López and Julio Lloret-Fillol.

-“Electrochemical CO₂ Conversion with Manganese Molecular Sites into Covalent-Organic Frameworks”. Conference Paper: Materials for Sustainable Development Conference (MAT-SUS), Proceedings of nanoGe Spring Meeting 2022 (NSM22).

DOI: <https://doi.org/10.29363/nanoge.nsm.2022.350>

Geyla C. Dubed Bandomo, Suvendu Sekhar Mondal, Federico Franco, Alberto Bucci, Vlad Martin-Diaconescu, Manuel A. Ortuño, Phebe H. van Langevelde, Alexandr Shafir, Núria López and Julio Lloret-Fillol.

-“Manganese Complexes for Electro-and Photocatalytic Transformations”. In *Manganese Catalysis in Organic Synthesis*, J.-B. Sortais (Ed.), Wiley-VCH, 2021, 137.

Sergio Fernandez, **Geyla C. Dubed Bandomo** and Julio Lloret-Fillol.

-“Recent highlights in the electrocatalytic CO₂ reduction with molecular complexes”, *Adv. Inorg. Chem.*

<https://doi.org/10.1016/bs.adioch.2022.01.001>

S. Fernández, **G. C. Dubed Bandomo**, J. Lloret-Fillol.

GLOSARY OF ABBREVIATIONS

2D: 2 dimensional
aq: Aqueous
ATR-IR: Attenuated Total Reflectance, (Fourier Transform) Infrared Spectroscopy
bpy: 2,2'-bipyridine
cal: Calorie
cat: Catalyst
CH₃CN: Acetonitrile
CO₂RR: Carbon Dioxide Reduction Reaction
COF: Covalent Organic Framework
CV: Cyclic voltammetry
E_{1/2}: Thermodynamic potential
ECSA: Electrochemical Surface Coverage
EDX: Energy-Dispersive X-ray Spectroscopy
EIS: Electrochemical Impedance Spectroscopy
EPR: Electron paramagnetic resonance
ET: Electron transfer
eV: Electronvolt
EXAFS: Extended X-Ray Adsorption Fine Structure
FY: Faradaic Yield
FESEM: Field Emission Scanning Electron microscope
FT-IR: (Fourier Transform) Infrared spectroscopy
GC: Gas chromatography
GC-MS: Gas chromatography coupled with a mass spectrometer detector
GD: Gas Diffusion Layer
GDE: Gas Diffusion Electrode
HER: Hydrogen Evolution Reaction
L: Liter
LED: Light emitting diode
M: Molar
MLCT: Metal-to-ligand charge transfer
MOF: Metal Organic Framework
Mol: Mole
MS: Mass spectrometry
MWCNTs: Multi Walled Carbon Nanotubes
NHE: Normal Hydrogen Electrode
NMR: Nuclear Magnetic Resonance
OCP: Open Circuit Potential
OER: Oxygen Evolution Reaction
ORR: Oxygen Reduction Reaction
PEMF: .Proton Exchange Membrane Fuel Cell
ppm: Part per million
PSM: Post Synthetic Modification

PT: Proton transfer

Py: Pyridine

RT: Room temperature, 298 K

SAC: Single Atom Catalysts

SBU: Secondary Building Units

SCE: Saturated Calomel Electrode

SEC: Spectroelectrochemistry

SEM: Scanning Electron Microscopy

SHE: Standard Hydrogen Electrode

TEM: Transmission Electron Microscopy

TGA: Thermogravimetric Analysis

TOF: Turnover frequency ($\text{TON} \cdot \text{h}^{-1}$)

TON: Turnover number, (number the molecules of product)/(number of molecules of catalyst used)

UV-Vis: Ultraviolet-visible spectroscopy

V: Volt

XANES: X-ray absorption near edge structure

XAS: X-ray absorption spectroscopy

XPS: X-ray Photoelectron Spectroscopy

XPS: X-ray photoelectron spectroscopy

XRD: X-ray Diffraction

η : Overpotential

TABLE OF CONTENTS

SUMMARY	1
RESUMEN.....	3

CHAPTER I.

General Introduction

I.1. Global Energy Situation.....	7
I.2. Electrochemical CO ₂ reduction.....	8
I.2.1. Important Parameters for Electrochemical CO ₂ Reduction....	9
I.2.2. Spectroscopic tools for mechanistic studies.....	11
I.3. Catalysts for the electrochemical CO ₂ reduction.....	11
I.3.1. Homogenous electrocatalysis	12
I.3.2. Heterogeneous electrocatalysis	14
I.3.2.1 Surface catalysis.....	15
I.3.2.2 Heterogenization of molecular catalysts	16
I.4. Catalysts with { <i>fac</i> -Mn(CO) ₃ } coordination for the electrochemical CO ₂ conversion	17
I.4.1 Homogeneous { <i>fac</i> -Mn(CO) ₃ } catalysts	17
I.4.1.1 Pyridine-based complexes.....	17
I.4.2. Heterogeneous { <i>fac</i> -Mn(CO) ₃ } catalysts	25
I.5. Reticular Catalysts for CO ₂ reduction.....	31
I.5.1. COFs electrocatalysts for CO ₂ reduction	32
I.6. References	38

CHAPTER II.

Main Objectives	49
-----------------------	----

CHAPTER III.

New Catalytic Mn(CO)₃Br Single Sites in a 2D-Covalent Organic Framework for the electrocatalytic CO₂ conversion in H₂O

III.1. General insight	55
III.2. Results and discussion.....	61
III.2.1 Synthesis and characterization	61
III.2.2 Electrocatalytic CO ₂ reduction in water.....	69
III.2.3 Catalyst optimization.....	74
III.2.4 Catalyst stability.....	85
III.2.5 Isotopic Labelling.....	87
III.2.6 Electrochemical impedance spectroscopy studies.....	90
III.3 Conclusions	92
III.4 Experimental section	94
III.4.1 Materials and reagents.....	94
III.4.2 Physical methods and experimental procedures.....	94
III.4.2.1. Physical methods.....	94
III.4.2.2. Synthesis Description.....	97
III.4.2.3. Computational Details.....	98
III.4.2.4. Electrochemistry.....	99
III.5 References	103

CHAPTER IV.

Detection of Key Catalytic Intermediates within Mechanical Constrained Mn(CO)₃Br Single Sites in a 2D-Covalent Organic Framework by Spectroelectrochemistry

IV.1. General insight	115
IV.2. Results and discussion.....	122

IV.2.1	Spectroelectrochemistry of the COF _{bpyMn} NT (SEC).....	122
IV.2.1.1	ATR-IR-SEC in water.....	122
IV.2.1.2	ATR-IR-SEC in CH ₃ CN.	130
IV.2.2	Proposed catalytic cycle.	134
IV.3.	Conclusions	135
IV.4.	Experimental section	137
IV.4.1.	Materials and reagents.....	137
IV.4.2.	Physical methods and experimental procedures.....	137
IV.4.2.1.	Cyclic Voltammetry	137
IV.4.2.2.	Spectroelectrochemistry	138
IV.4.2.2.1	ATR-IR-SEC	138
IV.4.2.2.2	FT-IR-SEC	140
IV.4.2.3.	Computational Details.....	141
IV.5	References	143

CHAPTER V.

Evidence of dynamic rearrangement in a 2D Covalent Organic Framework triggered by an electric stimulus.

V.1.	General insight	151
V.2.	Results and discussion.....	154
V.2.1	Spectroelectrochemistry of the COF _{bpyMn} NT.....	154
V.2.1.1.	SEIRA-SEC of COF _{bpyMn} NT in CH ₃ CN.....	154
V.2.1.2.	SEIRA-SEC of COF _{bpyMn} NT in water	159
V.2.1.3.	ATR-SEC of COF _{bpyMn} NT in CH ₃ CN	161
V.2.1.4.	COF _{bpyMn} NT EPR-SEC Signature.	164
V.2.1.5.	UV-vis-SEC.	170

V.2.1.6.	Dynamic rearrangement of COF _{bpyMn} with the electric field	174
V.3.	Conclusions	180
V.4.	Experimental section	181
V.4.1.	Materials and reagents.....	181
V.4.2.	Physical methods and experimental procedures.....	181
V.4.2.1.	Spectroelectrochemistry	181
V.4.2.1.1.	SEIRA-SEC.....	181
V.4.2.1.2.	UV-vis-SEC	185
V.4.2.1.3.	EPR-SEC.....	186
V.5	References	189

CHAPTER VI.

Novel Covalent Organic Framework with embedded Phenanthroline Mn(CO)₃Br Single Sites as CO₂ reduction electrocatalyst in aqueous media

VI.1.	General insight	197
VI.2.	Results and discussion.....	201
VI.2.1	Synthesis and characterization of COF _{PT} and COF _{PTMn}	201
VI.2.2	Electrocatalytic CO ₂ reduction in water with COF _{PTMn}	204
VI.2.3	Spectroelectrochemistry of the COF _{PTMn} NT in CH ₃ CN.	211
VI.2.4	Mechanistic proposal.....	216
VI.3.	Conclusions	217
VI.4	Experimental section	219
VI.4.1.	Materials and reagents.....	219
VI.4.2.	Synthesis and characterization	219
VI.4.3.	Physical methods and experimental procedures.....	224

VI.4.2.1.	Electrochemistry.....	224
VI.4.2.2.	Spectroelectrochemistry	227
VI.4.3.2.1	ATR-IR-SEC.....	227
VI.4.3.2.2	FT-IR-SEC	227
VI.5	References	228

CHAPTER VII.

VII.1.	General conclusions	233
--------	---------------------------	-----

SUMMARY

Global warming, climate change and our over-dependence on non-renewable fossil fuels demand long-term solutions to reduce CO₂ emissions and develop sustainable energy technologies. The electrochemical CO₂ reduction has the potential to accomplish a “carbon-neutral energy cycle”, which incorporates CO₂ as the unlimited carbon source for the production of high-density fuels, and renewable energy as the driving force behind the process. However, for an industrial application, there are still challenges to overcome, such as low selectivity, short durability and low current densities along with high overpotentials. New sustainable, modular, robust and efficient catalytic platforms are needed. In this regard, this PhD dissertation entails a fundamental understanding of the CO₂ mechanisms using Single Atom Catalyst (SAC) within Covalent Organic Frameworks (COFs). This thesis focuses on the investigation of the electrochemical CO₂ reduction (CO₂RR) in water using new Manganese based-Covalent Organic Frameworks with emphasis on understanding the relationship between structure and electrocatalytic activity. The initial center of interest of this work is to accomplish active performance and durability for CO₂RR using highly-organized {Mn(CO)₃} active sites within COFs. The catalytic activity of the materials was benchmarked against other molecular supported catalysts reported in the literature. Compared to equivalent Mn derivatives, COFs exhibited higher selectivity and activity towards CO₂ reduction. Additionally, mechanistic studies based on *in situ* / *in operando* spectroelectrochemical techniques (ATR-IR, UV-vis, SEIRA, EPR) together with DFT calculations were used to detect key catalytic intermediates and correlate the catalytic activity with the mechanical constraints impose to the {Mn(CO)₃} active sites by reticular framework. Of particular note is the detection of a radical intermediate within a Mn based COFs avoiding the detrimental formation of a dimeric specie determined as a resting state in the catalytic cycle. In addition, the study of the Mn centers within the COF was expanded and focused on the understanding of the mechanism and dynamic processes at the electrode interface. This study show case the richness and complexity of reticular

materials and can serve as a guide to investigate the dynamics of these organic frameworks.

The second part of this work was related to the study of the dependence of catalytic activity and selectivity on the structures and properties of the frameworks. A variation of the bipyridyl linker within the COF, by introducing larger phenanthroline ligand, tuned the structural and electronic properties of the catalyst, consequently influencing on the catalytic CO₂ reduction activity. The presence of both pyridyl and phenanthroline within the COFs was found to increase the activity respect the equivalent molecular catalysts. However, structural parameters like the crystallinity and porosity of the reticular frameworks proved to play an important role in the stability of the catalysts.

Overall, {Mn(CO)₃}-COFs exhibited higher catalytic activity than the equivalent molecular complexes; thereby suggesting the directions for developing COFs as ligands for CO₂ reduction. This doctoral thesis aims to contribute to the research community by providing key insights into the CO₂ reduction mechanism using reticular materials and demonstrates the concept of SAC as an alternative for the production of CO₂ feedstock.

RESUMEN

El calentamiento global, el cambio climático y nuestra excesiva dependencia de los combustibles fósiles exigen soluciones a largo plazo para reducir las emisiones de CO₂ y desarrollar tecnologías de energía sostenible. La reducción electroquímica de CO₂ (CO₂RR) tiene el potencial de lograr un “ciclo de energía neutro en carbono”, en el cual se utiliza CO₂ como fuente ilimitada de carbono para la producción de combustibles de alta densidad energética y energía renovable como la fuerza impulsora detrás del proceso. Sin embargo, para su implementación a nivel industrial aún existen desafíos que se deben superar, como la baja selectividad, corta durabilidad y bajas densidades de corriente con altos sobrepotenciales. Por lo que es necesario el desarrollo de nuevas plataformas catalíticas sostenibles, modulares, robustas y eficientes. En este sentido, esta tesis doctoral incluye una comprensión fundamental del mecanismo de reducción de CO₂ utilizando “Single Atom Catalysts” (SACs) en “Covalent Organic frameworks” (COFs). En esta disertación se investiga la reducción electroquímica de CO₂ en agua utilizando nuevos COFs de Mn, con especial énfasis en la comprensión de la relación entre la estructura de los materiales y la actividad electrocatalítica.

El centro de interés inicial de este trabajo es aumentar la actividad y estabilidad de los catalizadores de Mn utilizando sitios activos de {Mn(CO)₃} altamente organizados. La actividad catalítica de los materiales se comparó con otros catalizadores moleculares soportados reportados en la literatura. En comparación con los derivados de Mn equivalentes, los COFs exhibieron una mayor selectividad y actividad hacia la reducción de CO₂. Asimismo, mediante estudios mecanísticos, empleando técnicas espectroelectroquímicas *in situ* / *in operando* junto con cálculos DFT, se detectaron intermedios catalíticos claves y fue posible correlacionar la actividad catalítica con la restricción mecánica impuesta por los marcos orgánicos a los sitios activos de {Mn(CO)₃}. De particular interés es la detección de un intermedio radical dentro de los COFs, el cual evita la formación de especies diméricas, las cuales han sido reportadas como un estado de reposo en el ciclo catalítico. Adicionalmente, el estudio de los centros de Mn se amplió y se centró en la comprensión del mecanismo y

los procesos dinámicos que ocurren en la interfaz del electrodo. Este estudio muestra la riqueza y complejidad de los materiales reticulares y puede servir como guía para investigar la dinámica de estos marcos orgánicos.

La segunda parte de este trabajo estuvo relacionada con el estudio de la dependencia de la actividad y selectividad catalítica con las estructuras y propiedades de los marcos reticulares. Una variación del conector bipyridilo dentro del COF, al introducir un ligando de fenantrolina más grande, modificó las propiedades estructurales y electrónicas del catalizador, lo que influyó en la actividad catalítica de reducción de CO₂. Se concluyó que la presencia tanto del ligando piridilo como el de fenantrolina dentro de los COFs aumenta la actividad catalítica respecto a los catalizadores moleculares equivalentes. Sin embargo, parámetros estructurales como la cristalinidad y la porosidad también juega un papel importante en la estabilidad de los catalizadores.

En general, los {Mn(CO)₃}-COFs exhibieron mayor actividad catalítica que los complejos moleculares equivalentes, lo cual indica el potencial de los COFs como ligandos para la reducción de CO₂. Esta tesis doctoral tiene como objetivo contribuir a la comunidad científica proporcionando información clave sobre el mecanismo de reducción de CO₂ utilizando materiales reticulares y demuestra el concepto de SACs como una alternativa para la producción de materias primas a partir del CO₂.

CHAPTER I.

General Introduction

Chapter I: General Introduction

I.1. Global Energy Situation

The increment of the CO₂ concentration in the atmosphere by fossil fuel combustion caused the greenhouse effect and increased extreme climate events.¹⁻³ In response, a global consensus has been reached with efforts to limit the global temperature rise to 2 °C.⁴

Among renewable energy resources, solar energy is expected to share a dominant role in the world's generation by 2050, where about 0.3% of the Earth's surface would be enough to fulfill the expected needed energy.⁵ Nevertheless, to meet this objective, solar energy must be efficiently stored and used on demand. A desirable approach is storing solar energy in chemical bonds, as in natural photosynthesis.⁶ Therefore, the scientific challenge is to construct an "artificial leaf" that efficiently captures and converts solar energy and then stores it as chemical bonds in a high energy density fuel (Figure I.1). Truly, the conversion of renewable energy into chemical energy through an electrical potential is one of the most promising approaches.³

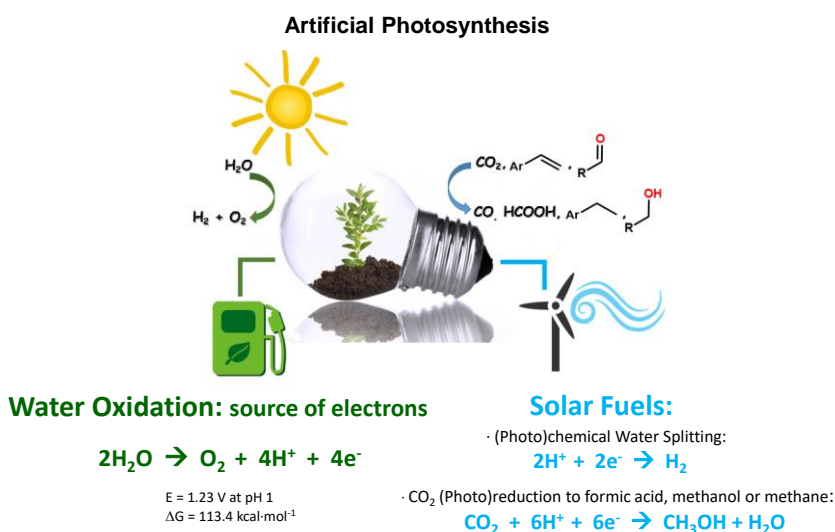


Figure I.1. Simplified artificial photosynthetic scheme representing the use of electrons from water oxidation to perform reductive transformations.

Moreover, CO₂ has become a target molecule to use as a C1 building block to synthesize high-value renewable solar fuels in the circular economy context.⁷ The turn-waste-into-wealth strategy will undoubtedly play a vital role in the green transformation of the chemical industry.⁸

The catalytic conversion of CO₂ into valuable products such as liquid fuels can not only reduce the increase of CO₂ accumulation in the atmosphere but also lead to pathways toward new renewable chemicals and high energy density fuels (Figure I.1).^{9, 10}

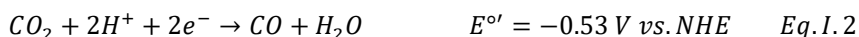
I.2. Electrochemical CO₂ reduction

CO₂ is a very stable and linear molecule with a closed-shell electronic configuration. The CO₂ reduction reaction (CO₂RR) is endergonic due to its low electron affinity (0.6 eV). This is related to the high energy of its LUMO and the increased repulsion between the free electron pairs in the oxygen atoms and the newly added electron in the carbon. Thus, stabilizing the carbon dioxide radical anion (CO₂^{•-}) is key to achieving efficient CO₂ reduction. Furthermore, the electronic and geometric structure of CO₂ makes it stable in front of electrophiles and one-electron reducing agents (Eq. I.1).¹¹ However, when coupled to a nucleophile (metal complex in a low oxidation state) and an electrophile (proton), the CO₂ reduction can be activated by an electrocatalytic process.

Another difficulty to be overcome is the selectivity of the CO₂RR. Depending on the number of proton/electron transfers, many different chemical products can be formed through CO₂ electroreduction. Eq. I.2-6 list the cathodic reactions for the typical CO₂ reduction products, and Eq. I.7 for the hydrogen evolution reaction (HER).¹² The thermodynamic cathodic potentials for all these electrochemical CO₂ reduction products are very similar, along with that of HER, which inevitably competes with CO₂ reduction in aqueous electrolytes. Therefore, the production of a single product cannot be controlled by just applying potential, and the nature of the electrocatalyst is critical to determining product selectivity. Consequently, a suitable catalyst must be highly selective.

The practical potentials required for CO₂ reduction reactions are more reducing than the thermodynamic ones, showing that CO₂ reduction

overpotentials are generally larger than the required for the H₂ evolution. An explanation could be that forming the multiple intermediates through the CO₂RR requires higher negative potentials to proceed, resulting in more reducing potentials than the theoretical equilibrium potential.¹³ In addition, several variables such as electrocatalyst, electrolyte, electrochemical reactor, and electrode design play a significant role in the product distribution obtained from the electrochemical CO₂ reduction.



The CO₂ reduction mechanisms have been studied extensively during the last years, identifying fundamental steps, thermodynamic and kinetic factors that govern this reaction may lead to rational catalyst optimization.¹⁴

I.2.1. Important Parameters for Electrochemical CO₂ Reduction

In general, extracting meaningful information about electrocatalytic transformations requires a combination of electrochemistry, spectroscopy, and computational modelling. Nevertheless, unique techniques for enlightening electrochemical reaction mechanisms are cyclic voltammetry (CV) analysis and spectroelectrochemistry (SEC).

Helpful notions: CV, together with controlled potential electrolysis (CPE), facilitates the evaluation and benchmarking of the catalyst in terms of overpotential (η), catalytic selectivity (CS), turnover number (TON) and turnover frequency (TOF), Faradaic yield (FY%) and the Tafel slope. For a given electrochemical reduction (A is reduced to B), the formal parameters can be defined as:

Overpotential (η): it usually refers to the difference between the thermodynamic reduction potential to reduce A to B ($E^{o'}_{A/B}$) and the applied electrode potential (E_{app}), at defined working conditions.^{7, 15}

$$\eta = E^{o'}_{A/B} - E_{app} \quad \text{Eq. I. 8}$$

Catalytic selectivity: CS refers to the fraction between the intended product and related reaction products and describes the effectiveness of the reaction. Therefore, CS takes values from 0 to 1, and the higher the CS higher the selectivity for a given product.

Turnover number (TON) and Turnover frequency (TOF): TON is the total number of product molecules converted per catalyst unit, and TOF is the TON divided by the time. The parameters are used to measure the efficiency of the catalysts.

Faradaic yield (FY): The FY can be calculated as the electrons consumed in the product formation divided by the total amount of electrons transferred from anode to cathode.

$$FY_B \% = \frac{Q_B}{Q_{tot}} \cdot 100 \quad \text{Eq. I. 9}$$

Where Q_B and Q_{tot} are the charge associated with the formation of the product B and the total charge that passes during the experiment, respectively.

Tafel slope: the logarithm of the current density changing with overpotential constructs the Tafel plot, and the Tafel slope is the gradient of the plot. A lower Tafel slope value indicates a better performance of electrocatalysts. Changes in the Tafel plot usually imply changes in the reaction mechanism.

Current density (j): Current density can be acquired by dividing the current by the surface area of the working electrode, which is a measure of reaction rate. More importantly, the partial current density for a specific product is a direct measure of the rate at which a given product is generated and can be calculated by multiplying the overall current density by the corresponding FY of this product (Eq. I.9):

$$j_B = j_t \cdot FY_B \quad \text{Eq. I. 10}$$

Electroactive surface coverage (Γ): The number of moles of electroactive material can be calculated using Eq. I.11. Where Q is the passed charge (C), n is the formal number of electrons transferred, F is Faraday's constant ($96485 \text{ C}\cdot\text{mol}^{-1}$) and S is the geometric surface area of the working electrode.

$$\Gamma = \frac{Q}{n \cdot F \cdot S} \quad \text{Eq. I. 11}$$

I.2.2. Spectroscopic tools for mechanistic studies

Spectroscopic techniques can be used as non-destructive complementary tools to identify reaction intermediates and/or products. In this regard, spectroelectrochemistry (SEC) allows the *in situ* spectroscopic detection (UV-vis, IR, X-ray, EPR, XAS, etc.) of reaction intermediates by application of a controlled potential.^{16f,17-19} Therefore, *in situ* SEC has emerged as a powerful technique to investigate the electrocatalytic CO₂ reduction mechanism on the electrode surface under working conditions.

While UV-vis, EPR and XAS spectroscopies can probe the redox state of the catalysts, IR and Raman spectroscopies can monitor the evolution of carbonyl groups involved in CO₂ reduction. IR-SEC, provides access to the detection of potential CO₂ reduction intermediates such as metal carboxylates and carbonyls. Moreover, the IR vibrations are sensitive to the chemical environment and the metal oxidation state.²⁰

I.3. Catalysts for the electrochemical CO₂ reduction

The greatest challenge in developing CO₂ reduction catalysts lies in the interplay between selectivity, activity and efficiency. An ideal catalyst would operate with a high current density at low overpotential to selectively produce the desired product. A deeper understanding of the CO₂RR mechanism and other factors influencing the reaction is needed to guide the search for catalysts that fulfill these criteria.

I.3.1. Homogenous electrocatalysis

In general, metal complexes are good candidates for catalytic CO₂ reduction.^{21, 22} Homogeneous molecular catalysts have well-defined coordination geometries and organic ligands.^{14, 23-25} In homogeneous systems, catalytically active sites and reaction intermediates are comparatively easy to characterize than heterogeneous ones, thereby, are better for elucidating the mechanistic details of the catalytic reaction.^{26, 27}

In the homogeneous electroreduction of CO₂, the electrocatalyst acts as the electron transfer agent (at an electrode) to facilitate and accelerate the reaction (Figure I.2).^{28, 29} Both the electron transfer and chemical kinetics must be fast for an efficient electrocatalyst. First, the catalyst accepts electrons from the electrode, giving it a highly reduced state. After reduction, the catalyst reacts with CO₂, following a series of PT and ET steps returning to the initial state and generating CO₂ reduction product.

Ideally, the reaction can be driven near the thermodynamic potential of the CO₂RR, $E^{\circ'}_{(\text{Products}/\text{CO}_2)}$. However, in most cases, the difference between the applied electrode potential, E_{app} and $E^{\circ'}_{(\text{Products}/\text{CO}_2)}$ is difficult to be reduced and in consequence, a significant overpotential is required for the electroreduction of CO₂, consequently lowering the energy efficiency. Therefore, to improve the catalysts, we must adjust the thermodynamic match between the catalyst's working potential, $E^{\circ'}(\text{Cat}^{n+/0})$ and the thermodynamic $E^{\circ'}_{(\text{Products}/\text{CO}_2)}$ to minimize the overpotential. However, at the same time, the kinetics of the reaction must be maximized (k_{cat}).

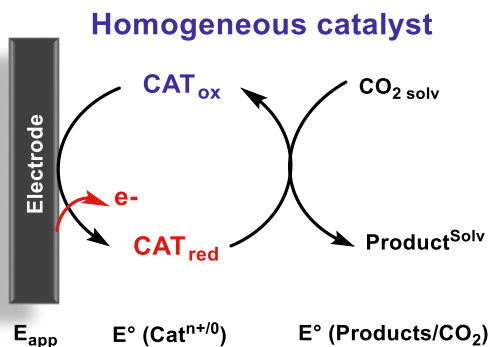


Figure I.2. Homogeneous electrochemical CO₂ reduction.

To mediate the multi-electron/multi-proton transformations necessary for the catalytic CO₂ reduction, molecular catalysts must have the ability to store multiple reducing equivalents. This can be achieved either by reducing the metal center, which necessitates a ligand field capable of stabilizing the reduced metal ions or by reducing the ligand scaffold, with the metal serving as a mediator for the electron relay.³⁰⁻³³ Notably, key strategies to improve reaction rates, selectivity, and mechanism understanding for the principal families of homogeneous catalysts have been reported.^{24, 25, 31, 34} For example, two factors can be optimized *via* ligand design and the judicious selection of metal centers (*i*) to adjust the redox potential for the electron transfer and (*ii*) the certain chemical reaction (i.e., CO₂ to CO).²⁹

Furthermore, molecular catalysts based on macrocyclic, polypyridyl, aminopyridyl and organometallic ligands are among the most thoroughly investigated ones, which usually exhibit high activity and selectivity for reducing CO₂ to CO.^{21, 25, 31, 35-41} Figure I.3 shows some representative examples of homogeneous catalysts evaluated for the electrochemical CO₂ reduction. Different strategies for the rational design of the metal's second coordination sphere have been explored to improve the catalytic performances of these systems.^{21, 24, 26, 42, 43}

Commonly, molecular catalysts are investigated in aprotic media, avoiding in this way the competing HER. In general, homogeneous catalysts deliver good selectivity and activity for CO₂RR. However, they usually suffer from drawbacks including low interfacial concentration,

product isolation, and poor stability. In addition, a significant drawback arises from the difficulty of catalyst recovery.

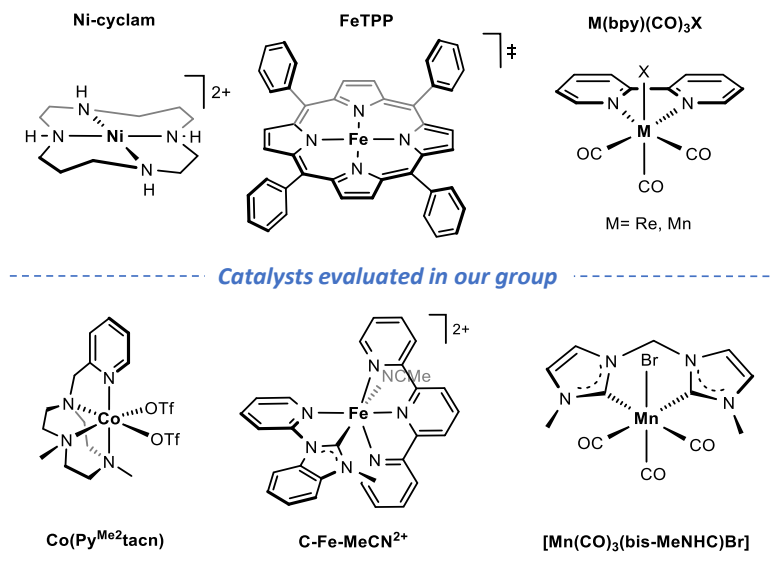


Figure I.3. Representative examples of homogeneous molecular catalysts for the electrochemical CO₂ reduction,^{31, 35-40} **Ni-cyclam**, **FeTPP** and **M(bpy)(CO)₃X** like complexes (TPP: porphyrin derivatives; M: Mn, Re; bpy: pyridine derivatives; X: Br, Cl, CH₃CN). Selected homogeneous catalysts evaluated in Lloret's group: **Co(Py^{Me2}tacn)**, (Py^{Me2}tacn: 1-[2-pyridylmethyl]-4,7-dimethyl-1,4,7-triazacyclononane); **C-Fe-MeCN²⁺** (*C-trans*-[Fe(tpy)(Mebim-py)-(MeCN)][PF₆]₂, (Mebim-py: 1-methylbenzimidazol-2-ylidene-3-(2-pyridine)); **[Mn(CO)₃(bis-MeNHC)Br]**, (bis-^{Me}NHC: bis(N-methylimidazolium)).

I.3.2. Heterogeneous electrocatalysis

Although molecular catalysts in the homogeneous phase have been widely studied, heterogeneous electrocatalysts present several advantages that point them out as promising candidates for CO₂ reduction. For example, outstanding efficiency and great potential for large-scale applications make them more promising materials to be applied in industrial processes than homogeneous ones.

I.3.2.1 Surface catalysis

Typically, heterogeneous electrocatalytic CO₂ reduction involves three steps (Figure I.4): (i) adsorption of CO₂ molecules onto the conductive materials; (ii) electron transfer and/or proton migration; (iii) configuration rearrangement and desorption of products.⁴⁴

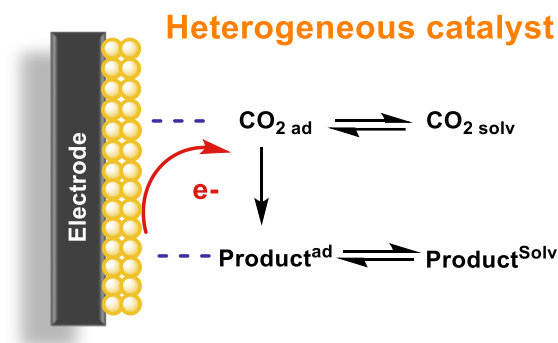


Figure I.4. Representation of heterogeneous electrocatalyst for CO₂ reduction.

In the early stages, polycrystalline monometallic catalysts were widely evaluated based on their simple structures and facile syntheses.⁴⁵⁻⁴⁷ Cu, Au, Sn, Hg, Ag, Zn, Pd, etc. have proved to be robust and effective as both metal electrodes and electrocatalysts. At the same time, several transition metal oxides and chalcogenides such as TiO₂, FeO_x, Cu₂O, ZnS, MoS₂, and VS₄, have been reported as versatile electrocatalysts for CO₂ reductions as well.⁴⁸

Compared with conventional electrodes, nanostructured catalysts can provide enhanced reactive surfaces with a considerable fraction of the reactive sites available for catalysis. The control of morphologies and compositions of supported nanocatalyst structures can lead to high reactivities and selectivities. However, the mechanistic understanding to explore the reactivities and optimize the catalytic rates on surface-based materials are challenging tasks. Another aspect of heterogeneous inorganic catalysis that must be put forward is that these materials are difficult to control on the molecular level, and the most active systems rely mainly on precious metals.⁴⁹⁻⁵¹

I.3.2.2 Heterogenization of molecular catalysts

A simple strategy for transitioning from homogeneous to heterogeneous systems is to functionalize or modify the working electrode with catalytic effective organic metal complexes (Figure I.5).⁵²⁻⁵⁶ Immobilized catalysts combine the advantages of homogeneous catalysis (activity and selectivity) with the ability of the heterogeneous ones (recycling and stability). Some conventional strategies for heterogeneous integration of discrete molecular catalysts include: (i) anchoring the catalysts on support through covalent linkages, (ii) non-covalent interactions (π - π stacking, coordination, electrostatic interactions, H-bonding and host-guest encapsulation) between support and catalyst molecule, (iii) directly polymerizing the molecules into films or (iiii) encapsulating into polymeric materials.^{18, 44, 57} For the heterogenization of molecular complexes, the support should present high conductivity and porosity to ensure effective electron transport and high-density anchoring of catalytically active molecules. Besides, the anchoring should be robust enough to warrant stability of the resulting configuration and smooth electron transfer between support and active molecule.

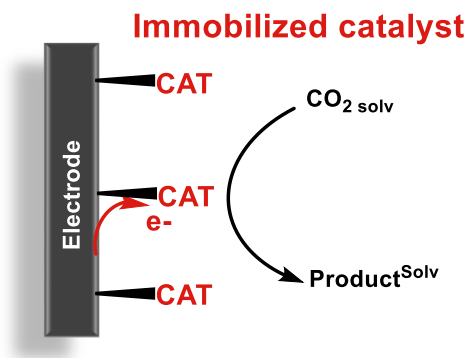


Figure I.5. Modified electrode for electrocatalytic CO₂ reduction.

Importantly, non-covalent immobilization strategies suffer from architecture fragility and deficient electron coupling between catalyst and support, thus lowering electron transfer efficiency.^{52, 58, 59} Covalent

immobilization is considered a better alternative to overcome these shortcomings.⁵²

A different approach for preparing surface-bound catalyst films is electropolymerization. In the electropolymerized films, electrons are conducted through the redox polymer by successive electron-self-exchange steps between neighbor oxidized and reduced sites. These films have enhanced reactivities with high surface catalyst concentrations at the electrode.⁶⁰

Alternatively, the heterogenization of well-defined catalysts has also been prepared by immobilizing them in reticular substrates, such as Metal-Organic Frameworks (MOFs) or Covalent Organic Frameworks (COFs) (see Section I.5 for details).⁶¹

I.4. Catalysts with $\{fac\text{-Mn}(\text{CO})_3\}$ coordination for the electrochemical CO₂ conversion

I.4.1 Homogeneous $\{fac\text{-Mn}(\text{CO})_3\}$ catalysts

In order to develop a catalyst that can overcome the kinetic challenges of CO₂ electroreduction, the ligands need to be well tuned and functionalized.²¹ In this line, efforts have been principally focused on the study of 2,2'-diimine-containing complexes of the type $fac\text{-}[\text{Mn}(\text{N}^{\wedge}\text{N})(\text{CO})_3(\text{X})]^{0/+}$, where the diimine ligand N[^]N is commonly 2,2' -bipyridine, 1,1'-phenanthroline, or derivatives, and X is either a halide or neutral N-donor ligand, e.g., CH₃CN.^{38, 62, 63}

I.4.1.1 Pyridine-based complexes

The pioneering work of Lehn and co-workers on the electrochemical CO₂ reduction catalyzed by $fac\text{-}[\text{Re}(\text{bpy})(\text{CO})_3\text{Cl}]$ dates from 1984.⁶⁴ It was not until 2011 that Chardon-Noblat and Deronzier *et al.* firstly reported carbonyl polypyridyl manganese complexes as highly active electrocatalysts for the selective CO₂-to-CO reduction in the presence of protons and at 400 mV less overpotential than its Re counterpart.^{65, 66}

Typically, complexes such as the $fac\text{-}[\text{Mn}(\text{bpy})(\text{CO})_3\text{X}]$ (**1a**, Figure I.6) exhibit a HOMO dominated by a Mn 3d-orbital (with additional carbonyl π^* contributions and π -orbital contributions) and a diimine π^* -

based LUMO. The electronic and photophysical properties of analogous Mn^I complexes can be significantly tuned through modification of the structure of the diimine ligand, modulating the energy of the LUMO. An additional strong dependence on the identity of the axially coordinated ligand (X) is also observed, which varies the energy of the HOMO. In general, this class of catalysts is versatile (in terms of ligand framework), allows access to mechanistic information, and develops heterogenized systems.

In this line, the *fac*-[Mn(L)(CO)₃X]ⁿ complexes (L = 2,2'-bipyridine (bpy) or 4,4'-dimethyl-2,2'-bipyridine (dmbpy) for X = Br, n = 0) (**1a** and **1b**, Figure I.6a) have exhibited an excellent efficiency and selectivity of CO₂-to-CO electroreduction in presence of protons.⁶⁵ Since this first report, a large collection of Mn systems has been described.

CV of **1a** showed two single irreversible electron reduction waves assigned to the reduction of Mn^{I/0} and Mn^{0/-1}, respectively (Figure I.6b). In the presence of CO₂, the CV was maintained equivalent. At the same time, the subsequent addition of water, as a proton source, produced an intense current enhancement, corresponding to catalytic CO₂ reduction. CPE in CH₃CN and 5% H₂O at -1.40 vs SCE showed quantitative FY for production of CO. However, the FY dropped slightly at extended CPE (FY_{CO} = 85% in 22 h), because of the formation of H₂ (FY_{H₂} 15%). UV-Vis recorded during the bulk reductive electrolysis showed the formation of the [Mn⁰(bpy)(CO)₃]₂ dimer and the unstable [Mn^I(bpy)(CO)₃]⁻, in agreement with spectroscopic results previously reported.⁶⁷⁻⁶⁹ The proposed mechanism involves the formation of the [Mn^I(bpy)(CO)₃]⁻ which reacts with CO₂ (Figure I.7). Later on, based on pulsed-EPR complemented with DFT studies, the authors also proposed that the Mn⁰-Mn⁰ dimer could also react with CO₂, although at slower reaction rates.⁶⁶ The oxidative addition of CO₂ and H⁺ over the Mn⁰-Mn⁰ dimer can lead to a Mn^{II}-carboxylic acid intermediate, which finally gets reduced with a second electron and protonated to evolve a CO and an H₂O molecule.^{38, 70}

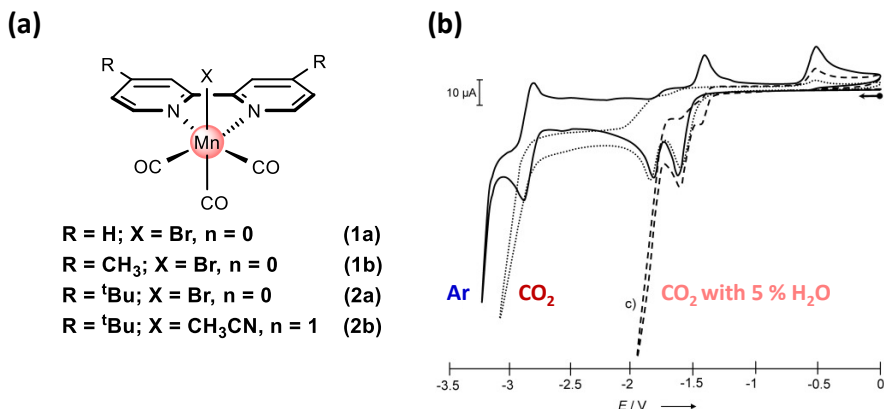


Figure I.6. (a) Selected carbonyl bipyridine manganese complexes. (b) Cyclic Voltammetry of **1a** (1 mM) in CH₃CN/TBAPF₆ (0.1 M) at 100 mV·s⁻¹ vs Ag/Ag⁺ under Ar (solid line) and under CO₂ without (dashed line) and with 5% of H₂O (dotted line).⁶⁵ Reproduced with permission from [65] Copyright 2011 WILEY-VCH Verlag GmbH & Co. KGaA, Weinheim.

Later on, Kubiak's group studied the influence of weak acids on the catalytic activity of [Mn(bpy*t*Bu)(CO)₃X]ⁿ (where X: Br⁻ (n=0), CH₃CN (n=1)) (**2a** and **2b**, Figure I.6a).⁷¹ They found a direct correlation between the acid concentration and its strength (H₂O, MeOH, and TFE) with increased catalytic current in CV. CPE of **2a** in CH₃CN with TFE (1.4 M at -2.2 V vs SCE), gave a TOF_{CO} of 340 s⁻¹ with quantitative FY. To gain further insights on the mechanism, IR-SEC of [Mn(bpy*t*Bu)(CO)₃Br] was performed. Upon the first reduction, the complex rapidly dimerizes to form a [Mn⁰(bpy-*t*Bu)(CO)₃]₂, which breaks upon further reduction to yield the catalytically active anionic species.^{71,72}

Since 2011, many groups have worked on the mechanistic understanding of the catalytic cycle for CO₂ reduction (Figure I.7).⁶² The different intermediates are easy to identify by the characteristic IR absorption pattern of the *fac*-CO ligands. Thus, IR-SEC has been widely used to identify and characterize catalytic intermediates in Mn *fac*-tricarbonyl complexes.⁷³ As a favorable consequence of the extensive mechanistic studies on this family of catalysts, some strategies based on modifying the catalyst environment provided promising results in the catalytic performance and even a change in the product selectivity.

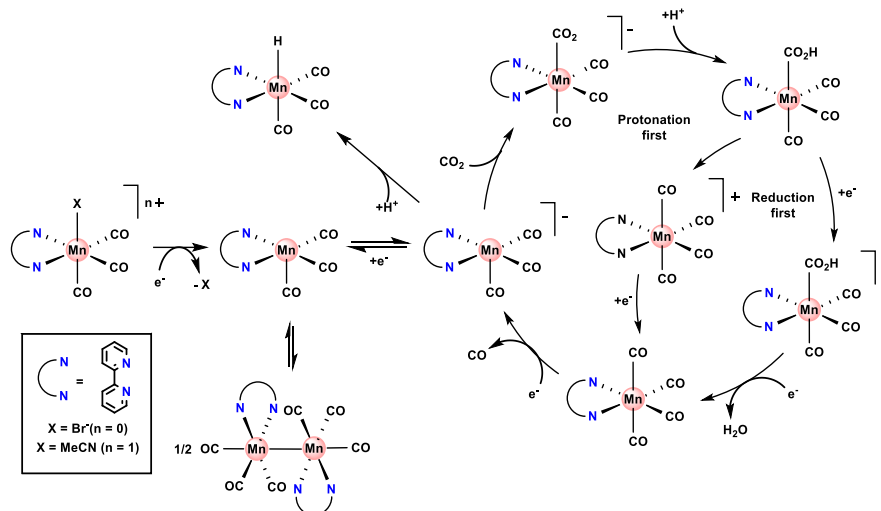


Figure I.7. General mechanistic proposal for the CO₂ reduction catalyzed by **1a** and derivatives.

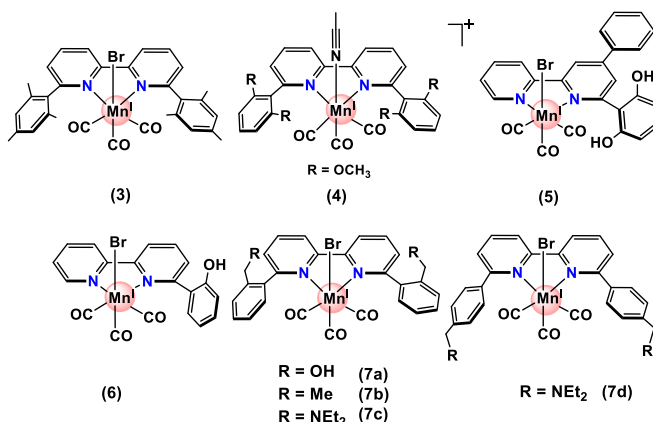


Figure I.8. I) Selected carbonyl bipyridine manganese complexes with ortho substituents introducing a steric influence (**3**, **7b**), weak hydrogen bonding interactions (**4**) and pendant base (**5**, **6**, **7a**, **7c**, **7d**).

One of the first effective modifications of the *fac*-[Mn(bpy)(CO)₃Br] complexes consisted on the introduction of bulky substituents such as mesityl groups at the 6 and 6' position of the bpy, [Mn(mesbpy)(CO)₃Br] (mesbpy = 6,6'-dimesityl-2,2'-bipyridine) (**3**, Figure I.8).^{74, 75} The steric effect induced by the bulky groups prevents the formation of the Mn⁰-Mn⁰ dimeric species, which results in a direct reduction of the [Mn^I] in one more electron to give [Mn⁰]. The anionic complex, [Mn(mesbpy)(CO)₃]⁻, was formed at 300 mV with more positive potential in comparison with its

analogous [Mn(bpy)(CO)₃Br]. However, the reaction with CO₂ does not occur until 400 mV regarding the redox feature. The catalytic activity was remarkable, with a maximum TOF of $5 \times 10^3 \text{ s}^{-1}$ (CH₃CN with 1.4 M TFE), and high FY for CO₂-to-CO reduction. The IR-SEC and chemically prepared reaction intermediates corroborated the formation of [Mn(mesbpy)(CO)₃]⁰ and [Mn(mesbpy)(CO)₃]⁻, with no evidence of dimerization.

Notably, by replacing the Brønsted acid with a Lewis acid,^{71, 74, 75} the catalytic mechanism for the CO₂ reduction is modified. Using Mg cations, [Mn(mesbpy)(CO)₃Br] binds CO₂ at significantly reduced overpotentials ($\eta = 0.3\text{--}0.45 \text{ V}$) and increases the rate of catalysis by 10-fold. The catalytic mechanism based on the variable concentration, CV, IR-SEC, and bulk electrolysis studies showed that, in this case, the catalysis proceeds *via* a reductive disproportionation reaction of $2\text{CO}_2 + 2\text{e}^-$ to give CO and CO₃²⁻ (Figure I.9). Besides the first CO₂ molecule that binds the Mn, a second CO₂ molecule plays the role of acid as an oxygen abstractor. It helps to cleave the C-O bond in the postulated Mn^I-CO₂-Mg intermediate adduct. As a result, a TOF_{CO} of 630 s⁻¹ was achieved at an overpotential as small as ca. 350 mV, showing the boosting effect of the Lewis acid on the catalytic process.

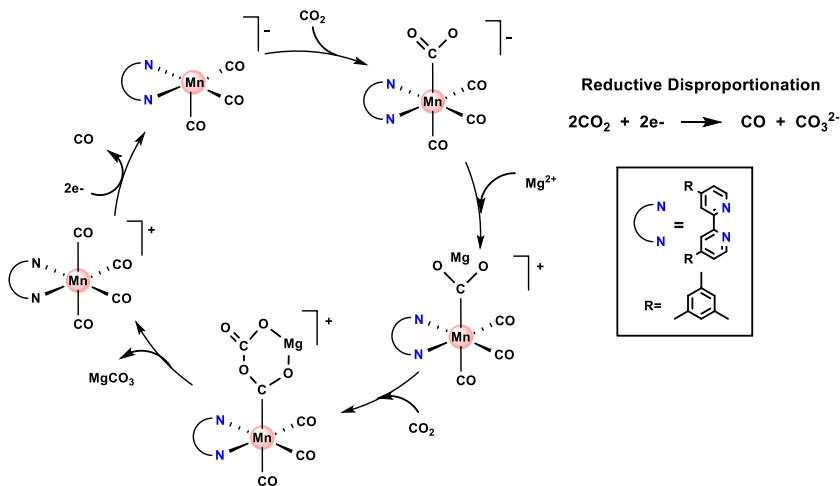


Figure I.9. Proposed mechanism for the electrocatalytic reductive disproportionation reaction of CO₂.

Besides the steric effect of the mesbpy ligand that prevents the dimerization,⁷⁵ Rochford and co-workers tested the $\{fac\text{-Mn}^I([\text{(MeO)}_2\text{Ph}]_2\text{bpy})(\text{CO})_3(\text{CH}_3\text{CN})\}^{\text{OTf}}$ (where $[\text{(MeO)}_2\text{Ph}]_2\text{bpy} = 6,6'\text{-bis}(2,6\text{-dimethoxyphenyl})\text{-}2,2'\text{-bipyridine}$) complex with the extra functionality of ortho-MeO groups at the phenyl rings (**4**, Figure I.8).⁷⁷ The authors proposed an allosteric hydrogen bonding interaction between the methoxy groups and the added Brønsted acid, facilitating the C-OH bond cleavage step. This system presents the first example of a protonation-first pathway and comprises the protonation of the $\{\text{Mn}^I\text{-CO}_2\}$ to give $\{\text{Mn}^I\text{-COOH}\}$ followed by its reduction, thus minimizing the overpotential. PhOH and TFE as proton sources exhibited the largest protonation-first catalytic currents, saving up to 0.55 V in overpotential regarding the thermodynamically demanding reduction-first pathway.

Another example of the effect of a local proton source on the activity of bipyridine Mn complexes was investigated by Gobetto *et al.*⁷⁸ The electrochemical behavior of $fac\text{-}[\text{Mn}(\text{dhbpy})(\text{CO})_3\text{Br}]$ (dhbpy = 4-phenyl-6-(1,3-dihydroxybenzen-2-yl) 2,2'-bipyridine) complex (**5**, Figure I.8) containing two acidic OH groups in the proximity of the metal center that acts as effective local proton sources was studied. This was the first experimental evidence of an intramolecular proton-assisted catalytic process for a Mn^I catalyst. **5** showed substantial catalytic activity, CPE at -1.8 V vs SCE under catalytic conditions showed an unusual change in selectivity for CO₂ reduction, giving a mixture of CO (FY_{CO} = 70%) and HCOOH (FY_{HCOOH} = 22%), suggesting an alternative reaction pathway in catalysis. The mechanism involves the formation of a hydride intermediate issued from intramolecular protonation in the reduced catalyst anion that would further insert CO₂ and evolve HCOOH (Figure I.9).

Bocarsly and co-workers⁷⁹ reported a ligand framework with a phenolic proton in proximity to the CO₂ binding site, $\text{Mn}(\text{HOPh-bpy})(\text{CO})_3\text{Br}$ (**6**, Figure I.8), which allowed easy proton-assisted C-O bond cleavage. In this system, the substitution reduced the overpotential and increased by seven-fold the electrocatalytic current compared to the classic $[\text{Mn}(\text{bpy})(\text{CO})_3\text{Br}]$, even with an added Brønsted acid. CPE produced CO with a FY of 76% after 4 h of electrolysis. Experimental and computational

studies suggested a key mechanistic role for the phenolic proton in the entropic contribution to the activation of free energy for the increased catalytic activity. In the proposed mechanism, the Mn-CO₂ adduct is stabilized *via* hydrogen bonding between the phenolic proton in the second coordination sphere and an O atom of the CO₂.

Recently, Daasbjerg and co-workers reported a series of manganese carbonyl complexes with bipyridine and phenanthroline ligands with modified pendant groups around the coordination sphere of the Mn (**7**, Figure I.8).⁸⁰ Among others, they positioned an alcohol (**7a**), a methyl (**7b**) and a dimethylamine groups (**7c**) at an equivalent location to the methoxide group in the {*fac*-Mn^I[(MeO)₂Ph]₂bpy)(CO)₃(CH₃CN)}(OTf) complex (**4**). Interestingly, the substituent dramatically affected the formed product from CO for **7a** and **7b** to HCOOH with **7c**. The tertiary amines strategically located near the center of the metal were essential for obtaining the HCOOH; CO was the major product if the amine groups were absent (**7a**, **7b**) or placed far from the metal center (**7d**). The amine-modified complexes are among the most active catalysts for reducing CO₂ to formic acid, with a TOF of up to 5500 s⁻¹ at 630 mV of overpotential. Experimental and theoretical studies revealed the role of the amines as proton shuttles, leading to the formation of a Mn-hydride species.

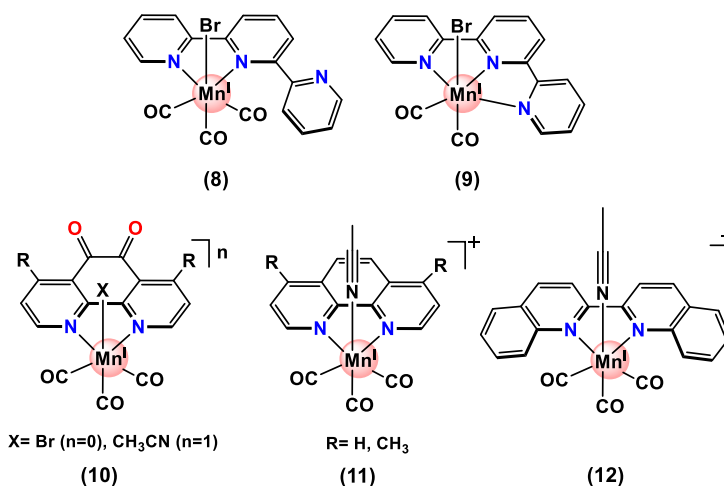


Figure I.10. Carbonyl pyridine-based manganese complexes as electrocatalyst for the CO₂ reduction.

Based on some initial reports on the photo- and electrochemical behavior of Mn with a 2,2':6,2''-terpyridine (tpy) ligand, Machan and Kubiak reported the electrocatalytic characterization of Mn(tpy) carbonyl complexes with k^2 -N,N' (k^2 -tpy) and k^3 -N,N',N'' (k^3 -tpy) coordination modes, Mn(k^2 -tpy)(CO)₃Br and Mn(k^3 -tpy)(CO)₂Br (**8**, **9**, Figure I.10).⁸¹ Although the k^3 form was active for CO₂ reduction, it was susceptible to fast degradation, achieving a maximum TON of 4 before a loss of selectivity. Results suggest that CO ligand replacement requires more strongly binding ligand classes to stabilize the Mn center.

A new manganese tricarbonyl complex bearing a redox-active ligand based on the N,N'-coordinated 1,10-phenanthroline-5,6-dione (phen-dione), *fac*-[Mn(phen-dione)(CO)₃X]ⁿ (where X: Br⁻ (n=0) or CH₃CN (n=1)) (**10**, Figure I.10), was reported by Chardon-Noblat and co-workers.⁸² After a first two-electrons ligand-based reduction, the complex can trap two molecules of CO₂, by ECEC reactions (E: electron transfers and C: chemical steps, respectively). In CH₃CN, the catalyst performed excellent selectivity for catalytic CO₂ reduction to CO or HCOOH through electrochemical or photochemical activation. In their study, when changing the solvent from DMF to CH₃CN, the selectivity towards HCOOH was enhanced. The presence of the π -accepting, redox-active phen-dione ligand resulted in different reduced intermediates compared with standard 2,2'-bipyridine and 1,1'-phenanthroline complexes, with the two first redox processes remaining localized on the ligand.

Systematic variation of the polypyridyl ligands from bpy to phen to dmphen and finally bqnl was reported by Rochford and co-workers (**11**, **12**, Figure I.10).⁸³ The authors concluded that the ligand has both steric and electronic-based influence on the activity of *fac*-[Mn(N^N)(CO)₃(CH₃CN)]⁺ catalysts for CO₂ reduction. In addition, they highlighted the *fac*-[Mn(bqnl)(CO)₃(CH₃CN)]⁺ (bqnl = 2,2'-biquinoline) complexes, where the bqnl ligand exhibited both steric and electronic influence over the fundamental redox properties of the complex and, it was related to the catalytic properties respect to the activation of CO₂.

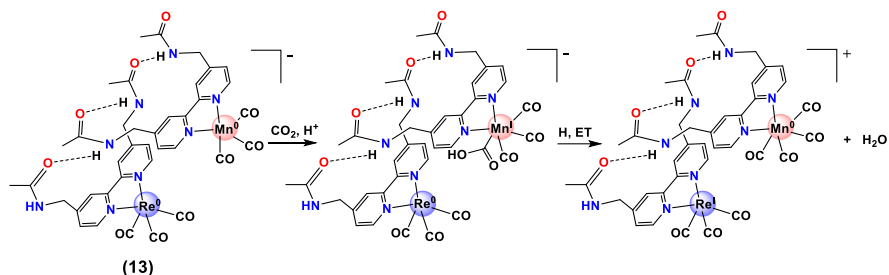


Figure I.11. Hydrogen-bonded heterobimetallic Mn-Re active species for the electrocatalytic CO₂ reduction.

Inspired by the supramolecular assembly of bimetallic species, Kubiak *et al.* studied the co-catalytic effects of a Re–Mn heterobimetallic supramolecular system (**13**, Figure I.11).⁸¹ They combined Re and Mn⁰-based complexes functionalized with methyl acetamidomethyl groups [(M(dacby)(CO)₃Br)] (M= Re, Mn). The formation of hydrogen bonds between the catalysts generated active bimetallic species that produce ~10% more current under catalytic conditions than the individual Re and Mn complexes. The F_YCO was 86% through 4 TONs, based on the total moles of added catalyst. FT-IR-SEC results supported a reaction pathway where a hydrogen-bonded heterobimetallic dimer is initially formed between the [Re⁰(dacby)(CO)₃] and the [Mn⁰(dacby)(CO)₃]⁻. Under CO₂ and a proton source, Mn binds and reduces CO₂ to yield a hydroxycarbonyl specie that can undergo either a protonation or reduction to initiate C–O bond cleavage. The reduced Re species can reduce the Mn hydroxycarbonyl through an electron transfer, and then the spontaneous CO release allows the dimer to re-enter the catalytic cycle.

I.4.2. Heterogeneous {*fac*-Mn(CO)₃} catalysts

Catalysts heterogenization has been a long-standing strategy to improve the stability of molecular catalysts that operate in the homogeneous phase.⁵³⁻⁵⁵ As mentioned above (Section I.3.2), the heterogenization of well-defined catalysts could be prepared by immobilizing them on conducting substrates (carbon supports), metal-oxide nanoparticles, and immobilization into well-defined reticular substrates, such as MOFs and COFs among others.⁶¹ Understanding the relationship

between structure and activity is key to improving robustness, performance, and selectivity, especially in CO₂ reduction reactions.

In order to develop efficient (high TOF_{max}, low η) and robust (high TON) [Mn(N[^]N)(CO)₃X]-based catalysts for CO₂ reduction, the immobilization in a heterogeneous fashion at a solid-state interface has been explored.^{18, 19, 25, 62} The reported strategies for the immobilization include drop-casting of *fac*-[Mn(bpy-R)(CO)₃Br] derivatives mixed with Nafion or Nafion/Multi Walled Carbon Nanotubes (NT) on top of glassy carbon,^{58, 59} *via* π - π stacking interactions,¹⁸ and more sophisticated alternatives like introducing the catalytic units into organic polymers,⁸⁴⁻⁸⁷ the covalently attached to carbon supports,⁸⁸ or on top of silicon nanowires (SiNWs) or photocathodes.^{57, 89} Some of these strategies to improve the stability of the [Mn(N[^]N)(CO)₃X]-based catalysts are included in Figure I.12 and discussed in this section.

The first example of a heterogeneous [Mn(N[^]N)(CO)₃X]-based electrocatalyst for CO₂ reduction was reported by Cowan and co-workers in 2014.⁹⁰ The [Mn(bpy)(CO)₃Br] **1a** (Figure I.12) was cast into a Nafion membrane on a glassy carbon electrode and evaluated in neutral aqueous electrolyte.⁹⁰ CPE of **1a**|Nafion films at -1.4 V *vs* Ag/AgCl produced a ratio of CO:H₂~1:2. A TON of 471 was reported over a 4 h of CPE, representing an improvement of an order-of-magnitude relative to the homogenous Mn(bpy)(CO)₃Br electrocatalyst. As a strategy to increase the electroactive Mn of the Nafion films, the authors added NTs to the catalytic ink (**1a**|Nafion|NT), which resulted in a 10-fold current enhancement and stable FY_{CO} of 22% and FY_{H₂} of 47% during the CPE at -1.4 V *vs* Ag/AgCl in water. In a following study, the catalytic system **1a**|Nafion|NT was modified by introducing hydrophilic ligands [Mn(bpy(^tBu)₂)(CO)₃Br] ((bpy(^tBu)₂) = 4,4'-di-*tert*-butyl-2,2'-bipyridine) (**2a**|Nafion|NT) (Figure I.12). The new catalyst yielded highly active electrodes for the reduction of CO₂ to CO in aqueous solutions at pH 7, exhibiting improved selectivity towards CO₂, with CO:H₂~1 at -1.4 V *vs* SCE, exceeding the reported value for **1a**|Nafion|NT.⁵⁸

On the other hand, Sato and co-workers recently studied a new Mn complex electrocatalyst, the [Mn{4,4'-di(1H-pyrrolyl-3-propyl carbonate)-

2,2'-bipyridine(CO)₃MeCN]⁺(PF₆)⁻ (**15**, Figure I.12).⁸⁵ The evaluation of **15** in homogeneous conditions did not promote the CO₂ reduction reaction. However, when the catalyst was polymerized on NTs interface (**15|NT**), selective reduction of CO₂ to CO (FY_{CO} of 80%,) at a very low overpotential ($\eta_{\text{CO}} = 0.10$ V) in an aqueous solution was observed. A maximum TON of 722 was measured over a 24 h period with a maximum current density of -2.6 mA·cm⁻², demonstrating the remarkable robustness of the catalytic system, with no deterioration of catalytic current. In their study, NTs and K⁺ ions (0.1 M K₂B₄O₇ + 0.2 M K₂SO₄ buffer), have a crucial role in catalysis. The K⁺ improved the double-layer capacitance of NTs electrode while concurrently promoting CO₂ adsorption, synergistically improving the current density and overpotential.

Taking advantage of the π - π self-assembly of a bpy_{pyr} ligand (4-Methyl-4'-(5-(pyren-1-yl)pentyl)-2,2'-bipyridine) on the NTs surface, Reisner and co-workers immobilized pre-catalyst **16** (Figure I.12) and evaluated its catalytic activity in water.¹⁸ The catalyst exhibited CO and HCOOH formation, with the product selectivity tuned by the surface coverage of the Mn complex. Under CPE, the catalyst presented high stability and a maximum TON_{CO} = 1800 and TON_{HCOOH} = 4100 at -1.1 V vs SHE ($\eta_{\text{CO}} = 0.55$ V, $\eta_{\text{HCOOH}} = 0.59$ V). Key intermediates of the CO₂ reduction mechanism were detected by SCE studies (UV-vis-SEC and IR-SEC). At low Mn concentrations, the supported catalyst has low mobility, preventing dimerization, and the Mn-H species is dominant. The Mn-H species are associated with the formation of HCOOH. However, at higher concentrations, the Mn⁰-Mn⁰ prevents the formation of Mn-H, leading to the CO product.

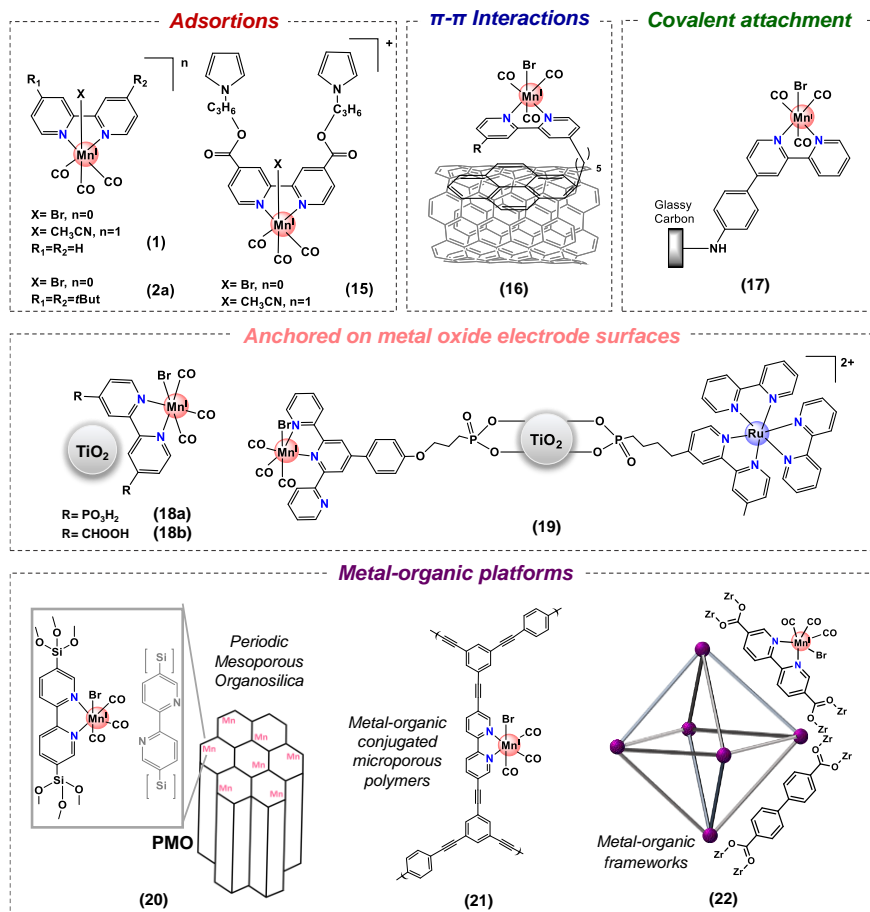


Figure I.12. Strategies to improve the stability of Mn molecular catalysts that operate in homogeneous systems.

On the other hand, Nervi and co-workers covalently attached the catalyst *fac*-Mn(apbpy)(CO)₃Br (17) (apbpy=4-(4-aminophenyl)-2,2'-bipyridine) to the surface of a glassy carbon electrode (Figure I.12).⁸⁸ The immobilization was achieved by two approaches: (i) direct electrochemical oxidation of the amino group with the formation of C–N bonds, and (ii) by diazonium salt derivatization of the amino group and subsequent electrochemical reduction to form a new interfacial C–C bond. The C–C bond resulted in a more stable attachment with a maximum $I_{\text{cat}}/I_{\text{p}}$ of 24 in CH₃CN with MeOH (20%). Products formed resulted in a FY_{CO} of 75% during CPE at -1.75 V vs Fc⁺/Fc, with a TON_{max} of 360, about 60 times higher than the corresponding catalysts in homogeneous solutions.

Immobilizing molecular manganese catalysts on mesoporous TiO₂ has also succeeded in enhancing electrocatalytic and solar-driven CO₂ reduction.¹⁹ In this regard, Reisner and co-workers have also reported a *fac*-[Mn(4,4'-bis(phosphonic acid)-2,2'-bipyridine)(CO)₃Br] (**18a**, Figure I.12) immobilized on a mesoporous TiO₂ electrode with FTO (fluorine-doped tin oxide glass surface), **18a|TiO₂**.⁹¹ The catalyst presented a surface coverage of 34 nmol cm⁻² at the TiO₂ interface and a 4-fold enhancement in current was observed at -1.7 V *vs* Fc⁺/Fc⁰ under CO₂ in CH₃CN with 5% of H₂O. At this potential, CPE resulted in a TON of 110 for CO production, with yields of FY_{CO} = 70% and FE_{H₂} = 13% after 2 hours. Mn⁰-Mn⁰ dimer intermediate was detected on the electrode surface, and its relation to the CO₂ reduction selectivity was studied. From those studies, the product selectivity (HCOO⁻/CO) was again found to be controlled by the Mn loading supported on the TiO₂.^{19, 91-93} These conclusions were similar to the previously obtained when using the assembly of **16**.¹⁸

Following an analogous approach, Walsh and co-workers evaluated [Mn(bpy(COOH)₂)(CO)₃Br] (**18b**) by post-adsorption on a mesoporous anatase TiO₂ film on FTO (**18b|TiO₂**, Figure I.12).¹⁹ Under Ar in CH₃CN, reduction of the **18b|TiO₂** was observed at -1.45 V *vs* Ag/AgNO₃.¹⁹ UV/Vis, cyclic voltammetry and *in situ* IR SEC were used to directly probe the redox behavior of **18b|TiO₂**, leading to elucidation of the CO₂ reduction mechanism by detecting the dimer and anionic intermediates.

Similarly, TiO₂ nanoparticles were successively functionalized with [Mn(k²N¹,N²-ttpy)(CO)₃Br] (ttpy = 4-tolyl-2,2':6'-2''-terpyridine) as catalyst and [Ru(bpy)₃]²⁺ as photosensitizer to yield Ru^{II}/TiO₂/Mn^I (**19**, Figure I.12).⁹² Under photocatalytic conditions with continuous irradiation at 470 nm and in the presence of a sacrificial electron donor, the system efficiently and selectively reduces CO₂ to HCOOH (TON_{max} = 27) with 100% selectivity and a quantum yield of 0.17%. Cyclic voltammetry suggested monomeric Mn⁰ was the catalytically active site in the Ru^{II}/TiO₂/Mn^I hybrid system. In contrast, in a mixed solution of Ru^{II} and Mn^I, a Mn⁰-Mn⁰ dimer was formed, suggesting that the heterogenization prevents the formation of dimers and achieves selectivity toward HCOOH production.

The immobilization of well-defined $\{\text{Mn}(\text{CO})_3\}$ on bpy-Periodic Mesoporous Organosilica (PMO) platform (**20**, Figure I.12) was also reported for the photocatalytic CO₂ reduction.⁹⁴ **20** produces CO (TON_{CO}=239) and HCOOH (TON_{HCOOH}=484). Spectroscopic and catalytic data showed that site isolation of the Mn complex into the PMO framework probably inhibits bimolecular processes, such as dimerization and disproportionation.

In the same way, Cowan and co-workers introduced $\{\text{Mn}(\text{CO})_3\}$ centers in an organic conjugated microporous polymer (CMP) as electrocatalyst for CO₂ reduction in water (**21**, Figure I.12).⁸⁴ They proposed that incorporating the Mn centers in the rigid framework changed the behavior of the catalyst, preventing the reductive dimerization. These studies demonstrated the feasibility of CMP electrodes in providing both high local CO₂ concentrations and well-defined electrocatalytic sites.

In 2015, Kubiak and co-workers reported the incorporation of Mn(bpydc)-(CO)₃Br (bpydc = 5,5'-dicarboxylate-2,2'-bipyridine) complex into a robust Zr(IV)-based metal-organic framework (MOF) platform.⁸⁷ The resulting UiO-67-Mn(bpy)(CO)₃Br (**22**, Figure I.12) presented high efficiency toward CO₂ reduction under visible-light irradiation to produce formate. The catalyst combines the efficient photochemical CO₂ performance of Mn active sites with the enhanced stability of the solid-state MOF host. The photochemical performance of **22** reached a TON_{HCOOH} of approximately 110 in 18 h, exceeding that of the homogeneous reference systems and presenting a selectivity of 96% over 4 h. The increased activity of the Mn catalyst in the MOF was ascribed to the strut of the framework, which provides isolated active sites, stabilizes the catalyst and inhibits dimerization of the one-electron reduced Mn complex.

Moving from homogeneous to immobilized molecular catalysts generally allows working in water, significantly reducing the overpotential but sometimes compromising selectivity. In addition, the loading of active molecules by surface immobilization commonly ranges from 10⁻¹² to 10⁻⁸ mol·cm⁻², limiting overall activity per geometric area. At the same time, higher loading could lead to aggregation or dense stacking of catalyst molecules, impeding the accessibility of substrates to the internal active

sites and hampering the electron transfer to the catalyst molecules far from the electrode surface, thus making it difficult to quantify the intrinsic activity of the catalyst by the TOF value.⁵²

1.5. Reticular Catalysts for CO₂ reduction

Homogeneous molecular catalysts can achieve high selectivity and efficiency but sometimes are inherently limited regarding the activity. In contrast, inorganic catalysts, such as metals and metal oxides, display high efficiency and activity. However, tuning the selectivity at the molecular level remains challenging. The prospect of performing all three aspects in a single system could be achieved in reticular materials.

Reticular materials are constructed by linking molecular building blocks through strong bonds into porous crystalline 2D and 3D frameworks in a designed manner.⁹⁵ The direct integration of discrete molecular catalysts as building blocks into ordered nanoporous framework materials represents a powerful and promising alternative for catalytic applications,⁹⁶ giving a novel way of immobilizing homogenous catalysts. Combining the merits of heterogeneous and homogeneous catalysts, the reticular chemistry endows the framework materials with high surface areas, porous structures, and potential rational tailored for optimizing CO₂RR performance.^{96, 97}

In particular, Metal Organic Frameworks (MOFs) and Covalent Organic Frameworks (COFs) are reticular materials that can be ideal platforms for CO₂RR.^{98, 99} In terms of selectivity, these materials are constructed from molecular building units, which allow the integration of well-defined, highly selective molecular catalysts within the backbone of the frameworks.^{100, 101} Their structures and properties can be precisely controlled by varying the constituent geometry and by grafting functional groups. Regarding activity, COFs and MOFs present high surface areas and tunable pore metrics, thus allowing for facile diffusion of substrates to the active sites.^{102, 103} The high-density integration of molecular catalysts and the uniform dispersion of active sites within those frameworks avoid aggregation, maximizing their utilization. Moreover, the uniform reaction microenvironment around the active sites and porous structures can be tuned to favor a specific reaction pathway, which benefits the activity and

selectivity of CO₂RR.¹⁰⁴ Finally, in efficiency, great strides have been made in engineering the band gaps and/or intrinsic charge carrier mobility of different MOF and COF structures.^{105, 106} In general, the MOFs and COFs backbones are responsible for activity and efficiency, and the framework handles the selectivity.^{95, 107}

I.5.1. COFs electrocatalysts for CO₂ reduction

COFs consist of purely organic linking units crystallizing as porous and extended structures in which strong covalent linkages build up the frameworks.⁹⁹⁻⁹⁵ Being extended frameworks linked by strong covalent bonds, COFs are expected to be more stable than their MOF counterparts, whose structures are based on metal–oxide links. Such strong covalent linkages, however, negatively affect the association and dissociation of bonds during the crystallization process, thus reducing the crystallinity of the resulting COFs.¹⁰⁸

In reticular chemistry, porosity is a critical factor. The porosity of COFs is attributed to the cages/pores formed by reticulating organic Secondary Building Units (SBUs) into extended structures. Unlike other amorphous materials (e.g., activated carbon, amorphous polymers), COFs crystallize from various organic SBUs by co-condensation, self-condensation, or ring-closing reaction.^{99, 109-110, 111} In addition, COF structures can be determined by X-ray diffraction (XRD), thus allowing structural optimization at the molecular level. High crystalline COFs have minimal defects. In this sense, the well-defined structure and high crystallinity distinguish COFs from amorphous polymers in many applications related to understanding molecular interactions, structure tailoring, Post Synthetic Modification (PSM), and synergic effects.¹¹¹⁻¹¹⁴

2D-COFs are typically stacked in AA mode, which may hinder access to the active sites.^{115, 116} Such drawbacks can be remediated by exfoliating the bulk material into a few layer nanosheets. In this regard, 3D frameworks seem preferable, which theoretically can completely spatially disperse every catalytically active unit to avoid being poisoned by dimerization, thus maximizing the spatial addressability.¹¹⁷⁻¹¹⁹

Reticular materials would be ideal systems to expand the study of the effect of the local microenvironment of molecularly defined catalytic sites by making the utmost of the second coordination sphere effects in molecular catalysis.^{120, 121} COFs, ensure with their periodic nanoporous structures a high-density encapsulation of guest molecules, consequently producing a potential spatial confinement effect on reaction substrates or intermediates and uniform microenvironment favorable for highly selective catalysis. In this sense, encapsulating molecular catalysts into ordered porous has been shown to govern the catalyst's reaction microenvironment and affect the delivery, local concentration, and activation of reaction substrates.¹⁰⁹

To date, porphyrins (Por), phthalocyanines (Pc) and bipyridine (bpy) - based complexes have been integrated as building blocks into COFs or MOFs for CO₂RR.¹²² In particular, this section will mainly focus on recent work of immobilizing metal complexes into COFs for CO₂RR applications.¹²³

In a pioneering work, a metalloporphyrin-based COF (**COF-366-Co**) was reported by Yaghi and co-workers as an active electrocatalyst for CO₂ reduction.¹¹⁹ The incorporation of catalytic cobalt porphyrin units into COFs generated highly active, stable, and selective electrocatalysts for CO₂ to CO reduction in aqueous solutions. CPE of **COF-366-Co** in water at an overpotential of -0.55 V vs RHE, produced 36 mL mg⁻¹ of CO during 24 h with a F_{YCO} of 90%, 10% higher than the observed for the molecular cobalt porphyrin. In this system, only the exposed metalloporphyrin centers of the COF nanocrystals were accessible to the molecular reactants due to AA co-facial stacks of the Co-porphyrins, which were estimated to correspond to 4% of all the Co centers. Interestingly, when the pore size of **COF-366-Co** was increased using isorecticular expansion (1.8 to 2.3 nm) (**COF-367-Co**), the catalytic activity toward CO₂ reduction was improved. The extended **COF-367-Co** produced 100 mL mg⁻¹ of CO under identical conditions and , presented a higher BET (Brunauer-Emmett-Teller) surface area and a wider channel, improving the surface concentration of the electroactive cobalt porphyrin sites, with the accessibility of 8% of the cobalt sites in the entire framework. At -0.67 V vs RHE, **COF-367-Co** yielded a TON of

48000 with a high FY_{CO} of 91%. Besides framework expansion, the catalyst performance was further tailored. Since it was hypothesized that not all electroactive sites (cobalt porphyrin moieties) in the parent material fully participate in the reaction, a partial replacement of these sites with catalytically inactive copper porphyrin units was examined (**COF-367-Co(1%)**). Indeed, the catalyst dilution strategy led to a material that achieved TONs of up to 290000, with an initial TOF of 9400 h^{-1} , resulting in a 26-fold performance improvement compared to the molecular cobalt complex.

Due to the efficient charge transport along the COF backbone, they were optimizing the electronic properties of the metal centers through proper remote functionalization of the linker units, consequently improving their activity and selectivity. In this sense, the reactivity of metal porphyrins was tuned by introducing different substituent groups on the building blocks of **COF-366-Co** (Figure I.13).¹²⁴ Yaghi and co-workers reported a series of COFs with different electronegative substituents on the BDA (1,4-benzenedicarboxaldehyde) units **COF-366-(OMe)₂-Co**, **COF-366-F-Co** and **COF-366-(F)₄-Co**. The matrixes of the structure of the COFs remained essentially unaltered, and their affinities to CO₂ were similar, revealing that those factors hardly contributed to their different CO₂RR reactivities. A cathodic wave was observed when the COFs were tested for CO₂RR in organic electrolytes. Additionally, in water, the electron-withdrawing character of the linkers also improved the catalytic behavior of the framework, increasing the current density for CO formation.

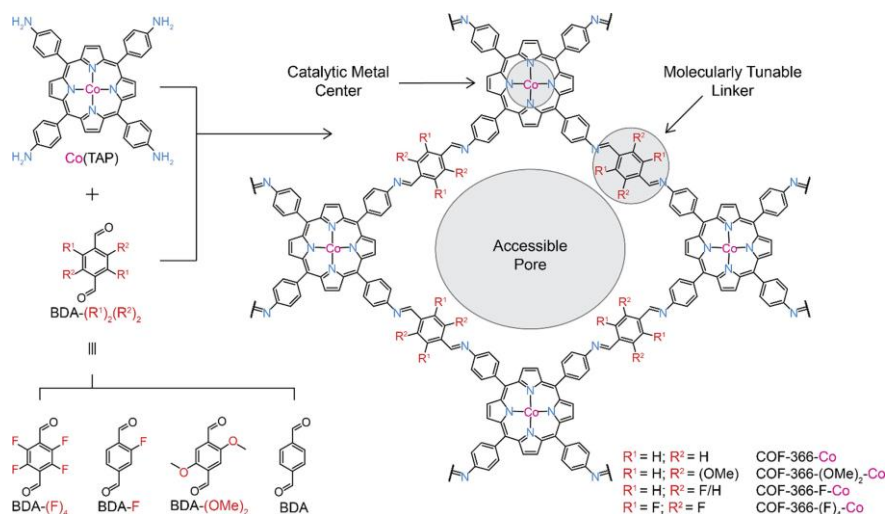


Figure I.13. Reticular electronic tuning of COF-366-Co for electrocatalytic CO₂ reduction. Reproduced with permission from [124] Copyright 2017 American Chemical Society.

The incorporation of molecular catalysts into the COFs' linkers has also been studied.^{125, 126} In particular, {Re(2,2'-bpy)(CO)₃} fragments were integrated into a COF (**COF-2,2'-bpy-Re**) by PSM. The material was evaluated for electrocatalytic CO₂ in an organic solvent. **COF-2,2'-bpy-Re** was selective for CO with a FY_{CO} of 81% but at a high overpotential -2.8 V vs Fc⁺/Fc.¹²⁶

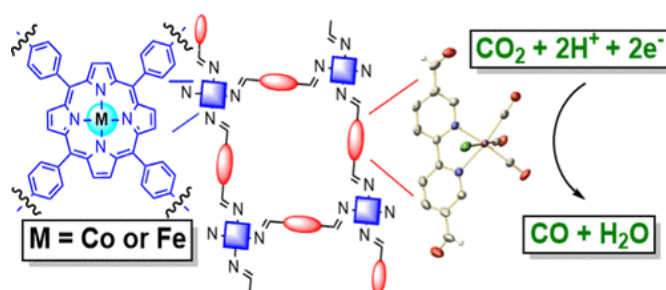


Figure I.14. Heterobimetallic Covalent-Organic Frameworks composed of Rhenium Bipyridine and Metal Porphyrins (COF-Re_{Co}, COF-Re_{Fe}) for the electrocatalytic CO₂ reduction. Reproduced with permission from [125]. Copyright 2018 American Chemical Society

Following a similar strategy, a COF with metalloporphyrin (Fe or Co) and metal bipyridine (Re) moieties were also synthesized (**COF-Re_Co** and **COF-Re_Fe**)(Figure I.14). XPS and FT-IR experiments confirmed the molecular nature of the incorporated catalysts and PXRD studies established the retention of long-range order of the frameworks after the integration of the two different metal sites. During CPE in water, the **COF-Re_Co** performed better activity toward CO₂ reduction but only reached a small FY_{CO} of 18%.¹²⁵

Additionally, COFs have been shown as excellent precursors or carriers for Single Atom Catalysts (SAC) due to their unique features allowing sophisticated control over the catalytic motif, support composition and microstructures. COFs minimize the sizes of catalytic nanoparticles and, as a result, expose more reactive sites to facilitate the mass/electron transfer at the interface and to achieve high catalytic reactivity.^{96, 127}

In addition, the tunability of COFs structure allows to accommodate different π -conjugated modules, with electron donor and acceptor groups, which could form excellent antennae and achieve effective harvesting of the whole sunlight spectrum^{96, 128, 129} In this sense, several examples of using COFs as a platform for the heterogeneous photocatalytic CO₂ reduction have been reported.^{97, 130, 131} For example, Re molecular complexes, a well-known photocatalyst for CO₂ reduction with intrinsic light absorption and charge separation (CS) properties, has also been combined with COF materials.^{132, 133} In 2018, Huang *et al.* reported the first **Re-COF** based hybrid photocatalyst system.¹³⁸ The **Re-COF** efficiently reduces CO₂ to CO under visible light with high selectivity (98%) and better activity than its homogeneous Re counterpart.¹³² Similarly, in 2019, Zou *et al.* introduced the photoactive Re complex (Re(CO)₅Cl) into a bipyridine-based COF (**Re-Tp-bpy-COF**).¹³³ The hybrid material also showed excellent photocatalytic CO₂ reduction activity and stability.

Following a similar strategy, the incorporation of Mn(bpy)(CO)₃Br into a TTA-COF (TTA: 4,4',4''-(1,3,5-triazine-2,4,6-triyl) trianiline) to form the **Mn TTA-COF** (Figure I. 15) was also reported.¹³⁴ The resulted **Mn TTA-COF** was active for CO₂ reduction to form CO under visible light

but with low efficiency due to the decomposition of Mn moiety through the elimination of the CO ligand.¹³⁴

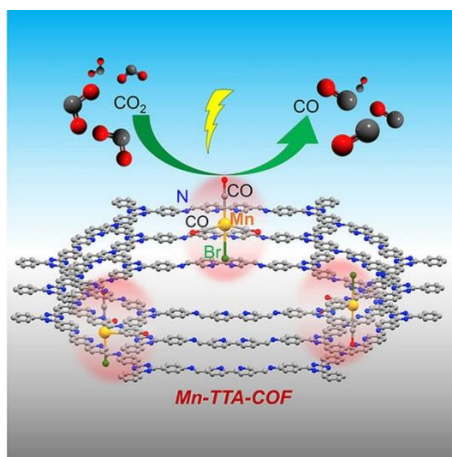


Figure I. 15. 2D Covalent Organic Frameworks with an incorporated Manganese complex for photocatalytic CO₂ reduction. Reproduced with permission from [134].

From the above examples, we can rationalize that bpy-based COFs can be excellent supporters, acting similar to non-innocent ligands to render stability for the homogeneous complex molecular catalyst, achieving a recyclable and reusable hybrid CO₂ catalytic reduction system.^{135, 136}

Additional review of some of the seminal and representative works of COFs for CO₂RR will be introduced in Chapters III and IV.

I.6. References

1. Beer, C.; Reichstein, M.; Tomelleri, E.; Ciais, P.; Jung, M.; Carvalhais, N.; Rödenbeck, C.; Arain, M. A.; Baldocchi, D.; Bonan, G. B.; Bondeau, A.; Cescatti, A.; Lasslop, G.; Lindroth, A.; Lomas, M.; Luysaert, S.; Margolis, H.; Oleson, K. W.; Rouspard, O.; Veenendaal, E.; Viogy, N.; Williams, C.; Woodward, F. I.; Papale, D., Terrestrial Gross Carbon Dioxide Uptake: Global Distribution and Covariation with Climate. *Science* **2010**, *329* (5993), 834.
2. Lu, Q.; Jiao, F., Electrochemical CO₂ reduction: Electrocatalyst, reaction mechanism, and process engineering. *Nano Energy* **2016**, *29*, 439-456.
3. Luna, P. D.; Hahn, C.; Higgins, D.; Jaffer, S. A.; Jaramillo, T. F.; Sargent, E. H., What would it take for renewably powered electrosynthesis to displace petrochemical processes? *Science* **2019**, *364* (6438), eaav3506.
4. Gao, Y.; Gao, X.; Zhang, X., The 2 °C Global Temperature Target and the Evolution of the Long-Term Goal of Addressing Climate Change—From the United Nations Framework Convention on Climate Change to the Paris Agreement. *Engineering* **2017**, *3* (2), 272-278.
5. Habisreutinger, S. N.; Schmidt-Mende, L.; Stolarczyk, J. K., Photocatalytic Reduction of CO₂ on TiO₂ and Other Semiconductors. *Angewandte Chemie International Edition* **2013**, *52* (29), 7372-7408.
6. Zhou, X.; Liu, R.; Sun, K.; Chen, Y.; Verlage, E.; Francis, S. A.; Lewis, N. S.; Xiang, C., Solar-Driven Reduction of 1 atm of CO₂ to Formate at 10% Energy-Conversion Efficiency by Use of a TiO₂-Protected III–V Tandem Photoanode in Conjunction with a Bipolar Membrane and a Pd/C Cathode. *ACS Energy Letters* **2016**, *1* (4), 764-770.
7. Bushuyev, O. S.; De Luna, P.; Dinh, C. T.; Tao, L.; Saur, G.; van de Lagemaat, J.; Kelley, S. O.; Sargent, E. H., What Should We Make with CO₂ and How Can We Make It? *Joule* **2018**, *2* (5), 825-832.
8. De Luna, P.; Hahn, C.; Higgins, D.; Jaffer, S. A.; Jaramillo, T. F.; Sargent, E. H., What would it take for renewably powered electrosynthesis to displace petrochemical processes? *Science* **2019**, *364* (6438).
9. Centi, G.; Perathoner, S., Opportunities and prospects in the chemical recycling of carbon dioxide to fuels. *Catal. Today* **2009**, *148* (3), 191-205.
10. Mikkelsen, M.; Jørgensen, M.; Krebs, F. C., The teraton challenge. A review of fixation and transformation of carbon dioxide. *Energy Environ. Sci.* **2010**, *3* (1), 43-81.
11. Schneider, J.; Jia, H.; Muckerman, J. T.; Fujita, E., Thermodynamics and kinetics of CO₂, CO, and H⁺ binding to the metal centre of CO₂reductioncatalysts. *Chemical Society Reviews* **2012**, *41* (6), 2036-2051.
12. Bard, A. J.; Parsons, R.; Jordan, J., *Standard Potentials in Aqueous Solution*. CRC Press: New York 1985.
13. Peterson, A. A.; Abild-Pedersen, F.; Studt, F.; Rossmeisl, J.; Nørskov, J. K., How copper catalyzes the electroreduction of carbon dioxide into hydrocarbon fuels. *Energy & Environmental Science* **2010**, *3* (9), 1311-1315.
14. Boutin, E.; Merakeb, L.; Ma, B.; Boudy, B.; Wang, M.; Bonin, J.; Anxolabéhère-Mallart, E.; Robert, M., Molecular catalysis of CO₂ reduction: recent advances and perspectives in electrochemical and light-driven processes with selected Fe, Ni and Co aza macrocyclic and polypyridine complexes. *Chemical Society Reviews* **2020**, *49* (16), 5772-5809.

15. Stratakes, B. M.; Dempsey, J. L.; Miller, A. J. M., Determining the Overpotential of Electrochemical Fuel Synthesis Mediated by Molecular Catalysts: Recommended Practices, Standard Reduction Potentials, and Challenges. *ChemElectroChem* **2021**, *8* (22), 4161-4180.
16. Mortimer, R. J., Spectroelectrochemistry, Applications. In *Encyclopedia of Spectroscopy and Spectrometry (Third Edition)*, Lindon, J. C.; Tranter, G. E.; Koppenaal, D. W., Eds. Academic Press: Oxford, 2017; pp 160-171.
17. Kornienko, N.; Zhao, Y.; Kley, C. S.; Zhu, C.; Kim, D.; Lin, S.; Chang, C. J.; Yaghi, O. M.; Yang, P., Metal–Organic Frameworks for Electrocatalytic Reduction of Carbon Dioxide. *Journal of the American Chemical Society* **2015**, *137* (44), 14129-14135.
18. Reuillard, B.; Ly, K. H.; Rosser, T. E.; Kuehnel, M. F.; Zebger, I.; Reisner, E., Tuning Product Selectivity for Aqueous CO₂ Reduction with a Mn(bipyridine)-pyrene Catalyst Immobilized on a Carbon Nanotube Electrode. *Journal of the American Chemical Society* **2017**, *139* (41), 14425-14435.
19. Walsh, J. J.; Forster, M.; Smith, C. L.; Neri, G.; Potter, R. J.; Cowan, A. J., Directing the mechanism of CO₂ reduction by a Mn catalyst through surface immobilization. *Physical Chemistry Chemical Physics* **2018**, *20* (10), 6811-6816.
20. Machan, C. W., Recent advances in spectroelectrochemistry related to molecular catalytic processes. *Current Opinion in Electrochemistry* **2019**, *15*, 42-49.
21. Elgrishi, N.; Chambers, M. B.; Wang, X.; Fontecave, M., Molecular polypyridine-based metal complexes as catalysts for the reduction of CO₂. *Chemical Society Reviews* **2017**, *46* (3), 761-796.
22. Grice, K. A.; Saucedo, C., Electrocatalytic Reduction of CO₂ by Group 6 M(CO)₆ Species without “Non-Innocent” Ligands. *Inorganic Chemistry* **2016**, *55* (12), 6240-6246.
23. Qiao, J.; Liu, Y.; Hong, F.; Zhang, J., A review of catalysts for the electroreduction of carbon dioxide to produce low-carbon fuels. *Chemical Society Reviews* **2014**, *43* (2), 631-675.
24. Bonin, J.; Maurin, A.; Robert, M., Molecular catalysis of the electrochemical and photochemical reduction of CO₂ with Fe and Co metal based complexes. Recent advances. *Coordination Chemistry Reviews* **2017**, *334*, 184-198.
25. Fernández, S.; Dubed Bandomo, G. C.; Lloret-Fillol, J., Recent advances in electrocatalytic CO₂ reduction with molecular complexes. In *Advances in Inorganic Chemistry*, Academic Press: 2022.
26. Takeda, H.; Cometto, C.; Ishitani, O.; Robert, M., Electrons, Photons, Protons and Earth-Abundant Metal Complexes for Molecular Catalysis of CO₂ Reduction. *ACS Catalysis* **2017**, *7* (1), 70-88.
27. Collin, J. P.; Sauvage, J. P., Electrochemical reduction of carbon dioxide mediated by molecular catalysts. *Coord. Chem. Rev.* **1989**, *93* (2), 245-268.
28. Grice, K. A., Carbon dioxide reduction with homogenous early transition metal complexes: Opportunities and challenges for developing CO₂ catalysis. *Coordination Chemistry Reviews* **2017**, *336*, 78-95.
29. Benson, E. E.; Kubiak, C. P.; Sathrum, A. J.; Smieja, J. M., Electrocatalytic and homogeneous approaches to conversion of CO₂ to liquid fuels. *Chemical Society Reviews* **2009**, *38* (1), 89-99.

30. Meshitsuka, S.; Ichikawa, M.; Tamaru, K., Electrocatalysis by metal phthalocyanines in the reduction of carbon dioxide. *Journal of the Chemical Society, Chemical Communications* **1974**, (5), 158-159.
31. Fisher, B. J.; Eisenberg, R., Electrocatalytic reduction of carbon dioxide by using macrocycles of nickel and cobalt. *Journal of the American Chemical Society* **1980**, *102* (24), 7361-7363.
32. Beley, M.; Collin, J.-P.; Ruppert, R.; Sauvage, J.-P., Nickel(II)-cyclam: an extremely selective electrocatalyst for reduction of CO₂ in water. *Journal of the Chemical Society, Chemical Communications* **1984**, (19), 1315-1316.
33. Tinnemans, A. H. A.; Koster, T. P. M.; Thewissen, D. H. M. W.; Mackor, A., Tetraaza-macrocyclic cobalt(II) and nickel(II) complexes as electron-transfer agents in the photo(electro)chemical and electrochemical reduction of carbon dioxide. *Recueil des Travaux Chimiques des Pays-Bas* **1984**, *103* (10), 288-295.
34. Grice, K. A.; Kubiak, C. P., Chapter Five - Recent Studies of Rhenium and Manganese Bipyridine Carbonyl Catalysts for the Electrochemical Reduction of CO₂. In *Advances in Inorganic Chemistry*, Aresta, M.; van Eldik, R., Eds. Academic Press: 2014; Vol. 66, pp 163-188.
35. Balazs, G. B.; Anson, F. C., The adsorption of Ni(cyclam)+ at mercury electrodes and its relation to the electrocatalytic reduction of CO₂. *Journal of Electroanalytical Chemistry* **1992**, *322* (1), 325-345.
36. Costentin, C.; Savéant, J.-M., Towards an intelligent design of molecular electrocatalysts. *Nature Reviews Chemistry* **2017**, *1* (11), 0087.
37. Gonell, S.; Lloret-Fillol, J.; Miller, A. J. M., An Iron Pyridyl-Carbene Electrocatalyst for Low Overpotential CO₂ Reduction to CO. *ACS Catalysis* **2021**, *11* (2), 615-626.
38. Riplinger, C.; Sampson, M. D.; Ritzmann, A. M.; Kubiak, C. P.; Carter, E. A., Mechanistic Contrasts between Manganese and Rhenium Bipyridine Electrocatalysts for the Reduction of Carbon Dioxide. *Journal of the American Chemical Society* **2014**, *136* (46), 16285-16298.
39. Franco, F.; Pinto, M. F.; Royo, B.; Lloret-Fillol, J., A Highly Active N-Heterocyclic Carbene Manganese(I) Complex for Selective Electrocatalytic CO₂ Reduction to CO. *Angewandte Chemie International Edition* **2018**, *57* (17), 4603-4606.
40. Fernández, S.; Franco, F.; Casadevall, C.; Martin-Diaconescu, V.; Luis, J. M.; Lloret-Fillol, J., A Unified Electro- and Photocatalytic CO₂ to CO Reduction Mechanism with Aminopyridine Cobalt Complexes. *Journal of the American Chemical Society* **2020**, *142* (1), 120-133.
41. Azcarate, I.; Costentin, C.; Robert, M.; Savéant, J.-M., Through-Space Charge Interaction Substituent Effects in Molecular Catalysis Leading to the Design of the Most Efficient Catalyst of CO₂-to-CO Electrochemical Conversion. *Journal of the American Chemical Society* **2016**, *138* (51), 16639-16644.
42. Chen, L.; Guo, Z.; Wei, X.-G.; Gallenkamp, C.; Bonin, J.; Anxolabéhère-Mallart, E.; Lau, K.-C.; Lau, T.-C.; Robert, M., Molecular Catalysis of the Electrochemical and Photochemical Reduction of CO₂ with Earth-Abundant Metal Complexes. Selective Production of CO vs HCOOH by Switching of the Metal Center. *J. Am. Chem. Soc.* **2015**, *137* (34), 10918-10921.
43. Liu, D.-C.; Zhong, D.-C.; Lu, T.-B., Non-noble metal-based molecular complexes for CO₂ reduction: From the ligand design perspective. *EnergyChem* **2020**, *2* (3), 100034.

44. Eren, E. O.; Özkar, S., Recent advances in heterogeneous catalysts for the effective electroreduction of carbon dioxide to carbon monoxide. *Journal of Power Sources* **2021**, *506*, 230215.
45. Zhao, G.; Huang, X.; Wang, X.; Wang, X., Progress in catalyst exploration for heterogeneous CO₂ reduction and utilization: a critical review. *Journal of Materials Chemistry A* **2017**, *5* (41), 21625-21649.
46. Kuhl, K. P.; Hatsukade, T.; Cave, E. R.; Abram, D. N.; Kibsgaard, J.; Jaramillo, T. F., Electrocatalytic conversion of carbon dioxide to methane and methanol on transition metal surfaces. *J Am Chem Soc* **2014**, *136* (40), 14107-13.
47. Zhu, D. D.; Liu, J. L.; Qiao, S. Z., Recent Advances in Inorganic Heterogeneous Electrocatalysts for Reduction of Carbon Dioxide. *Adv Mater* **2016**, *28* (18), 3423-52.
48. Asadi, M.; Kim, K.; Liu, C.; Addepalli, A. V.; Abbasi, P.; Yasaei, P.; Phillips, P.; Behranginia, A.; Cerrato, J. M.; Haasch, R.; Zapol, P.; Kumar, B.; Klie, R. F.; Abiade, J.; Curtiss, L. A.; Salehi-Khojin, A., Nanostructured transition metal dichalcogenide electrocatalysts for CO₂ reduction in ionic liquid. *Science* **2016**, *353* (6298), 467-70.
49. Cao, Z.; Kim, D.; Hong, D.; Yu, Y.; Xu, J.; Lin, S.; Wen, X.; Nichols, E. M.; Jeong, K.; Reimer, J. A.; Yang, P.; Chang, C. J., A Molecular Surface Functionalization Approach to Tuning Nanoparticle Electrocatalysts for Carbon Dioxide Reduction. *Journal of the American Chemical Society* **2016**, *138* (26), 8120-8125.
50. Chen, Y.; Li, C. W.; Kanan, M. W., Aqueous CO₂ Reduction at Very Low Overpotential on Oxide-Derived Au Nanoparticles. *Journal of the American Chemical Society* **2012**, *134* (49), 19969-19972.
51. Hisatomi, T.; Domen, K., Introductory lecture: sunlight-driven water splitting and carbon dioxide reduction by heterogeneous semiconductor systems as key processes in artificial photosynthesis. *Faraday Discussions* **2017**, *198* (0), 11-35.
52. Sun, C.; Gobetto, R.; Nervi, C., Recent advances in catalytic CO₂ reduction by organometal complexes anchored on modified electrodes. *New Journal of Chemistry* **2016**, *40* (7), 5656-5661.
53. Pittman, C. U.; Smith, L. R., Selective, high-yield, linear dimerization of 1,3-butadiene catalyzed by dibromobis(triphenylphosphine)nickel and sodium tetrahydroborate and its polymer-bound nickel(0) analog. *Journal of the American Chemical Society* **1975**, *97* (2), 341-344.
54. Yang, D.; Ni, B.; Wang, X., Heterogeneous Catalysts with Well-Defined Active Metal Sites toward CO₂ Electrocatalytic Reduction. *Advanced Energy Materials* **2020**, *10* (25), 2001142.
55. Wagner, A.; Sahm, C. D.; Reisner, E., Towards molecular understanding of local chemical environment effects in electro- and photocatalytic CO₂ reduction. *Nature Catalysis* **2020**.
56. Wang, J.; Dou, S.; Wang, X., Structural tuning of heterogeneous molecular catalysts for electrochemical energy conversion. *Science Advances* *7* (13), eabf3989.
57. Torralba-Peñalver, E.; Luo, Y.; Compain, J.-D.; Chardon-Noblat, S.; Fabre, B., Selective Catalytic Electroreduction of CO₂ at Silicon Nanowires (SiNWs) Photocathodes Using Non-Noble Metal-Based Manganese Carbonyl

Bipyridyl Molecular Catalysts in Solution and Grafted onto SiNWs. *ACS Catalysis* **2015**, 5 (10), 6138-6147.

58. Walsh, J. J.; Smith, C. L.; Neri, G.; Whitehead, G. F. S.; Robertson, C. M.; Cowan, A. J., Improving the efficiency of electrochemical CO₂ reduction using immobilized manganese complexes. *Faraday Discussions* **2015**, 183 (0), 147-160.

59. Neri, G.; Donaldson, P. M.; Cowan, A. J., In situ study of the low overpotential “dimer pathway” for electrocatalytic carbon dioxide reduction by manganese carbonyl complexes. *Physical Chemistry Chemical Physics* **2019**, 21 (14), 7389-7397.

60. O'Toole, T. R.; Margerum, L. D.; Westmoreland, T. D.; Vining, W. J.; Murray, R. W.; Meyer, T. J., Electrocatalytic reduction of CO₂ at a chemically modified electrode. *Journal of the Chemical Society, Chemical Communications* **1985**, (20), 1416-1417.

61. Strategies to Immobilized Catalysts. In *Catalyst Immobilization*, 2020; pp 1-22.

62. Grills, D. C.; Ertem, M. Z.; McKinnon, M.; Ngo, K. T.; Rochford, J., Mechanistic aspects of CO₂ reduction catalysis with manganese-based molecular catalysts. *Coordination Chemistry Reviews* **2018**, 374, 173-217.

63. Sinopoli, A.; La Porte, N. T.; Martinez, J. F.; Wasielewski, M. R.; Sohail, M., Manganese carbonyl complexes for CO₂ reduction. *Coordination Chemistry Reviews* **2018**, 365, 60-74.

64. Hawecker, J.; Lehn, J.-M.; Ziessel, R., Electrocatalytic reduction of carbon dioxide mediated by Re(bipy)(CO)₃Cl (bipy = 2,2'-bipyridine). *Journal of the Chemical Society, Chemical Communications* **1984**, (6), 328-330.

65. Bourrez, M.; Molton, F.; Chardon-Noblat, S.; Deronzier, A., [Mn(bipyridyl)(CO)₃Br]: An Abundant Metal Carbonyl Complex as Efficient Electrocatalyst for CO₂ Reduction. *Angewandte Chemie International Edition* **2011**, 50 (42), 9903-9906.

66. Bourrez, M.; Orio, M.; Molton, F.; Vezin, H.; Duboc, C.; Deronzier, A.; Chardon-Noblat, S., Pulsed-EPR Evidence of a Manganese(II) Hydroxycarbonyl Intermediate in the Electrocatalytic Reduction of Carbon Dioxide by a Manganese Bipyridyl Derivative. *Angewandte Chemie International Edition* **2014**, 53 (1), 240-243.

67. Hartl, F.; Rossenaar, B. D.; Stor, G. J.; Stufkens, D. J., Role of an electron-transfer chain reaction in the unusual photochemical formation of five-coordinated anions [Mn(CO)₃(α -diimine)]⁻ from fac-[Mn(X)(CO)₃(α -diimine)] (X = halide) at low temperatures. *Recl. Trav. Chim. Pays-Bas* **1995**, 114 (11-12), 565-570.

68. Stor, G. J.; Morrison, S. L.; Stufkens, D. J.; Oskam, A., The Remarkable Photochemistry of fac-XMn(CO)₃(α -diimine) (X = Halide): Formation of Mn₂(CO)₆(α -diimine)₂ via the mer Isomer and Photocatalytic Substitution of X- in the Presence of PR₃. *Organometallics* **1994**, 13 (7), 2641-2650.

69. Kokkes, M. W.; De Lange, W. G. J.; Stufkens, D. J.; Oskam, A., Photochemistry of metal—metal bonded complexes: III. MLCT photolysis of (CO)₅MM'(CO)₃(α -diimine) (M, M' = Mn, Re) in 2-Me-THF and THF at 293 K; Evidence of photocatalytic formation of [(Mn(CO)₃(α -diimine)(P(n-Bu)₃)]⁺ [M(CO)₅] - upon photolysis in the presence of P(n-Bu)₃. *J. Organomet. Chem.* **1985**, 294 (1), 59-73.

70. Neri, G.; Walsh, J. J.; Teobaldi, G.; Donaldson, P. M.; Cowan, A. J., Detection of catalytic intermediates at an electrode surface during carbon dioxide reduction by an earth-abundant catalyst. *Nature Catalysis* **2018**, *1* (12), 952-959.
71. Smieja, J. M.; Sampson, M. D.; Grice, K. A.; Benson, E. E.; Froehlich, J. D.; Kubiak, C. P., Manganese as a Substitute for Rhenium in CO₂ Reduction Catalysts: The Importance of Acids. *Inorg. Chem.* **2013**, *52* (5), 2484-2491.
72. Grills, D. C.; Farrington, J. A.; Layne, B. H.; Lyman, S. V.; Mello, B. A.; Preses, J. M.; Wishart, J. F., Mechanism of the Formation of a Mn-Based CO₂ Reduction Catalyst Revealed by Pulse Radiolysis with Time-Resolved Infrared Detection. *J. Am. Chem. Soc.* **2014**, *136* (15), 5563-5566.
73. Machan, C. W.; Sampson, M. D.; Chabolla, S. A.; Dang, T.; Kubiak, C. P., Developing a Mechanistic Understanding of Molecular Electrocatalysts for CO₂ Reduction using Infrared Spectroelectrochemistry. *Organometallics* **2014**, *33* (18), 4550-4559.
74. Sampson, M. D.; Kubiak, C. P., Manganese Electrocatalysts with Bulky Bipyridine Ligands: Utilizing Lewis Acids To Promote Carbon Dioxide Reduction at Low Overpotentials. *Journal of the American Chemical Society* **2016**, *138* (4), 1386-1393.
75. Sampson, M. D.; Nguyen, A. D.; Grice, K. A.; Moore, C. E.; Rheingold, A. L.; Kubiak, C. P., Manganese Catalysts with Bulky Bipyridine Ligands for the Electrocatalytic Reduction of Carbon Dioxide: Eliminating Dimerization and Altering Catalysis. *J. Am. Chem. Soc.* **2014**, *136* (14), 5460-5471.
76. Corrigan, N.; Shanmugam, S.; Xu, J.; Boyer, C., Photocatalysis in organic and polymer synthesis. *Chem. Soc. Rev.* **2016**, *45* (22), 6165-6212.
77. Ngo, K. T.; McKinnon, M.; Mahanti, B.; Narayanan, R.; Grills, D. C.; Ertem, M. Z.; Rochford, J., Turning on the Protonation-First Pathway for Electrocatalytic CO₂ Reduction by Manganese Bipyridyl Tricarbonyl Complexes. *J. Am. Chem. Soc.* **2017**, *139* (7), 2604-2618.
78. Franco, F.; Cometto, C.; Ferrero Vallana, F.; Sordello, F.; Priola, E.; Minero, C.; Nervi, C.; Gobetto, R., A local proton source in a [Mn(bpy-R)(CO)₃Br]-type redox catalyst enables CO₂ reduction even in the absence of Brønsted acids. *Chem. Commun.* **2014**, *50* (93), 14670-14673.
79. Agarwal, J.; Shaw, T. W.; Schaefer, H. F.; Bocarsly, A. B., Design of a Catalytic Active Site for Electrochemical CO₂ Reduction with Mn(I)-Tricarbonyl Species. *Inorg. Chem.* **2015**, *54* (11), 5285-5294.
80. Rønne, M. H.; Cho, D.; Madsen, M. R.; Jakobsen, J. B.; Eom, S.; Escoudé, É.; Hammershøj, H. C. D.; Nielsen, D. U.; Pedersen, S. U.; Baik, M.-H.; Skrydstrup, T.; Daasbjerg, K., Ligand-Controlled Product Selectivity in Electrochemical Carbon Dioxide Reduction Using Manganese Bipyridine Catalysts. *Journal of the American Chemical Society* **2020**, *142* (9), 4265-4275.
81. Machan, C. W.; Kubiak, C. P., Electrocatalytic reduction of carbon dioxide with Mn(terpyridine) carbonyl complexes. *Dalton Trans.* **2016**, *45* (43), 17179-17186.
82. Stanbury, M.; Compain, J.-D.; Trejo, M.; Smith, P.; Gouré, E.; Chardon-Noblat, S., Mn-carbonyl molecular catalysts containing a redox-active phenanthroline-5,6-dione for selective electro- and photoreduction of CO₂ to CO or HCOOH. *Electrochim. Acta* **2017**, *240*, 288-299.
83. McKinnon, M.; Belkina, V.; Ngo, K. T.; Ertem, M. Z.; Grills, D. C.; Rochford, J., An Investigation of Electrocatalytic CO₂ Reduction Using a

Manganese Tricarbonyl Biquinoline Complex. *Frontiers in Chemistry* **2019**, *7* (628).

84. Smith, C. L.; Clowes, R.; Sprick, R. S.; Cooper, A. I.; Cowan, A. J., Metal-organic conjugated microporous polymer containing a carbon dioxide reduction electrocatalyst. *Sustainable Energy & Fuels* **2019**, *3* (11), 2990-2994.

85. Sato, S.; Saita, K.; Sekizawa, K.; Maeda, S.; Morikawa, T., Low-Energy Electrocatalytic CO₂ Reduction in Water over Mn-Complex Catalyst Electrode Aided by a Nanocarbon Support and K⁺ Cations. *ACS Catalysis* **2018**, *8* (5), 4452-4458.

86. Zhang, X.; Wu, Z.; Zhang, X.; Li, L.; Li, Y.; Xu, H.; Li, X.; Yu, X.; Zhang, Z.; Liang, Y.; Wang, H., Highly selective and active CO₂ reduction electrocatalysts based on cobalt phthalocyanine/carbon nanotube hybrid structures. *Nature Communications* **2017**, *8* (1), 14675.

87. Fei, H.; Sampson, M. D.; Lee, Y.; Kubiak, C. P.; Cohen, S. M., Photocatalytic CO₂ Reduction to Formate Using a Mn(I) Molecular Catalyst in a Robust Metal-Organic Framework. *Inorganic Chemistry* **2015**, *54* (14), 6821-6828.

88. Sun, C.; Rotundo, L.; Garino, C.; Nencini, L.; Yoon, S. S.; Gobetto, R.; Nervi, C., Electrochemical CO₂ Reduction at Glassy Carbon Electrodes Functionalized by MnI and ReI Organometallic Complexes. *ChemPhysChem* **2017**, *18* (22), 3219-3229.

89. Walsh, J. J.; Neri, G.; Smith, C. L.; Cowan, A. J., Water-Soluble Manganese Complex for Selective Electrocatalytic CO₂ Reduction to CO. *Organometallics* **2019**, *38* (6), 1224-1229.

90. Walsh, J. J.; Neri, G.; Smith, C. L.; Cowan, A. J., Electrocatalytic CO₂ reduction with a membrane supported manganese catalyst in aqueous solution. *Chemical Communications* **2014**, *50* (84), 12698-12701.

91. Rosser, T. E.; Windle, C. D.; Reischer, E., Electrocatalytic and Solar-Driven CO₂ Reduction to CO with a Molecular Manganese Catalyst Immobilized on Mesoporous TiO₂. *Angewandte Chemie International Edition* **2016**, *55* (26), 7388-7392.

92. Le-Quang, L.; Stanbury, M.; Chardon-Noblat, S.; Mouesca, J.-M.; Maurel, V.; Chauvin, J., Immobilization of Mn(i) and Ru(ii) polypyridyl complexes on TiO₂ nanoparticles for selective photoreduction of CO₂ to formic acid. *Chemical Communications* **2019**, *55* (90), 13598-13601.

93. Woo, S.-J.; Choi, S.; Kim, S.-Y.; Kim, P. S.; Jo, J. H.; Kim, C. H.; Son, H.-J.; Pac, C.; Kang, S. O., Highly Selective and Durable Photochemical CO₂ Reduction by Molecular Mn(I) Catalyst Fixed on a Particular Dye-Sensitized TiO₂ Platform. *ACS Catalysis* **2019**, *9* (3), 2580-2593.

94. Wang, X.; Thiel, I.; Fedorov, A.; Copéret, C.; Mougél, V.; Fontecave, M., Site-isolated manganese carbonyl on bipyridine-functionalities of periodic mesoporous organosilicas: efficient CO₂ photoreduction and detection of key reaction intermediates. *Chemical Science* **2017**, *8* (12), 8204-8213.

95. Yaghi, O. M., Reticular Chemistry in All Dimensions. *ACS Central Science* **2019**, *5* (8), 1295-1300.

96. Diercks, C. S.; Liu, Y.; Cordova, K. E.; Yaghi, O. M., The role of reticular chemistry in the design of CO(2) reduction catalysts. *Nat Mater* **2018**, *17* (4), 301-307.

97. Li, J.; Zhao, D.; Liu, J.; Liu, A.; Ma, D., Covalent Organic Frameworks: A Promising Materials Platform for Photocatalytic CO₂ Reductions. *Molecules* **2020**, *25* (10), 2425.
98. Furukawa, H.; Cordova, K. E.; O'Keeffe, M.; Yaghi, O. M., The chemistry and applications of metal-organic frameworks. *Science* **2013**, *341* (6149), 1230444.
99. Diercks, C. S.; Yaghi, O. M., The atom, the molecule, and the covalent organic framework. *Science* **2017**, *355* (6328).
100. Lee, J.; Farha, O. K.; Roberts, J.; Scheidt, K. A.; Nguyen, S. T.; Hupp, J. T., Metal-organic framework materials as catalysts. *Chemical Society Reviews* **2009**, *38* (5), 1450-1459.
101. Zhang, T.; Lin, W., Metal-organic frameworks for artificial photosynthesis and photocatalysis. *Chemical Society Reviews* **2014**, *43* (16), 5982-5993.
102. Farha, O. K.; Eryazici, I.; Jeong, N. C.; Hauser, B. G.; Wilmer, C. E.; Sarjeant, A. A.; Snurr, R. Q.; Nguyen, S. T.; Yazaydin, A. Ö.; Hupp, J. T., Metal-Organic Framework Materials with Ultrahigh Surface Areas: Is the Sky the Limit? *Journal of the American Chemical Society* **2012**, *134* (36), 15016-15021.
103. Deng, H.; Grunder, S.; Cordova Kyle, E.; Valente, C.; Furukawa, H.; Hmadeh, M.; Gándara, F.; Whalley Adam, C.; Liu, Z.; Asahina, S.; Kazumori, H.; O'Keeffe, M.; Terasaki, O.; Stoddart, J. F.; Yaghi Omar, M., Large-Pore Apertures in a Series of Metal-Organic Frameworks. *Science* **2012**, *336* (6084), 1018-1023.
104. Zhou, Y.; Chen, S.; Xi, S.; Wang, Z.; Deng, P.; Yang, F.; Han, Y.; Pang, Y.; Xia, B. Y., Spatial Confinement in Copper-Porphyrin Frameworks Enhances Carbon Dioxide Reduction to Hydrocarbons. *Cell Reports Physical Science* **2020**, *1* (9), 100182.
105. Sun, L.; Campbell, M. G.; Dincă, M., Electrically Conductive Porous Metal-Organic Frameworks. *Angew Chem Int Ed Engl* **2016**, *55* (11), 3566-79.
106. Guo, J.; Xu, Y.; Jin, S.; Chen, L.; Kaji, T.; Honsho, Y.; Addicoat, M. A.; Kim, J.; Saeki, A.; Ihee, H.; Seki, S.; Irle, S.; Hiramoto, M.; Gao, J.; Jiang, D., Conjugated organic framework with three-dimensionally ordered stable structure and delocalized π clouds. *Nature Communications* **2013**, *4* (1), 2736.
107. Geng, K.; He, T.; Liu, R.; Dalapati, S.; Tan, K. T.; Li, Z.; Tao, S.; Gong, Y.; Jiang, Q.; Jiang, D., Covalent Organic Frameworks: Design, Synthesis, and Functions. *Chemical Reviews* **2020**, *120* (16), 8814-8933.
108. Ma, X.; Scott, T. F., Approaches and challenges in the synthesis of three-dimensional covalent-organic frameworks. *Communications Chemistry* **2018**, *1* (1), 98.
109. Côté, A. P.; Benin, A. I.; Ockwig, N. W.; O'Keeffe, M.; Matzger, A. J.; Yaghi, O. M., Porous, Crystalline, Covalent Organic Frameworks. *Science* **2005**, *310* (5751), 1166-1170.
110. Côté, A. P.; Benin, A. I.; Ockwig, N. W.; O'Keeffe, M.; Matzger, A. J.; Yaghi, O. M., Porous, crystalline, covalent organic frameworks. *Science* **2005**, *310* (5751), 1166-70.
111. El-Kaderi, H. M.; Hunt, J. R.; Mendoza-Cortés, J. L.; Côté, A. P.; Taylor, R. E.; O'Keeffe, M.; Yaghi, O. M., Designed synthesis of 3D covalent organic frameworks. *Science* **2007**, *316* (5822), 268-72.

112. Ding, H.; Mal, A.; Wang, C., Tailored covalent organic frameworks by post-synthetic modification. *Materials Chemistry Frontiers* **2020**, *4* (1), 113-127.
113. Gopalakrishnan, V. N.; Becerra, J.; Pena, E. F.; Sakar, M.; Béland, F.; Do, T.-O., Porphyrin and single atom featured reticular materials: recent advances and future perspective of solar-driven CO₂ reduction. *Green Chemistry* **2021**, *23* (21), 8332-8360.
114. Cheung, P. L.; Lee, S. K.; Kubiak, C. P., Facile Solvent-Free Synthesis of Thin Iron Porphyrin COFs on Carbon Cloth Electrodes for CO₂ Reduction. *Chemistry of Materials* **2019**, *31* (6), 1908-1919.
115. Matheu, R.; Gutierrez-Puebla, E.; Monge, M. Á.; Diercks, C. S.; Kang, J.; Prévot, M. S.; Pei, X.; Hanikel, N.; Zhang, B.; Yang, P.; Yaghi, O. M., Three-Dimensional Phthalocyanine Metal-Catecholates for High Electrochemical Carbon Dioxide Reduction. *Journal of the American Chemical Society* **2019**, *141* (43), 17081-17085.
116. Lu, M.; Zhang, M.; Liu, J.; Chen, Y.; Liao, J.-P.; Yang, M.-Y.; Cai, Y.-P.; Li, S.-L.; Lan, Y.-Q., Covalent Organic Framework Based Functional Materials: Important Catalysts for Efficient CO₂ Utilization. *Angewandte Chemie International Edition* **2022**, *61* (15), e202200003.
117. Han, B.; Ding, X.; Yu, B.; Wu, H.; Zhou, W.; Liu, W.; Wei, C.; Chen, B.; Qi, D.; Wang, H.; Wang, K.; Chen, Y.; Chen, B.; Jiang, J., Two-Dimensional Covalent Organic Frameworks with Cobalt(II)-Phthalocyanine Sites for Efficient Electrocatalytic Carbon Dioxide Reduction. *Journal of the American Chemical Society* **2021**, *143* (18), 7104-7113.
118. Hod, I.; Sampson, M. D.; Deria, P.; Kubiak, C. P.; Farha, O. K.; Hupp, J. T., Fe-Porphyrin-Based Metal–Organic Framework Films as High-Surface Concentration, Heterogeneous Catalysts for Electrochemical Reduction of CO₂. *ACS Catalysis* **2015**, *5* (11), 6302-6309.
119. Lin, S.; Diercks, C. S.; Zhang, Y. B.; Kornienko, N.; Nichols, E. M.; Zhao, Y.; Paris, A. R.; Kim, D.; Yang, P.; Yaghi, O. M.; Chang, C. J., Covalent organic frameworks comprising cobalt porphyrins for catalytic CO₂ reduction in water. *Science* **2015**, *349* (6253), 1208-13.
120. Guo, Y.; Shi, W.; Yang, H.; He, Q.; Zeng, Z.; Ye, J.-y.; He, X.; Huang, R.; Wang, C.; Lin, W., Cooperative Stabilization of the [Pyridinium-CO₂-Co] Adduct on a Metal–Organic Layer Enhances Electrocatalytic CO₂ Reduction. *Journal of the American Chemical Society* **2019**, *141* (44), 17875-17883.
121. Wang, Y.-R.; Ding, H.-M.; Ma, X.-Y.; Liu, M.; Yang, Y.-L.; Chen, Y.; Li, S.-L.; Lan, Y.-Q., Imparting CO₂ Electroreduction Auxiliary for Integrated Morphology Tuning and Performance Boosting in a Porphyrin-based Covalent Organic Framework. *Angewandte Chemie International Edition* **2022**, *61* (5), e202114648.
122. Ye, L.; Liu, J.; Gao, Y.; Gong, C.; Addicoat, M.; Heine, T.; Wöll, C.; Sun, L., Highly oriented MOF thin film-based electrocatalytic device for the reduction of CO₂ to CO exhibiting high faradaic efficiency. *Journal of Materials Chemistry A* **2016**, *4* (40), 15320-15326.
123. Fan, Y.; Chen, M.; Xu, N.; Wang, K.; Gao, Q.; Liang, J.; Liu, Y., Recent progress on covalent organic framework materials as CO₂ reduction electrocatalysts. *Frontiers in Chemistry* **2022**, *10*.
124. Diercks, C. S.; Lin, S.; Kornienko, N.; Kapustin, E. A.; Nichols, E. M.; Zhu, C.; Zhao, Y.; Chang, C. J.; Yaghi, O. M., Reticular Electronic Tuning of

Porphyrin Active Sites in Covalent Organic Frameworks for Electrocatalytic Carbon Dioxide Reduction. *Journal of the American Chemical Society* **2018**, *140* (3), 1116-1122.

125. Johnson, E. M.; Haiges, R.; Marinescu, S. C., Covalent-Organic Frameworks Composed of Rhenium Bipyridine and Metal Porphyrins: Designing Heterobimetallic Frameworks with Two Distinct Metal Sites. *ACS Applied Materials & Interfaces* **2018**, *10* (44), 37919-37927.

126. Popov, D. A.; Luna, J. M.; Orchanian, N. M.; Haiges, R.; Downes, C. A.; Marinescu, S. C., A 2,2'-bipyridine-containing covalent organic framework bearing rhenium(i) tricarbonyl moieties for CO₂ reduction. *Dalton Transactions* **2018**, *47* (48), 17450-17460.

127. Diercks, C. S.; Liu, Y.; Cordova, K. E.; Yaghi, O. M., The role of reticular chemistry in the design of CO₂ reduction catalysts. *Nature Materials* **2018**, *17* (4), 301-307.

128. Li, J.; Zhao, D.; Liu, J.; Liu, A.; Ma, D., Covalent Organic Frameworks: A Promising Materials Platform for Photocatalytic CO₂ Reductions. *Molecules* **2020**, *25* (10).

129. Zhong, W.; Sa, R.; Li, L.; He, Y.; Li, L.; Bi, J.; Zhuang, Z.; Yu, Y.; Zou, Z., A Covalent Organic Framework Bearing Single Ni Sites as a Synergistic Photocatalyst for Selective Photoreduction of CO₂ to CO. *Journal of the American Chemical Society* **2019**, *141* (18), 7615-7621.

130. Lu, M.; Li, Q.; Liu, J.; Zhang, F.-M.; Zhang, L.; Wang, J.-L.; Kang, Z.-H.; Lan, Y.-Q., Installing earth-abundant metal active centers to covalent organic frameworks for efficient heterogeneous photocatalytic CO₂ reduction. *Applied Catalysis B: Environmental* **2019**, *254*, 624-633.

131. Liu, W.; Li, X.; Wang, C.; Pan, H.; Liu, W.; Wang, K.; Zeng, Q.; Wang, R.; Jiang, J., A Scalable General Synthetic Approach toward Ultrathin Imine-Linked Two-Dimensional Covalent Organic Framework Nanosheets for Photocatalytic CO₂ Reduction. *Journal of the American Chemical Society* **2019**, *141* (43), 17431-17440.

132. Yang, S.; Hu, W.; Zhang, X.; He, P.; Pattengale, B.; Liu, C.; Cendejas, M.; Hermans, I.; Zhang, X.; Zhang, J.; Huang, J., 2D Covalent Organic Frameworks as Intrinsic Photocatalysts for Visible Light-Driven CO₂ Reduction. *Journal of the American Chemical Society* **2018**, *140* (44), 14614-14618.

133. Li, S.-Y.; Meng, S.; Zou, X.; El-Roz, M.; Teleguev, I.; Thili, O.; Liu, T. X.; Zhu, G., Rhenium-functionalized covalent organic framework photocatalyst for efficient CO₂ reduction under visible light. *Microporous and Mesoporous Materials* **2019**, *285*, 195-201.

134. Wang, D.; Streater, D.; Peng, Y.; Huang, J., 2D Covalent Organic Frameworks with an Incorporated Manganese Complex for Light Driven Carbon Dioxide Reduction. *ChemPhotoChem* **2021**, *5* (12), 1119-1123.

135. Sarkar, P.; Riyajuddin, S.; Das, A.; Hazra Chowdhury, A.; Ghosh, K.; Islam, S. M., Mesoporous covalent organic framework: An active photo-catalyst for formic acid synthesis through carbon dioxide reduction under visible light. *Molecular Catalysis* **2020**, *484*, 110730.

136. Lu, M.; Liu, J.; Li, Q.; Zhang, M.; Liu, M.; Wang, J.-L.; Yuan, D.-Q.; Lan, Y.-Q., Rational Design of Crystalline Covalent Organic Frameworks for Efficient CO₂ Photoreduction with H₂O. *Angewandte Chemie International Edition* **2019**, *58* (36), 12392-12397.

CHAPTER II.

Main Objectives

Chapter II: Main Objectives

The electrochemical conversion of CO₂ can generate a variety of valuable carbon-based chemicals with high current efficiency under ambient conditions. These products can be used as feedstocks for chemical synthesis or converted to hydrocarbon fuels. In this line, a viable CO₂ reduction catalyst should also rely on inexpensive, robust, sustainable, modular and efficient materials. To this end, a fundamental understanding of the parameters that control both the catalytic activity and selectivity of the catalysts is necessary. In particular, well-defined Manganese Catalysts have served as a workhorse in the field of homogeneous catalysis (Chapter I). However, at the beginning of this thesis, there was a gap in the understanding of CO₂RR in reticular materials, which was even more important in Covalent Organic Frameworks (COFs). Therefore, we postulated the possibility of better understanding the CO₂RR in COFs by the development and study of Mn-based COFs as single site catalysts.

In this line, the general objectives of the present PhD thesis are:

- i.* To develop new Single Atom Catalysts based on well-defined Mn COFs with N-chelating ligands embedded on the structure.
- ii.* To study the electrocatalytic CO₂RR in water.
- iii.* To exploit the characteristics of COFs for the stability of reaction intermediates and therefore increase the activity, stability and selectivity.
- iv.* To thoroughly analyze the reaction mechanisms to correlate structure-activity relationships on COFs.
- v.* To study the structural transformation, mechanisms and dynamic response of COFs triggered by an electric stimulus.

We envisioned that this study would allow us to advance in the identification of the factors that determine the activity and stability of reticular materials under catalytic conditions, as well as to elucidate the intermediates involved in the catalytic cycle.

Accordingly, to the general objectives, the first part of the thesis (Chapters III–IV) is focused on the study of the activity of Mn bipyridine-COF (**COF_{bpyMn}**) as well as its building blocks for the electrocatalytic CO₂ reduction in water. The difference in electronic and structural parameters, together with the detection of key intermediates in the catalytic cycle, would bring information about the improvement in the catalytic activity, stability and selectivity of COFs. Then, in Chapters V, the study of the mechanically constrain Mn centers within the COF was expanded and focused on the understanding of the mechanism and the dynamic involve in the interfaces layers of reticular materials using the **COF_{bpyMn}**.

The second part of the thesis (Chapter VI) is focused on the correlation between the reactivity and selectivity with the structural properties of COFs by changing the nature of the N-chelating building block in the linker position, larger linker moiety was introduced in the COF using a phenanthroline (**COF_{PTMn}**) instead of bipyridine.

Altogether, we envision the results obtained will allow a better understanding of reticular systems and the development of more efficient catalytic platforms for the production of fuels from CO₂.

CHAPTER III.

New Catalytic Mn(CO)₃Br Single Sites in a 2D- Covalent Organic Framework for the electrocatalytic CO₂ conversion in H₂O

Chapter III: New Catalytic Mn(CO)₃Br Single Sites in a Two-Dimensional Covalent Organic Framework for electrocatalytic CO₂ conversion in H₂O

III.1. General insight

The electrocatalytic CO₂ reduction reaction (CO₂RR) is an appealing approach to producing sustainable fuels and fine chemicals mediated by catalysts based on earth-abundant elements and renewable energy.¹⁻³ In this regard, homogeneous molecular complexes have shown good activity for CO₂ activation under milder reaction conditions;⁴⁻⁶ their high selectivity, well-defined catalytic sites and tunable morphology make them convenient platforms to study and finely tune the reactivity through rational ligand design.⁶⁻¹² However, the poor stability and cumbersome separation from reaction solutions restrict their application. Therefore, a significant focus has been turned to heterogeneous catalysts, which are expected to offer better long-term stability.^{13, 14} Nevertheless, heterogenous catalysis is a surface-driven process that causes limited utilization of metal centers.^{15, 16} Therefore, the prospective energy and environment restoration challenges demand the development of catalysts possessing features of both homogenous and heterogenous catalysts.

To bridge the gap between homogeneous and heterogeneous catalysis, the immobilization of molecular complexes¹⁷⁻²⁶ and atomically dispersed single-atom catalysts (SACs)²⁷⁻³⁰ on different supports have been attractive strategies that have rapidly progressed in the field of the electrocatalytic CO₂RR. The SACs as single-site catalysts present better utilization of the reactive sites and provide higher selectivity than their counter metal particles/clusters (Figure III. 1).³¹

Traditional homogeneous or heterogeneous catalysts involve compromises in activity, selectivity or recyclability. SACs integrate the merits of both these types of catalysts. The unsaturated coordination environment of the single atoms imparts superior catalytic activity per metal atom, and the uniform structure of the SACs results in unparalleled selectivity for the desired products compared with heterogeneous systems.

Besides, the strong covalent or electronic interactions with the support or another metal provide excellent stability. While the active site structures of SACs may be less uniform than those of homogeneous catalysts, the well-defined structures arising from the coordination between single atoms and the support provide SACs with promising properties to mimic homogeneous catalysis.^{32, 33}

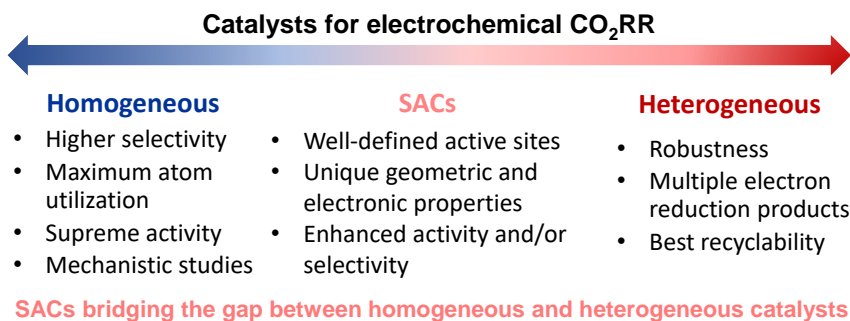


Figure III. 1. Advantages of different catalytic strategies.

In recent years, reticular materials been recognized as promising 2D and 3D crystalline polymers for producing SACs.³⁴⁻³⁹ These materials are formed through the strong bonding of molecular building blocks, leading to the formation of highly porous crystalline structures, which are a convenient platform to improve the catalyst activity by the rational design and tune of their well-defined active sites in the molecular units.^{40, 41} Given the diversity of the available building units and the easy modification and functionalization of these materials, a huge variety of reticular materials can be obtained, which can be classified as Metal-Organic (MOFs) or Covalent Organic (COFs) frameworks, depending on the nature of the building blocks. MOFs are formed by the joint of organic linkers and metal atoms, while COFs are exclusively made of organic linkers.^{42, 43} MOFs and COFs have many interesting properties, including high porosity, catalytic activity, conductivity or luminescence. Apart from their impressive surface area and synthetic versatility, they also present adequate pore shape, size and functionality that can be tailored toward specific applications.³⁴⁻³⁷

Since its initiation in 2012, progressive attempts to use framework materials in catalytic CO₂RR have been introduced in several reviews.^{44, 45}

CHAPTER III

Mn based 2D-COF_{bpy} for electrocatalytic CO₂RR

The judicious design, optimization, and utilization of MOFs, COFs, and their derivatives can improve the fundamental catalytic activity toward electrocatalytic CO₂ reduction. In this line, representative achievements since 2015 have been included (Figure III. 2).

Progressive timeline of representatives framework materials as catalysts for electrocatalytic CO₂RR

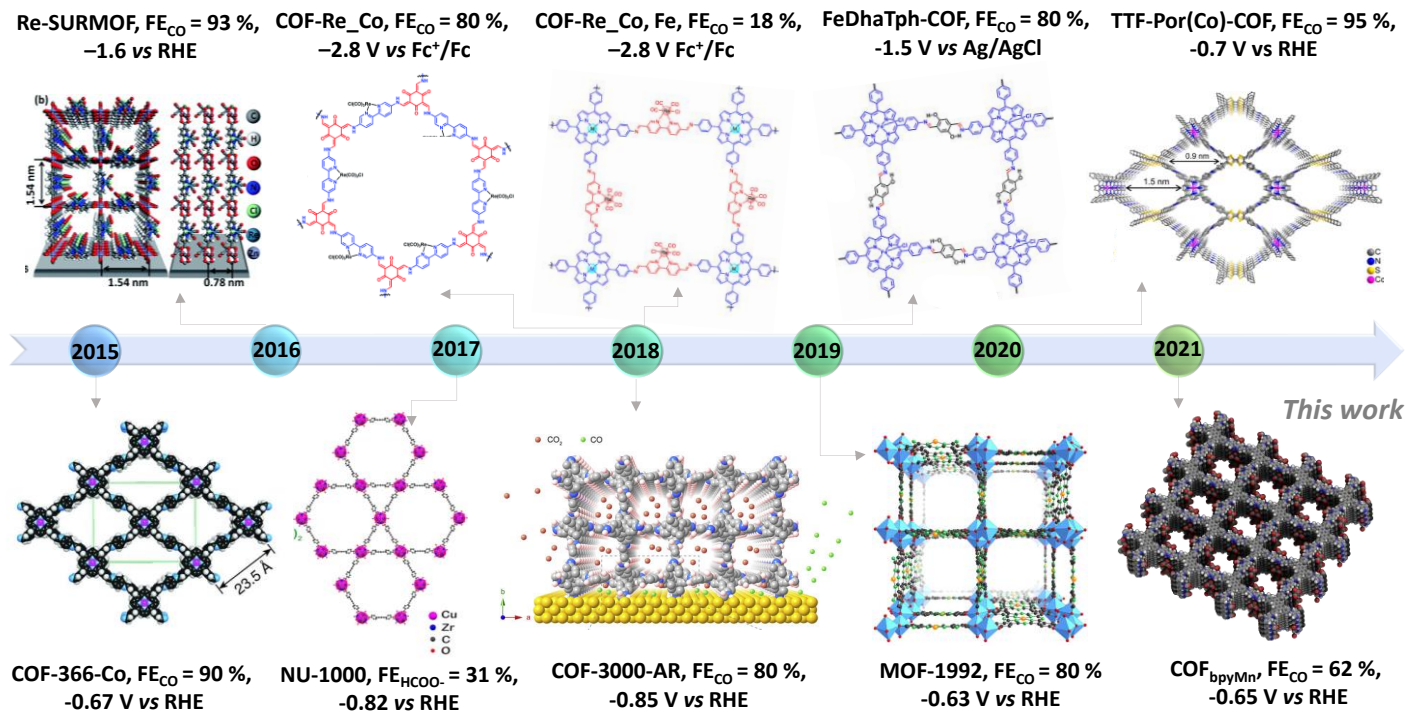


Figure III. 2. Representative organic framework materials as electrocatalysts for CO₂ reduction.⁴⁶⁻⁵²

COFs have triggered significant research perspectives on energy applications. Their unique physiochemical properties, various syntheses, tunable pore size, flexible structural design, and spatial π -conjugated orientation with the ultra-large surface area have driven the study of these materials in electrocatalytic transformations.^{34, 53-57} Besides, the tunable structure, inherent pores, and superior, strong covalent bonds in COFs are the advantage over other crystalline porous materials such as MOFs, mesoporous silica, and zeolites.⁵⁸ All of these merits of COFs cater to the substrate requirements for SACs stabilization. Nonetheless, the electrocatalytic applications of COFs are far less explored.^{38, 56, 59-61}

In a pioneering work, Yaghi and co-workers reported a COF integrating Co porphyrin units, which was highly active for selective electrochemical conversion of CO₂ to CO.^{62, 63} Since this study, several COFs have been evaluated for the electrocatalytic CO₂RR, more recently, the {Re(CO)₃Cl}⁶⁴⁻⁶⁶ fragment was placed in a COF structure, active for CO production, but suffered from large overpotential in organic solvents and low stability.⁶⁷ Additionally, COFs with two catalytically active building blocks were prepared through linkages of metallobipyridine and rhenium tricarbonyl fragments resulting in a CO₂-to-CO Faradaic yield of about 18% in water with good stability, ca. 2 h.⁶⁸ A COF based on an Fe porphyrin was also reported with promising turnover frequencies in organic solvents.⁶⁹

On the other hand, several studies have been shown that manganese tricarbonyl complexes containing polypyridyl⁷⁰⁻⁷² and non-pyridyl⁷³ ligands are efficient catalysts in the CO₂RR to generate CO with good Faradaic yields in protic organic media (see further information in Chapter I).^{74, 75} The heterogenization of homogeneous Mn-catalysts on solid supports (eg. CNT, TiO₂, CMP, etc...) could improve their performance,^{17-23, 76} and in some cases also allowed utilization of water as solvent (Figure III. 3), which enabled reduced overpotentials and increased turnover numbers.^{18, 19} More recently, the inclusion {Mn(bpy)(CO)₃Br} into a Metal–Organic Conjugated Microporous Polymer (CMP) framework was reported, but the catalyst presented poor activity toward CO₂ reduction in water.⁷⁶

Considering the advantages of the SACs produced from COFs and the reported improvement in catalysis by the heterogenization of the molecular catalyst^{23, 77-82} and in specific some manganese tricarbonyl complexes,^{17-23, 76} we report herein the first example of a Mn^I tricarbonyl based-2D covalent organic framework (COF_{bpyMn}) (Figure III. 3, Scheme III. 1). In fact, to the best of our knowledge, there are no examples of electrocatalysts based on tricarbonyl Mn sites incorporated into an ordered covalent organic framework. The synthesized materials were fully characterized by combining experimental and computational (DFT) techniques. The new COF_{bpyMn} resulted in a robust heterogeneous catalyst for CO₂ electroreduction in water that outperforms the molecular *fac*-Mn(bpy)(CO)₃Br counterpart in current density, onset potential, turnover number (TON) and turnover frequency (TOF).

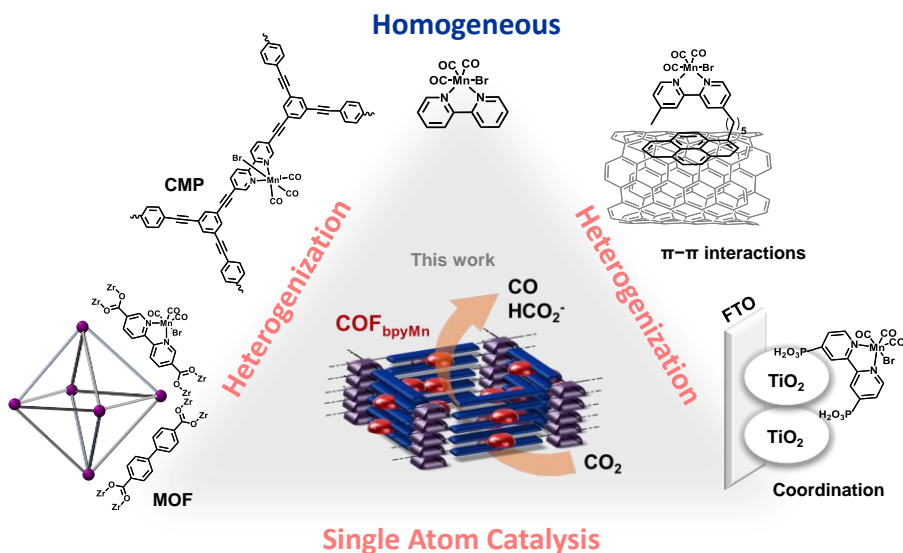
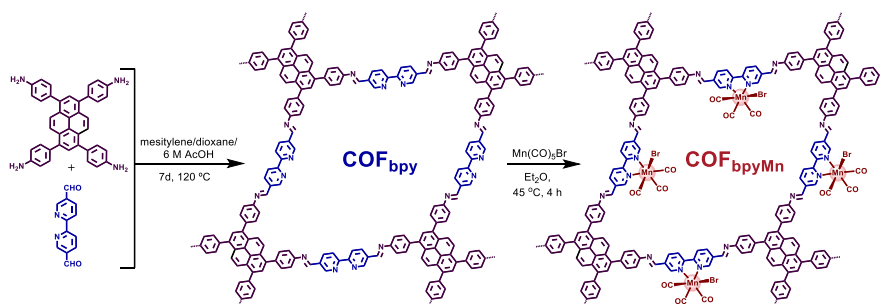


Figure III. 3. Selected immobilization strategies employed in manganese tricarbonyl complexes containing polypyridyl moieties for CO₂ conversion.

III.2. Results and discussion

III.2.1 Synthesis and characterization

Condensation of ,4',4'',4'''-(pyrene-1,3,6,8-tetrayl)tetraaniline (PyTTA) and 2,2'-bipyridyl-5,5'-dialdehyde (bpy^{CHO}) in mixture solvents in the presence of acetic acid at 120 °C afforded the crystalline COF_{bpy} (Scheme III. 1) with the two pyridine-nitrogen atoms having the same orientation as previously reported.⁸³ COF post-functionalization was performed by direct reaction of Mn(CO)₅Br with COF_{bpy} at 45 °C in diethyl ether for 4 hours, forming COF_{bpy}Mn as a microcrystalline dark brown powder in good isolated yields (90 %, Scheme III. 2), which was fully characterized.



Scheme III. 1 Synthetic Procedure of COF_{bpy}⁸³ and COF_{bpy}Mn.

The COF_{bpy} is a highly crystalline material with strong XRD signals. The main diffractions at 3.16°, 4.58°, 6.38°, 9.74°, 12.98° and 23.86° can be assigned to the (110), (020), (220), (330), (440), and (001) facets, respectively (Figure III. 4a).⁸³ The PXRD pattern of COF_{bpy}Mn exhibits diffraction peaks analogous to the metal-free COF_{bpy}, suggesting that the crystalline integrity of the porous framework is maintained upon metalation (Figure III. 4a). The reflection centered at ~23°, previously assigned to (001) facets, indicates a π - π stacking of 2D layers and periodic order in all three dimensions.⁸³

To investigate whether the channels of the COF_{bpy} and COF_{bpy}Mn are accessible and their porosity, nitrogen adsorption isotherm measurements at 77 K were conducted (Figure III. 4b). These COFs exhibited reversible type IV sorption curves,⁸⁴ characteristics of mesoporous materials.

CHAPTER III Mn based 2D-COF_{bpy} for electrocatalytic CO₂RR

Dinitrogen (N₂) adsorption isotherms (77 K) of COF_{bpy} and COF_{bpyMn} (Figure III. 4b) show a reversible type IV behavior, characteristics of mesoporous materials. The Brunauer–Emmett–Teller (BET) surface areas were calculated to be as high as 2127 for COF_{bpy} and 1601 m²/g for COF_{bpyMn} (Figure III. 4b). These surface areas are among the highest for the imine-linked COFs reported based on N₂ sorption.⁸⁵⁻⁸⁷ The decrease in the BET surface area for COF_{bpyMn} is consistent with incorporating the Mn complex into the COF framework.

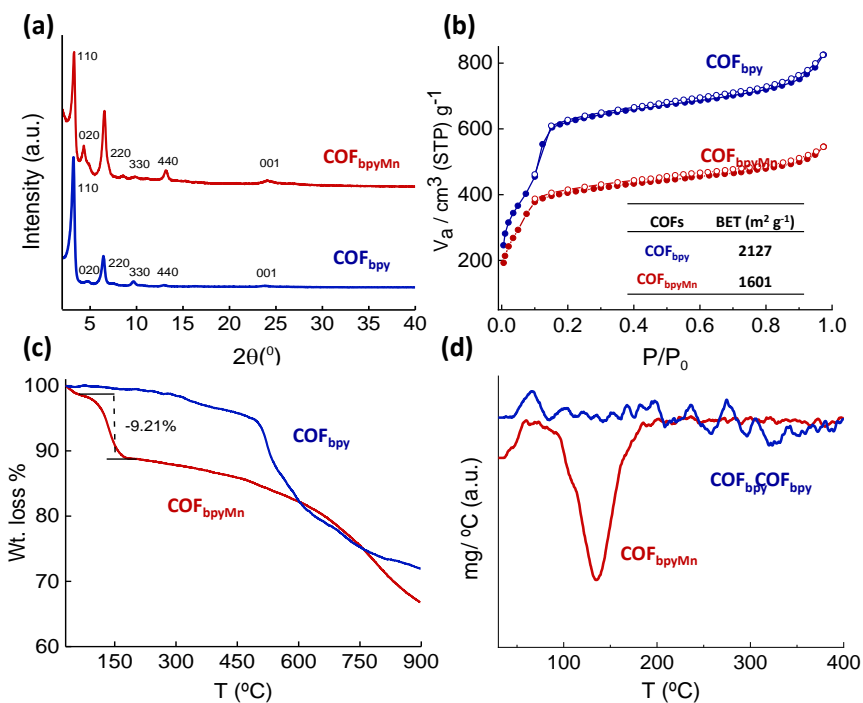


Figure III. 4. (a) PXRD patterns of COF_{bpy} and COF_{bpyMn}. (b) N₂ isotherms of COF_{bpy} and COF_{bpyMn} with BET surface areas of COFs. (c) TGA of COF_{bpy} and COF_{bpyMn}. (d) mg/°C vs T curves of COFs.

Thermal gravimetric analysis (TGA) suggested that COF_{bpy} is stable up to 400 °C. However, the COF_{bpyMn} showed a first step (~70–180°C) in the TGA, which is consistent with the thermal release of the three coordinated CO ligands of the Mn coordination shell in COF_{bpyMn} (obsd. 9.2%, calcd. 11.0% based on C₆₄H₃₈N₈(Mn(CO)₃Br)_{1.7}, Figure III. 4c,d).

CHAPTER III

Mn based 2D-COF_{bpy} for electrocatalytic CO₂RR

SEM and TEM microscopies of as-prepared COF_{bpy} and COF_{bpyMn} showed a globular morphology of μm size (Figure III. 5a-d). The Mn in COF_{bpyMn} was homogeneously distributed based on the EDX-mapping (Figure III. 5e). The amount of Mn measured by ICP-OES (obsd. 7.2%, Figure III. 5f), agreed with the EDX and accounted for ca ~85% of the COF bipyridines coordinated to Mn (calcd. 7.2%, based on C₆₄H₃₈N₈(Mn(CO)₃Br)_{1.7}). An analogous value was reported for the MOF UiO-67-Mn(bpy)(CO)₃Br.⁸⁸

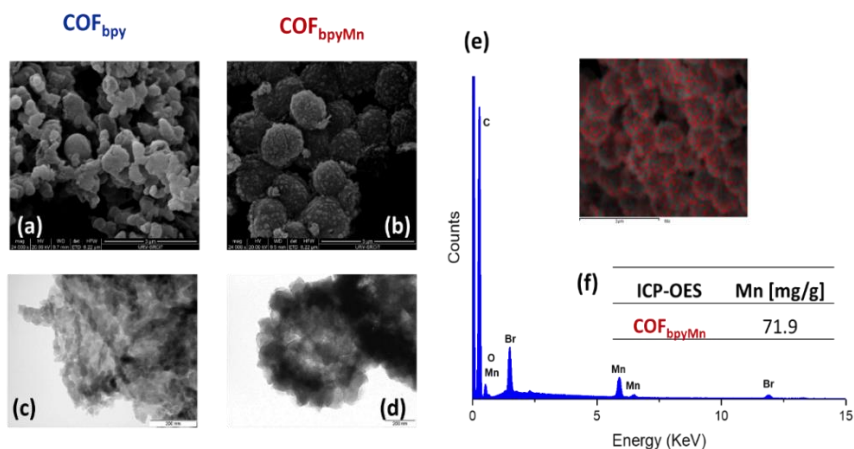


Figure III. 5. (a, b) SEM and (c, d) TEM measurements of COF_{bpy} (left) and COF_{bpyMn} (right). (e) EDX of COF_{bpyMn} and (f) Mn content detected by ICP OES (mg/g) in COF_{bpyMn}.

Periodic DFT (PBE+D3) studies were computed in collaboration with Prof. Nuria López (ICIQ) and Dr. Manuel Ortuño (ICIQ) and served to characterize the synthesized materials further. Considering the relative position of imine and bipyridine groups and the orientation of imine bonds,^{89, 90} they initially modeled COF_{bpy} using 14 different unit cells (Table III. 1).

Table III. 1. Relative energies (eV) for volume- and position-optimized COF isomers.

COF _{bpy} isomer	ΔE^a / eV	COF _{bpy} isomer	ΔE^a / eV
1a	1.15	4a	0.43
1b	0.14	4b	0.45
1c	0.27	5a	0.01
2a	0.35	5b (COF_{bpy}-A)	0.00
2b	0.12	6a	0.16
2c	0.26	6b	0.43
3a	0.23	-	-
3b	0.21	-	-

^aValues with respect to isomer **5b (COF_{bpy}-A)**.

The most stable structures and their lattice parameters are shown in Figure III. 6a. This model contains two identical layers in a stacked disposition.^{91,92} In this configuration, the stacked bipyridyl groups can point toward the same pore (**COF_{bpy}-A**, Figure III. 6b). However, in the most stable stacked structure, namely isomer B, one layer is rotated by 180° along the *b* axis to point the bipyridyl groups toward different pores (**COF_{bpy}-B**, Figure III. 6c). Isomer B is 0.57 eV (13.2 kcal·mol⁻¹) more stable than isomer A; thus, B was used as the initial structure for subsequent simulations.

The alternated nature of the bipyridines in Isomer B is of remarkable importance to understand the catalytic properties of **COF_{bpy}Mn** (see the discussion in Chapter IV regarding the absence of Mn⁰-Mn⁰ dimer). Indeed, the close contacts between {*fac*-Mn(CO)₃Br} moieties anchored to adjacent bipyridyl sites would limit the Mn incorporation to 50% for **COF_{bpy}-A**. However, **COF_{bpy}-B** would allocate higher than 50%, in agreement with the experimental high Mn loading (85%) for **COF_{bpy}Mn**.

CHAPTER III

Mn based 2D-COF_{bpy} for electrocatalytic CO₂RR

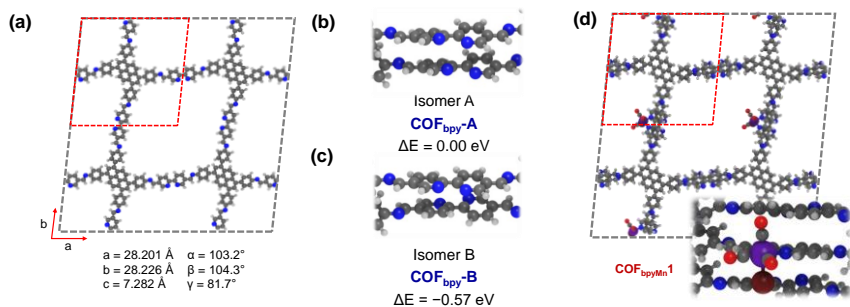


Figure III. 6. (a) Optimized unit cell of COF_{bpy}, (b) structural isomer A, (c) structural isomer B, (d) optimized structure of COF_{bpyMn1}. (Legend: Mn = purple, Br = wine, O = read, N = blue, C = grey, H = white).

Under this premise, it was considered several models with different metal loadings denoted as COF_{bpyMn}*n*, where *n* stands for the number of [Mn] units included in the simulation cell. First, it was modeled the coordination of 1 {*fac*-Mn(CO)₃Br} unit to COF_{bpy}-B, namely COF_{bpyMn1}, (Figure III. 6d). The adsorption energy for the precursor Mn(CO)₅Br is -0.09 eV. Although the process is only slightly exothermic, the reaction will be entropically driven due to the irreversible release of CO gas. It was discarded the coordination of {Mn(CO)₄Br} or {Mn(CO)₃Br} moieties to the imine since these are 0.64 and 1.96 eV higher in energy than the COF_{bpyMn1}, respectively (Figure III. 7).

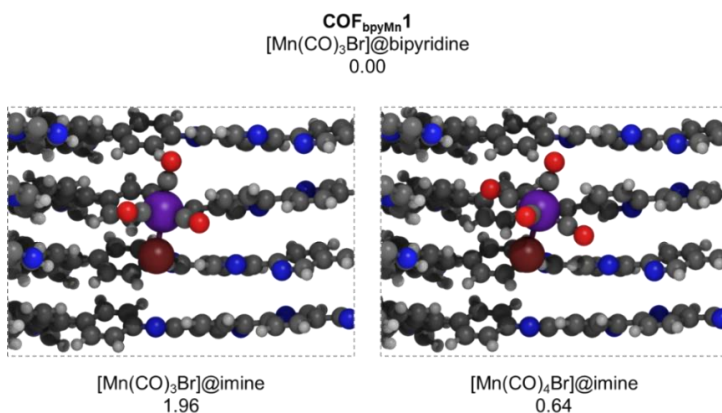


Figure III. 7. DFT-optimized structures of Mn complexes bound to imine groups. ΔE relative to COF_{bpyMn1} and CO in eV. The geometry constraints do not permit the binding of two N-imines to the {Mn(CO)₃Br} moiety. {Mn(CO)₄Br} coordinated to one imine of the COF is disfavored by +0.6 eV respect to the {Mn(CO)₃Br} to bpy of the COF and CO.

Then, it was optimized the COF structures with 6 and 8 *fac*-Mn(CO)₃Br} units (COF_{bpyMn}**6** and COF_{bpyMn}**8**, Figure III. 8), which correspond to loadings of 75% and 100%, respectively. The corresponding adsorption energy per molecule of -0.06 eV for both systems suggests that the <100% loading might be due to kinetic barriers during coordination or to a COF layer disorder, affecting bipyridyl ligands (similar to COF_{bpy}-**A** in Figure III. 6). The computed COF_{bpy}-**B** nicely reproduces the main diffraction peaks of the PXRD pattern (Figure III. 4a). As for COF_{bpyMn}**n**, we observe that higher loadings ($n = 6$ and 8) are necessary to fit better the experimental data (Figure III. 9b–d).

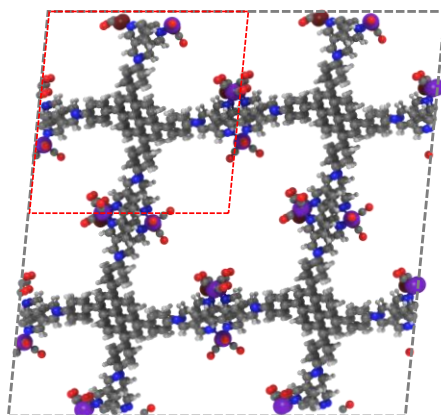


Figure III. 8. Optimized structures of 6 [MnCO₃Br] units immobilized within the COF. Unit cell in dashed red. (Legend: Mn = purple, Br = wine, O = read, N = blue, C = grey, H = white).

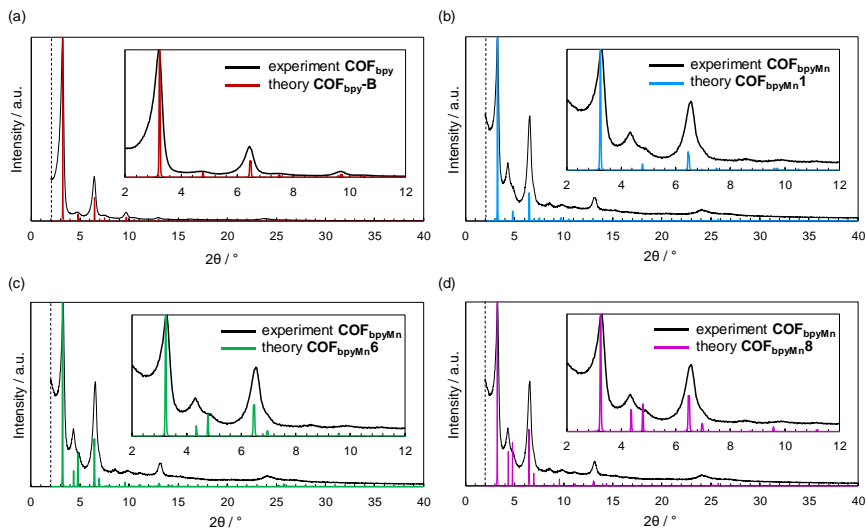


Figure III. 9. Comparison of PXRD spectra: experimental (black) and simulated for COF_{bpy}-B (red, a), COF_{bpyMn1} (blue, b), COF_{bpyMn6} (green, c), and COF_{bpyMn8} (purple, d).

To get insights into the COF matrix as a ligand and the capacity to modify the Mn center's electronic structure and coordination environment, IR and EXAFS studies were undertaken. The incorporation of $\{fac\text{-Mn}(\text{CO})_3\text{Br}\}$ fragments into the organic framework in COF_{bpyMn} was confirmed by Attenuated Total Reflectance Infrared Spectroscopy (ATR-IR), showing the presence of prominent CO stretching frequencies at 2025, 1941 and 1917 cm⁻¹ (Figure III. 10a). This pattern is analogous to the one shown by the molecular *fac*-Mn(bpy)(CO)₃Br counterpart and computed CO vibrations of COF_{bpyMn1} fall in the same range (2013, 1954, and 1922 cm⁻¹, Table III. 2). Additionally, the COFs exhibited characteristic C≡N vibration stretches for imines at 1608–1622 cm⁻¹.

CHAPTER III

Mn based 2D-COF_{bpy} for electrocatalytic CO₂RR

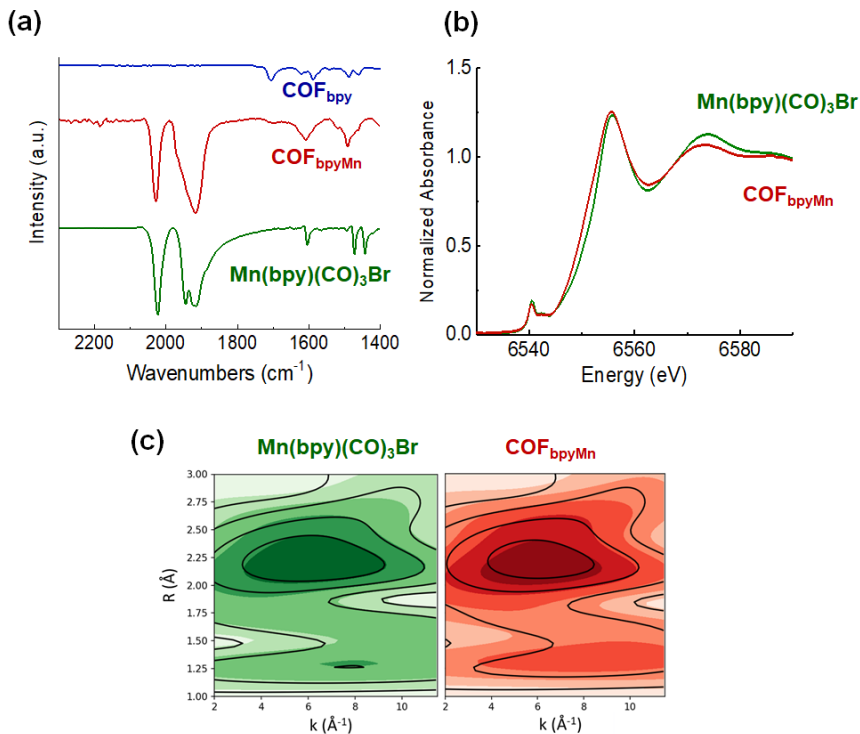


Figure III. 10. (a) IR spectra, (b) XANES spectra, and (c) Cauchy wavelet-transformed EXAFS data (Δk : 2–11.5 Å⁻¹) of Mn(bpy)(CO)₃Br **1** and COF_{bpy}Mn with best fit as black lines.

Table III. 2. Experimental (IR) and computed CO frequencies of COF_{bpy}Mn.

Species	$\nu_{\text{CO}}(\text{sym}) / \text{cm}^{-1}$	$\nu_{\text{CO}}(\text{asym}) / \text{cm}^{-1}$	$\nu_{\text{CO}}(\text{eq}) / \text{cm}^{-1}$
COF _{bpy} Mn 1	2013	1922	1954
COF _{bpy} ⁻ {Mn(CO) ₂ Br}	1957	1915	-
COF _{bpy} Mn 1 -red	1981	1915	1917
COF _{bpy} Mn 1 -red-acn	2020	1951	1947
IR COF _{bpy} Mn	2025	1917 (sh)	1941 (sh)

Manganese K-edge XAS analysis of complex *fac*-Mn(bpy)(CO)₃Br and COF_{bpy}Mn gave insights into the electronic structure and coordination environment of the Mn center (Figure III. 10b,c). From EXAFS analysis, the coordination environment of **1** consists of 3 CO molecules at 1.79 Å, a

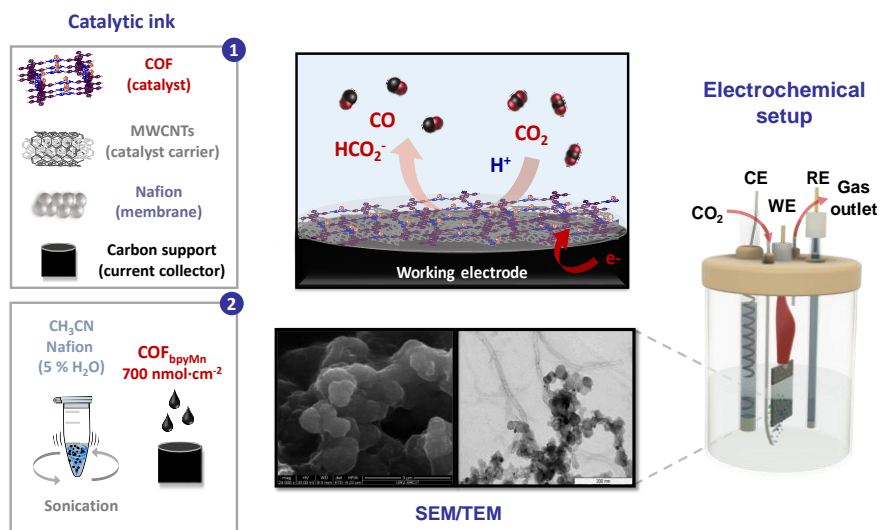
CHAPTER III

Mn based 2D-COF_{bpy} for electrocatalytic CO₂RR

bromide at 2.54 Å, and two bipyridine scattering nitrogen atoms at 2.03 Å. The coordination environment of COF_{bpyMn} is equivalent to the *fac*-Mn(bpy)(CO)₃Br, as confirmed by EXAFS data. Furthermore, both *fac*-Mn(bpy)(CO)₃Br and COF_{bpyMn} have similar pre-edge energies at ~6540.6 eV and intensities, consistent with a similar ligand field for the two species. Therefore, in general, the geometry of the Mn centers in the COF can be described as octahedral geometry with three carbonyls in *fac* disposition and one bromide atom completing the first coordination shell as in complex *fac*-Mn(bpy)(CO)₃Br.

III.2.2 Electrocatalytic CO₂ reduction in water.

To evaluate the catalytic activity of COF_{bpyMn} we performed cyclic voltammetry (CV) and controlled-potential electrolysis (CPE) in water (NaHCO₃, 0.5 M). The results were compared with the molecular counterpart *fac*-Mn(bpy)(CO)₃Br (Mnbpy) under identical reaction conditions. The working electrodes were prepared by depositing an ink containing the catalyst, multiwalled carbon nanotubes (NT) and Nafion on glassy carbon (GC) or carbon paper (CP) electrodes (see Experimental section for details, Scheme III. 2).



Scheme III. 2. Representation of the hybrid catalyst immobilization (cat|NT) (left), representation of the interface of COF_{bpyMn}|NT on the working electrode and SEM/TEM of COF_{bpyMn}|NT (center) and the electrochemical setup for the electrocatalytic CO₂ reduction reaction (right).

SEM images of deposited ink containing COF_{bpyMn}|NT showed a globular morphology, as in the COF_{bpyMn} powder (Scheme III. 2). Interestingly, TEM images of COF_{bpyMn}|NT showed COF bunches in contact with the multiwall carbon nanotubes (Scheme III. 2). The hybrid material morphology suggests a tight contact of the COF with the NT, which may favor the electric contact and, therefore, a catalytic activity increase (see EIS discussion below).^{23, 93-95}

We examined the CV of COF_{bpyMn}|NT ([Mn]_{total} = 700 nmol·cm⁻²) under Ar and CO₂ atmosphere (Figure III. 11). Under Ar the CV showed an intense irreversible cathodic wave, suggesting a catalytic hydrogen evolution reaction (HER), confirmed by the detection of H₂ after control potential electrolysis (see below). When the solution was saturated with CO₂ (pH 7.4), the onset of the catalytic wave shifted 150 mV to more positive potentials (overpotential (η), η_{CO} = 190 mV and η_{HCOO^-} = 220 mV, respectively) and the catalytic current increased 2.2-fold ($j_{\text{CO}_2}/j_{\text{Ar}}$ at -1.40 V). These values are 140 mV lower than those observed for **Mnbpy**|NT ([Mn]_{total} = 700 nmol·cm⁻²), showing only a small increase of catalytic current for **Mnbpy**|NT ($j_{\text{CO}_2}/j_{\text{Ar}}$ = 1.3, Figure III. 11). Another interesting difference between COF_{bpyMn}|NT and **Mnbpy**|NT was the backward CV scan features. **Mnbpy**|NT exhibits an intense peak at -0.45 V, which, according to the literature,^{18, 19, 96} was assigned to the reoxidation of Mn⁰-Mn⁰ dimer that forms during the forward scan. Notably, the feature barely appears for COF_{bpyMn}|NT (-0.49 V). We anticipate here that the formation of Mn dimers is inhibited by the mechanical constraint of the Mn centers in the reticular framework, which leads to Mn single-atom catalytic sites. A detailed discussion supported by *in situ* ATR-IR-SEC is presented in Chapter IV.

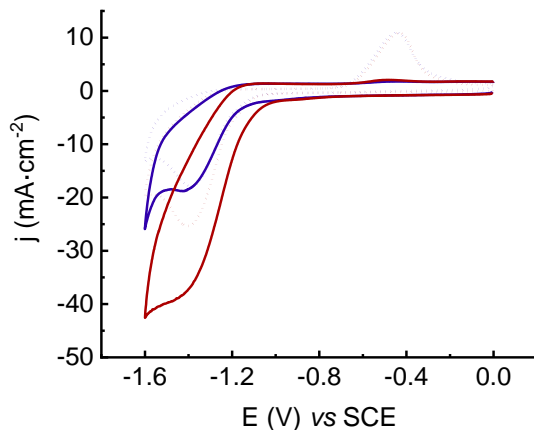


Figure III. 11. CVs on GC of COF_{bpyMn}|NT ($[Mn]_{total} = 700 \text{ nmol}\cdot\text{cm}^{-2}$, solid line) and 1|NT ($[Mn]_{total} = 700 \text{ nmol}\cdot\text{cm}^{-2}$, dotted line) in water (NaHCO₃ 0.5 M) under Ar (blue, pH 8.4) and CO₂ (red, pH 7.4) atm at $100 \text{ mV}\cdot\text{s}^{-1}$.

CPE experiments were carried out to benchmark the CO₂ reduction activity, selectivity, and stability of the COF_{bpyMn} compared to the homologous molecular complex **Mnbpy**. The generated products were analyzed by gas chromatography and ¹H-NMR (See experimental section for details). CPE at different applied potentials (from -1.1 to -1.8 V vs SCE) of COF_{bpyMn}|NT deposited on glassy carbon (GC) showed current densities from -0.5 to -12.5 mA·cm⁻² (Figure III. 12). Formation of CO and HCO₂⁻ were observed from a low η of 300 mV to 1000 mV, increasing the Faradaic efficiency up to 50-60% in the 500-600 mV η range. Nevertheless, the Faradaic efficiencies only slightly changed over a large η range (400-1000 mV)(Figure III. 12).

CHAPTER III

Mn based 2D-COF_{bpy} for electrocatalytic CO₂RR

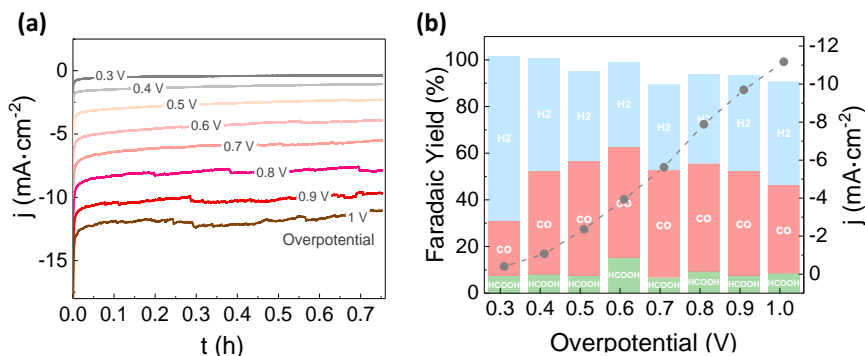


Figure III. 12. (a) Current density and b) Faradaic yield for CPEs of COF_{bpy}Mn|NT ([Mn]_{total} = 700 nmol·cm⁻²) in water (NaHCO₃ 0.5 M, pH 7.4) under CO₂ (GC) at different overpotentials.

Then, we performed long-term CPE ($E_{app} = -1.34$ V vs SCE) to evaluate the stability of COF_{bpy}Mn|NT (Figure III. 13). An average current density of ca. 2.4 mA·cm⁻² provided Faradaic yields of CO (FY_{CO}) and H₂ (FY_{H₂}) of 40±7% (14±3 μmol·cm⁻²) and 28±4% (9±2 μmol·cm⁻²), respectively, during the first hour of electrolysis (Figure III. 13b, c). During the following 7 h of the experiment, the FY_{H₂} slightly increased, whereas the FY_{CO} remained almost constant. The ¹H-NMR spectrum of the solution revealed only the formation of HCO₂⁻ with a FY_{HCO₂⁻} of 21±6% (38±13 μmol·cm⁻²). A total FY value of 97% for CO, HCO₂⁻, and H₂ discard a significant formation of other products. The CO₂-to-CO selectivity of COF_{bpy}Mn|NT is noticeably higher than previously reported for Mn**bpy**|NT (FY_{CO} = 14% and FY_{H₂} = 50% after 4 h).¹⁸ Moreover, under our conditions, the CO formed for COF_{bpy}Mn|NT was 10-fold higher than Mn**bpy**|NT (Figure III. 13d).

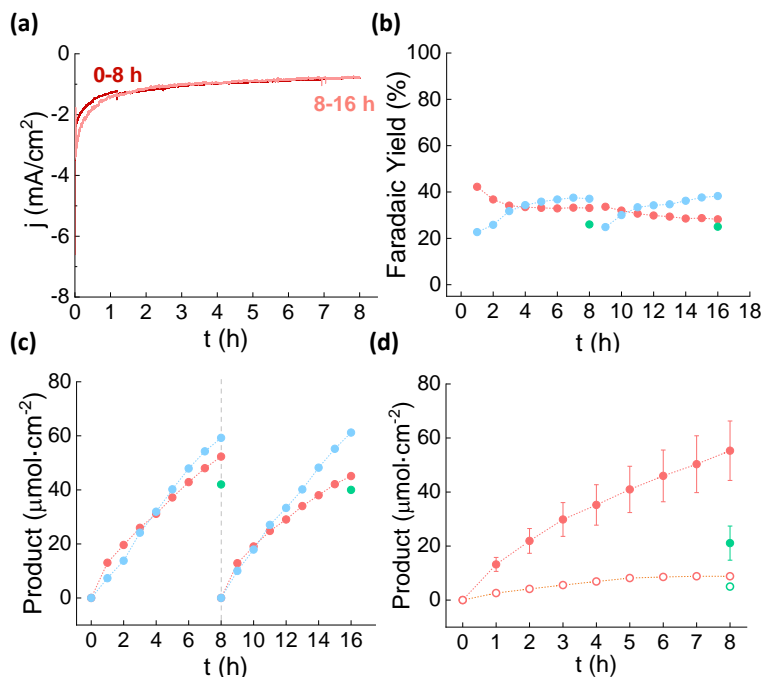


Figure III. 13. (a) Chronoamperogram of COF_{bpyMn}|NT ([Mn]_{total} = 700 nmol·cm⁻²) on Glassy Carbon plate over 8 h (red trace) and 16 h (pink trace) obtained in a CPE at -1.34 V vs SCE under CO₂ in 0.5 M NaHCO₃ (pH~7.4). (b) and (c) Faradaic yields and cumulative moles of generated CO (pink), H₂ (blue), and HCOO⁻ (green) over 16 h of CPE of COF_{bpyMn}|NT ([Mn]_{total} = 700 nmol·cm⁻²) on Glassy Carbon plate at -1.34 V vs SCE under CO₂ in 0.5 M NaHCO₃ (pH~7.4). Electrolysis evacuation measurement confirmed that the reaction rate recovered at 8 h by refreshing the solution and the reference and counter electrodes. (d) Comparison of the cumulative moles of generated CO (pink) and HCOO⁻ (green) of COF_{bpyMn}|NT ([Mn]_{total} = 700 nmol·cm⁻²) (full circle) and Mn_{bpy}|NT ([Mn]_{total} = 700 nmol·cm⁻²) (empty circle) on Glassy Carbon plate at -1.34 V vs SCE under CO₂ in 0.5 M NaHCO₃ (pH~7.4).

We recycled the electrode after 8 h of CPE ($E_{app} = -1.34$ V) and two days stored under air on the bench but protected from the light. A subsequent 8 h of CPE gave equivalent catalytic current profile (Figure III. 13a) and product distribution as previous CPE (Figure III. 13b,c).

Blank experiments support that the catalytic activity for CO₂ reduction is associated with the manganese centers. A CPE of the Mn-free COF_{bpy}|NT material gave negligible current, and no CO₂ reduction products were detected (Figure III. 14a,b). Moreover, under Ar, COF_{bpyMn}|NT yields a quantitative formation of H₂ ($FY_{H_2} = 91 \pm 2\%$),

CHAPTER III

Mn based 2D-COF_{bpy} for electrocatalytic CO₂RR

suggesting that the CO detected under CO₂ does not arise from catalyst decomposition (Figure III. 14c,d). On the other hand, COF_{bpy}|NT and bare Nafion/NT electrodes produce sustained H₂ evolution at working potential under CO₂ atmosphere (Table III. 7).

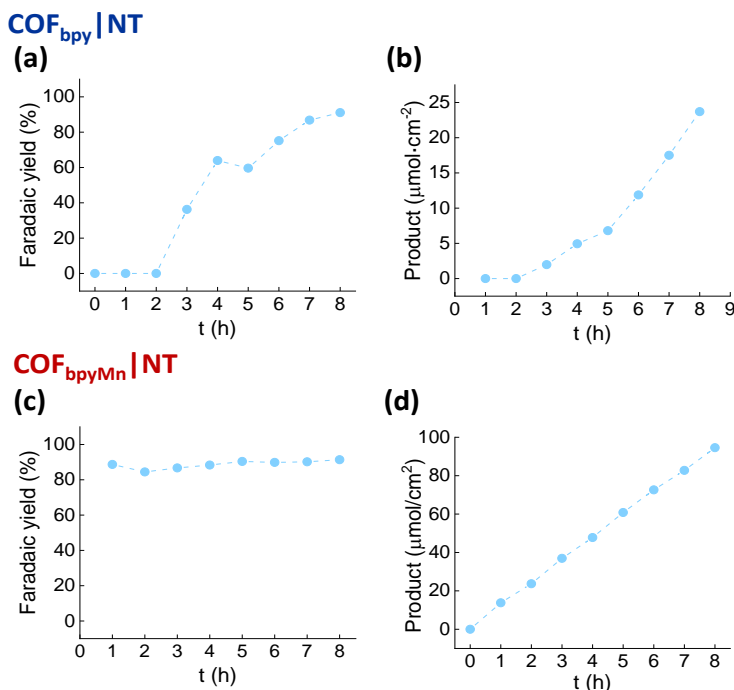


Figure III. 14. (a, b) Cumulative Faradaic Efficiency and moles of H₂ in the CPE at -1.34 V vs SCE of COF_{bpy}|NT on Glassy Carbon plate under CO₂ in 0.5 M NaHCO₃ (pH~7.4). (c, d) Cumulative Faradaic Efficiency and moles of H₂ in the CPE at -1.34 V vs SCE of COF_{bpyMn}|NT on Glassy Carbon plate under Ar in 0.5 M NaHCO₃ (pH~8.4).

III.2.3 Catalyst optimization.

To study the influence of catalyst surface loading of COF_{bpyMn}|NT in the CO₂RR performance, the electrochemical behavior of the electrodes with different surface loadings of COF_{bpyMn}|NT was subsequently examined. The catalyst loading was optimized to maximize the total current and the turnover frequency (TOF). The COF_{bpyMn}|NT was evaluated at loadings of 225 (E1), 350 (E2), 700 (E3) and 1400 nmol·cm⁻² (E4) of [Mn]_{total} and two additional electrodes: 1400 nmol·cm⁻² of [Mn]_{total} and the

CHAPTER III

Mn based 2D-COF_{bpy} for electrocatalytic CO₂RR

double amount of NT (**E5**) and with 700 nmol·cm⁻² of [Mn]_{total} of **Mnbpy**|NT loaded (**E0**) to compare.

First, to obtain the TOF and better compare the catalytic activity of the different catalyst loadings, we estimated the electroactive surface concentration for each loading. Γ values were obtained by the integration of the first reduction event in the CV for the COF_{bpyMn}|NT and the reoxidation wave of the dimer for the **Mnbpy**|NT under conditions related to the CPE (Figure III. 15, See details in the experimental Electrochemistry Section).

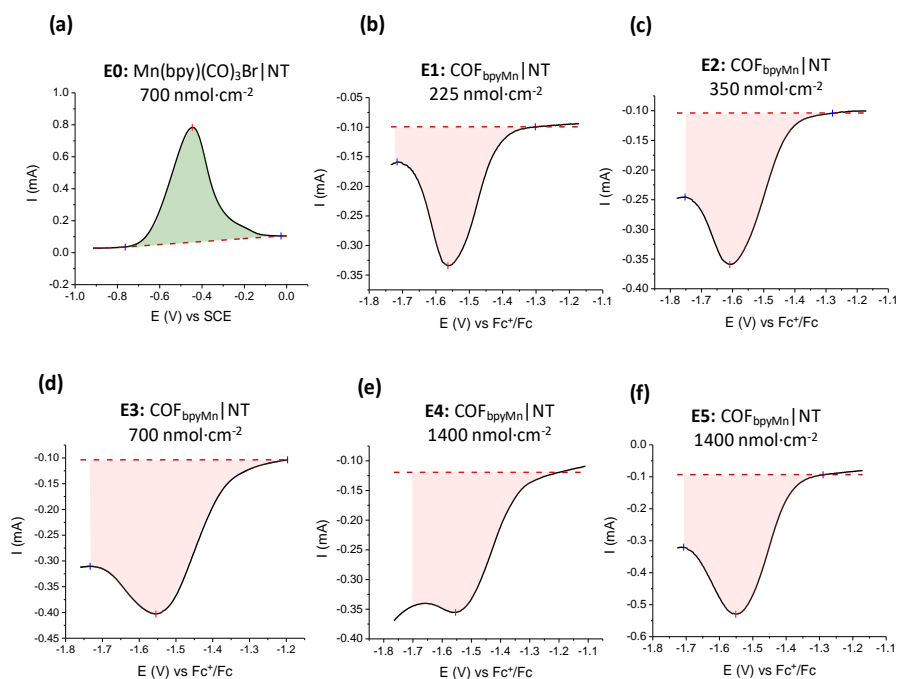


Figure III. 15. Cyclic voltammograms of different catalyst loadings recorded in water (0.5 M NaHCO₃) (a) and CH₃CN (0.1 M TBAPF₆) (b-f) under Ar at 100 mV·s⁻¹. Electrodes (GC, 0.0717 cm²) were prepared by drop casting 10 μ L of an ink containing the catalyst and NT (1 mg) dispersed in CH₃CN and Nafion 5% in water (1:1, 200 μ L) and let dry under dark. Catalyst deposited: E0) 700 nmol·cm⁻² of **Mn(bpy)(CO)₃Br**|NT, E1-E4) 225, 350, 700, 1400 nmol·cm⁻² of Mn in COF_{bpyMn}|NT, respectively. E5 was prepared by drop-casting 20 μ L of E3 ink (1400 nm·cm⁻² of Mn) and double the amount of NT than the rest of the electrodes.

In general, the quantity of electroactive Mn in the COF_{bpyMn}|NT electrodes was high; about 18-24% of the total Mn deposited; an exception was for the highest loading, which was reduced to 6-10% (Table III. 3). For

CHAPTER III Mn based 2D-COF_{bpy} for electrocatalytic CO₂RR

the **Mnbpy|NT** (700 nmol·cm⁻² deposited), the electroactive surface concentration represents 17% of the total Mn deposited, which is within the error of previously reported values⁹⁷ (11%) and equivalent to that obtained for **COF_{bpyMn}|NT** (18%) for the same amount of Mn loaded (Table III. 3).

Table III. 3. Electroactive surface concentration (Γ) values.

Electrode	Catalyst	[Mn] _{total}	Γ	Electroactive
		(nmol·cm ⁻²) ^a	(nmol·cm ⁻²) ^b	Mn (%)
E0	Mn(bpy)(CO)₃Br NT	700	120	17
E1	COF_{bpyMn} NT	225	50	24
E2	COF_{bpyMn} NT	350	80	23
E3	COF_{bpyMn} NT	700	120	18
E4	COF_{bpyMn} NT	1400	80	6
E5	COF_{bpyMn} NT	1400	140	10

*Working Electrodes (GC, 0.0717 cm²) were prepared by drop casting 10 μ L of an ink containing the catalyst and NT (1 mg) dispersed in CH₃CN and Nafion 5% in water (1:1, 200 μ L) and let dry under dark. Catalyst deposited: E0) 700 nmol·cm⁻² of **Mn(bpy)(CO)₃Br|NT**, E1-E4) 225, 350, 700, 1400 nmol·cm⁻² of Mn in **COF_{bpyMn}|NT**, respectively. E5 was prepared by drop-casting 20 μ L of E3 ink (1400 nm·cm⁻² of Mn) and double amount of NT than the rest of the electrodes. ^a nmol·cm⁻² of all the Mn in the ink. ^b nmol·cm⁻² of Mn considering the Γ .*

Next, we performed CVs on GC of Mn loading of 225 (**E1**), 350 (**E2**), 700 (**E3**), 1400 (**E4**) and 1400 nmol·cm⁻² (but with a double amount of NT **E5**) in water (0.5 M NaHCO₃) under Ar and under CO₂ (Figure III. 16). The CVs at different loadings present the characteristic profile of **COF_{bpyMn}|NT**. Under Ar, for all **COF_{bpyMn}|NT** surface loadings, an intense irreversible cathodic wave was observed and in the presence of CO₂ the increase in the current density and the shift in the onset of the catalytic wave were indicative of a catalytic CO₂RR. Notably, at surface loadings of 225 (**E1**), 350 (**E2**) the j_{CO_2}/j_{Ar} was similar, but higher currents were observed at loadings of 700 (**E3**) and 1400 nmol·cm⁻² (**E5**) where the ratio catalyst/NTs was 1:1 (Figure III. 16f). The decrease in activity observed at a surface loading of 1400 nmol·cm⁻² (**E4**) can also be rationalized in terms of

CHAPTER III

Mn based 2D-COF_{bpy} for electrocatalytic CO₂RR

conductivity, where the Mn centers are less accessible to be reduced.^{8g, 24} The feature of CV at different loadings illustrates NTs play an important role in the catalytic performance, increasing the conductivity of the catalyst and agrees with the Γ obtained at different loadings (Table III. 3, See further discussion in EIS section).

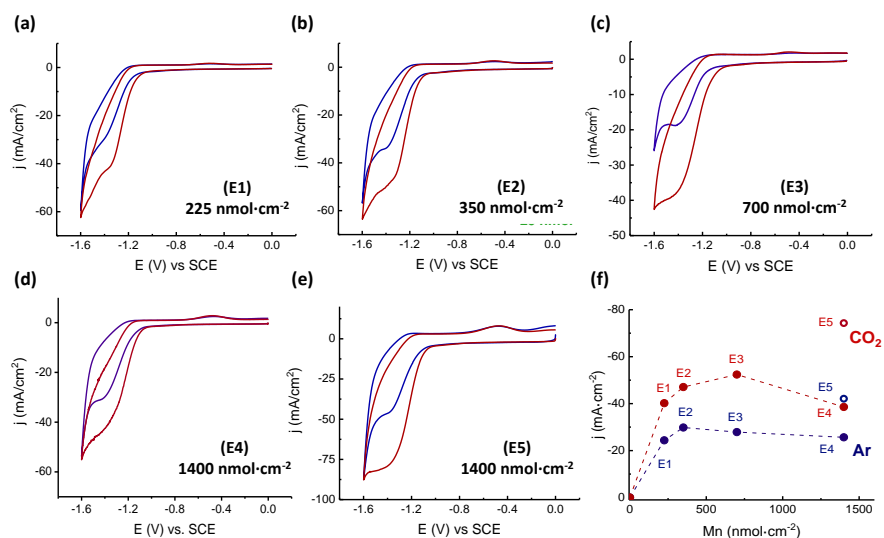


Figure III. 16. (a-e) Cyclic voltammograms of different catalyst loadings recorded in water (0.5 M NaHCO₃) under Ar and CO₂ at 100 mV·s⁻¹. Electrodes (GC, 0.0717 cm²) were prepared by drop casting 10 μ L of an ink containing the catalyst and NT (1 mg) dispersed in CH₃CN and Nafion 5% in water (1:1, 200 μ L) and let dry under dark. Catalyst deposited: E1-E4 225, 350, 700, 1400 nmol·cm⁻² of Mn in COF_{bpy}Mn|NT, respectively. E5 was prepared by drop-casting 20 μ L of E3 ink (1400 nm·cm⁻² of Mn) and double amount of NT than the rest of the electrodes. (f) Values of current densities under Ar and CO₂ (the values were taken from CV a-e) considering the nmol·cm⁻² of Mn on the electrode.

The effect of Γ of Mn on the catalytic activity and selectivity was studied by CPE. In order to improve the catalytic activity, we first replace the GC plate use as a working electrode for a gas diffusion layer electrode (GDL, carbon paper, CP) (see the experimental section for details). To our delight, with a surface loading of 700 nmol·cm⁻² (E3) the new electrode showed ca. 4-fold increase of the current density from our previous averaged -2.4 mA·cm⁻² during the first 1 h to > 10 mA·cm⁻² (Figure III. 17a). In general, TOF_(CO) and TOF_(HCO₂⁻) values and the total amount of CO

CHAPTER III

Mn based 2D-COF_{bpy} for electrocatalytic CO₂RR

produced were c.a. 3-fold higher for CP than for Glassy Carbon (GC) without significant modification of the Faradaic yield.

Table III. 4. Comparison between GC and CP as a current collector.

Current Collector	CO (μmol) ^a	TOF _(CO) (h ⁻¹) ^b	TOF _(HCO⁻) (h ⁻¹) ^b
Glassy Carbon (GC)	60	340	140
Carbon paper (CP) ^c	190	1100	510
Ratio CP/GC	3.2	3.2	3.6

CPEs were carried out in water (NaHCO₃ 0.5 M, pH 7.4) under CO₂ with electrodes (1 cm²) prepared by depositing COF_{bpyMn}/NT corresponding to 700 nmol·cm⁻² of Mn, MWCNTs and Nafion. ^[a] CO accumulated during 8 h of CPE at -1.34 V vs SCE, pH 7.4. ^[b] TOF values after 1 h of CPE. ^[c] Freudenberg H23C6.

We further enhanced the catalytic activity up to 12-fold by doubling the amount of catalyst and carbon nanotubes deposited on the CP (1400 nmol·cm⁻², **E5**) (Figure III. 17a-c). In both cases (CP_{E3} and CP_{E5}), the Faradaic yields were equivalent to those obtained with GC.

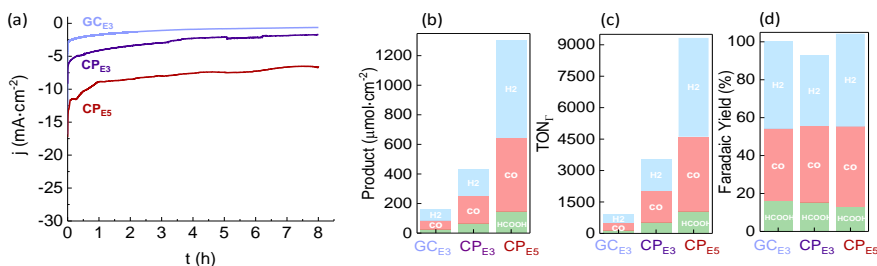


Figure III. 17. Evaluation of the effect of catalyst loading and current collector by CPE at -1.34 V vs SCE under CO₂ in water (NaHCO₃ 0.5 M, pH 7.4) during 8 h with different supporting materials and loadings. a) Current densities, b) products formed and c-d) TOFs and Faradaic yields. **GC** and **CP** stand for glassy carbon and carbon paper, respectively. **E3** and **E5** stand for electrodes prepared with COF_{bpyMn}/NT with a loading of 700 and 1400 nmol·cm⁻² of Mn.

We note that an advantage of the CP support is the possibility of increasing the catalyst loading per geometrical area, maintaining excellent mechanical stability of the deposited film. From CPE the current density increases with the concomitant increase of the COF_{bpyMn}/NT loading (Figure III. 18a). The FY for all the loadings was similar, while the μmol of the generated products increased with the deposited COF_{bpyMn}/NT (Figure III. 18b,c). Considering the measured Γ , the TOF_(CO) values (at -1.34 V vs SCE) for COF_{bpyMn}/NT ranged from 430 to 1100 h⁻¹ depending on the amount of deposited COF_{bpyMn}/NT (Figure III. 18). The obtained

CHAPTER III Mn based 2D-COF_{bpy} for electrocatalytic CO₂RR

TOF_(CO) values are much larger than the ones measured for **Mn(bpy)(CO)₃Br|NT** (TOF_(CO) = 40 h⁻¹), and those previously reported in the literature (Table III. 8).

Table III. 5. Electroactive surface concentration (Γ) values.

Electrode	Catalyst	[Mn] _{total}	Γ	Electroactive
		(nmol·cm ⁻²) ^a	(nmol·cm ⁻²) ^b	Mn (%)
E0	Mn(bpy)(CO)₃Br NT	700	120	17
E1	COF_{bpyMn} NT	225	50	24
E2	COF_{bpyMn} NT	350	80	23
E3	COF_{bpyMn} NT	700	120	18
E4	COF_{bpyMn} NT	1400	80	6
E5	COF_{bpyMn} NT	1400	140	10

*Working Electrodes (GC, 0.0717 cm²) were prepared by drop casting 10 μL of an ink containing the catalyst and NT (1 mg) dispersed in CH₃CN and Nafion 5% in water (1:1, 200 μL) and let dry under dark. Catalyst deposited: E0) 700 nmol·cm⁻² of **Mn(bpy)(CO)₃Br|NT**, E1-E4) 225, 350, 700, 1400 nmol·cm⁻² of Mn in **COF_{bpyMn}|NT**, respectively. E5 was prepared by drop-casting 20 μL of E3 ink (1400 nm·cm⁻² of Mn) and double amount of NT than the rest of the electrodes. ^a nmol·cm⁻² of all the Mn in the ink. ^b nmol·cm⁻² of Mn considering the Γ.*

Therefore, the TOF_(CO) resulted in 16-fold higher for **COF_{bpyMn}|NT (E3)** than **Mnbpy|NT (E0)** (630 and 40 h⁻¹, respectively (Figure III. 18, Table III. 6.)), highlighting the benefit of integrating the {Mn(bpy)(CO)₃Br} in the COF structure. At higher catalyst loading (**E4**, [Mn]_{total} = 1400 nmol·cm⁻²) the TOF_{CO} (**COF_{bpyMn}|NT**) arrived up to 1100 h⁻¹. This unexpected TOF increment with the catalyst loading results from the lower NT and **COF_{bpyMn}|NT** ratio, reflecting the lower Γ. This effect was minimized when we doubled the amount of deposited NT while maintaining the Mn loading (**E5**, [Mn]_{total} = 1400 nmol·cm⁻²). The current density increased, yielding a higher CO formation (114 vs 87 μmol·cm⁻², 1 h CPE at -1.34 V vs SCE).

CHAPTER III Mn based 2D-COF_{bpy} for electrocatalytic CO₂RR

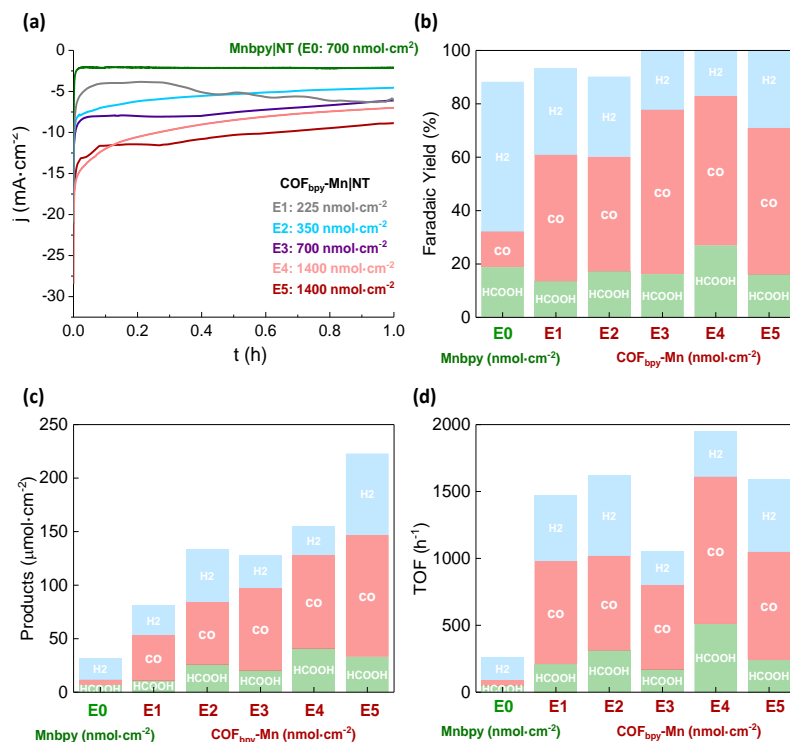


Figure III. 18. CPEs at different catalyst loadings in water (NaHCO₃ 0.5 M, pH 7.4) under CO₂ at -1.34 V vs SCE for 1 h. Electrodes (CP, 1 cm²) were prepared by spraying an ink containing the catalyst and NT dispersed in CH₃CN and Nafion 5% in water (1:1) and let dry under dark. Catalyst deposited: 700 nmol·cm⁻² of Mn(bpy)(CO)₃Br|NT (E0) and 225, 350, 700, 1400 nmol·cm⁻² of Mn contained in COF_{bpy}Mn|NT (E1-E4), respectively. E5 contains 1400 nmol·cm⁻² of Mn in COF_{bpy}Mn|NT with double amount of NT than the other samples.

Table III. 6. CO₂RR performances by CPE in water according to the catalyst loadings.

WE	Cat.	[Mn] _{total} (nmol·cm ⁻²)		TOF [Mn] _{total} (h ⁻¹) ^c			TOF Mn _r ·(h ⁻¹) ^d		
		Deposited ^a	Γ ^b	CO	HCO ₂ H	H ₂	CO	HCO ₂ H	H ₂
E0	1 NT	700	120	7	10	30	40	50	170
E1	COF _{bpyMn} NT	225	50	190	50	120	770	210	490
E2	COF _{bpyMn} NT	350	80	170	70	140	710	310	600
E3	COF _{bpyMn} NT	700	120	110	30	40	630	170	250
E4	COF _{bpyMn} NT	1400	80	60	30	20	1100	510	340
E5	COF _{bpyMn} NT	1400	140	80	25	50	810	240	540

CPEs at different catalyst loadings were carried out in water (NaHCO₃ 0.5 M, pH 7.4) under CO₂ at -1.34 V (vs SCE) for 1 h. Electrodes (Carbon Paper, 1 cm²) were prepared by spraying an ink containing the catalyst and NT dispersed in CH₃CN and Nafion 5% in water (1:1) and let dry under dark. Catalyst deposited: E0) 700 nmol·cm⁻² of Mn(bpy)(CO)₃Br|NT (1|NT), E1-E4) 225, 350, 700, 1400 nmol·cm⁻² of [Mn]_{total} in COF_{bpyMn}|NT, respectively. E5 was prepared by drop-casting 20 μL of E3 ink (1400 nmol·cm⁻² of [Mn]_{total}) and double amount of NT than the rest of the electrodes. ^a nmol·cm⁻² of Mn considering the deposited^b nmol·cm⁻² of Mn considering the Γ. ^c TOF (n(P) / (n(Mn_(total))·t)). ^d TOF (n(P) / (n(Mn_(Γ))·t))

Table III. 7. CPE comparison of catalytic activity using GC and CP as working electrode.

Glassy Carbon

Catalyst	[Mn]	Faradaic Yield (%) (8 h)			Products ($\mu\text{mol}\cdot\text{cm}^{-2}\cdot\text{h}^{-1}$)			TOF _r (h^{-1})			j ($\text{mA}\cdot\text{cm}^{-2}$) (1 h)
		CO	HCO ₂ ⁻	H ₂	CO	HCO ₂ ⁻	H ₂	CO	HCO ₂ ⁻	H ₂	
COF _{bpyMn} NT /CO ₂	E3	40	20	40	7	5	8	56	40	61	-1.4
*COF _{bpyMn} NT /CO ₂	E3	34	10	46	2.5	5	3	20	5	26	-1.2
COF _{bpyMn} NT /Ar	E3	-	-	91	-	-	12	-	-	97	-0.8
COF _{bpy} NT /CO ₂	-	-	-	91	-	-	3	-	-	-	-0.1
MWCNTs /CO ₂	-	-	-	85	-	-	7	-	-	-	-0.4

Carbon paper

Mn(bpy)(CO)Br NT	E0	13	19	56	5	7	20	40	56	168	-2
COF _{bpyMn} NT /CO ₂	E1	48	14	32	42	11	27	768	201	494	-4
COF _{bpyMn} NT /CO ₂	E2	43	17	30	58	26	49	705	316	596	-6
COF _{bpyMn} NT /CO ₂	E3	62	16	22	77	20	31	627	163	252	-7
COF _{bpyMn} NT /CO ₂	E4	56	27	18	87	41	27	1064	501	330	-10.5
COF _{bpyMn} NT /CO ₂	E5	55	16	36	114	33	76	805	233	536	-10

*This CPE was performed at -1.25 V vs SCE and the rest at -1.34 V vs SCE.

Table III. 8. Performance of a selection of CO₂ reduction catalysts.

Catalyst	η^a	Electrolyte	j^b	FY _{co} ^c	nco ^d	TOF _{co} ^e	Ref
COF _{bpyMn}	550	NaHCO ₃ (0.5 M) pH 7.4	15	55	114	805	This work
COF _{bpyMn}	550	NaHCO ₃ (0.5 M) pH 7.4	8	62	77	627	This work
Mn(bpy)(CO) ₃ Br NT	550	NaHCO ₃ (0.5 M) pH 7.4	2	13	5	40	This work
[Mn-MeCN]/MWCNT	380	K ₂ B ₄ O ₇ (0.1 M) K ₂ SO ₄ (0.2 M) pH 6.6	5.2	82	74	70	20
CMP-(bpy) ₂₀ -Mn	850	PB (0.06 M) pH 7	2	0.4	0.2	-	76
CNT Mnpyr	550	KHCO ₃ (0.5 M) pH 7.4	2	34	46	175	19
Mnbpy/MWCNT	610	PB (0.1 M)	1.8	14	1.5	4.6	18
Mnbpy/MWCNT	650	BP (0.06 M) pH 7.4	1	22	3	25	97
[Mn(bpy)(COOH) ₂](CO) ₃ Br]	650	K ₂ CO ₃ (0.5 M) + KCl (0.1 M) pH 9	0.25 ^g	65	-	2.5	98

Mn-MOF	652	CH ₃ CN + 0.25% acetic acid	-	-	0.03	3.5	99
TiO ₂ /MnP	420	CH ₃ CN + 5% H ₂ O	0.15	67	1.9	52	100
[Mnbpy(CO) ₃ Br]/GC	980	CH ₃ CN + 4% H ₂ O	-	75	0.45	300	17
[Mnbpy(CO) ₃ Br]/GC	1180	CH ₃ CN + 8% MeOH	-	66	0.54	362	17
COF-2,2'-bpy (Re)	2030	CH ₃ CN	0.3	57	0.03	51	67
COF-Re	550	KHCO ₃ (0.5 M)	3	0	0	-	68
COF-Re_Co	550	KHCO ₃ (0.5 M)	0.5	18	3	-	68
COF-Re_Fe	550	KHCO ₃ (0.5 M)	4	<2	1.3	-	68

^a(mV), ^b(mA·cm⁻²), ^c(%), ^d(μmol·cm⁻²·h⁻¹), ^e(h⁻¹), ^f mA in Hg/ Au amalgam, PB stands for Phosphate buffer. Mnbpy stands for Mn(bpy)(CO)₃Br

III.2.4 Catalyst stability

COF_{bpyMn}|NT electrodes show excellent stability under catalytic conditions. A superimposition of linear sweep voltammetry (LSV) traces recorded before and after 16 h of CPE indicates negligible catalyst decomposition (Figure III. 19a). The Mn coordination in COF_{bpyMn}|NT is also preserved after CPE as confirmed by the absence of changes in the ATR-IR spectra recorded before and after CPE (Figure III. 19b), further highlighting the robustness of the COF.

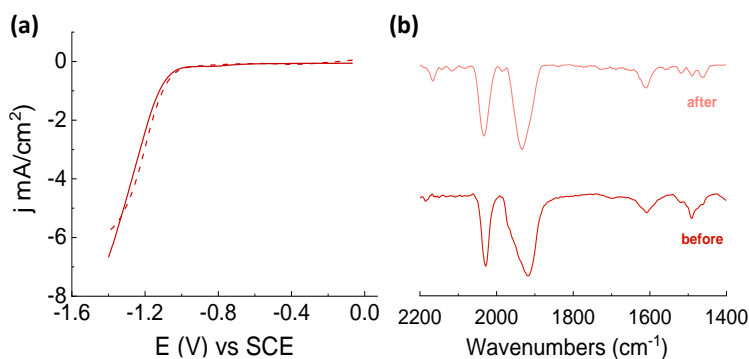


Figure III. 19. (a) Linear Sweep Voltammetry of COF_{bpyMn}|NT ([Mn]_{total} = 700 nmol·cm⁻²) on Glassy Carbon plate before (solid trace) and after (dashed trace) CPE of 16 h at -1.34 V vs SCE under CO₂ in 0.5 M NaHCO₃ (pH~7.4) at 10 mV·s⁻¹. (b) ATR-IR spectra of COF_{bpyMn}|NT were measured before (red line) and after (pink line) 16 h of CPE at -1.34 V vs SCE under CO₂ in 0.5 M NaHCO₃ (pH~7.4).

Given these results, we rationalized that the decrease in current density observed during the bulk electrolysis (Figure III. 13a) could be attributed to other factors such as the local depletion of the CO₂ concentration inside the porous material rather than the deactivation of the catalytic sites.¹⁸ An alternative explanation is that the gaseous CO produced could be partially trapped inside the pores, thus diminishing the actual CO₂ concentration available in the electroactive layer.¹⁸

In general, no significant changes were observed by XPS, SEM and TEM analysis before and after 1 or 8 h of electrocatalysis in water under CO₂ (Figure III. 20). EDX showed the homogeneous distribution of Mn before and after catalysis. In agreement, ICP-OES of the solution after 1 h of CPE indicates that only 2% of the total amount of Mn on the

CHAPTER III Mn based 2D-COF_{bpy} for electrocatalytic CO₂RR

COF_{bpyMn}|NT electrode leached out. The amount of Mn in solution did not increase in the following 8 h of CPE.

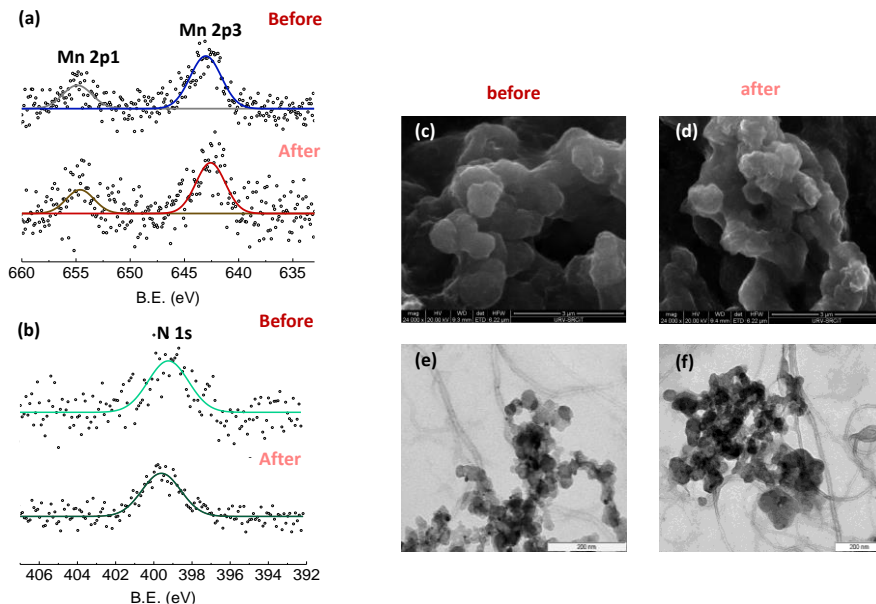


Figure III. 20. (a, b) XPS analysis of COF_{bpyMn}|NT (E3: 700 nmol·cm⁻² of Mn deposited) before and after CPE in water (0.5 M NaHCO₃) under CO₂ at -1.34 V vs SCE. (a) Mn 2p¹, 2p³ core levels XPS spectrum; (b) N 1s core level XPS spectrum. (c, d) SEM and (e, f) TEM measurements of COF_{bpyMn}|NT (E3) before (left) and after 8 h of CPE (right) at -1.34 V vs SCE in water (0.5 M NaHCO₃) under CO₂ (pH 7.4).

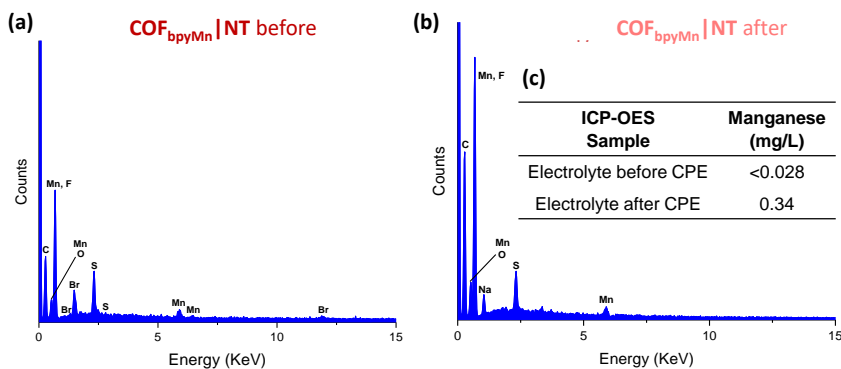


Figure III. 21. EDX spectra of COF_{bpyMn}|NT (E3) before (left) and after 8 h of CPE (right) at -1.34 V vs SCE in water (0.5 M NaHCO₃) under CO₂ (pH 7.4). Mn content by ICP OES (mg/L) in the electrolyte (0.5 m NaHCO₃) before and after 8 h of CPE of COF_{bpyMn}|NT (E3) at -1.34 V vs SCE under CO₂.

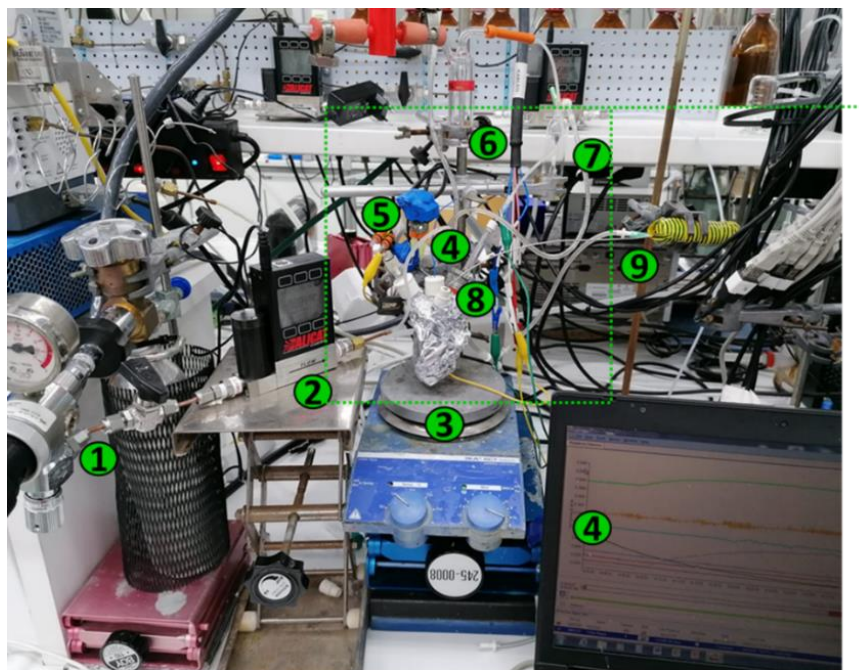
III.2.5 Isotopic Labelling

On the other hand, the large number of TONs (> 1000), current densities obtained, the correct mass balance and the formation of only H₂ (FY_{H₂} = 91±2%) under Ar, indicate that the CO₂ reduction is authentic and the catalyst decomposition does not form the detected product. Nevertheless, to unequivocally demonstrate the carbon source in the products, we have performed labelling experiments in electrolysis, saturating the solution (0.5 M NaH¹³CO₃) with ¹³CO₂. We analyzed the headspace by on-line MS and the liquid phase by ¹H-NMR.

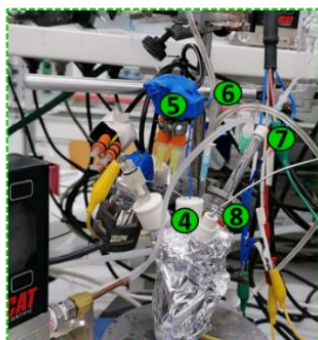
We carried out an equivalent experimental setup as described for the CPE under CO₂ with some modifications (Figure III. 22). First, NaH¹³CO₃ (0.5 M, aq) was used as electrolyte and ¹³CO₂ as CO₂ source. The electrochemical cell was connected to one port of a differential pressure transducer and the other port to a reference vial to control de pressure. Before the CPE, the headspace of the electrochemical cell was purged with Ar for 30 min. Then, ¹²CO₂ or ¹³CO₂ were introduced at a flow rate of 2 mL·min⁻¹ with a mass flow controller and under vigorous stirring to guarantee the solution's complete saturation (Figure III. 23). The cell outlet was connected to the inlet of the online-MS for continuous analysis of the headspace during CPE. The working electrode was a COF_{bpyMn}|NT CP of 1cm² (E5: 1400 nmol·cm⁻²) and the CPE was performed at -1.4 V vs SCE for 800 s.

CHAPTER III

Mn based 2D-COF_{bpy} for electrocatalytic CO₂RR



Electrochemical cell



Setup components

- ① ¹³CO₂ bottle
- ② Mass flow controller (2 mL·min⁻¹)
- ③ Stirring plate
- ④ ¹³CO₂ inlet (2 mL/min)
- ⑤ Pressure sensor
- ⑥ Bubbler 1 (outlet of EC-cell)
- ⑦ Bubbler 2 (outlet of CE)
- ⑧ Capillary (OD 1.59 mm, ID 0.13 mm)
- ⑨ Online-MS

Figure III. 22. Setup and components for the isotope labeling experiments in the electrochemical ¹³CO₂ reduction in flow conditions.

CHAPTER III

Mn based 2D-COF_{bpy} for electrocatalytic CO₂RR

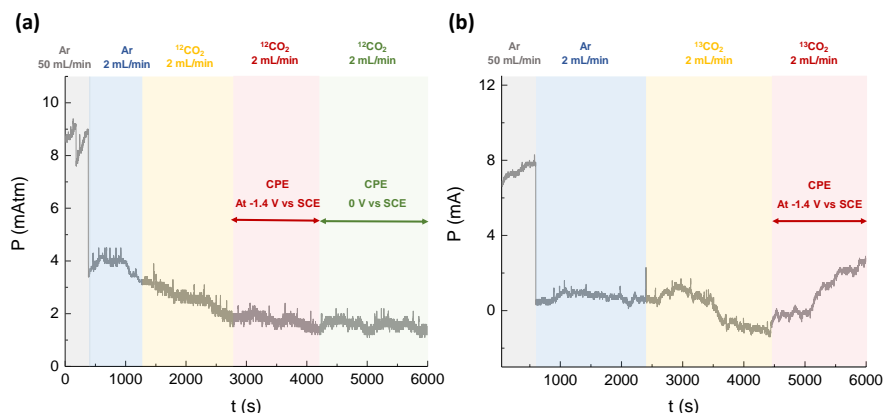
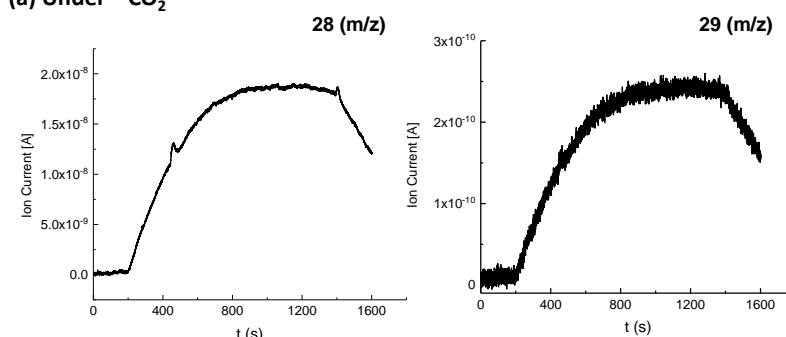


Figure III. 23. Control of the pressure inside the electrochemical cell before and during the CPE at -1.4 V vs SCE under a) ¹²CO₂ and b) ¹³CO₂.

From the online-MS analysis of the headspace during CPE ¹²CO (m/z=28) was the main product under ¹²CO₂ and ¹³CO (m/z=29) under ¹³CO₂ (Figure III. 24). During the CPE the current density was similar under ¹²CO₂ and ¹³CO₂ with a value of c.a. 12 mA·cm⁻² (Figure III. 25a).

(a) Under ¹²CO₂



(b) Under ¹³CO₂

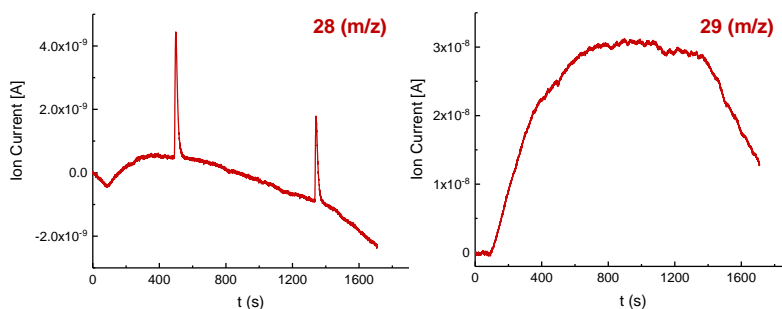


Figure III. 24. Evolution of the ions 28 and 29 (m/z) during the isotopic labeling experiment in the CPE at -1.4 V vs SCE. Spikes in plot b were due to eventual pressure changes.

CHAPTER III Mn based 2D-COF_{bpy} for electrocatalytic CO₂RR

The experiments yielded almost exclusively the carbon 13 labelled ¹³CO and H¹³CO₂H products, indicating that the reduced products proceed from the CO₂ reduction (Figure III. 25).

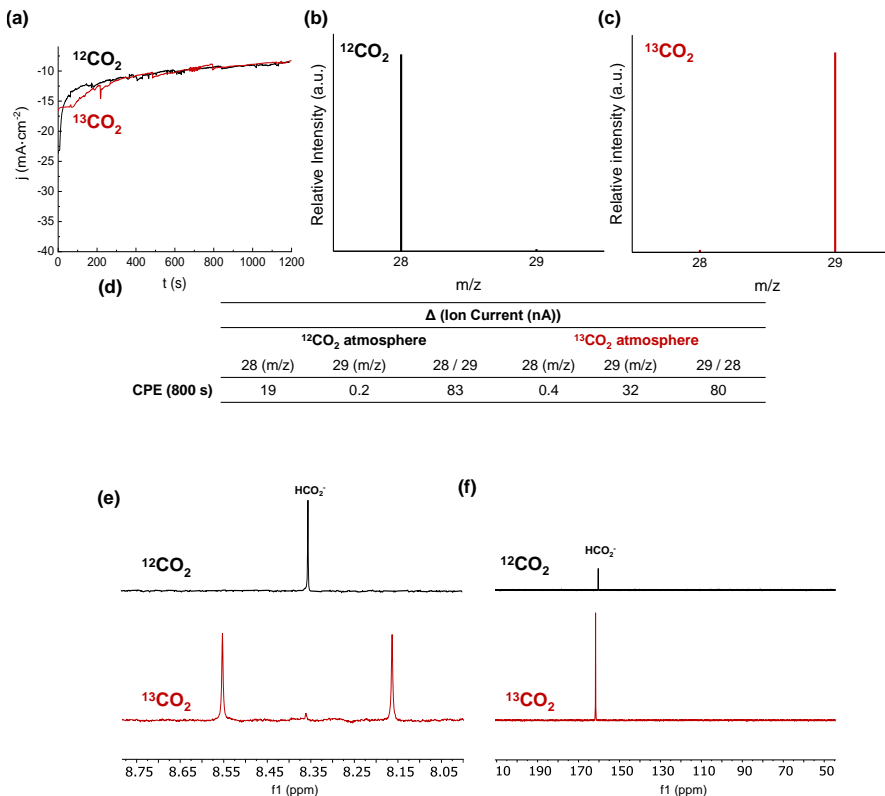


Figure III. 25. CPE isotopic labeling experiment with COF_{bpyMn}|NT (E5: 1400 nmol·cm⁻²) at -1.4 V vs SCE. MS analyses of the gas phase in 0.5 M NaHCO₃ under ¹²CO₂ (a) CA during the CPE isotopic labeling experiment with COF_{bpyMn}|NT (E5: 1400 nmol·cm⁻²) at -1.4 V vs SCE in 0.5 M NaHCO₃ under ¹²CO₂ (black) and in 0.5 M NaH¹³CO₃ under ¹³CO₂ (red) and (b) in 0.5 M NaH¹³CO₃ under ¹³CO₂. (c) Comparison of relative detection of ions 28 and 29 (m/z) after 800 s of CPE (background signal before CPE was subtracted). (d) ¹H-NMR and ¹³C-NMR spectra (500 MHz, D₂O) on 600 μ L electrolyte aliquot after 800 s of CPE in 0.5 M NaHCO₃ under ¹²CO₂ (e) and in 0.5 M NaH¹³CO₃ under ¹³CO₂ (f).

III.2.6 Electrochemical impedance spectroscopy (EIS) studies.

To evaluate the effect of the carbon nanotubes, we have compared the hybrid COF_{bpyMn}|NT (E3, [Mn]_{total} = 700 nmol·cm⁻²) with the bare COF_{bpyMn} ([Mn]_{total} = 700 nmol·cm⁻²) and NT using EIS (Figure III. 26). The measured capacitance of COF_{bpyMn} was very low (0.15 μ F, at -0.85 V

CHAPTER III

Mn based 2D-COF_{bpy} for electrocatalytic CO₂RR

vs SCE), due to the poor conductivity. In contrast, the COF_{bpyMn}|NT capacitance was three orders of magnitude higher (322 μF). This value matches the NT alone (315 μF, Figure III. 26c), implying that the NT contribution dominates the capacitance. However, there is a clear difference between them. Above -0.95 V, there is an increment of COF_{bpyMn}|NT capacitance (800 μF), associated with reducing the Mn centers (catalysis); it is absent for the NT alone, which remains constant at 312 μF.

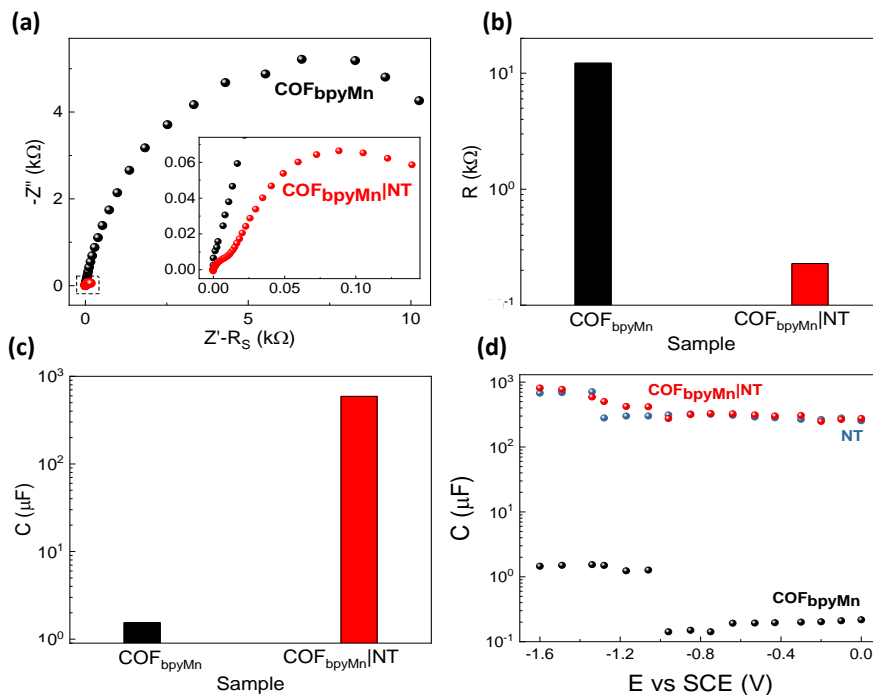


Figure III. 26. (a) Nyquist plot for COF_{bpyMn} (black) and COF_{bpyMn}|NT (red) under CO₂ at E = -1.3 V vs SCE. Capacitance (b) and resistance (c) in the -1.1 and -1.6 V range. (d) Trend of capacitance versus the applied potential for COF_{bpyMn} (black), COF_{bpyMn}|NT (red) and NT alone (blue).

An analogous increase was observed for COF_{bpyMn} in the same redox region but about 660 times lower (1.2 μF vs 800 μF). Since the capacitance is strictly related to the electroactive surface area (ECSA), this is a signature of redox-active Mn centres (number of catalytic sites). Moreover, the capacitance increment correlates well with the observed 62-fold catalytic current improvement of COF_{bpyMn}|NT vs COF_{bpyMn} (1.57 mA vs 0.025 mA at -1.3 V, respectively). Likewise, at the same redox potential, the charge

transfer resistance associated with the Faradaic current (CO₂ reduction) decreases ca. 50-fold for the hybrid system. Therefore, the hybridization strategy of the COF with the NT serves to improve the electrical connection of the active catalytic sites with the current collector. Indeed, Γ values showed the highest values, ca. 25% of the total amount of catalytic sites, when the higher NTs and COF_{bpyMn} ratio.

III.3 Conclusions

We have prepared the first manganese electrocatalytically active covalent organic framework COF_{bpyMn} by post-synthetic modification of COF_{bpy} with Mn(CO)₅Br.

The COF_{bpy} feature ordered alignment of binding sites that offer open docking sites on the channel walls and allow to obtain high loading of Mn atoms (85 %) in COF_{bpyMn}. Metallation converts the frameworks into dense and aligned catalytic Mn sites confined within the nanochannels. Its spectroscopic characterization by IR, PXRD, and XAS, along with correlation to theoretical calculations, clearly shows that the Mn centers at the COF have an equivalent coordination environment to the homologous molecular complex [*fac*-Mn(bpy)(CO)₃Br]. Furthermore, the lowest energy structure obtained for COF_{bpy} by periodic calculations has the nitrogen atoms of bipyridines of consecutive stacked layers in alternated directions. This spatial bipyridine arrangement is a key feature not reported previously that helps explain the high Mn loading and the existence of Mn single sites.

The hybrid COF_{bpyMn}|NT was found active for electrochemical CO₂ reduction in water at lower overpotential than the molecular counterpart by 140 mV, having among the lowest reported (190 mV). The encapsulation of a Mn molecular catalyst for CO₂RR into an ordered 3D porous framework substantially improves the activity and selectivity for CO₂RR over HER in aqueous media. The combined selectivity for the CO₂ reduction products versus H₂ was up to 72% (1 h) with high current densities (> 12 mA·cm⁻²). TOF_{CO} and TON_{CO} values are as high as 1100 h⁻¹ and 5800 (after 16 h), respectively, which are more than 10-fold higher than that obtained with the homologous complex under equivalent

conditions. The robust heterogeneous COF_{bpyMn} remains catalytically active even after 16 h during two consecutive recycling of 8 h CPE.

These results envision the use of crystalline structures of COFs for energy conversion applications.

III.4 Experimental section

III.4.1 Materials and reagents

Commercial reagents and solvents were purchased from Sigma Aldrich, Alfa Aesar, TCI Chemicals, Fluorochem or abcr and used as received without further purification. Multi-walled Carbon Nanotubes (MWCNTs) (purity 95%) and FTO plates were purchased from Sigma-Aldrich. NaHCO₃ (99.95% purity), TBAPF₆, Nafion, acetonitrile and other chemicals and solvents were purchased from commercial suppliers and used as received.

III.4.2 Physical methods and experimental procedures

III.4.2.1. Physical methods

Nuclear Magnetic Resonance (NMR)

NMR spectra were recorded on Bruker AV400 and AV500 spectrometers using standard conditions (300 K). All ¹H and ¹³C chemical shifts (in ppm) have been internally calibrated to the H or C atoms of the deuterated solvent, respectively. The coupling constants were measured in Hz. Magic angle spinning (MAS) solid-state Nuclear magnetic resonance (ssNMR) spectra were recorded using a Bruker Avance III-500 spectrometer.

Powder X-Ray Diffraction (PXRD)

PXRD measurements were made using a Siemens D5000 diffractometer (Bragg-Brentano parafocusing geometry and vertical θ - θ goniometer) fitted with a curved graphite diffracted-beam monochromator, incident and diffracted -beam Soller slits, a 0.06° receiving slit and scintillation counter as a detector. The angular 2 θ diffraction range was between 2 and 40°. The data was collected with an angular step of 0.02° at 12s per step and sample rotation. A low background Si(510) wafer was used as sample holder. Cu_{k α} radiation was obtained from a copper X-ray tube operated at 40 kV and 30 mA.

CHAPTER III

Mn based 2D-COF_{bpy} for electrocatalytic CO₂RR

Scanning Electron Microscopy-Energy Dispersed X-ray Spectroscopy (SEM-EDX)

The ESEM is from FEI company, model Quanta 600 in low vacuum mode (vacuum pressure 0.68 Torr). The EDX is from Oxford Instruments. The conditions for the ESEM are 20 kV accelerating voltage and working distance close to 10 mm.

Transmission electron microscopy (TEM)

TEM images were collected using a JEOL 1011 Transmission Electron Microscope operating at 80 kV. Samples were dispersed in ethanol and a drop of resultant suspensions was poured on carbon coated-copper grids.

Gas Adsorption (GA)

Nitrogen sorption isotherms were measured on Autosorb iQ adsorption analyzer (Quantachrome). Nitrogen measurements were performed at 77 K and the temperature was held constant using liquid N₂. The pressure range used to calculate the BET surface area was selected to fulfill the two “consistency criteria.”

Elemental Analyses (EA)

EA were performed using a CHNS-O EA-1108 elemental analyzer from Fisons.

Inductively Coupled Plasma Optical Emission Spectrometry (ICP-OES)

ICP-OES measurement was performed on the Perkin Elmer Optical Emission Spectrometer Optima 5300 DV (Scott-Chamber/Cross-Flow-Nebulizer). Mn was observed at $\lambda = 257.610$ nm.

Fourier-Transformed Infrared (FTIR) Spectroscopy

FTIR measurements were measured using a Bruker Optics FT-IR Alpha spectrometer equipped with a DTGS detector, KBr beamsplitter at 4 cm⁻¹ resolution using a one bounce ATR accessory with diamond windows.

Thermogravimetric Analysis (TGA)

TGA curves were measured using Mettler Toledo TGA/SDTA/851 in N₂, heating ramp 5 °C/min.

X-ray Photoelectron Spectroscopy (XPS)

(XPS, K-ALPHA, Thermo Scientific) was used to analyze the surface of the samples. All spectra were collected using Al-K_α radiation (1486.6 eV), monochromatized by a twin crystal monochromator, yielding a focused X-ray spot (elliptical in shape, primary axis length of 400 μm) at 3 mA × 12 kV. The alpha hemispherical analyser was operated in the constant energy mode with survey scan pass energies of 200 eV to measure the whole energy band and 50 eV in a narrow scan to selectively measure the particular elements. XPS data were analysed with Avantage software. A smart background function was used to approximate the experimental backgrounds and surface elemental composition were calculated from background-subtracted peak areas. Charge compensation was achieved with the system flood gun that provides low energy electrons and low energy argon ions from a single source.

Manganese K-Edge EXAFS Analysis

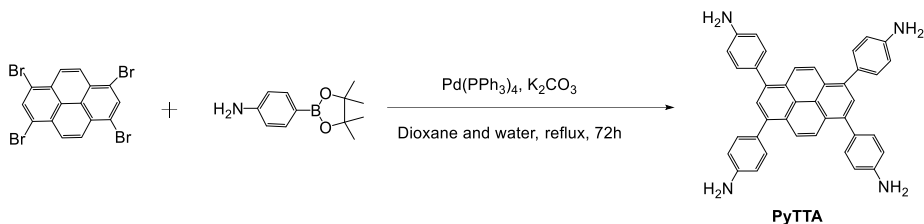
Samples for Mn K-edge X-ray absorbance were prepared in boron nitride. The data was acquired at the SOLEIL synchrotron SAMBA beamline. The powders were measured in transmission. Measurements were taken at 25 K using a liquid helium cryostat and a Si(220) double crystal monochromator. The Athena software package was used for data calibration and normalization.¹⁰¹ Energies were calibrated to the first inflection point of Mn foil spectra set at 6539.0 eV.¹⁰² EXAFS analysis was carried out with the Artemis software program running the IFEFFIT engine and the FEFF6 code.^{103, 104} The k³-weighted data was fit in r-space using a Hannings window (dk=1) over a k-range of 2 to 12.0 Å⁻¹, and an r-range of 1 to 3 Å, unless otherwise specified. The S₀² value was set to 0.9, and a global E₀ was employed with the initial E₀ value set to the inflection point of the rising edge. Single and multiple scattering paths were fit in terms of

CHAPTER III

Mn based 2D-COF_{bpy} for electrocatalytic CO₂RR

a Δr_{eff} and σ^2 as previously described. To assess the goodness of the fits, both the R_{factor} (%R) and the reduced χ^2 (χ^2_{v}) were minimized, ensuring not data over-fit.^{105, 106}

III.4.2.2. Synthesis Description



Synthesis of 4,4',4'',4'''-(pyrene-1,3,6,8-tetra-yl)tetraaniline (PyTTA):

PyTTA is synthesized according to the published procedure.¹⁰⁷ A reaction mixture containing 1,3,6,8-tetrabromopyrene (0.74 g, 1.43 mmol, 1.0 eq.), 4-aminophenylboronic acid pinacol ester (1.50 g, 6.85 mmol, 4.8 eq.), K₂CO₃ (1.08 g, 7.85 mmol, 5.5 eq.) and Pd(PPh₃)₄ (0.16 g, 0.14 mmol, 10 mol%) in 20 mL 1,4-dioxane and 4 mL H₂O was heated to reflux (115 °C) for 3 d under N₂ atmosphere. After cooling to room temperature (r.t.), H₂O was added. The resulting yellow precipitate was collected via filtration and was washed with H₂O and MeOH. Recrystallization from hot 1,4-dioxane, followed by drying under high vacuum furnished the title compound (0.90 g, 91%). ¹H NMR (DMSO-*d*₆, 400 MHz) δ , (ppm): 8.14 (s, 4H), 7.80 (s, 2H), 7.36 (d, *J* = 7.94 Hz, 8H), 6.77 (d, *J* = 8.00 Hz, 8H), 5.30 (s, 8H), 3.56 (s, 13H, dioxane); ¹³C NMR (DMSO-*d*₆, 400 MHz) δ , (ppm): 148.3, 137.3, 131.2, 129.2, 127.7, 126.8, 126.3, 124.6, 113.7, 66.5 (dioxane).

Mn(bpy)(CO)₃Br complex (**1**):⁷⁰ bpy (110 mg, 0.71 mmol) and Mn(CO)₅Br (200 mg, 0.72 mmol) are dissolved in 30 mL of Et₂O, stirred and maintained at reflux for 3 h. After cooling at room temperature, the yellow solid was filtered off, washed with diethyl ether and dried under vacuum. ¹H NMR (CDCl₃, 400 MHz) δ , (ppm): 9.28 (d, 2H), 8.12 (d, 2H), 8.0 (td, 2H), 7.53 (t, 2H).

Synthesis of COF_{bpy}: COF_{bpy} was synthesized according to the published procedure.⁸³ PyTTA (0.02 mmol, 11.3 mg) and 2,2'-bipyridyl-

5,5'-dialdehyde (bpy^{CHO}) (0.04 mmol, 8.5 mg) linkers were placed in a Pyrex tube (20 mL), followed by adding a solution of mesitylene/dioxane/6 M AcOH (5/5/1 by vol.; 1.1 mL). The mixture was sonicated for 10 min and then degassed by three freeze-pump-thaw cycles. The reaction was heated at 120 °C for 7 days yielding a brown precipitate, which was isolated by filtration. The wet sample was then transferred to a Soxhlet extractor and thoroughly washed with THF (24 h) and acetone (24 h). The powder was dried at 120 °C under vacuum overnight to give COF_{bpy} an isolated yield of 78%. Elemental analysis (%) calcd. for 100% COF_{bpy}, [(C₆₄H₃₈N₈)_n]: C (83.6), H (4.2), and N (12.2), found C (75.5), H (4.8), and N (10.2).

Synthesis of COF_{bpyMn}: COF_{bpy} (16 mg, 0.035 mmol; 1 eq. of bpy) was suspended in 10 mL of Et₂O. Mn(CO)₅Br (10.5 mg, 0.038 mmol; 1.1 bpy eq.) was added into the suspension under N₂ atmosphere. The material was heated to reflux for 4 h. Then, the dark brown solid was isolated by filtration, and washed profusely with Et₂O (3 × 10 mL) until the supernatant was colorless. The resulting material was dried under vacuum at room temperature and kept in inert atmosphere (Isolated yield ca. 90 %). *Due to the potential light-sensitive nature of the resulting {Mn(CO)₃} COF, the reaction, washing, and drying were performed minimizing the exposure to light.* ICP OES in COF_{bpyMn} (mg Mn/g)= 71.9. IR, ν(CO); 2026 cm⁻¹, 1941 2026 cm⁻¹ (sh), 1917 cm⁻¹ (sh)

III.4.2.3. Computational Details

Periodic simulations were performed at the Density Functional Theory (DFT) level using the PBE functional¹⁰⁸ and Grimme's D3 dispersion scheme¹⁰⁹ as implemented in the Vienna Ab-initio Simulation Package (VASP).^{110, 111} Single-point calculation using HSE03^{112, 113} was performed to evaluate the impact of hybrid density functionals. Core electrons were described by projector augmented wave (PAW)¹¹⁴ and valence electrons by plane waves with a kinetic energy cutoff of 600 eV for cell optimizations and 450 eV for atomic optimizations. For the initial exploration of pristine COF isomers, we employed a model composed by two layers, where a and b > 25 Å and c ≈ 7 Å. For the subsequent study on immobilization of Mn

CHAPTER III

Mn based 2D-COF_{bpy} for electrocatalytic CO₂RR

compounds, we considered the most stable isomer and built a supercell by extending the *c* direction to account for four layers, i.e., *a* and *b* \approx 28 Å and *c* \approx 14 Å. For the two models mentioned before, the Brillouin zone was sampled at $1 \times 1 \times 3$ and Γ -point, respectively, through the Monkhorst–Pack method.¹¹⁵ Frequency calculations were carried out by diagonalizing the numerical Hessian matrix obtained by ± 0.015 Å displacements, where only selected atoms were free to move.

All inputs, outputs, and final structures are freely available at the ioChem-BD repository.^{116, 117}

Link to iochem-bd: <https://iochem-bd.iciq.es/browse/review-collection/100/21562/1ff53f5be015ec89ad0071e3>

III.4.2.4. Electrochemistry

Cyclic Voltammetry

Working electrode: Glassy carbon (GC) electrodes (99.9995% trace metal basis, purchased from Bio-Logic) were polished with diamond paste and alumina (3 and 1 μm for 60 seconds each), thoroughly rinsed and sonicated in water and acetone, and dried before functionalization.

Working electrodes (GC, 0.0717 cm^2) were prepared by drop-casting 10 μL of an ink containing the catalyst and MWCNTs (NT) (1 mg) dispersed in CH_3CN and Nafion 5% in water (1:1, 200 μL) and let dry under dark. Catalyst deposited ($[\text{Mn}]_{\text{total}}$): E0) 700 $\text{nmol}\cdot\text{cm}^{-2}$ of **Mn(bpy)(CO)₃Br|NT**, E1-E4) 225, 350, 700 and 1400 $\text{nmol}\cdot\text{cm}^{-2}$ of Mn in **COF_{bpyMn}|NT**, respectively. E5 was prepared by drop-casting 20 μL of E3 ink (1400 $\text{nmol}\cdot\text{cm}^{-2}$ of Mn and double amount of NT than the rest of the electrodes).

Electrochemical measurements were performed using a Biologic potentiostat/galvanostat with a glass cell in the dark. The three-electrodes setup consisted of a working electrode, a Pt wire counter electrode, and a reference electrode. The working electrode was glassy carbon (99.9995% trace metal basis) and purchased from Bio-Logic. The reference electrode used in water was SCE (3.5 M KCl solution), while in CH_3CN was Ag wire,

a pseudo reference calibrated with Fc⁺/Fc vs a freshly clean glassy carbon electrode before and after experiments.

All experiments were performed in water (0.5 M NaHCO₃) or CH₃CN (0.2 M TBAPF₆) electrolyte under Ar or CO₂ atmosphere at 25 °C. The cell was purged for 10 minutes before each experiment. The pH was measured using a CyberScan pH510. Ohmic drop was compensated using the positive feedback compensation implemented in the instrument.

Controlled Potential Electrolysis (CPE)

For CPE experiments, an H-type electrochemical cell was used, in which the counter electrode was a Pt wire immersed in a bridge tube containing electrolyte solution and separated from the cathodic compartment by a ceramic frit. As a working electrode, we employed a glassy carbon plate (GC) or carbon paper (CP, Freudenberg H23C6), and SCE electrode as reference. To saturate with Ar or CO₂, a constant gas flow (30 ml·min⁻¹, fixed with a mass-flow controller, Alicat®) was continuously passed over the solution and on-line analyzed with a gas chromatography every 10 minutes. An Agilent 490 micro gas chromatograph equipped with a thermal conductivity detector and a Molesieve 5Å column was calibrated with different H₂/He/CO/CH₄ mixtures of known composition. The products formed during the reaction in liquid phases were analyzed by ¹H-NMR recorded on Bruker AV400 and AV500 spectrometers using standard conditions (300 K) and maleic acid as analytical standard.

Catalyst deposited ([Mn]_{total}): E0) 700 nmol·cm⁻² of Mn(bpy)(CO)₃Br|NT, E1-E4) 225, 350, 700, 1400 nmol·cm⁻² of Mn in COF_{bpyMn}|NT, respectively. E5 was prepared by drop-casting 20 μL of E3 ink (1400 nmol·cm⁻² of Mn and double amount of NT than the rest of the electrodes).

The Faradaic Yield has been calculated by the following equation

$$FY(\%) = n_e \frac{mol_{product}}{mol_e} \cdot 100$$

Where:

n_e is the number of electrons of the redox transformation (2 for H₂, CO and HCO₂⁻) and $mol_{product}$ and mol_e are the number of moles of product

generated and moles of electrons consumed in the CPE at a given time. mol_{product} was determined by integrating the chromatogram areas, considering the flow of gas and Δt between each measurement. mol_e was determined by integrating the charge.

Electroactive surface coverage

The amount of electroactive material was calculated using the following equation:

$$\Gamma = \frac{Q}{n \cdot F \cdot S}$$

Where Γ is the electroactive surface coverage, Q the charge, n the number of electrons (in our case, we have considered 1 electron for COF_{bpyMn}|NT and 2 electrons for Mn(bpy)(CO)₃Br|NT), F the Faraday constant and S the geometric area of the working electrode (GC, 0.0717 cm²). The Q for COF_{bpyMn}|NT was obtained by integration of the first redox wave of CV of COF_{bpyMn}|NT in anhydrous CH₃CN (0.1 M TBAPF₆) under Ar at 100 mV/s, where the system is not catalytic, and the integral of the redox feature can be associated to the number of redox-active species. (Electrochemical Methods: Fundamentals and Applications, 2nd Edition Allen J. Bard, Larry R. Faulkner ISBN: 978-0-471-04372-0).

Isotopic labeling

The online detection was performed using an Omnistar™ GSD 320 with a single quadrupole MS with a 1-meter interphase of capillary stainless steel (OD 1.59 mm, ID 0.13 mm) with an aspiration rate of 1-2 mL·min⁻¹.

Differential pressure transducer sensor: (Honeywell-ASCX15DN ± 15 psi) connected to a hardware data-acquisition system (base on Atmega microcontroller) controlled by a home-developed software program. The differential pressure transducer Honeywell-ASCX15DN is a 100 microseconds response, signal-conditioned (high level span, 4.5 V) output, calibrated and temperature compensated (0 °C to 70 °C) sensor. The differential sensor has two sensing ports that can be used for differential pressure measurements. The pressure devices were offset and span calibrated (± 0.5 matm) *via* software with a high-precision pressure

transducer (PX409-030GUSB, 0.08 % Accuracy). The differential pressure transducers (Honeywell-ASCX15DN, ± 15 psi) produce a voltage outputs that can be directly transformed to a pressure difference between the two measuring ports. The voltage outputs were digitalized with a resolution of 0.25 matm from 0 to 175 matm and 1 matm from 176 to 1000 matm using an Atmega microcontroller with an independent voltage auto-calibration. Firmware Atmega microcontroller and control software were home-developed.

The electrochemical cell and the reference vial were kept under the same experimental conditions to compensate the noise due to temperature-pressure fluctuations.

Electrochemical Impedance Spectroscopy (EIS)

EIS measurements were performed with using GC electrode functionalized with $[\text{Mn}]_{\text{total}} = 700 \text{ nmol}\cdot\text{cm}^{-2}$ of catalyst. The frequencies adopted ranged from 200 kHz to 100 mHz with an AC-modulation of 25 mV amplitude. The scan step is -100 mV for 16 measures between 0 to -1.6 V. EIS data were fitted using ZView software.

III.5 References

1. Spurgeon, J. M.; Kumar, B., A comparative technoeconomic analysis of pathways for commercial electrochemical CO₂ reduction to liquid products. *Energy Environ. Sci.* **2018**, *11* (6), 1536-1551.
2. Jouny, M.; Luc, W.; Jiao, F., General Techno-Economic Analysis of CO₂ Electrolysis Systems. *Industrial & Engineering Chemistry Research* **2018**, *57* (6), 2165-2177.
3. Aresta, M.; Dibenedetto, A.; Angelini, A., Catalysis for the Valorization of Exhaust Carbon: from CO₂ to Chemicals, Materials, and Fuels. Technological Use of CO₂. *Chem. Rev.* **2014**, *114* (3), 1709-1742.
4. Sordakis, K.; Tang, C.; Vogt, L. K.; Junge, H.; Dyson, P. J.; Beller, M.; Laurency, G., Homogeneous Catalysis for Sustainable Hydrogen Storage in Formic Acid and Alcohols. *Chemical Reviews* **2018**, *118* (2), 372-433.
5. Artz, J.; Müller, T. E.; Thenert, K.; Kleinekorte, J.; Meys, R.; Sternberg, A.; Bardow, A.; Leitner, W., Sustainable Conversion of Carbon Dioxide: An Integrated Review of Catalysis and Life Cycle Assessment. *Chemical Reviews* **2018**, *118* (2), 434-504.
6. Grice, K. A., Carbon dioxide reduction with homogenous early transition metal complexes: Opportunities and challenges for developing CO₂ catalysis. *Coordination Chemistry Reviews* **2017**, *336*, 78-95.
7. Takeda, H.; Cometto, C.; Ishitani, O.; Robert, M., Electrons, Photons, Protons and Earth-Abundant Metal Complexes for Molecular Catalysis of CO₂ Reduction. *ACS Catalysis* **2017**, *7* (1), 70-88.
8. Costamagna, J.; Canales, J.; Vargas, J.; Ferraudi, G. J., Electrochemical reduction of carbon dioxide by hexa-azamacrocyclic complexes. In *Pure Appl. Chem.*, 1995; Vol. 67, p 1045.
9. Franco, F.; Fernández, S.; Lloret-Fillol, J., Advances in the electrochemical catalytic reduction of CO₂ with metal complexes. *Curr. Opin. Electrochem* **2019**, *15*, 109-117.
10. Wang, M.; Torbensen, K.; Salvatore, D.; Ren, S.; Joulí, D.; Dumoulin, F.; Mendoza, D.; Lassalle-Kaiser, B.; İsci, U.; Berlinguette, C. P.; Robert, M., CO₂ electrochemical catalytic reduction with a highly active cobalt phthalocyanine. *Nat. Comm.* **2019**, *10* (1), 3602.
11. Ren, S.; Joulí, D.; Salvatore, D.; Torbensen, K.; Wang, M.; Robert, M.; Berlinguette, C. P., Molecular electrocatalysts can mediate fast, selective CO₂ reduction in a flow cell. *Science* **2019**, *365* (6451), 367-369.
12. Franco, F.; Rettenmaier, C.; Jeon, H. S.; Roldan Cuenya, B., Transition metal-based catalysts for the electrochemical CO₂ reduction: from atoms and molecules to nanostructured materials. *Chem. Soc. Rev.* **2020**, *49* (19), 6884-6946.
13. Zhao, G.; Huang, X.; Wang, X.; Wang, X., Progress in catalyst exploration for heterogeneous CO₂ reduction and utilization: a critical review. *Journal of Materials Chemistry A* **2017**, *5* (41), 21625-21649.
14. Zheng, T.; Jiang, K.; Wang, H., Recent Advances in Electrochemical CO₂-to-CO Conversion on Heterogeneous Catalysts. *Advanced Materials* **2018**, *30* (48), 1802066.

15. Ciriminna, R.; Ghahremani, M.; Karimi, B.; Pagliaro, M.; Luque, R., Single-atom catalysis: A practically viable technology? *Current Opinion in Green and Sustainable Chemistry* **2020**, *25*, 100358.
16. Hasija, V.; Nguyen, V.-H.; Kumar, A.; Raizada, P.; Krishnan, V.; Khan, A. A. P.; Singh, P.; Lichtfouse, E.; Wang, C.; Thi Huong, P., Advanced activation of persulfate by polymeric g-C₃N₄ based photocatalysts for environmental remediation: A review. *Journal of Hazardous Materials* **2021**, *413*, 125324.
17. Sun, C.; Rotundo, L.; Garino, C.; Nencini, L.; Yoon, S. S.; Gobetto, R.; Nervi, C., Electrochemical CO₂ Reduction at Glassy Carbon Electrodes Functionalized by MnI and ReI Organometallic Complexes. *ChemPhysChem* **2017**, *18* (22), 3219-3229.
18. Walsh, J. J.; Smith, C. L.; Neri, G.; Whitehead, G. F. S.; Robertson, C. M.; Cowan, A. J., Improving the efficiency of electrochemical CO₂ reduction using immobilized manganese complexes. *Faraday Discussions* **2015**, *183* (0), 147-160.
19. Reuillard, B.; Ly, K. H.; Rosser, T. E.; Kuehnel, M. F.; Zebger, I.; Reisner, E., Tuning Product Selectivity for Aqueous CO₂ Reduction with a Mn(bipyridine)-pyrene Catalyst Immobilized on a Carbon Nanotube Electrode. *Journal of the American Chemical Society* **2017**, *139* (41), 14425-14435.
20. Sato, S.; Saita, K.; Sekizawa, K.; Maeda, S.; Morikawa, T., Low-Energy Electrocatalytic CO₂ Reduction in Water over Mn-Complex Catalyst Electrode Aided by a Nanocarbon Support and K⁺ Cations. *ACS Catalysis* **2018**, *8* (5), 4452-4458.
21. Walsh, J. J.; Forster, M.; Smith, C. L.; Neri, G.; Potter, R. J.; Cowan, A. J., Directing the mechanism of CO₂ reduction by a Mn catalyst through surface immobilization. *Physical Chemistry Chemical Physics* **2018**, *20* (10), 6811-6816.
22. Torralba-Peñalver, E.; Luo, Y.; Compain, J.-D.; Chardon-Noblat, S.; Fabre, B., Selective Catalytic Electroreduction of CO₂ at Silicon Nanowires (SiNWs) Photocathodes Using Non-Noble Metal-Based Manganese Carbonyl Bipyridyl Molecular Catalysts in Solution and Grafted onto SiNWs. *ACS Cat.* **2015**, *5* (10), 6138-6147.
23. Zhanaidarova, A.; Jones, S. C.; Despagnet-Ayoub, E.; Pimentel, B. R.; Kubiak, C. P., Re(tBu-bpy)(CO)₃Cl Supported on Multi-Walled Carbon Nanotubes Selectively Reduces CO₂ in Water. *Journal of the American Chemical Society* **2019**, *141* (43), 17270-17277.
24. Nam, D.-H.; De Luna, P.; Rosas-Hernández, A.; Thevenon, A.; Li, F.; Agapie, T.; Peters, J. C.; Shekhah, O.; Eddaoudi, M.; Sargent, E. H., Molecular enhancement of heterogeneous CO₂ reduction. *Nature Materials* **2020**, *19* (3), 266-276.
25. Abdinejad, M.; Hossain, M. N.; Kraatz, H.-B., Homogeneous and heterogeneous molecular catalysts for electrochemical reduction of carbon dioxide. *RSC Advances* **2020**, *10* (62), 38013-38023.
26. Fernández, S.; Dubed Bandomo, G. C.; Lloret-Fillol, J., Recent advances in electrocatalytic CO₂ reduction with molecular complexes. In *Advances in Inorganic Chemistry*, Academic Press: 2022.
27. Li, X.; Zhu, Q.-L., MOF-based materials for photo- and electrocatalytic CO₂ reduction. *EnergyChem* **2020**, *2* (3).
28. Zhang, J.; Cai, W.; Hu, F. X.; Yang, H.; Liu, B., Recent advances in single atom catalysts for the electrochemical carbon dioxide reduction reaction. *Chemical Science* **2021**, *12* (20), 6800-6819.

29. Vijay, S.; Ju, W.; Brückner, S.; Tsang, S.-C.; Strasser, P.; Chan, K., Unified mechanistic understanding of CO₂ reduction to CO on transition metal and single atom catalysts. *Nature Catalysis* **2021**, *4* (12), 1024-1031.
30. Back, S.; Lim, J.; Kim, N.-Y.; Kim, Y.-H.; Jung, Y., Single-atom catalysts for CO₂ electroreduction with significant activity and selectivity improvements. *Chemical Science* **2017**, *8* (2), 1090-1096.
31. Liu, L.; Corma, A., Metal Catalysts for Heterogeneous Catalysis: From Single Atoms to Nanoclusters and Nanoparticles. *Chemical Reviews* **2018**, *118* (10), 4981-5079.
32. Yang, X.-F.; Wang, A.; Qiao, B.; Li, J.; Liu, J.; Zhang, T., Single-Atom Catalysts: A New Frontier in Heterogeneous Catalysis. *Accounts of Chemical Research* **2013**, *46* (8), 1740-1748.
33. Zhang, L.; Ren, Y.; Liu, W.; Wang, A.; Zhang, T., Single-atom catalyst: a rising star for green synthesis of fine chemicals. *National Science Review* **2018**, *5* (5), 653-672.
34. Wang, D.-G.; Qiu, T.; Guo, W.; Liang, Z.; Tabassum, H.; Xia, D.; Zou, R., Covalent organic framework-based materials for energy applications. *Energy & Environmental Science* **2021**, *14* (2), 688-728.
35. Zhong, W.; Sa, R.; Li, L.; He, Y.; Li, L.; Bi, J.; Zhuang, Z.; Yu, Y.; Zou, Z., A Covalent Organic Framework Bearing Single Ni Sites as a Synergistic Photocatalyst for Selective Photoreduction of CO₂ to CO. *Journal of the American Chemical Society* **2019**, *141* (18), 7615-7621.
36. Wang, X.; Fu, Z.; Zheng, L.; Zhao, C.; Wang, X.; Chong, S. Y.; McBride, F.; Raval, R.; Bilton, M.; Liu, L.; Wu, X.; Chen, L.; Sprick, R. S.; Cooper, A. I., Covalent Organic Framework Nanosheets Embedding Single Cobalt Sites for Photocatalytic Reduction of Carbon Dioxide. *Chemistry of Materials* **2020**, *32* (21), 9107-9114.
37. Liu, W.; Zhang, H.; Li, C.; Wang, X.; Liu, J.; Zhang, X., Non-noble metal single-atom catalysts prepared by wet chemical method and their applications in electrochemical water splitting. *Journal of Energy Chemistry* **2020**, *47*, 333-345.
38. Diercks, C. S.; Liu, Y.; Cordova, K. E.; Yaghi, O. M., The role of reticular chemistry in the design of CO₂ reduction catalysts. *Nature Materials* **2018**, *17* (4), 301-307.
39. Huang, X.; Zhang, Y.-B., Reticular materials for electrochemical reduction of CO₂. *Coordination Chemistry Reviews* **2021**, *427*, 213564.
40. Heidary, N.; Harris, T.; Ly, K. H.; Kornienko, N., Artificial photosynthesis with metal and covalent organic frameworks (MOFs and COFs): challenges and prospects in fuel-forming electrocatalysis. *Physiol Plant* **2019**, *166* (1), 460-471.
41. Diercks, C. S.; Liu, Y.; Cordova, K. E.; Yaghi, O. M., The role of reticular chemistry in the design of CO(2) reduction catalysts. *Nat Mater* **2018**, *17* (4), 301-307.
42. Lyu, H.; Ji, Z.; Wuttke, S.; Yaghi, O. M., Digital Reticular Chemistry. *Chem* **2020**, *6* (9), 2219-2241.
43. Zhang, Y.-B.; Li, Q.; Deng, H., Reticular chemistry at the atomic, molecular, and framework scales. *Nano Research* **2021**, *14* (2), 335-337.

44. Lei, Z.; Xue, Y.; Chen, W.; Qiu, W.; Zhang, Y.; Horike, S.; Tang, L., MOFs-Based Heterogeneous Catalysts: New Opportunities for Energy-Related CO₂ Conversion. *Advanced Energy Materials* **2018**, *8* (32), 1801587.
45. Mahmood, A.; Guo, W.; Tabassum, H.; Zou, R., Metal-Organic Framework-Based Nanomaterials for Electrocatalysis. *Advanced Energy Materials* **2016**, *6* (17), 1600423.
46. Kornienko, N.; Zhao, Y.; Kley, C. S.; Zhu, C.; Kim, D.; Lin, S.; Chang, C. J.; Yaghi, O. M.; Yang, P., Metal–Organic Frameworks for Electrocatalytic Reduction of Carbon Dioxide. *Journal of the American Chemical Society* **2015**, *137* (44), 14129-14135.
47. Lin, S.; Diercks, C. S.; Zhang, Y. B.; Kornienko, N.; Nichols, E. M.; Zhao, Y.; Paris, A. R.; Kim, D.; Yang, P.; Yaghi, O. M.; Chang, C. J., Covalent organic frameworks comprising cobalt porphyrins for catalytic CO₂ reduction in water. *Science* **2015**, *349* (6253), 1208-13.
48. Ye, L.; Liu, J.; Gao, Y.; Gong, C.; Addicoat, M.; Heine, T.; Wöll, C.; Sun, L., Highly oriented MOF thin film-based electrocatalytic device for the reduction of CO₂ to CO exhibiting high faradaic efficiency. *Journal of Materials Chemistry A* **2016**, *4* (40), 15320-15326.
49. Wang, Y.-R.; Huang, Q.; He, C.-T.; Chen, Y.; Liu, J.; Shen, F.-C.; Lan, Y.-Q., Oriented electron transmission in polyoxometalate-metalloporphyrin organic framework for highly selective electroreduction of CO₂. *Nature Communications* **2018**, *9* (1), 4466.
50. Matheu, R.; Gutierrez-Puebla, E.; Monge, M. Á.; Diercks, C. S.; Kang, J.; Prévot, M. S.; Pei, X.; Hanikel, N.; Zhang, B.; Yang, P.; Yaghi, O. M., Three-Dimensional Phthalocyanine Metal-Catecholates for High Electrochemical Carbon Dioxide Reduction. *Journal of the American Chemical Society* **2019**, *141* (43), 17081-17085.
51. Kung, C.-W.; Audu, C. O.; Peters, A. W.; Noh, H.; Farha, O. K.; Hupp, J. T., Copper Nanoparticles Installed in Metal–Organic Framework Thin Films are Electrocatalytically Competent for CO₂ Reduction. *ACS Energy Letters* **2017**, *2* (10), 2394-2401.
52. Liu, H.; Chu, J.; Yin, Z.; Cai, X.; Zhuang, L.; Deng, H., Covalent Organic Frameworks Linked by Amine Bonding for Concerted Electrochemical Reduction of CO₂. *Chem* **2018**, *4* (7), 1696-1709.
53. Wang, J.; Zhuang, S., Covalent organic frameworks (COFs) for environmental applications. *Coordination Chemistry Reviews* **2019**, *400*, 213046.
54. Feng, X.; Ding, X.; Jiang, D., Covalent organic frameworks. *Chem. Soc. Rev.* **2012**, *41* (18), 6010-6022.
55. Waller, P. J.; Gándara, F.; Yaghi, O. M., Chemistry of Covalent Organic Frameworks. *Acc. Chem. Res.* **2015**, *48* (12), 3053-3063.
56. Huang, N.; Wang, P.; Jiang, D., Covalent organic frameworks: a materials platform for structural and functional designs. *Nat. Rev. Mater.* **2016**, *1*, 16068.
57. Yaghi, O. M.; O’Keeffe, M.; Ockwig, N. W.; Chae, H. K.; Eddaoudi, M.; Kim, J., *Nature* **2003**, *423*, 705-714.
58. Hu, L.; Li, W.; Wang, L.; Wang, B., Turning metal-organic frameworks into efficient single-atom catalysts via pyrolysis with a focus on oxygen reduction reaction catalysts. *EnergyChem* **2021**, *3* (3), 100056.

59. Karak, S.; Kumar, S.; Pachfule, P.; Banerjee, R., Porosity Prediction through Hydrogen Bonding in Covalent Organic Frameworks. *J. Am. Chem. Soc.* **2018**, *140* (15), 5138-5145.
60. Ascherl, L.; Sick, T.; Margraf, J. T.; Lapidus, S. H.; Calik, M.; Hettstedt, C.; Karaghiosoff, K.; Döblinger, M.; Clark, T.; Chapman, K. W.; Auras, F.; Bein, T., Molecular docking sites designed for the generation of highly crystalline covalent organic frameworks. *Nat. Chem.* **2016**, *8*, 310.
61. Ma, D.; Wang, Y.; Liu, A.; Li, S.; Lu, C.; Chen, C., Covalent Organic Frameworks: Promising Materials as Heterogeneous Catalysts for C-C Bond Formations. *Catalysts* **2018**, *8* (9), 404.
62. Lin, S.; Diercks, C. S.; Zhang, Y.-B.; Kornienko, N.; Nichols, E. M.; Zhao, Y.; Paris, A. R.; Kim, D.; Yang, P.; Yaghi, O. M.; Chang, C. J., Covalent organic frameworks comprising cobalt porphyrins for catalytic CO₂ reduction in water. *Science* **2015**, *349* (6253), 1208-1213.
63. Diercks, C. S.; Lin, S.; Kornienko, N.; Kapustin, E. A.; Nichols, E. M.; Zhu, C.; Zhao, Y.; Chang, C. J.; Yaghi, O. M., Reticular Electronic Tuning of Porphyrin Active Sites in Covalent Organic Frameworks for Electrocatalytic Carbon Dioxide Reduction. *Journal of the American Chemical Society* **2018**, *140* (3), 1116-1122.
64. Liang, Z.; Qu, C.; Guo, W.; Zou, R.; Xu, Q., Pristine Metal–Organic Frameworks and their Composites for Energy Storage and Conversion. *Advanced Materials* **2018**, *30* (37), 1702891.
65. Rosen, B. A.; Hod, I., Tunable Molecular-Scale Materials for Catalyzing the Low-Overpotential Electrochemical Conversion of CO₂. *Advanced Materials* **2018**, *30* (41), 1706238.
66. Wang, Y.; He, D.; Chen, H.; Wang, D., Catalysts in electro-, photo- and photoelectrocatalytic CO₂ reduction reactions. *Journal of Photochemistry and Photobiology C: Photochemistry Reviews* **2019**, *40*, 117-149.
67. Popov, D. A.; Luna, J. M.; Orchanian, N. M.; Haiges, R.; Downes, C. A.; Marinescu, S. C., A 2,2'-bipyridine-containing covalent organic framework bearing rhenium(i) tricarbonyl moieties for CO₂ reduction. *Dalton Transactions* **2018**, *47* (48), 17450-17460.
68. Johnson, E. M.; Haiges, R.; Marinescu, S. C., Covalent–Organic Frameworks Composed of Rhenium Bipyridine and Metal Porphyrins: Designing Heterobimetallic Frameworks with Two Distinct Metal Sites. *ACS Applied Materials & Interfaces* **2018**, *10* (44), 37919-37927.
69. Cheung, P. L.; Lee, S. K.; Kubiak, C. P., Facile Solvent-Free Synthesis of Thin Iron Porphyrin COFs on Carbon Cloth Electrodes for CO₂ Reduction. *Chemistry of Materials* **2019**, *31* (6), 1908-1919.
70. Bourrez, M.; Molton, F.; Chardon-Noblat, S.; Deronzier, A., [Mn(bipyridyl)(CO)₃Br]: An Abundant Metal Carbonyl Complex as Efficient Electrocatalyst for CO₂ Reduction. *Angewandte Chemie International Edition* **2011**, *50* (42), 9903-9906.
71. Sampson, M. D.; Nguyen, A. D.; Grice, K. A.; Moore, C. E.; Rheingold, A. L.; Kubiak, C. P., Manganese Catalysts with Bulky Bipyridine Ligands for the Electrocatalytic Reduction of Carbon Dioxide: Eliminating Dimerization and Altering Catalysis. *J. Am. Chem. Soc.* **2014**, *136* (14), 5460-5471.
72. Ngo, K. T.; McKinnon, M.; Mahanti, B.; Narayanan, R.; Grills, D. C.; Ertem, M. Z.; Rochford, J., Turning on the Protonation-First Pathway for

Electrocatalytic CO₂ Reduction by Manganese Bipyridyl Tricarbonyl Complexes. *J. Am. Chem. Soc.* **2017**, *139* (7), 2604-2618.

73. Franco, F.; Pinto, M. F.; Royo, B.; Lloret-Fillol, J., A Highly Active N-Heterocyclic Carbene Manganese(I) Complex for Selective Electrocatalytic CO₂ Reduction to CO. *Angew. Chem.* **2018**, *130* (17), 4693-4696.

74. Stanbury, M.; Compain, J.-D.; Chardon-Noblat, S., Electro and photoreduction of CO₂ driven by manganese-carbonyl molecular catalysts. *Coord. Chem. Rev.* **2018**, *361*, 120-137.

75. Grills, D. C.; Ertem, M. Z.; McKinnon, M.; Ngo, K. T.; Rochford, J., Mechanistic aspects of CO₂ reduction catalysis with manganese-based molecular catalysts. *Coordination Chemistry Reviews* **2018**, *374*, 173-217.

76. Smith, C. L.; Clowes, R.; Sprick, R. S.; Cooper, A. I.; Cowan, A. J., Metal-organic conjugated microporous polymer containing a carbon dioxide reduction electrocatalyst. *Sustainable Energy & Fuels* **2019**, *3* (11), 2990-2994.

77. Wu, Y.; Liang, Y.; Wang, H., Heterogeneous Molecular Catalysts of Metal Phthalocyanines for Electrochemical CO₂ Reduction Reactions. *Accounts of Chemical Research* **2021**, *54* (16), 3149-3159.

78. Tatin, A.; Comminges, C.; Kokoh, B.; Costentin, C.; Robert, M.; Savéant, J.-M., Efficient electrolyzer for CO₂ splitting in neutral water using earth-abundant materials. *Proceedings of the National Academy of Sciences* **2016**, *113* (20), 5526.

79. Maurin, A.; Robert, M., Noncovalent Immobilization of a Molecular Iron-Based Electrocatalyst on Carbon Electrodes for Selective, Efficient CO₂-to-CO Conversion in Water. *Journal of the American Chemical Society* **2016**, *138* (8), 2492-2495.

80. Maurin, A.; Robert, M., Catalytic CO₂-to-CO conversion in water by covalently functionalized carbon nanotubes with a molecular iron catalyst. *Chemical Communications* **2016**, *52* (81), 12084-12087.

81. Choi, J.; Kim, J.; Wagner, P.; Gambhir, S.; Jalili, R.; Byun, S.; Sayyar, S.; Lee, Y. M.; MacFarlane, D. R.; Wallace, G. G.; Officer, D. L., Energy efficient electrochemical reduction of CO₂ to CO using a three-dimensional porphyrin/graphene hydrogel. *Energy & Environmental Science* **2019**, *12* (2), 747-755.

82. Hu, X.-M.; Rønne, M. H.; Pedersen, S. U.; Skrydstrup, T.; Daasbjerg, K., Enhanced Catalytic Activity of Cobalt Porphyrin in CO₂ Electroreduction upon Immobilization on Carbon Materials. *Angewandte Chemie International Edition* **2017**, *56* (23), 6468-6472.

83. Chen, X.; Huang, N.; Gao, J.; Xu, H.; Xu, F.; Jiang, D., Towards covalent organic frameworks with predesignable and aligned open docking sites. *Chem. Commun.* **2014**, *50* (46), 6161-6163.

84. Sing, K. S. W., Reporting physisorption data for gas/solid systems with special reference to the determination of surface area and porosity (Recommendations 1984). *Pure and Applied Chemistry* **1985**, *57* (4), 603-619.

85. Ding, S.-Y.; Gao, J.; Wang, Q.; Zhang, Y.; Song, W.-G.; Su, C.-Y.; Wang, W., Construction of Covalent Organic Framework for Catalysis: Pd/COF-LZU1 in Suzuki-Miyaura Coupling Reaction. *Journal of the American Chemical Society* **2011**, *133* (49), 19816-19822.

86. Xu, H.; Chen, X.; Gao, J.; Lin, J.; Addicoat, M.; Irle, S.; Jiang, D., Catalytic covalent organic frameworks via pore surface engineering. *Chemical Communications* **2014**, 50 (11), 1292-1294.
87. Wan, S.; Gándara, F.; Asano, A.; Furukawa, H.; Saeki, A.; Dey, S. K.; Liao, L.; Ambrogio, M. W.; Botros, Y. Y.; Duan, X.; Seki, S.; Stoddart, J. F.; Yaghi, O. M., Covalent Organic Frameworks with High Charge Carrier Mobility. *Chemistry of Materials* **2011**, 23 (18), 4094-4097.
88. Fei, H.; Sampson, M. D.; Lee, Y.; Kubiak, C. P.; Cohen, S. M., Photocatalytic CO₂ Reduction to Formate Using a Mn(I) Molecular Catalyst in a Robust Metal–Organic Framework. *Inorganic Chemistry* **2015**, 54 (14), 6821-6828.
89. Xu, S.-Q.; Liang, R.-R.; Zhan, T.-G.; Qi, Q.-Y.; Zhao, X., Construction of 2D covalent organic frameworks by taking advantage of the variable orientation of imine bonds. *Chem. Commun.* **2017**, 53 (16), 2431-2434.
90. Albacete, P.; Martínez, J. I.; Li, X.; López-Moreno, A.; Mena-Hernando, S. a.; Platero-Prats, A. E.; Montoro, C.; Loh, K. P.; Pérez, E. M.; Zamora, F., Layer-Stacking-Driven Fluorescence in a Two-Dimensional Imine-Linked Covalent Organic Framework. *J. Am. Chem. Soc.* **2018**, 140 (40), 12922-12929.
91. Lukose, B.; Kuc, A.; Heine, T., The Structure of Layered Covalent-Organic Frameworks. *Chem. Eur. J.* **2011**, 17 (8), 2388-2392.
92. Lukose, B.; Kuc, A.; Frenzel, J.; Heine, T., On the reticular construction concept of covalent organic frameworks. *Beilstein J. Nanotechnol.* **2010**, 1, 60-70.
93. Zhang, X.; Wu, Z.; Zhang, X.; Li, L.; Li, Y.; Xu, H.; Li, X.; Yu, X.; Zhang, Z.; Liang, Y.; Wang, H., Highly selective and active CO₂ reduction electrocatalysts based on cobalt phthalocyanine/carbon nanotube hybrid structures. *Nat. Comm.* **2017**, 8 (1).
94. Karapinar, D.; Zitolo, A.; Huan, T. N.; Zanna, S.; Taverna, D.; Galvão Tizei, L. H.; Giaume, D.; Marcus, P.; Mougél, V.; Fontecave, M., Carbon-Nanotube-Supported Copper Polyphthalocyanine for Efficient and Selective Electrocatalytic CO₂ Reduction to CO. *ChemSusChem* **2019**, 13 (1), 173-179.
95. Walsh, J. J.; Smith, C. L.; Neri, G.; Whitehead, G. F. S.; Robertson, C. M.; Cowan, A. J., Improving the efficiency of electrochemical CO₂ reduction using immobilized manganese complexes. *Faraday Discuss.* **2015**, 183, 147-160.
96. Neri, G.; Walsh, J. J.; Teobaldi, G.; Donaldson, P. M.; Cowan, A. J., Detection of catalytic intermediates at an electrode surface during carbon dioxide reduction by an earth-abundant catalyst. *Nature Catalysis* **2018**, 1 (12), 952-959.
97. Walsh, J. J.; Neri, G.; Smith, C. L.; Cowan, A. J., Electrocatalytic CO₂ reduction with a membrane supported manganese catalyst in aqueous solution. *Chemical Communications* **2014**, 50 (84), 12698-12701.
98. Walsh, J. J.; Neri, G.; Smith, C. L.; Cowan, A. J., Water-Soluble Manganese Complex for Selective Electrocatalytic CO₂ Reduction to CO. *Organometallics* **2019**, 38 (6), 1224-1229.

99. Heidary, N.; Morency, M.; Chartrand, D.; Ly, K. H.; Iftimie, R.; Kornienko, N., Electrochemically Triggered Dynamics within a Hybrid Metal–Organic Electrocatalyst. *J. Am. Chem. Soc.* **2020**, *142* (28), 12382-12393.
100. Dalle, K. E.; Warnan, J.; Leung, J. J.; Reuillard, B.; Karmel, I. S.; Reisner, E., Electro- and Solar-Driven Fuel Synthesis with First Row Transition Metal Complexes. *Chem. Rev.* **2019**, *119* (4), 2752-2875.
101. Ravel, B.; Newville, M., ATHENA, ARTEMIS, HEPHAESTUS: data analysis for X-ray absorption spectroscopy using IFEFFIT. *Journal of Synchrotron Radiation* **2005**, *12*, 537-541.
102. Leto, D. F.; Jackson, T. A., Mn K-Edge X-ray Absorption Studies of Oxo- and Hydroxo-manganese(IV) Complexes: Experimental and Theoretical Insights into Pre-Edge Properties. *Inorganic Chemistry* **2014**, *53* (12), 6179-6194.
103. Newville, M., EXAFS analysis using FEFF and FEFFIT. *Journal of Synchrotron Radiation* **2001**, *8*, 96-100.
104. Rehr, J. J.; Albers, R. C., Theoretical approaches to x-ray absorption fine structure. *Reviews of Modern Physics* **2000**, *72* (3), 621-654.
105. Martin-Diaconescu, V.; Bellucci, M.; Musiani, F.; Ciurli, S.; Maroney, M. J., Unraveling the *Helicobacter pylori* UreG zinc binding site using X-ray absorption spectroscopy (XAS) and structural modeling. *Journal of Biological Inorganic Chemistry* **2012**, *17* (3), 353-361.
106. Zambelli, B.; Berardi, A.; Martin-Diaconescu, V.; Mazzei, L.; Musiani, F.; Maroney, M. J.; Ciurli, S., Nickel binding properties of *Helicobacter pylori* UreF, an accessory protein in the nickel-based activation of urease. *Journal of Biological Inorganic Chemistry* **2014**, *19* (3), 319-334.
107. Auras, F.; Ascherl, L.; Hakimioun, A. H.; Margraf, J. T.; Hanusch, F. C.; Reuter, S.; Bessinger, D.; Döblinger, M.; Hettstedt, C.; Karaghiosoff, K.; Herbert, S.; Knochel, P.; Clark, T.; Bein, T., Synchronized Offset Stacking: A Concept for Growing Large-Domain and Highly Crystalline 2D Covalent Organic Frameworks. *Journal of the American Chemical Society* **2016**, *138* (51), 16703-16710.
108. Perdew, J. P.; Burke, K.; Ernzerhof, M., Generalized Gradient Approximation Made Simple. *Physical Review Letters* **1996**, *77* (18), 3865-3868.
109. Grimme, S.; Antony, J.; Ehrlich, S.; Krieg, H., A consistent and accurate ab initio parametrization of density functional dispersion correction (DFT-D) for the 94 elements H-Pu. *The Journal of Chemical Physics* **2010**, *132* (15), 154104.
110. Kresse, G.; Furthmüller, J., Efficient iterative schemes for ab initio total-energy calculations using a plane-wave basis set. *Physical Review B* **1996**, *54* (16), 11169-11186.
111. Kresse, G.; Furthmüller, J., Efficiency of ab-initio total energy calculations for metals and semiconductors using a plane-wave basis set. *Computational Materials Science* **1996**, *6* (1), 15-50.
112. Heyd, J.; Scuseria, G. E.; Ernzerhof, M., Hybrid functionals based on a screened Coulomb potential. *The Journal of Chemical Physics* **2003**, *118* (18), 8207-8215.
113. Heyd, J.; Scuseria, G. E.; Ernzerhof, M., Erratum: "Hybrid functionals based on a screened Coulomb potential" [J. Chem. Phys. 118, 8207 (2003)]. *The Journal of Chemical Physics* **2006**, *124* (21), 219906.
114. Kresse, G.; Joubert, D., From ultrasoft pseudopotentials to the projector augmented-wave method. *Physical Review B* **1999**, *59* (3), 1758-1775.

115. Monkhorst, H. J.; Pack, J. D., Special points for Brillouin-zone integrations. *Physical Review B* **1976**, *13* (12), 5188-5192.
116. Álvarez-Moreno, M.; de Graaf, C.; López, N.; Maseras, F.; Poblet, J. M.; Bo, C., Managing the Computational Chemistry Big Data Problem: The ioChem-BD Platform. *Journal of Chemical Information and Modeling* **2015**, *55* (1), 95-103.
117. Bo, C.; Maseras, F.; López, N., The role of computational results databases in accelerating the discovery of catalysts. *Nature Catalysis* **2018**, *1* (11), 809-810.

CHAPTER III

Mn based 2D-COF_{bpy} for electrocatalytic CO₂RR

CHAPTER IV.
Detection of Key Catalytic Intermediates within
Mechanical Constrained Mn(CO)₃Br Single Sites in a
2D-Covalent Organic Framework by
Spectroelectrochemistry

Chapter IV: Detection of Key Catalytic Intermediates within Mechanical Constrained Mn(CO)₃Br Single Sites in a 2D-Covalent Organic Framework by Spectroelectrochemistry.

IV.1. General insight

Significant progress has been made to understand the mechanisms behind the activity and selectivity of electrocatalysts for CO₂ reduction.¹⁻⁸ Traditional homogeneous and heterogeneous catalysts have served as models to understand the mechanism of the electrochemical reduction of CO₂, not only for the optimization of the existing catalysts but also to aid in the rational design of new catalysts. Nevertheless, the study of molecularly defined transition metal coordination compounds is a more attractive strategy that allows the identification of any bottlenecks in the electrocatalytic CO₂ by spectroscopic studies, contrary to the classical solid-state counterparts, where the mechanistic study is more challenging.⁹⁻¹¹ In addition, spectroelectrochemical (SEC) techniques can provide beneficial information about the nature of the reaction intermediates involved in the CO₂ reduction, the relevance of double-layer effects in controlling the activity, and selectivity of the electrocatalysts, as well as the nature of the species causing deactivation.^{1, 12-14}

In this line, COFs and MOFs are convenient platforms for gaining insights into the mechanism of heterogeneous material; their high molecular level suited their study by *in situ* spectroelectrochemical investigations. However, studies of electrocatalytic CO₂ reduction mechanisms with this family of catalysts are still scarce.^{1, 15-19}

Previous studies using spectroelectrochemistry (UV-vis, Raman and infrared spectroscopy) on MOFs and COFs provided insight into speciation changes (Figure IV. 1).¹⁹⁻²¹ Specially, *in situ* infrared spectroelectrochemistry (IR-SEC) may facilitate the study of the CO₂ reduction mechanism accessing to the detection of potential CO₂ reduction intermediates such as metal carboxylates and carbonyls as well. Additionally, it could indicate the chemical environment and oxidation state

of the metal centers.²²⁻²⁶ However, only a few examples have been described for MOF like materials,^{15, 27-29} and no experimental ATR-IR-SEC data of *in situ* monitoring of electrochemically active COF materials have been reported so far.¹⁵

Our understanding of catalytic mechanisms and structure-activity relationships for COFs is still limited, but essential to the rational design of these catalysts. Therefore, SEC of COFs will play a substantial role in fully understanding the electrocatalytic reticular materials' function and getting key insights into the reaction intermediates to develop design rules for constructing next-generation systems.

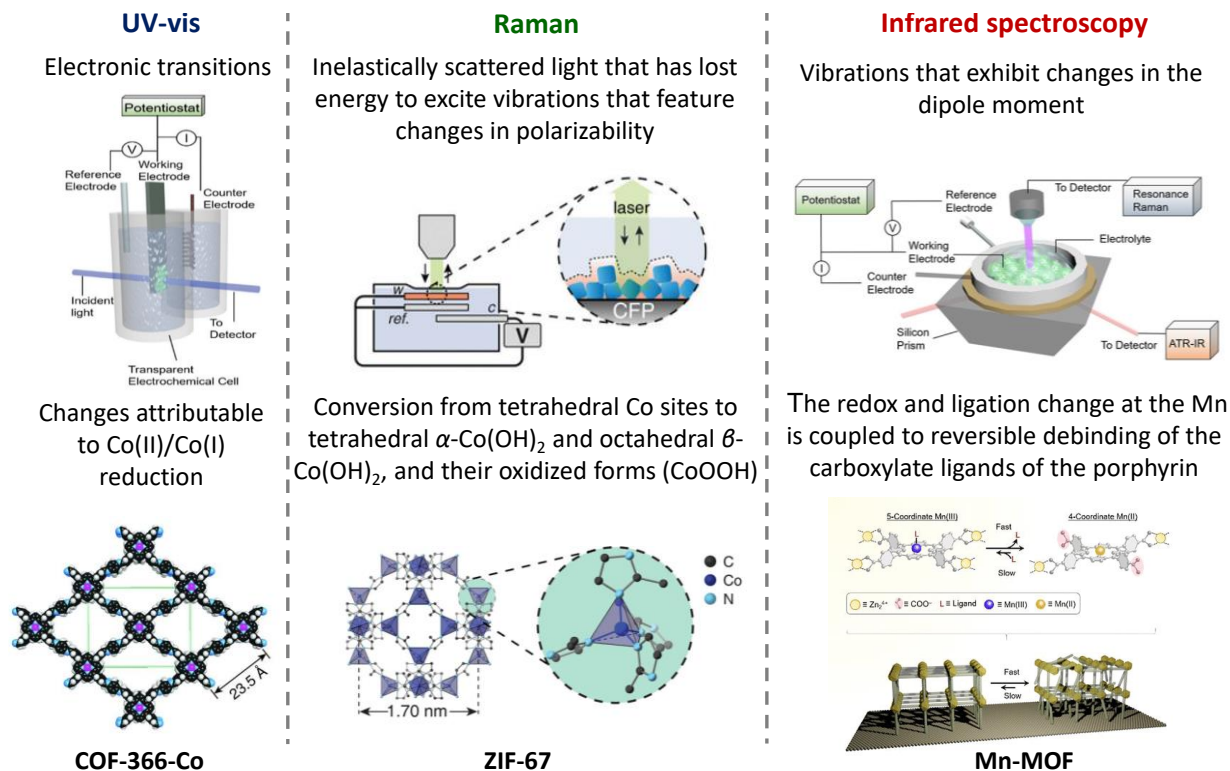


Figure IV. 1. Reported *operando* spectroscopic techniques and illustrations of representative spectroelectrochemical cells and studied electrocatalytic frameworks.¹

Important information on the CO₂ reduction catalytic cycle has been reported for manganese tricarbonyl complexes containing polypyridyl and non-pyridyl ligands.^{7, 8, 30} In this line, this family of catalysts has been widely studied by FT-IR-SCE, taking advantage of the presence of the carbonyl ligands. The CO stretching vibrations ($\nu_{(\text{CO})}$) serve as a probe for the metal center's oxidation state and coordination environment since these strongly depend on the electronic structure.^{31, 32}

By FT-IR-SCE and DFT calculation have been determined that a drawback of Mn(I) tricarbonyl complexes is their tendency to form the Mn⁰-Mn⁰ dimeric species, which cannot efficiently catalyze CO₂RR (Figure IV. 2, see Chapter I for detailed information).^{30, 33-38} Mn⁰-Mn⁰ dimers are formed during the fast dimerization of the one-electron reduced Mn radical species [Mn[•]]. Electronic structure calculations suggest that the first one-electron reduction is metal-centered, better represented as *fac*-[Mn⁰(bpy)(CO)₃].³⁰ This dimer intermediate contribute to the catalytic overpotential since the efficient catalytic specie is the double reduced five-coordinate anion [Mn]⁻, better described as a *fac*-[Mn⁰(bpy)⁻(CO)₃] specie.

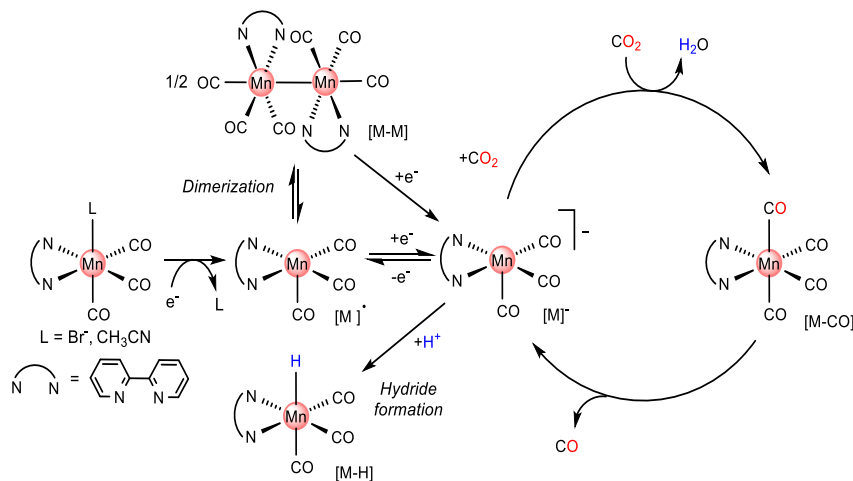


Figure IV. 2. General mechanistic proposal for the CO₂ reduction catalyzed by manganese tricarbonyl polypyridyl catalysts.

Additionally, ATR-IR-SEC is a powerful technique for investigating catalytic intermediates bonded to an electrode surface. In this regard, recent examples of heterogenized Mn molecular complexes for CO₂RR, anchored to TiO₂^{24, 26} and NT²⁶ have been reported. The results pointed that the

immobilization of manganese tricarbonyl polypyridyl catalysts alters the electrochemical response relative to solution (Figure IV. 3).^{24, 25} The formation of Mn⁰-Mn⁰ dimers in the heterogenized catalysts were explained considering several consecutive steps. First, the monomer is chemisorbed on the surface of the working electrode and upon electrochemical reduction, the bromide is lost and the reduced radical desorbs at least sufficiently to enable re-orientation. Later, the desorbed radical complex dimerizes and re-binds to the electrode surface. This step likely occurs near the surface of the electrode. The subsequent reduction results in the formation of the doubly reduced anion. The anionic species can be fully deoxidized to the adsorbed monomer.

Moreover, the influence of the catalyst loading on the product selectivity was also reported.²⁵ Two different intermediates were identified as responsible for the change in selectivity of the heterogenized Mn catalyst. The formation of a dimeric Mn⁰-Mn⁰ species at higher surface loading preferentially leads to CO formation. In contrast, at lower surface loading, the electrochemical generation of a monomeric Mn-hydride is suggested to enhance formate production (Figure IV. 3) significantly.

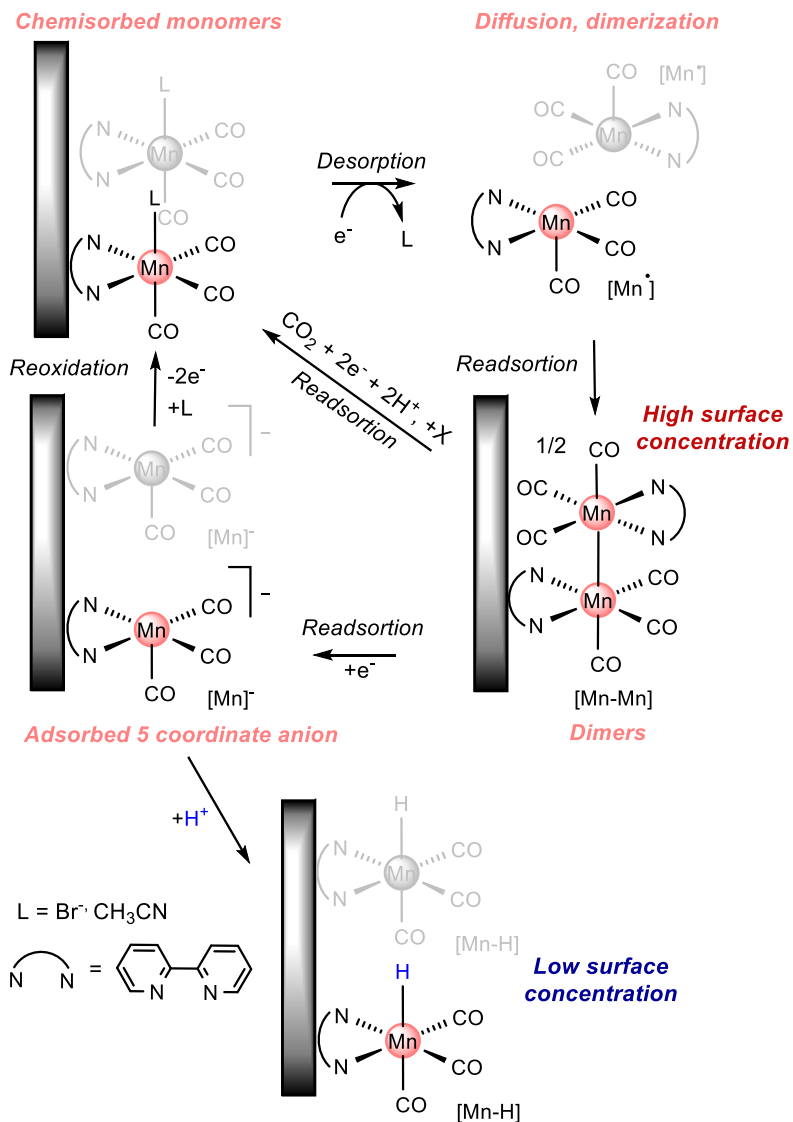


Figure IV. 3. Proposed surface mechanism of heterogenized manganese tricarbonyl polypyridyl catalysts.

As introduced in Chapter III, we have synthesized a new efficient electrocatalyst for CO₂RR, **COF_{bpyMn}**. Interestingly, the catalytic activity of the **COF_{bpyMn}** was 10-fold higher than the equivalent *fac*-**Mn(bpy)(CO)₃Br** molecular complex under equivalent conditions.

With these considerations in mind, we try to get further insights into the nature of the generated intermediates in the CO₂ reduction mechanism within the **COF_{bpyMn}** and attempt to understand their structure-activity relationships. In this chapter, ATR-IR-SEC was employed to obtain structural information on the catalytically relevant species of the **COF_{bpyMn}|NT**. We accessed key catalytic intermediates within a COF matrix by combining experimental and computational (DFT) techniques in collaboration with Prof. Nuria López (ICIQ) and Dr. Manel Ortuño (ICIQ). The results indicate that the COF framework imposes mechanical constraints on the {*fac*-Mn(CO)₃S} centers offering a strategy to avoid forming the detrimental dimeric Mn⁰-Mn⁰, resting-state typically observed for the homologous molecular complex (Figure IV. 4). Furthermore, the absence of dimeric species correlates to the observed catalytic enhancement.

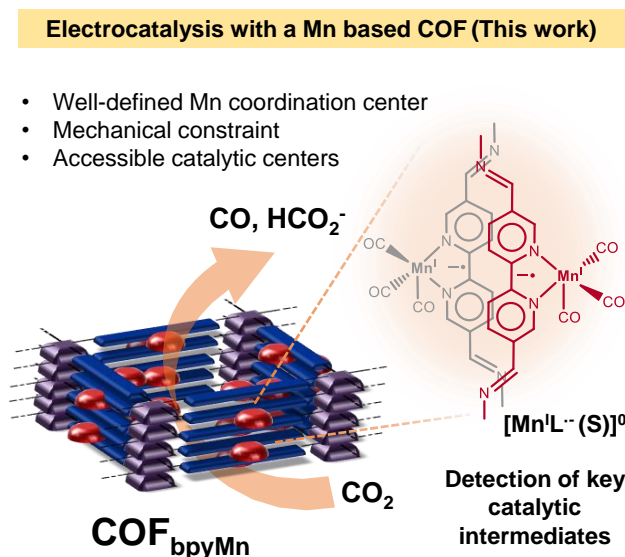


Figure IV. 4. Representation of the mechanically constrained Mn center within the **COF_{bpyMn}** and the key catalytic intermediate detected under reductive conditions.

IV.2. Results and discussion

IV.2.1 Spectroelectrochemistry of the COF_{bpyMn}|NT (SEC).

IV.2.1.1 ATR-IR-SEC in water.

To ensure a good sensitivity of the measurements, we have designed a customized three-electrode ATR-IR-SEC cell in which a COF_{bpyMn}|NT dispersion is drop-casted onto the working electrode, in close contact with the Si prism of the ATR instrument (Figure IV. 5, see the experimental section for details about the ATR-IR-SEC cell). A similar approach has been previously employed to study the CO₂RR mediated by an NT-supported Mn catalyst containing a pyrene substituted bipyridine ligand.²⁵ This setup allowed us to develop a detailed study of the changes in the CO stretching vibrations on the COF_{bpyMn}|NT at relevant redox potentials for catalysis.

ATR-IR Spectroelectrochemical cell

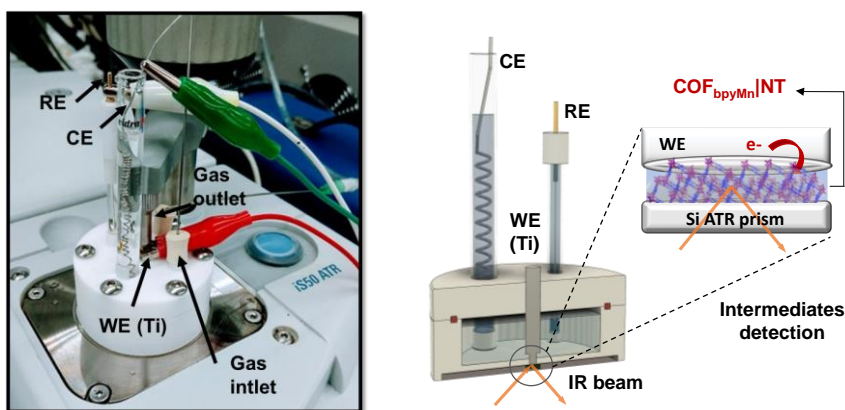


Figure IV. 5. Homemade ATR-IR-SEC cell used for the characterization of COF_{bpyMn}|NT.

Before performing ATR-IR-SEC, we compared the FT-IR of *fac*-Mn(bpy)(CO)₃Br (Mnbpy) and *fac*-Mn(bpy)(CO)₃(CH₃CN)](PF₆) (Mnbpy^{CH₃CN}) in solution (CH₃CN, OTTLE cell) with the supported Mnbpy|NT and COF_{bpyMn}|NT (CH₃CN, ATR-IR-SEC cell, Figure IV. 6a-d). Then, the IR spectrum of COF_{bpyMn}|NT was recorded in water (ATR-IR-SEC cell, Figure IV. 6e). The comparison between the IR spectra

indicated that the designed ATR-IR-SEC cell was sufficiently sensitive to probe the SEC of **COF_{bpyMn}|NT** in water.

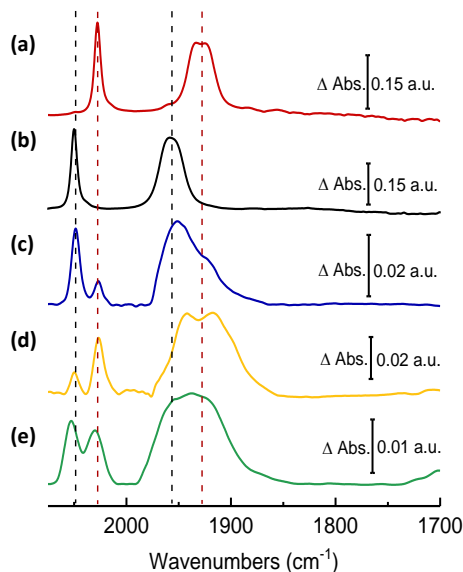


Figure IV. 6. Comparison between IR absorbance spectra in solution and supported on NT. (a) **fac-Mn(bpy)(CO)₃Br** and (b) **fac-Mn(bpy)(CO)₃(CH₃CN)](PF₆)** in CH₃CN solution by FT-IR (OTTLE cell). Supported (c) **fac-Mn(bpy)(CO)₃Br|NT** and (d) **COF_{bpyMn}|NT** by CH₃CN (0.2 M TBAPF₆) by ATR-IR. Supported (e) **COF_{bpyMn}|NT** in water (0.5 M NaHCO₃) by ATR-IR. All experiments were measured at room temperature.

This comparison can also show the extent of electronic and coordination alterations of the typical **fac-{Mn(CO)₃S}** structure by the COF. As observed in Figure IV. 6a-e, the ATR-IR spectra of **COF_{bpyMn}|NT** showed two $\nu_{(\text{CO})}$ bands at 2053 and, 2028 cm^{-1} , and a broad feature at 1937 cm^{-1} , respectively. This IR pattern corresponds to two facial tricarbonyl metal environments,²⁴ matching well with complexes **Mnbpy** and **Mnbpy^{CH₃CN}** (Figure IV. 6a, b). The IR stretches remains when **Mnbpy** is supported on NTs (**Mnbpy|NT**). These IR bands appeared in the same region, showing an unresolved band of the symmetric and asymmetric equatorial CO vibration (Figure IV. 6c). The latter results also agree with the previously reported immobilized facial tricarbonyl manganese bipyridine complexes.²⁵ Therefore, the bands observed for the deposited **COF_{bpyMn}|NT** correspond to partial Br⁻ solvolysis produced in the ink (Figure IV. 6d, e). Although

the bands are broad, and frequencies can be slightly drifted, the comparison between the IR spectrum indicates that the electronic structure and geometry imposed by the **COF_{bpy}** as a ligand to the {Mn(CO)₃S} moiety is similar to the bpy (Table IV.2.).

Then, ATR-IR-SEC was performed to identify the reduction events of **COF_{bpyMn}|NT** by a stepwise decrease of the potential from 0 V to -1.6 V *vs* SCE in water and under Ar (NaHCO₃ 0.5 M, pH 8.4). At -1.15 V *vs* SCE, the band at 2053 cm⁻¹ decreases with a concomitant broadening of the peak at 2028 cm⁻¹ and a small shift to lower energies. The evolution of the broad peak at 1937 cm⁻¹ to lower energies was also evident (Figure IV. 7b). No further changes were observed at potentials more reducing than -1.4 V *vs* SCE.

In contrast, under identical conditions, the ATR-IR-SEC of **Mnbpy|NT** is clearly different (Figure IV. 7e). The first reductive redox event starts at ca. -50 mV more reducing electrochemical potential (-1.2 V *vs* SCE). Another striking difference is observed in the IR vibration spectra. **Mnbpy|NT** has $\nu_{(\text{CO})}$ bands characteristic of a Mn⁰-Mn⁰ dimer species.^{24, 25} It is well known that the first reduction event of *fac*-Mn(bpy)(CO)₃L complexes is associated with the formation of the Mn⁰-Mn⁰ dimer and has been previously reported in water and organic solvents.^{13, 39, 40} In fact, the IR recorded for **Mnbpy|NT** is within the error to that previously reported for supported *fac*-[MnBr(4,4'-bis(phosphonicacid)-2,2'-bipyridine)(CO)₃] on TiO₂ and for the Mn⁰-Mn⁰ dimer formed during catalysis.²⁴ Moreover, the Mn⁰-Mn⁰ dimer is also observed in the re-oxidation peak for **Mnbpy|NT** in the CV but negligible for the **COF_{bpyMn}|NT**. No further changes were observed at potentials more reducing than -1.5 V *vs* SCE (Figure IV. 7d).

CHAPTER IV

Detection of key catalytic intermediates by SEC

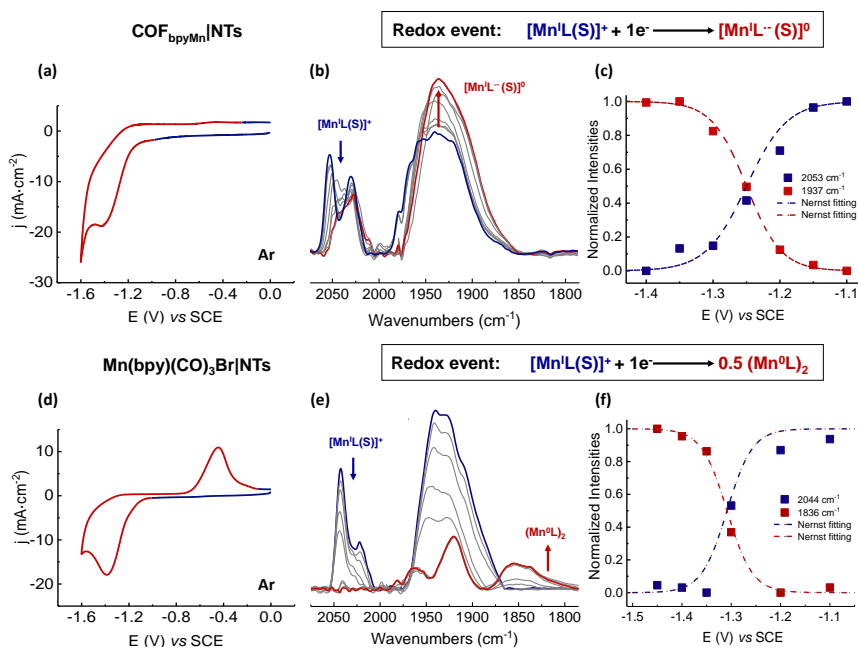


Figure IV. 7. Comparison of CVs at $100 \text{ mV} \cdot \text{s}^{-1}$ (a, d) and ATR-IR absorbance potential dependent spectra of **COF_{bpyMn}|NT** (b) and the model **Mn**bpy**|NT** (e) in water (0.5 M NaHCO_3) under Ar at room temperature. Reduction causes different changes regarding the material. For **COF_{bpyMn}|NT** (b), the $\nu(\text{CO})$ centered at 1937 cm^{-1} increases (in red) and bands at 2053 cm^{-1} disappear (in blue), while for the immobilized **Mn**bpy**|NT** (e), the $\text{Mn}^0\text{-Mn}^0$ dimer formation is evident by vibrations at 1860 and 1836 cm^{-1} (in red). Comparison of the Nernst fittings for ATR-IR-SEC of **COF_{bpyMn}|NT** and the model **Mn**bpy**|NT** (c, f).

Further analysis of the ATR-IR-SEC bands as a function of electrode potential reveals a small but significant difference between the redox potential of the **COF_{bpyMn}|NT** and **Mn**bpy**|NT** reduction events ($\Delta E_{1/2} = 50 \text{ mV}$). Figure IV. 7c and Figure IV. 7f showed the normalized intensity of the evolving bands as a function of the redox potential applied. The selected bands are diagnostic for the two different redox species and showed the disappearance of the starting compound concomitantly with the formation of the reduced one. In both cases, the evolution of the bands can be fitted to the Nernst equation. For **COF_{bpyMn}|NT**, the evolution of the bands crossed at an equivalent apparent midpoint potential (Figure IV. 7c). This suggests that both species correspond to the same redox event. The same trend was observed for **Mn**bpy**|NT** (Figure IV. 7e, f). However, the midpoint (or crossing) potential is different in value, -1.25 and -1.3 V for **COF_{bpyMn}|NT**

and **Mnbpy|NT**, respectively (See Experimental section, spectroelectrochemical section for details). The easier reduction of **COF_{bpyMn}** concerning **Mnbpy** could be attributed due to the electronic delocalization of the COF structure.

To understand the absence of dimers in the **COF_{bpyMn}**, we first studied the dimerization process within the porous framework at DFT level (Figure IV. 8). Starting from structure **COF_{bpy}-B**, we anchored two {Mn(CO)₃Br} units to nearby bipyridyl ligands, **COF_{bpyMn2}-B**. Then, one COF layer was rotated as in **COF_{bpy}-A** so the stacked bipyridyl groups could accommodate two adjacent Mn units. The resulting structure, **COF_{bpyMn2}-A** is, however, uphill in energy by 1.76 eV. Subsequent reduction *via* elimination of bromine atoms yields **COF_{bpyMn2}-A1**, displaying a distance of 7.29 Å between Mn atoms. The next intermediate **COF_{bpyMn2}-A2** shows a Mn···Mn distance of 4.94 Å and is less stable by 0.10 eV. Further approach up to 3.22 Å *via* **COF_{bpyMn2}-A3** (the distance in the molecular complex is 3.08 Å)³⁰ is again uphill by 0.52 eV. Such endothermicity comes from the unique environment of the COF, which leads to (i) stabilization of {Mn(CO)₃} **A1** reactants *via* bpy ligands in neighboring layers,⁴¹ and (ii) destabilization of {Mn₂(CO)₆} **A3** dimers *via* geometric constraints imposed by the stacking pattern of the COF framework (Figure IV. 8b).

CHAPTER IV Detection of key catalytic intermediates by SEC

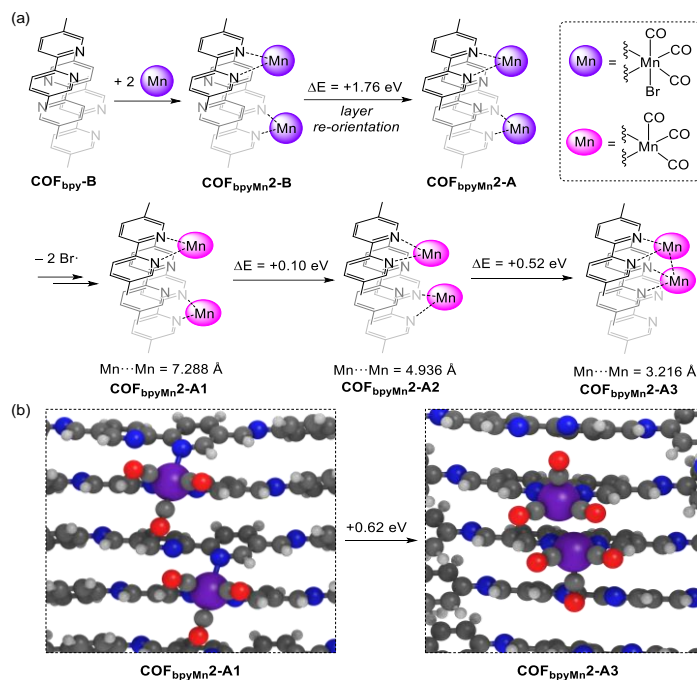


Figure IV. 8. DFT energies for the a) endergonic dimerization mechanism process within the COF material and b) optimized structures for COF_{bpyMn2-A1} and COF_{bpyMn2-A3}.

Table IV. 1. Experimental (IR) and computed CO frequencies of COF_{bpyMn}.

Species	$\nu_{\text{CO}}(\text{sym}) / \text{cm}^{-1}$	$\nu_{\text{CO}}(\text{asym}) / \text{cm}^{-1}$	$\nu_{\text{CO}}(\text{eq}) / \text{cm}^{-1}$
COF _{bpyMn1}	2013	1922	1954
COF _{bpy} -{Mn(CO) ₂ Br}	1957	1915	-
COF _{bpyMn1-red}	1981	1915	1917
COF _{bpyMn1-red-acn}	2020	1951	1947
IR COF _{bpyMn}	2025	1917 (sh)	1941 (sh)

To better comprehend the first redox process intermediate within the COF_{bpyMn}, CO stretching frequencies were computed at the DFT level using two reduced models prepared by removing Br⁻ from COF_{bpyMn1} (COF_{bpyMn1-red}) and exchanging Br⁻ by CH₃CN (COF_{bpyMn1-red-acn}). Compared to COF_{bpyMn1}, the ν_{CO} bands for the former are red-shifted by 30–40 cm⁻¹ and the values for the latter barely change (Table IV. 2). These

results can be explained by looking at the electronic structure. In **COF_{bpyMn}1-red** the unpaired electron is shared between the Mn and the COF, while in **COF_{bpyMn}1-red-acn** the electron is delocalized in the COF framework, leading to a formal Mn^I center. Therefore, the observed relatively small shift of the $\nu_{(\text{CO})}$ bands centered at 1937 cm⁻¹ upon reduction the **COF_{bpyMn}|NT** agree with the experimental observation and is incompatible with the formation of Mn⁰-Mn⁰ dimer species.

More insights can be obtained by analyzing equivalent DFT calculations of the monomeric complexes **[Mn^I(bpy)(CO)₃(Br)]** and **[Mn⁰(bpy)(CO)₃]**, showing that the IR $\nu_{(\text{CO})}$ band at lower energy is shifted about 40 cm⁻¹ upon reduction.

This shift in value is much more significant than the observed experimentally for the COF, suggesting that the metal center is significantly less reduced than the Mn molecular complex. However, for **[Mn^I(bpy⁻)(CO)₃(CH₃CN)]** the most stable electronic configuration is the one that has formally one electron delocalized over the bpy ligand. Interestingly, in the latter case, the $\nu_{(\text{CO})}$ bands in **[Mn^I(bpy⁻)(CO)₃(CH₃CN)]** are slightly shifted to lower energies than in **[Mn^I(bpy)(CO)₃(Br)]**, resembling the experimental features in the COF.

Experimental ATR-IR-SEC and DFT data clearly indicate the formation of different one-electron Mn species upon the first redox event for **COF_{bpyMn}|NT** and **Mnbpy|NT**, respectively. While the 1e⁻ reduction of **Mnbpy|NT** leads to the formation of a Mn⁰-Mn⁰ dimer analogous to the one observed for the homogeneous **[Mn^I(bpy)(CO)₃(X)]** complexes in organic^{40, 42} and aqueous media,²⁵ we found that the encapsulation of molecular-like {Mn^I(bpy)(CO)₃} moieties into an ordered rigid 2D-Organic framework suppress the dimer formation, mimicking the effect of bulky bipydyl ligands in molecular homogeneous catalysis.⁴³ In the case of **COF_{bpyMn}|NT**, the formation of a novel Mn species in a *fac*-(CO)₃ fashion was observed upon reduction, which can be described as a Mn^I radical anion species. Notably, these results suggest a direct mechanical constraint of the framework on the redox pathway of the Mn molecular units, in terms of both steric hindrance, imposed by the rigidity of the COF structure, and electronic effect of the organic framework. The latter strongly contributes

to delocalize the extra-electron in a significantly higher extent compared to bare bipyridyl ligand, significantly reducing the electron density over the metal center. Therefore, we could rationalize the first redox process of **COF_{bpyMn}|NT** monitored by ATR-IR-SEC, as the one-electron reduction of the COF framework.

As introduced above, for both **COF_{bpyMn}|NT** and **Mnbpy|NT**, no further changes were observed at potentials more reducing than -1.5 V vs SCE by ATR-IR-SEC in water. The detection of the 2e-reduced five-coordinate Mn anion (considered as the active species for HER and CO₂RR)^{13, 30, 33, 40, 43} is prevented by its fast reactivity with protons in an aqueous environment, leading to H₂ evolution *via* the formation of a short-lived Mn-H intermediate.⁴⁴ This also agrees with the sustained HER activity observed in this potential range during CPE under Ar atmosphere (see Chapter III). On the other hand, the singly reduced Mn intermediates presumably do not react fast enough with water and, consequently, accumulate as the resting state.^{25, 45} Therefore, the absence of detection of formal Mn(-I) intermediates at catalytic potentials suggests that the following chemical steps are fast.

We also monitored the reoxidation of the reduced **COF_{bpyMn}|NT** material by ATR-IR-SEC (Figure IV. 9). During the backward scan, an inverse evolution of the $\nu_{(\text{CO})}$ bands was observed and the $\nu_{(\text{CO})}$ pattern of the initial spectrum was restored, indicating that the chemical transformation upon the redox process is reversible.

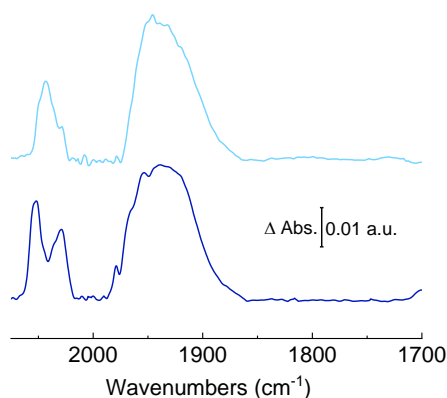


Figure IV. 9. ATR-IR spectra of the **COF_{bpyMn}|NT** before (bottom) and after (top) the reversible re-oxidation in the ATR-IR-SEC experiment in 0.5 M NaHCO₃ under Ar at room temperature.

IV.2.1.2 ATR-IR-SEC in CH₃CN.

We have also studied the ATR-IR-SEC in aprotic media (CH₃CN/ 0.2 M TBAPF₆ electrolyte) to get insights into subsequent reduced Mn species formed at more negative applied potentials. Unlike in aqueous electrolyte, the CV of **COF_{bpyMn}|NT** in CH₃CN displays two distinct one-electron reduction peaks at -1.55 (R1) and -1.92 V (R2) vs. Fc⁺/Fc (Figure IV. 10a), like the ones shown in the CV of the homogeneous **Mnbpy** complex (-1.62 and -1.83 V vs. Fc⁺/Fc, Figure IV. 11a). Comparable to the spectroelectrochemical experiments in water, the [Mn(bpy)(CO)₃]₂ dimeric species was predominantly formed upon R1 for **Mnbpy|NT** and **Mnbpy** (Figure IV. 11). At the same time, any evidence of Mn⁰-Mn⁰ dimer formation was observed for **COF_{bpyMn}|NT** (Figure IV. 10). Instead, for the latter, the growth of bands at 2028 and 1937 cm⁻¹ suggests the formation of an analogous intermediate to that found in aqueous media and previously assigned to a Mn^I intermediates in a *fac*-(CO)₃ fashion where the extra-electron is delocalized on the organic framework.

CHAPTER IV

Detection of key catalytic intermediates by SEC

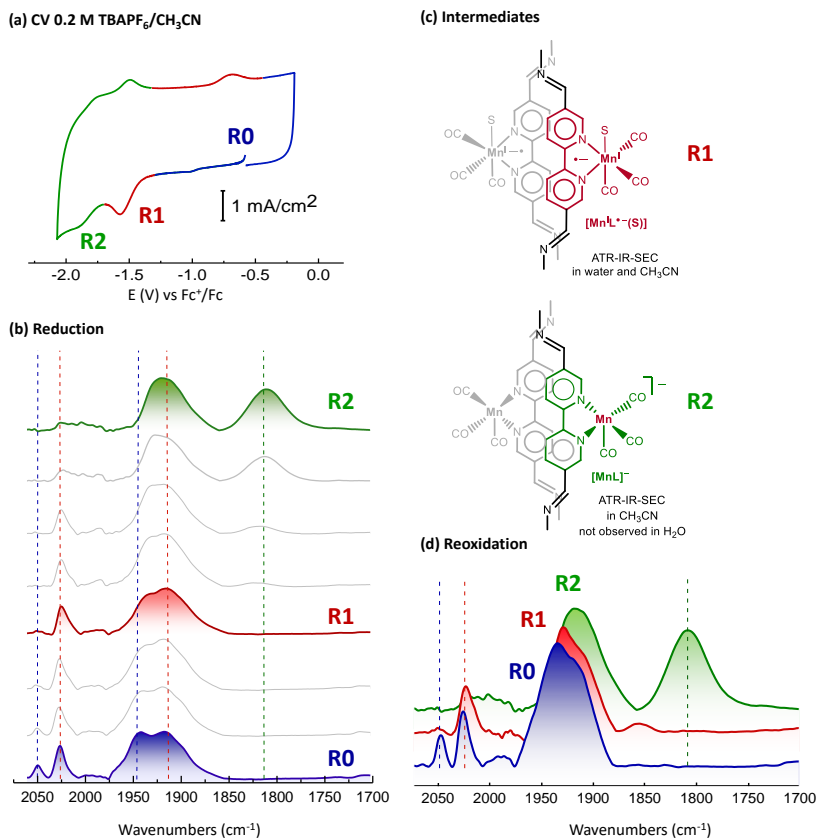


Figure IV. 10. (a) Cyclic voltammogram of $\text{COF}_{\text{bpyMn}}|\text{NT}$ at scan rate of $100 \text{ mV} \cdot \text{s}^{-1}$ in CH_3CN (0.2 M TBAPF_6). (b) ATR-IR absolute spectra of the reduction of the $\text{COF}_{\text{bpyMn}}|\text{NT}$ at different potentials (at open circuit potential (E_{OCP}) = R0, R1 = -1.55 V , R2 = -2 V vs Fc^+/Fc). (c) Proposed intermediates of $\text{COF}_{\text{bpyMn}}$ at R1: $[\text{Mn}^{\text{I}}\text{L}^-(\text{S})]^0$ and R2: $[\text{MnL}]^-$. (d) ATR-IR spectra of the reoxidation of the $[\text{MnL}]^-$ centers at different potentials (vs Fc^+/Fc), the first spectra was recorded at -2 V (R2), the second at -1.1 V (R1, reoxidation of $[\text{MnL}]^-$) and the last one at 0.1 V (reversible $[\text{Mn}^{\text{I}}\text{L}^-(\text{S})]^0$). All the experiments were performed in $0.2 \text{ M TBAPF}_6/\text{CH}_3\text{CN}$ saturated with Ar at room temperature. The blue curve is the starting $\text{COF}_{\text{bpyMn}}|\text{NT}$ (R0). Reference spectra were recorded at the open circuit potential (R0).

Then, applying a further negative potential to $\text{COF}_{\text{bpyMn}}|\text{NT}$ produced a second modification of the IR spectra at -2.0 V vs Fc^+/Fc (R2). Bands at 2028 and 1937 cm^{-1} decrease with a concomitant increase of bands at 1915 and 1808 cm^{-1} . This is consistent with the formation of a formal Mn(-I) five-coordinate anion species (Figure IV. 10), analogous to the previously characterized $[\text{Mn}(\text{bpy})(\text{CO})_3]^-$ complex (1910 and 1808 cm^{-1} , Figure IV.

CHAPTER IV

Detection of key catalytic intermediates by SEC

11) observed for **Mnbpy** (Table IV. 2).^{24, 30, 46, 47} Monitoring the reoxidation of the formal Mn(-I) centers at the COF showed the inverse evolution of the ν_{CO} bands from the di-reduced species to Mn(I), going through the monoreduced COF, regenerating the starting compound (Figure IV. 10). Consistently, the CV of **COF_{bpyMn}NT** in CH₃CN also illustrated two different reduction processes (Figure IV. 10).

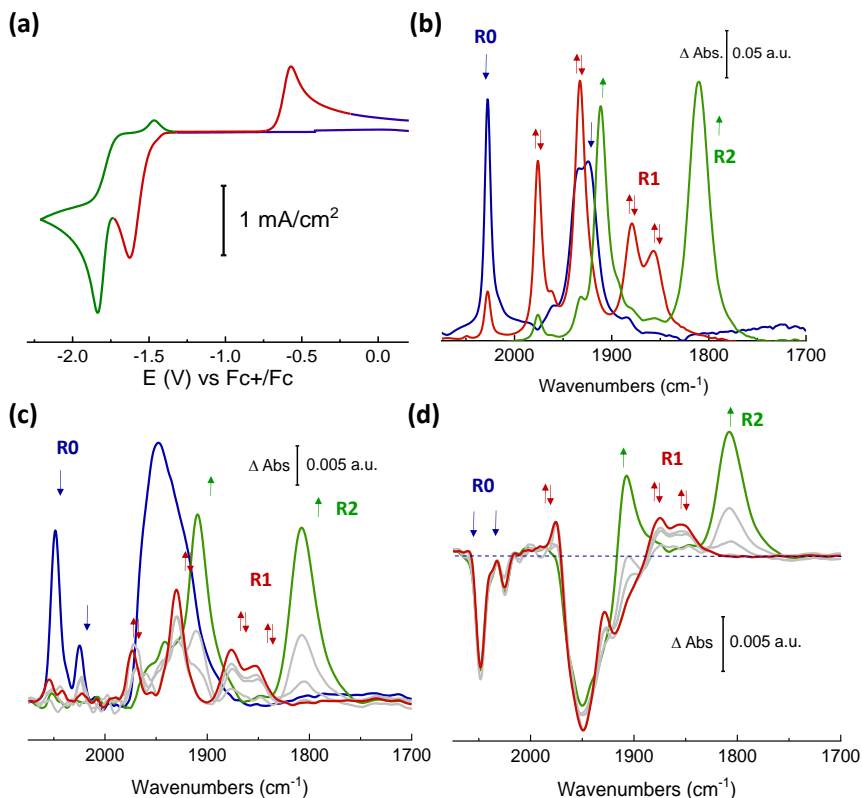


Figure IV. 11. (a) Cyclic voltammogram of **Mnbpy** (~5 mM) at a scan rate of 100 mV·s⁻¹. (b) FT-IR-SEC changes were observed during reduction at -1.71 V (red line) R1 and -2.14 V (green line) R2 vs Fc⁺/Fc of **Mnbpy** (~5 mM) in 0.2 M TBAPF₆/CH₃CN under Ar. The blue curve is the starting complex at R0. Absolute (a) and differential (b) ATR-IR-SEC spectra of **Mn(bpy)(CO)₃Br/NT** under Ar in 0.2 M TBAPF₆/CH₃CN. Green curve describes the final spectra (at R2 = -2 vs Fc⁺/Fc, [MnL]⁻ intermediate), whereas red line refers to selected intermediate spectra (at R1 = -1.65 V vs Fc⁺/Fc, [Mn⁰L]₂ intermediate). The blue curve is the starting complex (R0). Reference spectra were recorded at the open circuit potential (R0).

Table IV. 2. Frequencies of $\nu(\text{CO})$ under different conditions and respective assignment to different $\text{Mn}(\text{bpy})(\text{CO})_3\text{Br}$ species based on comparison to literature values obtained in solution and with the immobilized catalysts.

Catalyst	$\nu(\text{CO})/\text{cm}^{-1}$			Reference	
	$[\text{Mn}^{\text{I}}\text{L}(\text{S})]^+$	$[\text{Mn}^{\text{I}}\text{L}^{\cdot-}(\text{S})]^0$	$(\text{Mn}^{\text{0}}\text{L})_2$		
$\text{COF}_{\text{bpyMn}} \text{NT}^a$	2053, 2028, 1939 (sh)	2026, 1937		-	This work
$\text{COF}_{\text{bpyMn}} \text{NT}^b$	2050, 2025, 1941, 1915	2023, 1930		1915, 1808	This work
$\text{Mn}(\text{bpy})(\text{CO})_3\text{Br} \text{NT}^a$	2042, 2021, 1933 (sh)		1960, 1919, 1860, 1836	-	This work
$\text{Mn}(\text{bpy})(\text{CO})_3\text{Br} \text{NT}^b$	2050, 2025, 1935 (sh)		1971, 1930, 1876, 1853	1910, 1808	This work
$\text{Mn}(\text{bpy})(\text{CO})_3\text{Br}^b$	2027, 1936, 1923		1975, 1932, 1877, 1855	1910, 1809	Inorg. Chem. 2013, 52, 5, 2484–2491
MnBy-pyrene^a	2022, 1930, 1912		1968, 1921, 1870, 1844	-	J. Am. Chem. Soc. 2017, 139, 41, 14425–14435
$\text{MnBy-pyrene}_{\text{H}_2\text{O}}^a$	2025, 1938, 1903		1968, 1921, 1870, 1844	-	J. Am. Chem. Soc. 2017, 139, 41, 14425–14435

All the experiments were performed under Ar at room temperature. ^a 0.5 M NaHCO₃, ^b 0.2 M TBAPF₆/CH₃CN.

IV.2.2 Proposed catalytic cycle.

Figure IV. 12 presents a proposal for the CO₂ electroreduction mechanism obtained from the most relevant information gathered in this study. First, the manganese centers of the initial **COF_{bpyMn}** suffer from a ligand exchange with the solvent, followed by a reduction event. The monoreduced **COF_{bpyMn}** species are critical in the catalytic cycle. First, there is a beneficial electronic effect of the COF. The **COF_{bpyMn}** reduction occurs at 50 mV lower than in homologous molecular Mn complex **Mnbpy**, without an apparent penalty for catalytic TOF. Based on IR spectroscopy and DFT calculations, we hypothesized the COF facilitates the first reduction event *via* the electron delocalization in the COF framework. Then, and more remarkably, the COF structure does not allow the formation of the detrimental Mn⁰-Mn⁰ dimer typically found in molecular catalysts.³⁰ As previously discussed,³⁰ in molecular complexes, the formation of a Mn⁰-Mn⁰ dimer is endergonic, which negatively affects other catalytic events. Therefore, employing 2D-**COF_{bpy}** with alternated bpy disposition between layers is a valuable strategy for generating isolated Mn catalytic sites avoiding the formation of Mn dimeric species. Following the reductions events, IR studies in water and CH₃CN point towards the formal Mn(-I) detected as the intermediate that reacts with CO₂ and water to form the CO₂ reduced species.

CHAPTER IV

Detection of key catalytic intermediates by SEC

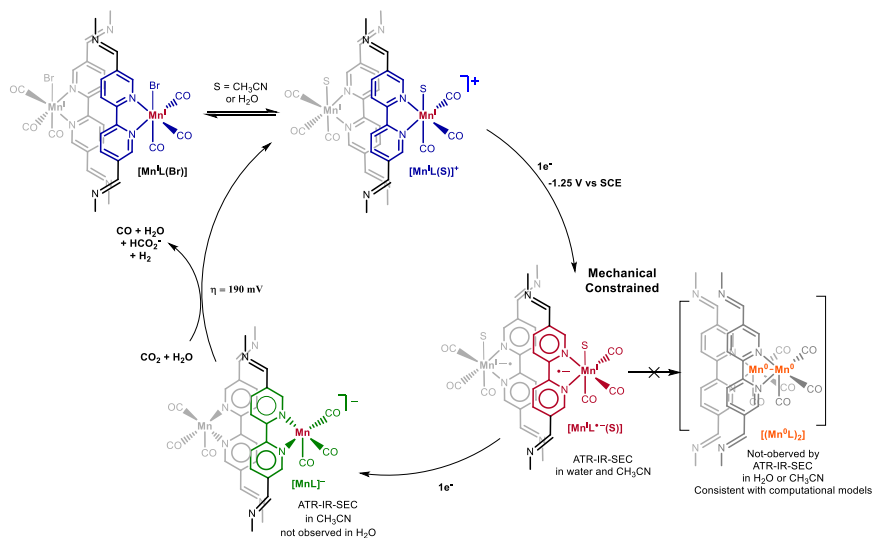


Figure IV. 12. Proposed catalytic cycle for $\text{COF}_{\text{bpyMn}}$ in the based on spectroelectrochemical evidence and computational models.

IV.3. Conclusions

We provide insights into the CO_2 reduction mechanism based on experimental and theoretical techniques. For the first time, we have demonstrated that the encapsulation of a Mn molecular catalyst for CO_2RR into an ordered 2D porous framework not only leads to a substantial improvement of the activity and selectivity for CO_2RR over HER in aqueous media but also induces a drastic change of the redox mechanism, allowing to stabilize different intermediates than those observed for the molecular counterpart.

The Mn center's defined structure in the reticular framework identified key catalytic intermediates by spectroelectrochemistry (ATR-IR). A striking difference between the first redox species of the COF and the molecular counterpart was observed. The small change in the carbonyl vibration bands upon the first reduction of $\text{COF}_{\text{bpyMn}}$ and computational modeling supports the electron's delocalization in the reticular framework. In particular, whereas a Mn^0-Mn^0 dimeric intermediate is rapidly formed after $1e^-$ reduction of the molecular $\text{Mn}(\text{CO})_3(\text{bpy})\text{Br}$ complex, the mechanically constrained configuration of the $\{\text{Mn}(\text{CO})_3\}$ units in $\text{COF}_{\text{Mnbpy}}$ prevents the dimerization reaction, leading to the formation of a

six-coordinated Mn^I solvent complex radical anion species instead. Notably, the dimer formation is observed for the heterogenized fac-Mn(bpy)(CO)₃Br complex, which is functionalized onto MWCNTs by π - π stacking interactions. Hence, unlike the classical approaches for the heterogenization of molecular catalysts, the reticular approach leads to total suppression of a diffusional behavior which may effectively contribute to altering the redox pathway of a well-defined catalyst. Besides steric hindrance, the increased electron-withdrawing character of the COF framework compared to the bare bpy ligand further contributes to delocalizing the extra negative charge localized on the Mn⁰ center, thus disfavoring the formation of a dimer. Consequently, this strategy to avoid Mn⁰-Mn⁰ dimer could reduce the overpotential and increase the overall catalytic activity since the Mn anion is the one engaging in reaction with CO₂.

We envision that the presented study will be instrumental in understanding further and guiding the rational design of COFs, and other reticular materials for CO₂ reduction and other catalytic applications, highlighting the importance of well-defined single-atom catalysis.

IV.4. Experimental section

IV.4.1. Materials and reagents

All chemicals used in this study were purchased from commercial sources and used as received, without further purification. Solvents were purchased from SDS and Scharlab. Water (18.2 M Ω ·cm) was purified with a Milli-Q Millipore Gradient AIS system. NaHCO₃ (99.999% trace metals basis), TBAPF₆ (electrochemical grade), MWCNTs, and Nafion (5 % in water) were purchased from Sigma-Aldrich®.

IV.4.2. Physical methods and experimental procedures

IV.4.2.1. Cyclic Voltammetry

Working electrode: Glassy carbon (GC) electrodes (99.9995% trace metal basis, purchased from Bio-Logic) were polished with diamond paste and alumina (3 and 1 μ m for 60 seconds each), thoroughly rinsed and sonicated in water and acetone, and dried before functionalization.

Working electrodes (GC, 0.0717 cm²) were prepared by drop casting 10 μ L of an ink containing the catalyst and MWCNTs (NT) (1 mg) dispersed in CH₃CN and Nafion 5% in water (1:1, 200 μ L) and let dry under dark (Figure IV. 13).

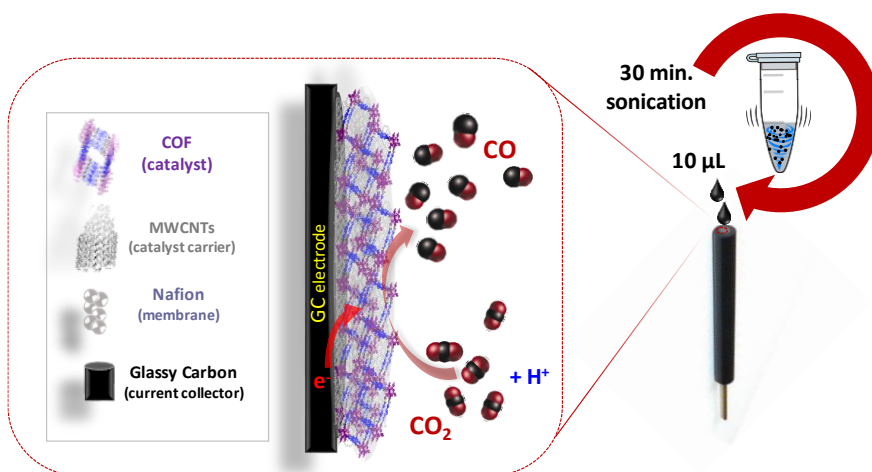


Figure IV. 13. Schematic representation of the hybrid catalyst immobilization (cat|NT).

Electrochemical measurements were performed using a Biologic potentiostat/galvanostat with a glass cell in the dark. The three-electrodes setup consisted of a working electrode, a Pt wire counter electrode, and a reference electrode. The working electrode was glassy carbon (99.9995% trace metal basis) and purchased from Bio-Logic. The reference electrode used in water was SCE (3.5 M KCl solution), while in CH₃CN was Ag wire, a pseudo reference calibrated with Fc⁺/Fc vs a freshly clean glassy carbon electrode before and after experiments.

All experiments were performed in water (0.5 M NaHCO₃) or CH₃CN (0.2 M TBAPF₆) electrolyte under Ar at 25 °C. The cell was purged for 10 minutes before each experiment.

IV.4.2.2. Spectroelectrochemistry

IV.4.2.2.1 ATR-IR-SEC

Infrared spectroscopy measures molecular vibrations that exhibit changes in the molecular dipole moment. This can also inform of COF structural dynamics and reaction intermediates. In the most commonly used configuration (attenuated total reflection mode), the infrared source penetrates approx. 1 μm deep into the electrolyte. IR spectroscopy does not require any resonance or surface enhancement to obtain high-quality spectra.

To study the different intermediates generated during the reduction of the COF_{bpyMn} we developed a homemade ATR-IR-SEC cell (Figure IV. 14). The cell has 2 main parts, the electrolyte chamber and the cap of the cell, both made of Teflon. The electrolyte chamber presents a volume of 4 mL and its base fix with the sample compartment of the ATR module. The cap of the cell has 5 holes, 3 for the working, reference and counter electrodes, respectively, and the last 2 closed with septums and used for the inlet and outlet of the purging gas (Ar). To ensure gas-tight, we introduce a black rubber between the cap and the electrolyte chamber of the cell and both compartments were closed with 6 screws.

The cat|NT ink was deposited over the Si prism of the ATR module and let dry under dark conditions. Then, the catalytic ink was electrically

connected and pressed by a titanium bare electrode (tip $d = 0.25$ cm) that acts as a working electrode (WE). The reference (RE) and counter electrodes (CE) were introduced through the cap of the SEC cell. The RE used in water (0.5 M NaHCO₃) was SCE (3.5 M KCl solution), while in CH₃CN (0.2 M TBAPF₆) was Ag wire, a pseudo reference calibrated with Fc⁺/Fc vs a freshly clean glassy carbon electrode before and after experiments. The counter electrode was a Pt wire immersed in a bridge tube containing electrolyte solution and separated from the cathodic compartment by a ceramic frit. To saturate the solution with Ar, a constant gas flow was continuously passed over the solution. All measurements were carried out at room temperature. The spectral region was set to a range from 2100 to 1700 cm⁻¹. A total of 128 scans were co-added for a spectrum with a resolution of 4 cm⁻¹. ATR-IR spectra were recorded on a Nicolet iS50 spectrometer using ATR accessory. Potentials were applied using a Biologic potentiostat/galvanostat.

Absorbance (A) spectra were generated according to Lambert–Beer’s equation. The normalized band intensities as a function of applied electrode potential E were fitted using a transformed Nernst equation. The following equations were used to analyze the Nernstian behavior assuming the Beer’s law and considering the “apparent” excess of chemical potential.^{48, 49} The "apparent" excess chemical potentials are introduced to correct for the large deviations between the predicted behavior and the Nernst plots obtained from the absorption spectra. It is then shown that the "apparent" excess chemical potentials from the COF_{ppyMn} films may result from coulombic interactions between charged sites and the mechanical work required to achieve the expansion of the COF lattice caused by the insertion of counterions and solvent molecules.⁴⁸

Oxidized

$$E = E^0 - \frac{RT}{nF} \log \frac{1 - I_{ox}}{I_{ox}} + \frac{\Delta\mu}{F}$$

Reduced

$$E = E^0 - \frac{RT}{nF} \log \frac{I_{red}}{1 - I_{red}} + \frac{\Delta\mu}{F}$$

Where:

E is the measured equilibrium potential at each point

R is the gas constant ($8.314 \text{ J}\cdot\text{mol}^{-1}\cdot\text{K}^{-1}$)

T is the experimental temperature in Kelvin

n is the number of electrons in the half-reaction

F is the Faraday constant ($96485 \text{ C}\cdot\text{mol}^{-1}$)

$\Delta\mu/F$ is the apparent excess of chemical potential

Homemade ATR-IR Spectroelectrochemical cell

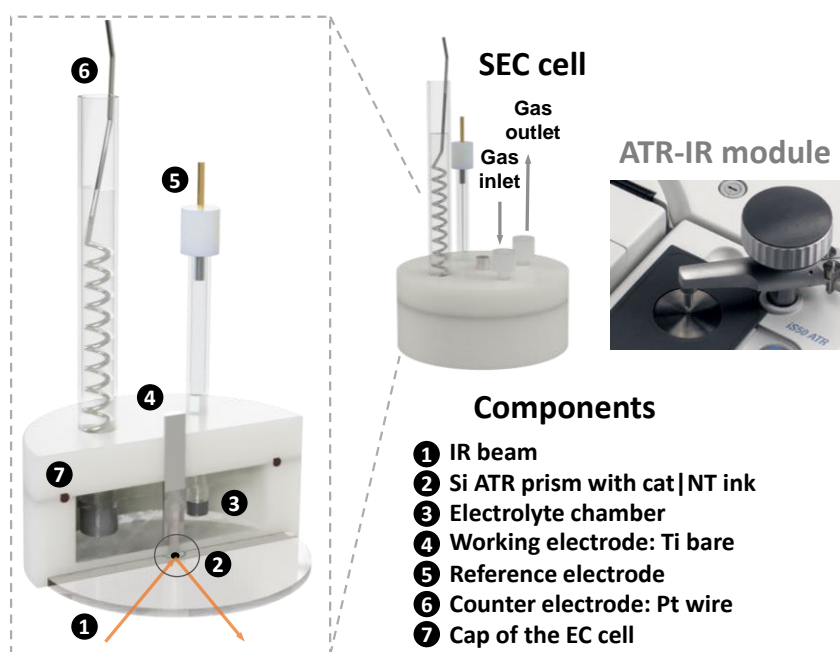


Figure IV. 14. Schematic representation of the homemade ATR-IR-SEC cell developed in our group to detect key intermediates in the catalytic cycle of $\text{COF}_{\text{bpyMn}}$.

IV.4.2.2.2 FT-IR-SEC

Spectroelectrochemical experiments with the molecular catalyst in solution were carried out in dry 0.2 M TBAPF₆/CH₃CN electrolyte within an optically transparent thin-layer electrode (OTTLE) cell (Figure IV. 15), equipped with a Pt mini-grid working and auxiliary electrodes, an Ag microwire pseudo-reference electrode and a CaF₂ window. FTIR spectra were recorded on a Nicolet iS50 FT-IR spectrometer.

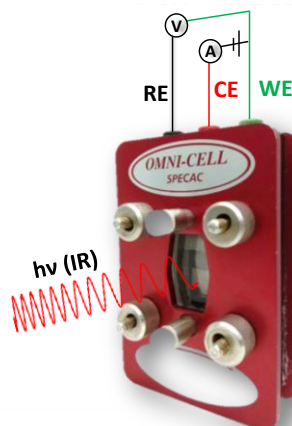


Figure IV. 15. OTTLE cell for FT-IR-SEC experiments.

IV.4.2.3. Computational Details

Periodic simulations were performed at the Density Functional Theory (DFT) level using the PBE functional⁵⁰ and Grimme's D3 dispersion scheme⁵¹ as implemented in the Vienna Ab-initio Simulation Package (VASP).^{52, 53} Single-point calculation using HSE03^{54, 55} was performed to evaluate the impact of hybrid density functionals. Core electrons were described by projector augmented wave (PAW)⁵⁶ and valence electrons by plane waves with a kinetic energy cutoff of 600 eV for cell optimizations and 450 eV for atomic optimizations. For the initial exploration of pristine COF isomers, we employed a model composed by two layers, where a and $b > 25 \text{ \AA}$ and $c \approx 7 \text{ \AA}$. For the subsequent study on immobilization of Mn compounds, we considered the most stable isomer and built a supercell by extending the c direction to account for four layers, i.e., a and $b \approx 28 \text{ \AA}$ and $c \approx 14 \text{ \AA}$. For the two models mentioned before, the Brillouin zone was sampled at $1 \times 1 \times 3$ and Γ -point, respectively, through the Monkhorst–Pack method.⁵⁷ Frequency calculations were carried out by diagonalizing the numerical Hessian matrix obtained by $\pm 0.015 \text{ \AA}$ displacements, where only selected atoms were free to move.

CHAPTER IV

Detection of key catalytic intermediates by SEC

All inputs, outputs, and final structures are freely available at the ioChem-BD repository:^{58, 59} Link: <https://iochem-bd.iciq.es/browse/review-collection/100/21562/1ff53f5be015ec89ad0071e3>

IV.5 References

1. Kornienko, N., Operando spectroscopy of nanoscopic metal/covalent organic framework electrocatalysts. *Nanoscale* **2021**, *13* (3), 1507-1514.
2. Liang, F.; Zhang, K.; Zhang, L.; Zhang, Y.; Lei, Y.; Sun, X., Recent Development of Electrocatalytic CO₂ Reduction Application to Energy Conversion. *Small* **2021**, *17* (44), 2100323.
3. Mena, S.; Ribas, E.; Richart, C.; Gallardo, I.; Farauto, J.; Shaw, S. K.; Guirado, G., Electrochemical tools to disclose the electrochemical reduction mechanism of CO₂ in aprotic solvents and ionic liquids. *Journal of Electroanalytical Chemistry* **2021**, 895, 115411.
4. Boutin, E.; Merakeb, L.; Ma, B.; Boudy, B.; Wang, M.; Bonin, J.; Anxolabéhère-Mallart, E.; Robert, M., Molecular catalysis of CO₂ reduction: recent advances and perspectives in electrochemical and light-driven processes with selected Fe, Ni and Co aza macrocyclic and polypyridine complexes. *Chemical Society Reviews* **2020**, *49* (16), 5772-5809.
5. Costentin, C.; Robert, M.; Savéant, J.-M., Catalysis of the electrochemical reduction of carbon dioxide. *Chemical Society Reviews* **2013**, *42* (6), 2423-2436.
6. Robert, M.; Costentin, C.; Daasbjerg, K., *Carbon Dioxide Electrochemistry: Homogeneous and Heterogeneous Catalysis*. Royal Society of Chemistry: 2020.
7. Fernández, S.; Dubed Bandomo, G. C.; Lloret-Fillol, J., Recent advances in electrocatalytic CO₂ reduction with molecular complexes. In *Advances in Inorganic Chemistry*, Academic Press: 2022.
8. Fernandez, S.; Dubed Bandomo, G. C.; Lloret-Fillol, J., Manganese Complexes for Electro- and Photocatalytic Transformations. In *Manganese Catalysis in Organic Synthesis*, 2021; pp 137-181.
9. Morlanés, N.; Takanahe, K.; Rodionov, V., Simultaneous Reduction of CO₂ and Splitting of H₂O by a Single Immobilized Cobalt Phthalocyanine Electrocatalyst. *ACS Catalysis* **2016**, *6* (5), 3092-3095.
10. Willkomm, J.; Muresan, N. M.; Reisner, E., Enhancing H₂ evolution performance of an immobilised cobalt catalyst by rational ligand design. *Chemical Science* **2015**, *6* (5), 2727-2736.
11. Rosser, T. E.; Reisner, E., Understanding Immobilized Molecular Catalysts for Fuel-Forming Reactions through UV/Vis Spectroelectrochemistry. *ACS Catalysis* **2017**, *7* (5), 3131-3141.
12. Kas, R.; Ayemoba, O.; Firet, N. J.; Middelkoop, J.; Smith, W. A.; Cuesta, A., In-Situ Infrared Spectroscopy Applied to the Study of the Electrocatalytic Reduction of CO₂: Theory, Practice and Challenges. *ChemPhysChem* **2019**, *20* (22), 2904-2925.
13. Neri, G.; Walsh, J. J.; Teobaldi, G.; Donaldson, P. M.; Cowan, A. J., Detection of catalytic intermediates at an electrode surface during carbon dioxide reduction by an earth-abundant catalyst. *Nature Catalysis* **2018**, *1* (12), 952-959.
14. Mortimer, R. J., Spectroelectrochemistry, Applications. In *Encyclopedia of Spectroscopy and Spectrometry (Third Edition)*, Lindon, J. C.; Tranter, G. E.; Koppelaar, D. W., Eds. Academic Press: Oxford, 2017; pp 160-171.

15. Kornienko, N., Operando spectroscopy of nanoscopic metal/covalent organic framework electrocatalysts. *Nanoscale* **2020**.
16. Wei, Y.-S.; Zhang, M.; Zou, R.; Xu, Q., Metal–Organic Framework-Based Catalysts with Single Metal Sites. *Chem. Rev.* **2020**, *120* (21), 12089-12174.
17. Heidary, N.; Morency, M.; Chartrand, D.; Ly, K. H.; Iftimie, R.; Kornienko, N., Electrochemically Triggered Dynamics within a Hybrid Metal–Organic Electrocatalyst. *J Am Chem Soc* **2020**, *142* (28), 12382-12393.
18. Bushuyev, O. S.; De Luna, P.; Dinh, C. T.; Tao, L.; Saur, G.; van de Lagemaat, J.; Kelley, S. O.; Sargent, E. H., What Should We Make with CO₂ and How Can We Make It? *Joule* **2018**, *2* (5), 825-832.
19. Kornienko, N.; Zhao, Y.; Kley, C. S.; Zhu, C.; Kim, D.; Lin, S.; Chang, C. J.; Yaghi, O. M.; Yang, P., Metal–Organic Frameworks for Electrocatalytic Reduction of Carbon Dioxide. *Journal of the American Chemical Society* **2015**, *137* (44), 14129-14135.
20. Diercks, C. S.; Lin, S.; Kornienko, N.; Kapustin, E. A.; Nichols, E. M.; Zhu, C.; Zhao, Y.; Chang, C. J.; Yaghi, O. M., Reticular Electronic Tuning of Porphyrin Active Sites in Covalent Organic Frameworks for Electrocatalytic Carbon Dioxide Reduction. *Journal of the American Chemical Society* **2018**, *140* (3), 1116-1122.
21. Lin, S.; Diercks, C. S.; Zhang, Y.-B.; Kornienko, N.; Nichols, E. M.; Zhao, Y.; Paris, A. R.; Kim, D.; Yang, P.; Yaghi, O. M.; Chang, C. J., Covalent organic frameworks comprising cobalt porphyrins for catalytic CO₂ reduction in water. *Science* **2015**, *349* (6253), 1208-1213.
22. Machan, C. W., Recent advances in spectroelectrochemistry related to molecular catalytic processes. *Current Opinion in Electrochemistry* **2019**, *15*, 42-49.
23. Walsh, J. J.; Smith, C. L.; Neri, G.; Whitehead, G. F. S.; Robertson, C. M.; Cowan, A. J., Improving the efficiency of electrochemical CO₂ reduction using immobilized manganese complexes. *Faraday Discussions* **2015**, *183* (0), 147-160.
24. Walsh, J. J.; Forster, M.; Smith, C. L.; Neri, G.; Potter, R. J.; Cowan, A. J., Directing the mechanism of CO₂ reduction by a Mn catalyst through surface immobilization. *Physical Chemistry Chemical Physics* **2018**, *20* (10), 6811-6816.
25. Reuillard, B.; Ly, K. H.; Rosser, T. E.; Kuehnel, M. F.; Zebger, I.; Reisner, E., Tuning Product Selectivity for Aqueous CO₂ Reduction with a Mn(bipyridine)-pyrene Catalyst Immobilized on a Carbon Nanotube Electrode. *Journal of the American Chemical Society* **2017**, *139* (41), 14425-14435.
26. Rosser, T. E.; Windle, C. D.; Reisner, E., Electrocatalytic and Solar-Driven CO₂ Reduction to CO with a Molecular Manganese Catalyst Immobilized on Mesoporous TiO₂. *Angewandte Chemie International Edition* **2016**, *55* (26), 7388-7392.
27. Heidary, N.; Morency, M.; Chartrand, D.; Ly, K. H.; Iftimie, R.; Kornienko, N., Electrochemically Triggered Dynamics within a Hybrid Metal–Organic Electrocatalyst. *J. Am. Chem. Soc.* **2020**, *142* (28), 12382-12393.
28. Zhong, H.; Ghorbani-Asl, M.; Ly, K. H.; Zhang, J.; Ge, J.; Wang, M.; Liao, Z.; Makarov, D.; Zschech, E.; Brunner, E.; Weidinger, I. M.; Zhang, J.; Krashennnikov, A. V.; Kaskel, S.; Dong, R.; Feng, X., Synergistic electroreduction of carbon dioxide to carbon monoxide on bimetallic layered conjugated metal-organic frameworks. *Nat. Comm.* **2020**, *11* (1).

CHAPTER IV

Detection of key catalytic intermediates by SEC

29. Guo, Y.; Shi, W.; Yang, H.; He, Q.; Zeng, Z.; Ye, J.-y.; He, X.; Huang, R.; Wang, C.; Lin, W., Cooperative Stabilization of the [Pyridinium-CO₂-Co] Adduct on a Metal–Organic Layer Enhances Electrocatalytic CO₂ Reduction. *Journal of the American Chemical Society* **2019**, *141* (44), 17875-17883.
30. Riplinger, C.; Sampson, M. D.; Ritzmann, A. M.; Kubiak, C. P.; Carter, E. A., Mechanistic Contrasts between Manganese and Rhenium Bipyridine Electrocatalysts for the Reduction of Carbon Dioxide. *Journal of the American Chemical Society* **2014**, *136* (46), 16285-16298.
31. Hartl, F.; Mahabiersing, T.; Le Floch, P.; Mathey, F.; Ricard, L.; Rosa, P.; Zális, S., Electronic Properties of 4,4',5,5'-Tetramethyl-2,2'-biphosphinine (tmbp) in the Redox Series fac-[Mn(Br)(CO)₃(tmbp)], [Mn(CO)₃(tmbp)]₂, and [Mn(CO)₃(tmbp)]⁻: Crystallographic, Spectroelectrochemical, and DFT Computational Study. *Inorg. Chem.* **2003**, *42* (14), 4442-4455.
32. Abel, E. W.; Stone, F. G. A., The chemistry of transition-metal carbonyls: structural considerations. *Q. Rev. Chem. Soc.* **1969**, *23* (3), 325-371.
33. Stanbury, M.; Compain, J.-D.; Chardon-Noblat, S., Electro and photoreduction of CO₂ driven by manganese-carbonyl molecular catalysts. *Coord. Chem. Rev.* **2018**, *361*, 120-137.
34. Grills, D. C.; Ertem, M. Z.; McKinnon, M.; Ngo, K. T.; Rochford, J., Mechanistic aspects of CO₂ reduction catalysis with manganese-based molecular catalysts. *Coordination Chemistry Reviews* **2018**, *374*, 173-217.
35. Sinopoli, A.; La Porte, N. T.; Martinez, J. F.; Wasielewski, M. R.; Sohail, M., Manganese carbonyl complexes for CO₂ reduction. *Coord. Chem. Rev.* **2018**, *365*, 60-74.
36. Rossenaar, B. D.; Hartl, F.; Stufkens, D. J.; Amatore, C.; Maisonhaute, E.; Verpeaux, J.-N., Electrochemical and IR/UV–Vis Spectroelectrochemical Studies of fac-[Mn(X)(CO)₃(iPr-DAB)]_n (n = 0, X = Br, Me, Bz; n = +1, X = THF, MeCN, nPrCN, P(OMe)₃; iPr-DAB = 1,4-Diisopropyl-1,4-diaza-1,3-butadiene) at Variable Temperatures: Relation between Electrochemical and Photochemical Generation of [Mn(CO)₃(α-diimine)]. *Organometallics* **1997**, *16* (21), 4675-4685.
37. Sung, S.; Li, X.; Wolf, L. M.; Meeder, J. R.; Bhuvanesh, N. S.; Grice, K. A.; Panetier, J. A.; Nippe, M., Synergistic Effects of Imidazolium-Functionalization on fac-Mn(CO)₃ Bipyridine Catalyst Platforms for Electrocatalytic Carbon Dioxide Reduction. *J. Am. Chem. Soc.* **2019**, *141* (16), 6569-6582.
38. Grills, D. C.; Farrington, J. A.; Layne, B. H.; Lyman, S. V.; Mello, B. A.; Preses, J. M.; Wishart, J. F., Mechanism of the Formation of a Mn-Based CO₂ Reduction Catalyst Revealed by Pulse Radiolysis with Time-Resolved Infrared Detection. *J. Am. Chem. Soc.* **2014**, *136* (15), 5563-5566.
39. Hartl, F.; Rossenaar, B. D.; Stor, G. J.; Stufkens, D. J., Role of an electron-transfer chain reaction in the unusual photochemical formation of five-coordinated anions [Mn(CO)₃

(α-diimine)]⁻

from fac

-[Mn(X)(CO)₃

- (α -diimine)] (X = halide) at low temperatures. *Recl. Trav. Chim. Pays-Bas* **1995**, *114* (11-12), 565-570.
40. Bourrez, M.; Molton, F.; Chardon-Noblat, S.; Deronzier, A., [Mn(bipyridyl)(CO)₃Br]: An Abundant Metal Carbonyl Complex as Efficient Electrocatalyst for CO₂ Reduction. *Angewandte Chemie International Edition* **2011**, *50* (42), 9903-9906.
41. Romero-Muñiz, I.; Mavrandonakis, A.; Albacete, P.; Vega, A.; Briois, V.; Zamora, F.; Platero-Prats, A. E., Unveiling the Local Structure of Palladium Loaded into Imine-Linked Layered Covalent Organic Frameworks for Cross-Coupling Catalysis. *Angew. Chem. Int. Ed.* **2020**, *59* (31), 13013-13020.
42. Smieja, J. M.; Sampson, M. D.; Grice, K. A.; Benson, E. E.; Froehlich, J. D.; Kubiak, C. P., Manganese as a Substitute for Rhenium in CO₂ Reduction Catalysts: The Importance of Acids. *Inorg. Chem.* **2013**, *52* (5), 2484-2491.
43. Sampson, M. D.; Nguyen, A. D.; Grice, K. A.; Moore, C. E.; Rheingold, A. L.; Kubiak, C. P., Manganese Catalysts with Bulky Bipyridine Ligands for the Electrocatalytic Reduction of Carbon Dioxide: Eliminating Dimerization and Altering Catalysis. *J. Am. Chem. Soc.* **2014**, *136* (14), 5460-5471.
44. Franco, F.; Cometto, C.; Nencini, L.; Barolo, C.; Sordello, F.; Minero, C.; Fiedler, J.; Robert, M.; Gobetto, R.; Nervi, C., Local Proton Source in Electrocatalytic CO₂ Reduction with [Mn(bpy-R)(CO)₃Br] Complexes. *Chemistry – A European Journal* **2017**, *23* (20), 4782-4793.
45. Walsh, J. J.; Neri, G.; Smith, C. L.; Cowan, A. J., Water-Soluble Manganese Complex for Selective Electrocatalytic CO₂ Reduction to CO. *Organometallics* **2018**, *38* (6), 1224-1229.
46. Hartl, F.; Rosa, P.; Ricard, L.; Le Floch, P.; Zális, S., Electronic transitions and bonding properties in a series of five-coordinate “16-electron” complexes [Mn(CO)₃(L₂)]⁻ (L₂=chelating redox-active π -donor ligand). *Coord. Chem. Rev.* **2007**, *251* (3-4), 557-576.
47. Scarborough, C. C.; Wieghardt, K., Electronic Structure of 2,2'-Bipyridine Organotransition-Metal Complexes. Establishing the Ligand Oxidation Level by Density Functional Theoretical Calculations. *Inorg. Chem.* **2011**, *50* (20), 9773-9793.
48. Amemiya, T.; Hashimoto, K.; Fujishima, A.; Itoh, K., Analyses of Spectroelectrochemical Behavior of Polypyrrole Films Using the Nernst Equation: “Monomer Unit Model” and Polaron/Bipolaron Model. *Journal of The Electrochemical Society* **1991**, *138* (10), 2845-2850.
49. Nechtschein, M.; Devreux, F.; Genoud, F.; Vieil, E.; Pernaut, J. M.; Genies, E., Polarons, bipolarons and charge interactions in polypyrrole: Physical and electrochemical approaches. *Synthetic Metals* **1986**, *15* (1), 59-78.
50. Perdew, J. P.; Burke, K.; Ernzerhof, M., Generalized Gradient Approximation Made Simple. *Physical Review Letters* **1996**, *77* (18), 3865-3868.
51. Grimme, S.; Antony, J.; Ehrlich, S.; Krieg, H., A consistent and accurate ab initio parametrization of density functional dispersion correction (DFT-D) for the 94 elements H-Pu. *The Journal of Chemical Physics* **2010**, *132* (15), 154104.
52. Kresse, G.; Furthmüller, J., Efficient iterative schemes for ab initio total-energy calculations using a plane-wave basis set. *Physical Review B* **1996**, *54* (16), 11169-11186.

53. Kresse, G.; Furthmüller, J., Efficiency of ab-initio total energy calculations for metals and semiconductors using a plane-wave basis set. *Computational Materials Science* **1996**, *6* (1), 15-50.
54. Heyd, J.; Scuseria, G. E.; Ernzerhof, M., Hybrid functionals based on a screened Coulomb potential. *The Journal of Chemical Physics* **2003**, *118* (18), 8207-8215.
55. Heyd, J.; Scuseria, G. E.; Ernzerhof, M., Erratum: "Hybrid functionals based on a screened Coulomb potential" [J. Chem. Phys. 118, 8207 (2003)]. *The Journal of Chemical Physics* **2006**, *124* (21), 219906.
56. Kresse, G.; Joubert, D., From ultrasoft pseudopotentials to the projector augmented-wave method. *Physical Review B* **1999**, *59* (3), 1758-1775.
57. Monkhorst, H. J.; Pack, J. D., Special points for Brillouin-zone integrations. *Physical Review B* **1976**, *13* (12), 5188-5192.
58. Álvarez-Moreno, M.; de Graaf, C.; López, N.; Maseras, F.; Poblet, J. M.; Bo, C., Managing the Computational Chemistry Big Data Problem: The ioChem-BD Platform. *Journal of Chemical Information and Modeling* **2015**, *55* (1), 95-103.
59. Bo, C.; Maseras, F.; López, N., The role of computational results databases in accelerating the discovery of catalysts. *Nature Catalysis* **2018**, *1* (11), 809-810.

CHAPTER IV

Detection of key catalytic intermediates by SEC

CHAPTER V.

Evidence of dynamic rearrangement in a 2D Covalent Organic Framework triggered by an electric stimulus.

Chapter V: Evidence of dynamic rearrangement in a 2D Covalent Organic Framework triggered by an electric stimulus.

V.1. General insight

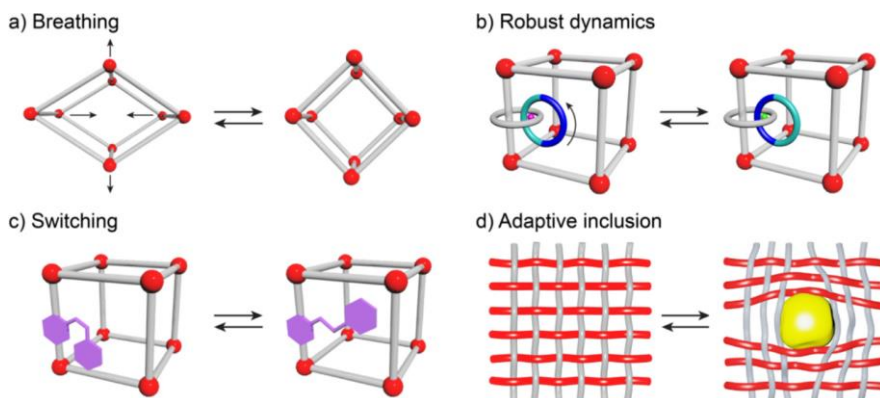
Materials that are structurally transformable in response to external stimuli (such as light, heat, electric field, pressure and chemical analytes) are attracting increasing attention.¹⁻³ The dynamic and adaptive features of these materials make them promising candidates for optoelectronic devices, sensors, energy storage, etc.⁴⁻⁹

While it is common to think of reticular frameworks as static systems, in many cases, they exhibit structural dynamics upon external perturbation while retaining the same or similar topologies.¹⁰⁻¹² In like manner, reticular chemistry has become possible to introduce motions into solids by using flexible building blocks and dangling switchable or mechanically interlocked units into the pores (Scheme V.1).¹³

In this sense, reticular frameworks with well-defined and regular arrays are ideal for studying dynamic processes within infinitely extended skeletons and specific polymeric packings during external stimuli. Among various porous crystalline frameworks, Metal Organic Frameworks (MOFs)^{11, 14-16} and Covalent Organic Frameworks (COFs),¹⁷⁻²⁸ are the most promising and extensively studied. In particular, the highly ordered and porous structures of COFs facilitate their real-time responsive behaviors. Their crystallinity makes the energy transfer between external-stimulus signals and responsive sites much faster and more efficient, while pores provide reasonable flexibility for structural transformations.²⁰ In addition, these switching processes can change the dipole-dipole interactions, the electron transport channels, and the size and pore environments, which can change at the same time the molecular stacking and the existing free volume of COFs, as well as the selectivity and mobility of the COFs and their components.^{10, 27, 29}

CHAPTER V

Dynamic rearrangement of 2D-COF by electric field



Scheme V.1. Modes of dynamics in solids: (a) flexible constituents yield frameworks that distort in response to external stimuli, (b) mechanically interlocked molecules (blue and green) appended onto the struts move within the constraints imposed by their interlocking, (c) switchable units (purple) dangling in the pores respond to external stimuli by conformational changes, and (d) woven frameworks where large degrees of freedom of the threads allow for adaptive inclusion of guests (yellow).¹³ Reproduced with permission from [13]. Copyright 2018 American Chemical Society.

Surprisingly, despite the rapid expansion of applications of COFs and the studies related to their different properties, studies of their dynamic response to external perturbations are still unusual.³⁰

Furthermore, studying the dynamics and structural transitions of COFs could provide detailed information on the local environment of catalytic sites and their evolution. Structural elucidation and fundamental understandings are needed to propel COFs as stimuli-responsive materials, with potential applications related to molecular machines, sensors, or actuators but also to improve their electrocatalytic properties.

In situ spectroscopic methods could be instrumental in gaining insights into the dynamic structural changes in COFs during an external stimulus, especially if crystallinity is lost or if motions of the framework do not correspond to crystallographic changes, such as linker rotations.³¹⁻³³ Besides, the application of *ex situ* solid-state characterization methods is often insufficient to understand all the processes occurring in a system.

In particular, vibrational methods are one of the most powerful techniques to provide information about the molecular structure, orientation and interactions of adsorbed species at the interfaces.^{34, 35} In fact, Infrared (IR) spectroscopy has been established as a routine technique to obtain

valuable information at the secondary structure level and for detecting structural changes from the multilayers of molecular complexes, polymers and reticular frameworks.^{36,37} Usually, a thick film of catalyst (from 0.5- 5 μm) is necessary to achieve sufficient absorbance in Attenuated Total Reflection (ATR-IR).³⁸ Then, an ATR-IR limitation is the study of the interface due to the interference from the bulk, providing mixed information on both interface and bulk. An alternative variation of the conventional IR spectroscopy, the Surface Enhancement Infrared Absorption spectroscopy (SEIRA),³⁹ overcomes this limitation and can detect IR changes at a monolayer level.

SEIRA is based on the surface enhancement effect of the IR absorption on rough metals. SEIRA effect has been observed on almost all coinage metals such as Au, Ag, Cu, etc.^{40,41} The IR signal of an adsorbed monolayer on the top of the metal can be enhanced from 10 to 1000 times. The effective signal enhancement is only observed near the metal surface (≈ 10 nm) because of the plasmonic metal field is the reason for the enhancement effect (optical near-field effect).⁴²⁻⁴⁶ Therefore, the optical near-field effect eliminates vibrational contributions from the bulk in the IR spectrum and selectively detects changes of adsorbed macromolecules at the interface at the level of a few layers.⁴⁷⁻⁴⁹

SEIRA has been successfully used in dynamic studies of electrochemical interfaces (SEIRA-SEC) in systems that are not readily accessible by conventional spectroelectrochemical techniques.⁵⁰⁻⁵⁴ SEIRA-SEC is a powerful technique for studying chemical processes at the surface or surface-liquid interphase, surface electrochemistry, and single molecule studies like protein films.⁴⁷⁻⁴⁹

The SEIRA-SEC advantages motivated us to examine potential structural changes or COF dynamics at the electrode interface. Then, in this chapter we have combined advanced *in situ* / *in operando* spectroelectrochemical techniques to provide new experimental information on the reticular materials upon redox stimulus. We have studied the $\text{COF}_{\text{bpyMn}}$ at the electrode-COF interface (see Chapters III and IV for previous physicochemical and electrochemical characterizations of $\text{COF}_{\text{bpyMn}}$). The high sensitivity of SEIRA-SEC served to identify the

evolution of **COF**_{bpyMn} upon applying a negative potential within the closest layers to the working electrode (≈ 10 nm, e.i. for our **COF**_{bpyMn} corresponds to c.a. 30 layers considering a perfect stacking). Interestingly, different chemical speciation evolution was detected in SEIRA-SEC experiments. Instead of the clean formation of radical intermediates detected by ATR-IR, we identified the formation of Mn⁰-Mn⁰ dimer species by SEIRA-SEC. The results suggest that the polarized electrode (electric field) rearranges the **COF**_{bpyMn} layers at the electrode-COF interface allowing the Mn-Mn bond formation. This implies structural changes/dynamics from both X and Y axes, or alternatively, the Z axe. We also performed EPR-SEC to obtain more information about the spins at the bulk, and confirmed the formation of the radical intermediate, consistent with the ATR-IR measurements. Besides, transmittance UV-vis-SEC is consistent with the radical and dimer intermediates formation. We hypothesize that the stronger electric field at the COF-electrode interface could help dynamically restructure the 2D material by an expansion and translocation mechanism. This study shows the richness and complexity of reticular materials and can serve as a guide to investigating the dynamics of these organic frameworks.

V.2. Results and discussion

V.2.1 Spectroelectrochemistry of the **COF**_{bpyMn}|NT

V.2.1.1. SEIRA-SEC of **COF**_{bpyMn}|NT in CH₃CN

To study the electrode-**COF**_{bpyMn} interface, we have performed SEIRA-SEC in CH₃CN. First, to obtain a good SEIRA sensitivity, a nanostructured Au film was deposited on a silicon prism to perform the spectroscopy in the attenuated total reflection (ATR) mode (Figure V.1, see SI for details, Configuration 1). The prism covered with the nanostructured Au film was used as IR signal amplifier and as a working electrode for the SEIRA-SEC. Next, the **COF**_{bpyMn} was dispersed with NTs in CH₃CN and Nafion to form a hybrid ink of the catalyst (**COF**_{bpyMn} |NT) (see Experimental Section for details). Then, the catalytic ink was deposited by drop casting on the nanostructured Au. FESEM image of deposited ink containing **COF**_{bpyMn}|NT showed a thickness of the film of ca. 4 μ m (Figure V.1).

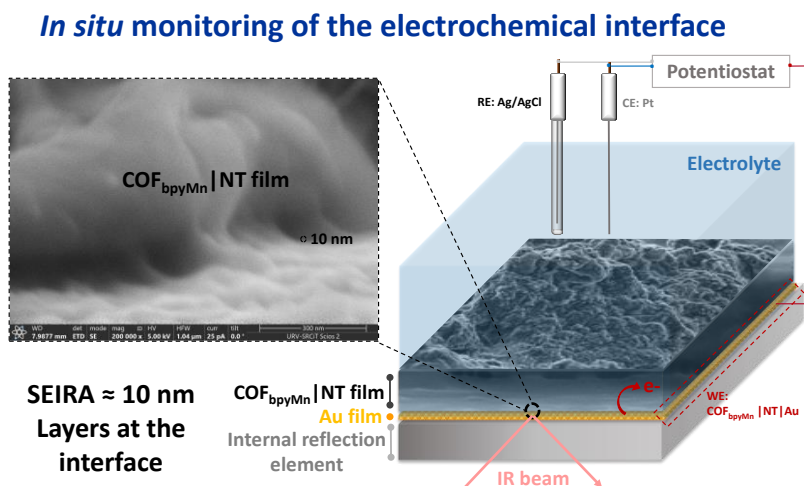


Figure V.1. Schematic representation of the SEIRA-SEC cell (Configuration 1) and the COF_{bpyMn}|NT-electrode interface. FESEM of COF_{bpyMn}|NT. The nanostructured Au film was used as IR signal amplifier and current collector.

With SEIRA configuration, the surface plasmon polariton generated at the rough Au surface penetrates the adjacent interface with a decay length of ≈ 8 -10 nm, sampling only those molecular moieties within this short distance from the solid surface.⁴²⁻⁴⁴ Due to the distance-dependent attenuation of the signal enhancement, SEIRA allowed the detection of molecular vibrations exclusively of the closest COF_{bpyMn}|NT layers at the interface of the working electrode (≈ 30 layers), thus eliminating the vibrational contributions from the bulk in the IR spectrum.

To get further insights into the behavior of the COF_{bpyMn} under reductive conditions, SEIRA-SEC was performed by the stepwise decrease of the potential from the open circuit potential ($E_{\text{OCP}} = +0.450$ mV) to -1.6 V (*vs* Ag/AgCl, all redox potentials in the SEIRA-SEC will be referred to Ag/AgCl, otherwise indicated) in CH₃CN (0.2 M TBAPF₆) under N₂ (Figure V.2).

CHAPTER V

Dynamic rearrangement of 2D-COF by electric field

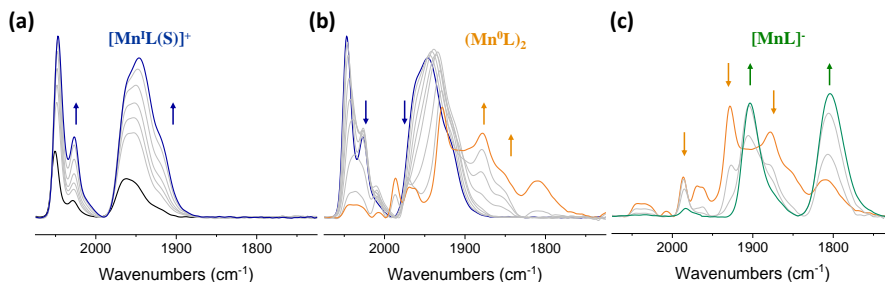


Figure V.2. Potential-dependent SEIRA spectra of **COF_{bpyMn}|NT** recorded on nanostructure Au in CH₃CN (0.2 M TBAPF₆) under N₂ from E_{OCP} to -1.6 V vs Ag/AgCl. (a) **COF_{bpyMn}|NT** before a redox transformation from E_{OCP} (black) to E = -0.7 V vs Ag/AgCl, [Mn^{II}L(S)]⁺, R0 (blue), (b) after 1e⁻ reduction to form [Mn⁰L]₂, R1 (orange) from E = -0.7 V to -1.2 V vs Ag/AgCl and (c) the di-reduced intermediate [MnL]⁻, R2 (green) from E = -1.2 to -1.6 V vs Ag/AgCl.

At E_{OCP}, **COF_{bpyMn}|NT** showed well-resolved ν(CO) bands with frequencies at 2022, 1930, and 1912 cm⁻¹ (black spectrum in Figure V.2a). These ν(CO) correspond to a facially coordinated tricarbonyl metal complex and matched well those of **COF_{bpyMn}|NT** and other {*fac*-Mn(CO)₃S}, (S = Br, CH₃CN, H₂O) derivatives observed by ATR-FT-IR,^{36, 37} indicating that the loading of single-Mn centers within **COF_{bpyMn}** and on the nanostructured Au does not significantly influence the electronic properties of the Mn center (see Chapter IV for details).

Then, we studied the evolution of the **COF_{bpyMn}|NT** spectra versus the potential (Figure V.2). When the negative potential was stepwise increased from the E_{OCP} to -0.7 V, the ν(CO) of the **COF_{bpyMn}|NT** began to increase in intensity (Figure V.2a). In contrast, the width of the signals does not change substantially in the E_{OCP} to -0.7 V range. To explain these observations, we considered one of the SEIRA's fundamentals: the changes in the intensity of an IR absorption band (I) depend on the thickness and the number of molecules per area, also denoted as surface concentration C_{surf} (Equation V.1).⁵⁵⁻⁵⁷

$$I \propto C_{surf} \left| \vec{E} \cdot \frac{d\vec{\mu}}{dQ} \right|^2 = C_{surf} \cos^2\theta |\vec{E}|^2 \left| \frac{d\vec{\mu}}{dQ} \right|^2 \quad \text{Eq. V.1}$$

Where $\frac{d\vec{\mu}}{dQ}$ is the derivative of the dipole moment to the normal (Q), \vec{E} is the electric field exciting the molecules, and θ is the angle between $\frac{d\vec{\mu}}{dQ}$ and \vec{E} .^{40, 45, 58}

Therefore, the $\nu(\text{CO})$ bands growth of the **COF_{bpyMn}|NT** at potentials more negative than E_{OCP} , but lower than the first redox transformation, may be rationalized with an increase of the C_{surf} . This suggests a modification of the adsorbate coverage at the electrode interface induced by the external electric field. This effect is well-known and typically observed for polymers self-assembled monolayers.^{40, 48, 59, 60}

In our case, we propose that upon application of negative potentials, attractive electrostatic forces between the adsorbed layers ($E_{\text{OCP}} = +0.450$ mV) and the negatively charged electrode interface drag the **COF_{bpyMn}|NT** layers towards the Au electrode, increasing the effective surface concentration. Consequently, the SEIRA signal intensity increases (Figure V.2a). It is reasonable to consider that the **COF_{bpyMn}|NT** layers are cationic since the $\{\text{fac-Mn}^{\text{I}}(\text{CO})_3\text{Br}\}$ centers experience ligand exchange with the solvent to yield $\{\text{fac-Mn}^{\text{I}}(\text{CO})_3\text{L}\}^+$ and free Br^- ions in solution. Then, the positive charged Mn(I) centers, together with the large π -conjugated system of the **COF_{bpyMn}|NT** framework, may favor layer polarizations with the potential and the electrostatic adsorbate-substrate interactions.

Moreover, these electrostatic interactions may induce a collective movement of the **COF_{bpyMn}|NT** layers, with a potential reorganization of the layers. The **COF_{bpyMn}|NT** sheets could be gradually distorted as the potential increases, yielding a disordered stacking. Movements derived from the electric fields have been previously reported in polymers and conjugated systems.⁶¹⁻⁶⁵

Major spectral differences were observed at potentials more negative than -1.0 V. Upon this potential, the appearance of bands located at 1966, 1928, 1878, and 1851 cm^{-1} was accompanied by a decrease of bands at 2044, 2026, and 1938 cm^{-1} (R1 (orange line), Figure V.2b). These $\nu(\text{CO})$ bands are characteristic of a $[\text{Mn}^{\text{0}}\text{L}]_2$ dimer species.^{36, 66} In contrast, under identical conditions, the previous results of ATR-IR-SEC of **COF_{bpyMn}|NT** at similar potential range was clearly different (Figure IV.7 and 10, Chapter

IV), where a radical intermediate $[fac-Mn^I(CO_3)L^-(S)]^0$ was the only species detected at this potential range. In Chapter IV, the radical formation was attributed to the reticular material's mechanical constraint, which avoids the formation of the detrimental Mn^0-Mn^0 dimer typically found in molecular catalysts. The difference between the intermediates detected by ATR-SEC and SEIRA-SEC illustrates the dynamics of the COF system depending on the distance to the electrode. Indeed, the combination of the different probing capabilities of ATR-SEC and SEIRA-SEC resulted very powerfully.

While SEIRA experiments probe the COF at the electrode surface vicinity (≈ 10 nm), without contributions from the bulk, ATR-SEC experiments provide information on the COF-electrolyte interface ($\approx 1-2$ μm , for our setup), far away from the COF-electrode interface since the deposited **COF_{bpyMn}|NT** is about 4 μm thick. Unfortunately, attempts to perform ATR-SEC with thinner enough layers to probe the electrode interface were problematic due to sensitivity problems.

The SEIRA spectroscopic changes should be rationalized, considering that the detection happens at the closest layers on the nanostructure Au (COF-electrode interface). A potential reason for the Mn^0-Mn^0 formation could be the electrostatic interactions that produce enough dynamics to allow them. Indeed, between E_{OCP} to -0.7 V potentials, a restructuring of the COFs layers is already occurring close to the electrode. A subsequent section will discuss in more detail the dynamics that can contribute to forming Mn^0-Mn^0 bonds and their consequence for the overall framework.

Further changes occurred at more reducing potentials, SEIRA-SEC spectra revealed the formation of a new specie at potentials < -1.4 V. The bands at 2044, 2026, and 1938 cm^{-1} decreased with the concomitant increase of 1903 and 1802 cm^{-1} bands. These new $\nu(CO)$ bands are consistent with the formation of a formal Mn(-I) five-coordinate anionic species $[fac-Mn(CO)_3L]^-$ (R2 (green), Figure V.2c), analogous to the di-reduced species previously observed for **COF_{bpyMn}|NT** by ATR-IR-SEC (Figure IV.10, Chapter IV).

We further analyzed the SEIRA-SEC experiments by normalizing the intensity of the 2025 and 1879 cm^{-1} bands as the function of electrode

CHAPTER V Dynamic rearrangement of 2D-COF by electric field

potential (Figure V.3). The selected bands are diagnostic of the same redox species and showed the disappearance of the starting compound before redox transformations, concomitantly with the formation of the first reduced intermediate. Furthermore, the evolution of the bands yielded sigmoidal curves that could be fitted with the Nernst equation, affording matching midpoint potentials at -1.2 V for both redox transitions (see the Experimental Section for details).

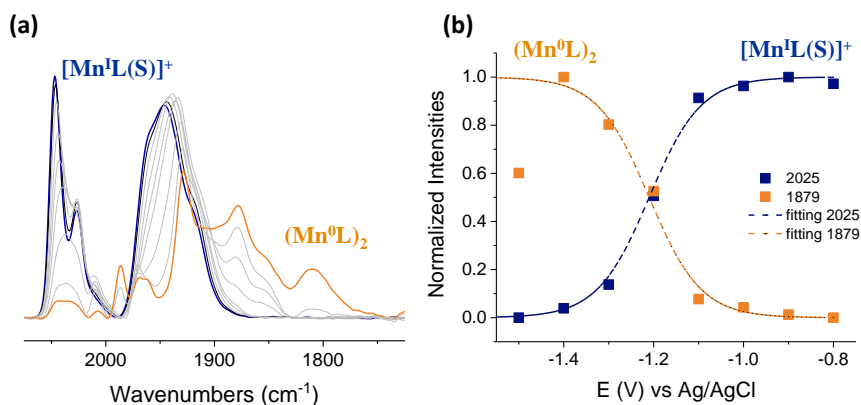


Figure V.3. (a) Potential-dependent SEIRA spectra of $\text{COF}_{\text{bpyMn}}|\text{NT}$ recorded on nanostructures Au in CH_3CN (0.2 M TBAPF_6) under N_2 from -0.7 V to -1.5 V vs. Ag/AgCl. $\nu(\text{CO})$ bands of R0 (blue) refer to $\text{COF}_{\text{bpyMn}}|\text{NT}$ before a redox transformation $[\text{Mn}^{\text{I}}\text{L}(\text{S})]^+$ and the bands located at 1987, 1966, 1928, 1878 and 1851 cm^{-1} increase at the expense of the pre-catalyst bands, after 1e^- reduction the dimer $[\text{Mn}^{\text{0}}\text{L}]_2$ (R2, orange) is formed. (b) Intensity of the bands at 2025 (blue squares) and 1879 cm^{-1} (orange squares) as a function of electrode potential. Lines correspond to a fit of the Nernst equation to the data set.

V.2.1.2. SEIRA-SEC of $\text{COF}_{\text{bpyMn}}|\text{NT}$ in water

To get further insights into the dynamic and reorganization of the $\text{COF}_{\text{bpyMn}}$ layers at the COF-electrode interface, we performed SEIRA-SEC in water (0.5 NaHCO_3) under N_2 (Figure V.4).

CHAPTER V

Dynamic rearrangement of 2D-COF by electric field

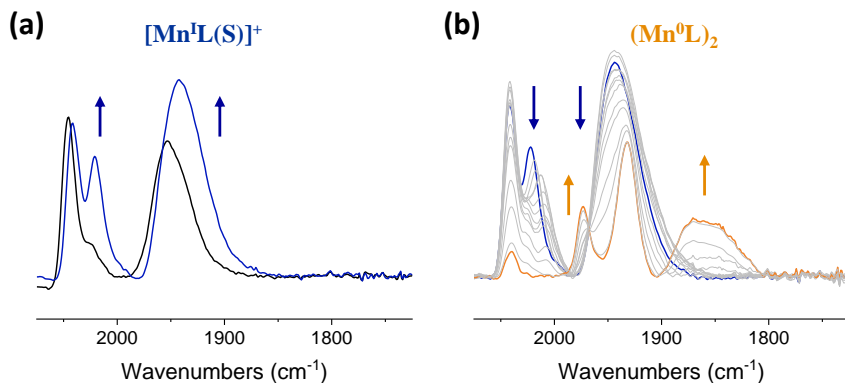


Figure V.4. Potential-dependent SEIRA spectra of **COF_{bpyMn}|NT** recorded on nanostructures Au in water (0.5 M NaHCO₃) under N₂, (a) $\nu(\text{CO})$ bands of R0 (blue) refers to **COF_{bpyMn}|NT** before a redox transformation $[\text{Mn}^{\text{I}}(\text{S})]^+$ from the E_{OCP} to $-0.7 \text{ V vs. Ag/AgCl}$ and (b) the bands located at 1987, 1966, 1928, 1878 and 1851 cm^{-1} increase at the expense of the pre-catalyst bands, after 1e- reduction the dimer $[\text{Mn}^{\text{0}}\text{L}]_2$ (R2, orange) is formed.

At E_{OCP} , **COF_{bpyMn}|NT** showed similar $\nu(\text{CO})$ bands than in CH₃CN with frequencies at 2045, 2024 and 1953 cm^{-1} (R0 (blue), Figure V.4a). A striking difference was observed in the IR vibration spectra of **COF_{bpyMn}|NT** in SEIRA when the negative potential was increased until -0.7 V , the growth of the intensity of the $\nu(\text{CO})$ stretching was lower in water than in CH₃CN. This difference in intensity change is consistent with the dielectric constant change between solvents (ϵ_{water} and $\epsilon_{\text{CH}_3\text{CN}}$) are 78.5 and 37.5, respectively). The higher dipole moment of water and their solvation properties shield the charges better; therefore, the electrostatic interactions are lower in water than in CH₃CN. The greater the degree of polarity of the solvent, the lower the level of preferred orientation and the electric-field effect on the **COF_{bpyMn}|NT** layers.

On the other hand, it is also important to consider the ionic strength of the electrolyte. The decay of the electrical potential is faster the greater the ionic strength. By increasing the ionic strength of the medium (because of the concentration of the electrolyte or the charges of the ions), the ionic layer that surrounds the electrode becomes more compact and better shields the electrical potential of the electrode. Therefore, the ionic strength of the medium determines whether the diffuse ionic layer that forms around the electrode is more or less compact and therefore more or less effective in

shielding the electrical potential. The greater the ionic strength, the greater the shielding of the potential. Based on this, the nature of the electrolyte (ionic strength and counterions involving the layers of the framework) also contributes to making the shielding of the electric field in water more efficient than in CH₃CN. This may result in a slight decrease in the level of preferred orientation and packing arrangement of the **COF_{bpyMn}|NT** layers with the electric field.

In addition, SEIRA-SEC spectra revealed the formation of a new species at the potential regime from -1.1 V to -1.4 V (R1 (orange), Figure V.4b). At these potentials, the $\nu(\text{CO})$ of the pre-catalyst start to decrease with the concomitant increase of a new intermediate with bands at 1973, 1931, 1870, 1847 cm⁻¹. These $\nu(\text{CO})$ are again consistent with the formation of the dimer intermediate [Mn⁰L]₂ (R1) (Figure V.4b), previously observed in the SEIRA-SEC spectra of **COF_{bpyMn}|NT** on Au in CH₃CN and other {*fac*-Mn(CO)₃S} (S = Br, CH₃CN, H₂O) derivatives.^{36, 67, 68}

The formation of the dimeric species [Mn⁰L]₂ (R1) detected in SEIRA-SEC on the Au (Figure V.4b) was again correlated with the reorganization of the **COF_{bpyMn}|NT** at potentials more negative than E_{OCP} and before the first redox process of **COF_{bpyMn}|NT**. The reorganization of the **COF_{bpyMn}|NT** layers at the electrode interface due to the effect of the electric field results in nearest neighbor {*fac*-Mn(CO)₃S} centers which consequently favor the formations of the dimer intermediate. In addition, no further changes were observed at potentials more reducing than -1.4 V as the anionic intermediate [MnL]⁻ (R2) is electrocatalytically active for H₂ evolution.³⁶

V.2.1.3. ATR-SEC of **COF_{bpyMn}|NT** in CH₃CN

In order to clarify and get further insights into the effect of the electric field on the nearest **COF_{bpyMn}|NT** layers on Au, we have also studied the $\nu(\text{CO})$ evolution by ATR-IR-SEC using the same SEC-cell as in SEIRA but without the surface enhancement effect of the IR absorption on nanostructure Au (Figure V.5, see SI for details, Configuration 2).

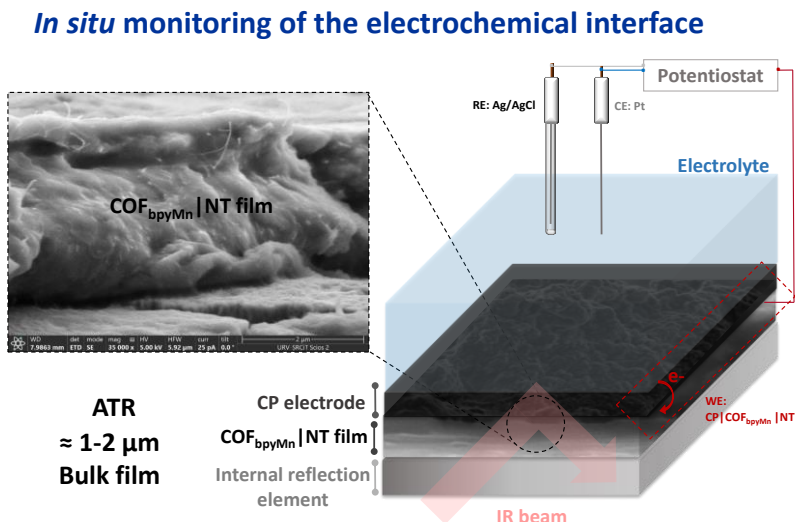


Figure V.5. Schematic representation of the ATR-SEC cell (Configuration 2) and the $\text{COF}_{\text{bpyMn}}|\text{NT}$ -electrode interface.

With this configuration, the detected intermediates are on the opposite side of the electric contact. Then, the IR detection will indicate the species generated in the bulk of the $\text{COF}_{\text{bpyMn}}$ film.

Unlike in SEIRA-SEC, in ATR-SEC (CH_3CN , 0.2 M TBAPF_6) the $\nu(\text{CO})$ bands growth of the pre-catalyst at -0.7 V was not observed (Figure V.6a). Alternatively, an increase of the bands at 2028 and 1937 cm^{-1} at potentials related with the first redox transformation of the $\text{COF}_{\text{bpyMn}}|\text{NT}$ suggest the formation of the $[\text{Mn}^{\text{I}}\text{L}^-(\text{S})]^0$ radical, previously reported by ATR-SEC in CH_3CN (See Chapter IV for details).³⁷

Then, applying a further negative potential to $\text{COF}_{\text{bpyMn}}|\text{NT}$ produced a second modification of the IR spectra at -1.6 V (R2). Bands at 2028 and 1937 cm^{-1} decrease with a concomitant increase of bands at 1915 and 1808 cm^{-1} . This is consistent with the formation of a formal Mn(-I) five-coordinate anion species, analogous to the previously characterized $[\text{Mn}(\text{bpy})(\text{CO})_3]^-$ complex⁶⁸ and the detected specie by SEIRA-SEC generated after the second reduction of $\text{COF}_{\text{bpyMn}}$.

CHAPTER V Dynamic rearrangement of 2D-COF by electric field

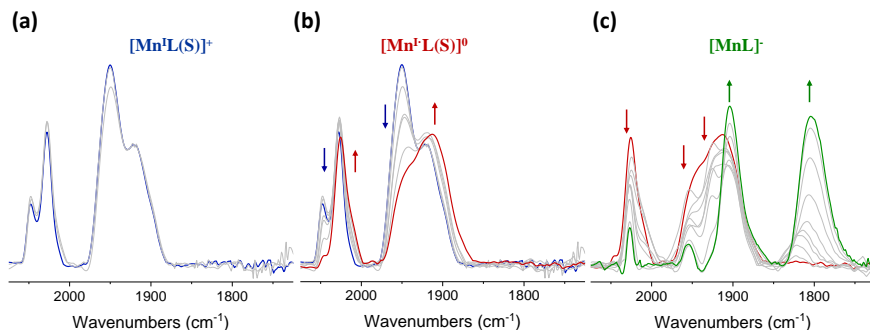


Figure V.6. Potential-dependent ATR spectra of $\text{COF}_{\text{bpyMn}}|\text{NT}$ in CH_3CN (0.2 M TBAPF_6) under N_2 from E_{OCP} to -1.6 V vs. Ag/AgCl . (a) R0 (blue) refers to $\text{COF}_{\text{bpyMn}}|\text{NT}$ before a redox transformation from E_{OCP} to -0.7 V vs Ag/AgCl , (b) after $1e^-$ reduction to form $[\text{Mn}^{\text{I}}\text{L}(\text{S})]^0$, R1 (red) from -0.7 V to -1.3 V vs Ag/AgCl and (c) the di-reduced intermediate, $[\text{MnL}]$, R2 (green) from -1.3 V to -1.6 V vs. Ag/AgCl

Figure V.7 shows the normalized intensity of the evolving bands as a function of the redox potential applied. The selected bands can be fitted to the Nernst equation and are diagnostic of the same redox event, showing the disappearance of the starting compound concomitantly with the formation of the reduced one.

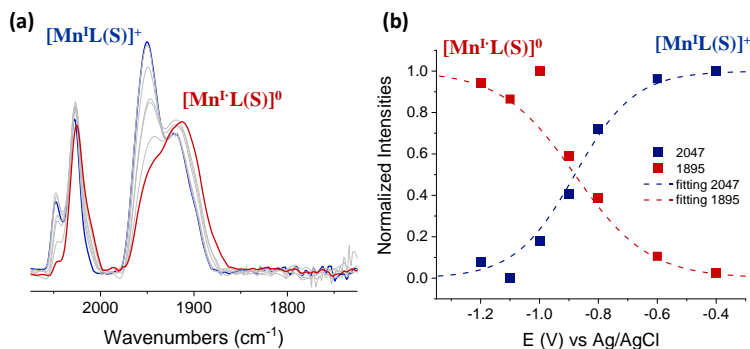


Figure V.7. (a) Potential-dependent ATR spectra of $\text{COF}_{\text{bpyMn}}|\text{NT}$ recorded in CH_3CN (0.2 M TBAPF_6) under N_2 between from -0.7 V to -1.3 V vs Ag/AgCl . $\nu(\text{CO})$ bands of R0 (blue) refer to $\text{COF}_{\text{bpyMn}}|\text{NT}$ before a redox transformation and the bands located at 2022 and 1895 cm^{-1} increase at the expense of the pre-catalyst bands, after $1e^-$ reduction the radical $[\text{Mn}^{\text{I}}\text{L}(\text{S})]^0$, R1 (red) is formed. (b) Intensity of the bands at 2047 (blue squares) and 1895 cm^{-1} (red squares) as a function of electrode potential. Lines correspond to a fit of the Nernst equation to the data set.

Monitoring the reoxidation of the formal Mn(-I) centers, the inverse evolution of the $\nu(\text{CO})$ bands was observed, from the di-reduced species to Mn(I), going through the monoreduced COF and regenerating the starting compound (Figure V.8).

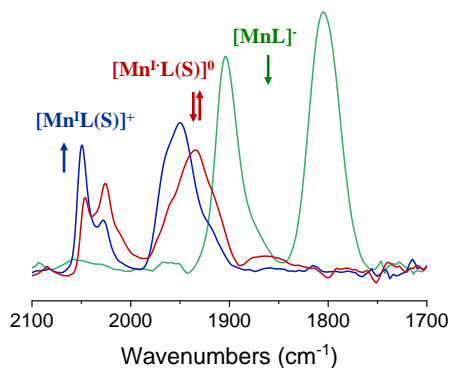


Figure V.8. ATR-IR spectra of the reoxidation of the $[\text{MnL}]^-$ centers at different potentials (*vs* Ag/AgCl), the first spectrum was recorded at -1.6 V (R2), the second at -0.8 V (R1, reoxidation of $[\text{MnL}]^-$) and the last one at 0.5 V (reversible $[\text{Mn}^{\text{I}}\text{L}^- (\text{S})]^0$, R0). All the experiments were performed in CH_3CN (0.2 M TBAPF_6) saturated with N_2 at room temperature.

Altogether, show for the first time the electric field-dependent molecular reorganization of a Mn-based reticular framework. The field-dependent attraction of the layers may induce the observed variations in the first electron-reduced species in function to the electrode distance. SEIRA-SEC has shown to be a sensitive tool for monitoring the stepwise structural transformation of $\text{COF}_{\text{bpyMn}}|\text{NT}$. The results involve the collective motions of the framework structures that decrease the distance between neighbor $\{\text{fac-Mn}(\text{CO})_3\}$ centers. This suggests the intriguing prospect of using electrochemistry in Covalent Organic Frameworks to tune surface interactions and drive surface transformations.

V.2.1.4. $\text{COF}_{\text{bpyMn}}|\text{NT}$ EPR-SEC Signature.

Electron Paramagnetic Resonance (EPR) is a highly sensitive, versatile, and specific technique that enables static and dynamic studies of materials, chemical samples, and biological systems.⁶⁹⁻⁷¹

In this sense, to give irrefutable evidence of the formation of the previously detected $[\text{Mn}^{\text{I}}\text{L}^-(\text{S})]^0$ radical intermediates within the COF matrix after the first e⁻ reduction, we performed *in situ* EPR-SEC studies.

The design of the EPR-SEC cell is shown in Figure V.9. It consists of a Pt counter electrode, an Ag wire as a pseudo-reference electrode, and in parallel, the working electrode is the $\text{COF}_{\text{bpyMn}}|\text{NT}$ ($[\text{Mn}]_{\text{total}} = 700 \text{ nmol}\cdot\text{cm}^{-2}$), deposited on Carbon Paper (CP) (see Experiment Section for details).

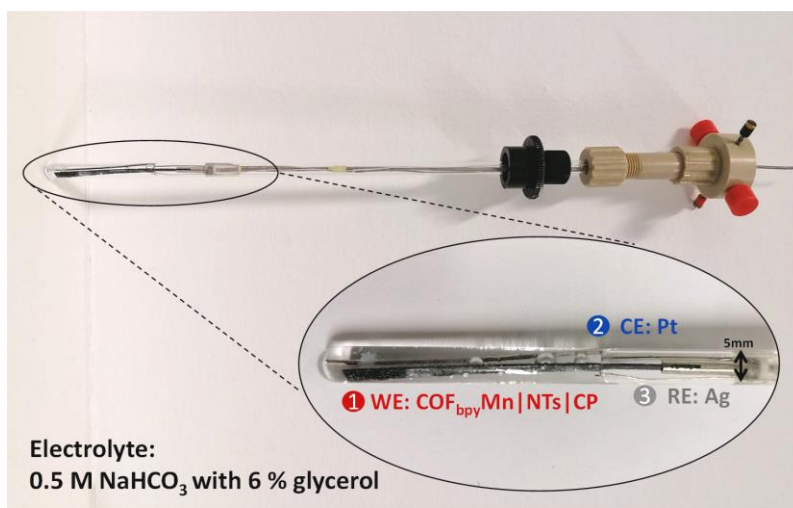


Figure V.9. EPR-SEC cell used in this study with a zoomed view of the electrodes. The cell was filled until the electrolyte reached the reference electrode. A Carbon Paper with the $\text{COF}_{\text{bpyMn}}|\text{NT}$ film was used as a working electrode (WE: $\text{COF}_{\text{bpyMn}}|\text{NT}$); Platinum as a counter electrode (CE: Pt) and Ag wire as pseudo-reference electrode (RE: Ag). The bubbles are formed during catalysis and correspond to H₂ evolution.

Before performing EPR-SEC, we recorded the EPR spectrum of $\text{COF}_{\text{bpyMn}}|\text{NT}$ ($[\text{Mn}]_{\text{total}} = 700 \text{ nmol}\cdot\text{cm}^{-2}$) deposited on CP inside the EPR-SEC cell in water (NaHCO₃, 6% glycerol) under Ar (Figure V.10a) and compare with the spectrum of dispersion of 5 mM $\text{COF}_{\text{bpyMn}}$ in NaHCO₃ (6% glycerol) in the EPR tube (Figure V.10b). The EPR signals in both cases are relatively similar, ensuring a high sensitivity for EPR detection using the EPR-cell.

CHAPTER V **Dynamic rearrangement of 2D-COF by electric field**

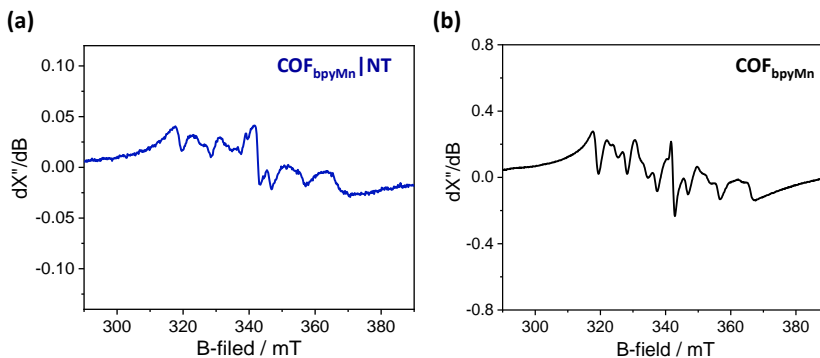


Figure V.10. Comparison of X-band CW EPR spectra of (a) the film-covered electrode $\text{COF}_{\text{bpyMn}}|\text{NT}$ (WE) in water (0.5 M NaHCO_3 , 6 % glycerol) in the EPR-SEC cell and (b) 5 mM $\text{COF}_{\text{bpyMn}}$ dispersion in water (0.5 M NaHCO_3 , 6 % glycerol) in the EPR tube.

Next, EPR-SEC of $\text{COF}_{\text{bpyMn}}|\text{NT}$ on CP was performed by a stepwise decrease of the potential from E_{OCP} to -1.1 V vs Ag in water (0.5 M NaHCO_3 , 6 % glycerol) under Ar.

At -0.6 V vs Ag , a narrow transition at $g = 2.006$ starts to increase in the EPR spectrum (Figure V.11a). When subjecting the $\text{COF}_{\text{bpyMn}}|\text{NT}$ film to electrolysis below the threshold of H_2 evolution ($E < -1.1 \text{ V vs Ag}$), the new EPR signal continues to grow with the increase in potentials. This observation confirmed that the first reduced intermediate in the $\text{COF}_{\text{bpyMn}}|\text{NT}$ is not EPR silence. Based on its spectral position and line shape, the signal was assigned to a low-spin Mn^{I} radical specie with octahedral geometry, which is consistent with the formation of the $[\text{Mn}^{\text{I}}\text{L}^{\cdot}(\text{S})]^0$ intermediate previously detected by ATR-SEC at the first electron reduction of $\text{COF}_{\text{bpyMn}}|\text{NT}$.

In addition, the derivate of the normalized intensity of the evolving transitions as a function of the applied redox potential (Figure V.11b) showed that for potentials in the range of -0.6 to -0.9 V vs Ag the EPR signal was dominated by the narrow $[\text{Mn}^{\text{I}}\text{L}^{\cdot}(\text{S})]^0$ transition, with a maximum of the evolution of the radical at -0.9 V vs Ag and an apparent midpoint potential at -0.7 V vs Ag (Figure V.11b). Interestingly, the application of more reductive potentials was accompanied by subtle changes in the position and shape of the $[\text{Mn}^{\text{I}}\text{L}^{\cdot}(\text{S})]^0$, indicating possible changes in the surroundings for a part of the Mn^{I} population.

CHAPTER V Dynamic rearrangement of 2D-COF by electric field

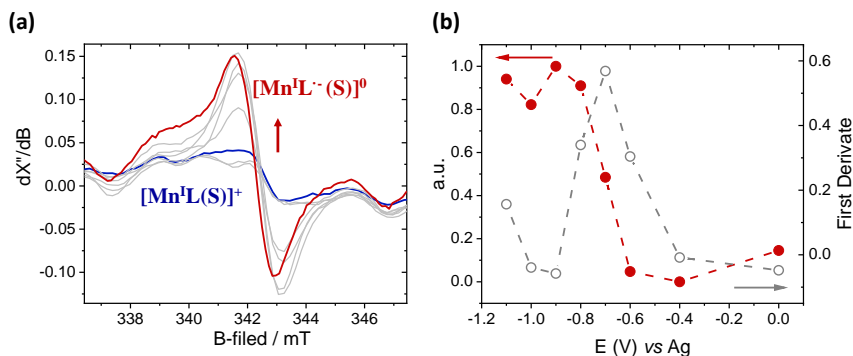


Figure V.11. (a) X-band CW EPR spectra of **COF_{bpyMn}|NT** on Carbon Paper electrode electrolyzed at increasing potentials from E_{OCP} (blue, $[Mn^I(L(S))^+]$) to -1.1 V vs Ag to form the $[Mn^I(L^-(S))^0]$ intermediate (red); $P_{MW} = 63$ mW, $T = 10$ K. (c) Increase of the intensity of the $[Mn^I(L^-(S))^0]$ radical signal as a function of the applied potential (red) and the first derivate correlation (gray). The measured was recorded in water (0.5 M $NaHCO_3$, 6% glycerol) under Ar with $T = 10$ K in the EPR-SEC cell.

Obtaining a higher $[Mn^I(L^-(S))^0]$ EPR intensity was limited by the physical deterioration of the catalyst film at reductive potentials higher than ≈ -1.1 V vs Ag, presumably due to excessive release of H_2 -bubbles forming on the surface of the electrode, leading to the fall of the film.

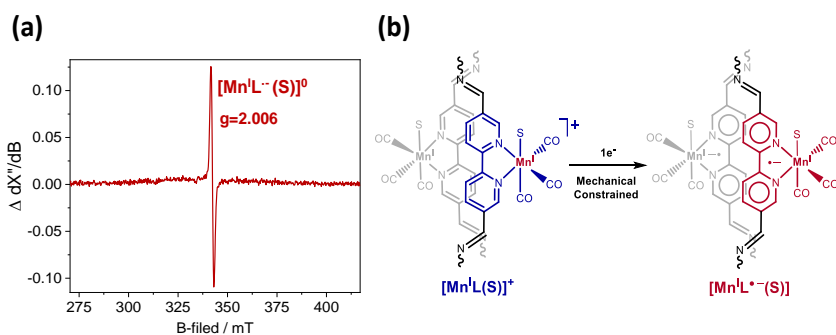


Figure V.12. (a) Differential X-band CW EPR spectra of **COF_{bpyMn}|NT** catalyst at -0.9 V and -0.6 V vs Ag in water (0.5 M $NaHCO_3$, 6% glycerol) under Ar with $T = 10$ K. (b) Proposed catalytic intermediate after the first electron reduction for **COF_{bpyMn}|NT** based on spectroelectrochemical evidence and computational models.³⁷

Isolation of the $[\text{Mn}^{\text{II}}\text{L}^{\cdot\cdot}(\text{S})]^0$ EPR line was achieved by scaled subtraction of the $\text{COF}_{\text{bpyMn}}|\text{NT}$ spectral feature before radical formation (Figure V.12a).

The reversibility of the process was also confirmed with the measurement of $\text{COF}_{\text{bpyMn}}|\text{NT}$ spectrum ($[\text{Mn}]_{\text{total}} = 700 \text{ nmol}\cdot\text{cm}^{-2}$) after the reoxidation of the generated intermediate at 0 V *vs* Ag in the EPR-SEC cell (Figure V.13).

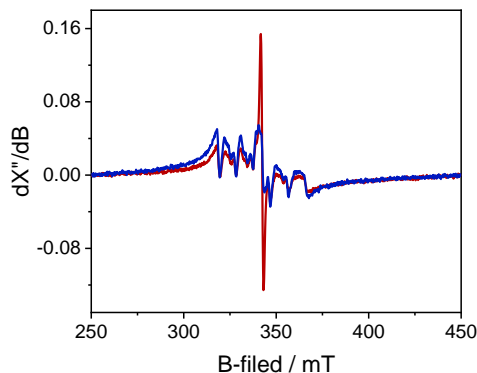


Figure V.13. X-band CW EPR spectra of the modified working CP electrode with $\text{COF}_{\text{bpyMn}}|\text{NT}$ ($[\text{Mn}]_{\text{total}} = 700 \text{ nmol}\cdot\text{cm}^{-2}$) after control potential electrolysis at -1 V *vs* Ag (red) and after reoxidation at 0 V *vs* Ag (blue). The blue spectrum shows the reversibility of the redox transformation under Ar in water (0.5 M NaHCO_3 , 6 % glycerol) in the EPR-SEC cell, $P_{\text{MW}} = 63 \text{ mW}$, $T = 10 \text{ K}$. X-band CW.

In contrast, under identical conditions, the EPR-SEC spectrum of $\text{COF}_{\text{bpy}}|\text{NT}$ and NT (Figure V.14) showed no evidence of radical formation with potential. These results support that the evolution of the observed transitions for $\text{COF}_{\text{bpyMn}}|\text{NT}$ after the first reduction is associated with the Mn centers.

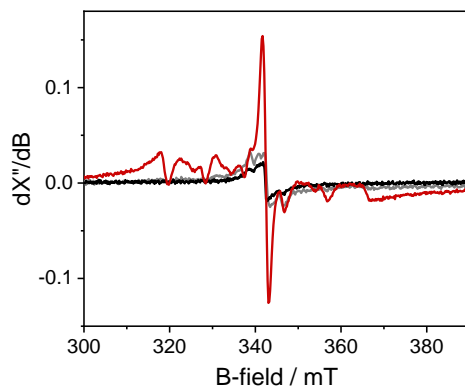


Figure V.14. X-band CW EPR spectra of the modified CP working electrode with **COF_{bpyMn}|NT** ($[\text{Mn}]_{\text{total}} = 700 \text{ nmol} \cdot \text{cm}^{-2}$) (red), **COF_{bpy}|NT** (gray) and **NT** (black) after control potential electrolysis at -1 V vs Ag in water (0.5 M NaHCO_3 , 6 % glycerol) in the EPR-SEC cell under Ar, $P_{\text{MW}} = 63 \text{ mW}$, $T = 10 \text{ K}$.

Temperature dependence of the EPR signal

Figure V.15 shows the EPR spectra of the **COF_{bpyMn}|NT** film at different temperatures. At 10 K, the EPR spectrum is better resolved with enhanced signal intensity due to the redistribution of electrons at the energy levels. In contrast, a broadening of the Mn spectrum was observed upon heating from 10 K to 30 K and 60 K, respectively. The signal of the radical $[\text{Mn}^{\text{I}}\text{L}^{\cdot}(\text{S})]^0$ at $g \sim 2.006$ starts to decrease in intensity as the temperature increases. The weak integral intensity dependence on temperature could be originated from delocalized conduction electrons within the framework. In **COF_{bpyMn}**, the organic framework's electronic effect strongly delocalizes the extra electron significantly more than the bare bipyridyl ligand, reducing the electron density over the metal center. In consequence, the one-electron reduction is more delocalized on the reticular framework.

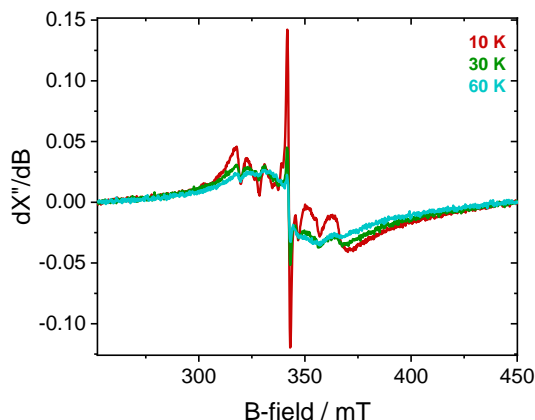


Figure V.15. (a) X-band CW EPR spectra of $\text{COF}_{\text{bpyMn}}|\text{NT}$ modified working Carbon Paper electrode electrolyzed at -1.1 V vs Ag ; $P_{\text{MW}} = 63 \text{ mW}$. Intensity of the radical $[\text{Mn}^{\text{I}}\text{L}^{\cdot-}(\text{S})]^0$ as a function of the T from 10 K (red), 30 K (green) and 60 K (blue). The measurements were recorded in water (0.5 M NaHCO_3 , 6% glycerol) under Ar in the EPR-SEC cell.

The EPR-SEC gave irrefutable evidence of forming a paramagnetic intermediate after the first electron reduction of $\text{COF}_{\text{bpyMn}}$. The spectra showed a signal with a partially resolved transition at $g = 2.006$, which we attributed to the formation of the $[\text{Mn}^{\text{I}}\text{L}^{\cdot-}(\text{S})]^0$. We propose that the radical detected is dominated by ligand localized events due to the extensive delocalization of the electrons in the framework, which is also consistent with our previous observations by ATR-SEC.

V.2.1.5. UV-vis-SEC.

We have performed UV-vis-SEC studies to give confidence to the assignment of the intermediates observed during the reduction of $\text{COF}_{\text{bpyMn}}$ at different distances from the current collector.

UV-vis-SEC was carried out using $\text{COF}_{\text{bpyMn}}$ deposited on a transparent FTO glass substrate ($\text{COF}_{\text{bpyMn}}|\text{FTO}$, see the Experimental Section for details). The experiments were performed in transmittance mode in CH_3CN (0.1 M TBAPF_6) and water (0.5 M NaHCO_3), respectively.

UV-vis spectra recorded in CH_3CN during polarization of the working electrode, from E_{OCP} to $-1.55 \text{ V vs Fc}^+/\text{Fc}$, show the progressive growth of new intense absorption bands with maxima at 654 and 730 nm at $-1.55 \text{ V vs Fc}^+/\text{Fc}$ (Figure V.16). These bands are in good agreement with those

previously reported for the electro-^{36, 67, 72, 73} and photo-⁷⁴ generated parent dimer $[\text{Mn}^0\text{L}]_2$ species (Figure V.18b). However, the increase of bands at 314, 562 and 880 was also observed at -1.55 V vs Fc^+/Fc . We propose these bands are a contribution of the radical ligand-localized transient species $[\text{Mn}^{\text{I}}\text{L}^{\cdot-}(\text{S})]^0$, which, to the best of our knowledge, there are no examples of the detection of this intermediate by UV-vis-SEC. So then, the UV-vis spectra suggest that after the first reduction process, we probably have the formation of two different intermediates, the $[\text{Mn}^0\text{L}]_2$ and the $[\text{Mn}^{\text{I}}\text{L}^{\cdot-}(\text{S})]^0$.

Stepwise measurements 50 mV intervals across the first reduction show the increase in the UV-vis of the bands at 654, 730 and a broad band at 1000 nm. The small differences in the shape of the UV-vis spectra as the potential changes suggest that the stepwise formation of multiple products can occur upon reduction between -1.4 and -1.85 V vs Fc^+/Fc . The presence of these intense bands and the shoulder could be attributed to the formation of the five-coordinate anion $[\text{MnL}]^-$, with spectral combinations from residual dimer $[\text{Mn}^0\text{L}]_2$ and/or $[\text{Mn}^{\text{I}}\text{L}^{\cdot-}(\text{S})]^0$ radical intermediate (Figure V.16). This may result of the two sequential one-electron reductions that are closely spaced and not well resolved in this experiment.

The UV-vis-SEC spectra of the equivalent $\text{Mn}(\text{bpy})(\text{CO})_3\text{Br}$ (Figure V.18b) also show the formation of the dimer $[\text{Mn}^0\text{L}]_2$ and the anionic $[\text{MnL}]^-$ intermediates after the first and second reduction, respectively.²⁶

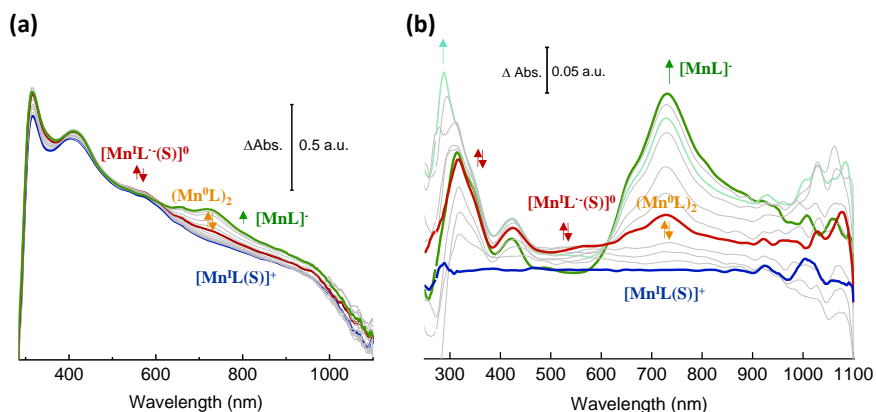


Figure V.16. UV-vis potential dependent spectra of $\text{COF}_{\text{bpyMn}}|\text{FTO}$. (a) Absolute and (b) differential UV-vis spectra of the reduction of the $\text{COF}_{\text{bpyMn}}|\text{FTO}$ at different potentials ($R_0 = \text{OCP}$, $R_1 = -1.55 \text{ V}$, $R_2 = -1.85 \text{ V vs Fc}^+/\text{Fc}$). Proposed intermediates of $\text{COF}_{\text{bpyMn}}$ at R_1 : $[\text{Mn}^{\text{I}}\text{L}^-(\text{S})]^0$ and $(\text{Mn}^0\text{L})_2$ and R_2 : $[\text{MnL}]^-$. All the experiments were performed in 0.2 M TBAPF₆/CH₃CN saturated with Ar at room temperature. The blue curve is the starting $\text{COF}_{\text{bpyMn}}|\text{FTO}$ (R_0 , $[\text{Mn}^{\text{I}}\text{L}(\text{S})]^+$). The reference spectra were recorded at the open circuit potential (R_0).

To get more insights into the intermediates generated after the reduction of the $\text{COF}_{\text{bpyMn}}$, we have also studied the UV-vis-SEC in water (0.5 M NaHCO₃) under Ar. Unlike in an aprotic electrolyte, the SEC experiments in an aqueous electrolyte are more challenging due to the H₂ evolution. However, we have been able to study the first reduction of $\text{COF}_{\text{bpyMn}}|\text{FTO}$ in pure water. The UV-vis spectra showed new positive bands when the potential was stepwise decreased from 0 to -1.25 V vs SCE, indicating the formation of new species with bands at 355, 430, 579, 657, 737 and 730 nm (Figure V.17). The growth of these bands suggests the formation of an analogous intermediate to that found in CH₃CN at potentials of the first reduction of $\text{COF}_{\text{bpyMn}}$. Therefore, we assign the first reduction to the formation of two species, previously assigned to a combination of the dimer $(\text{Mn}^0\text{L})_2$ and the $[\text{Mn}^{\text{I}}\text{L}^-(\text{S})]^0$ intermediates. No further changes were observed at potentials more reducing than -1.25 V vs SCE. The detection of the 2e-reduced five-coordinate Mn anion (considered the active species for HER and CO₂RR) is prevented by its fast reactivity with protons in an aqueous environment, leading to H₂ evolution *via* the formation of a short-lived Mn-H intermediate.⁷⁵

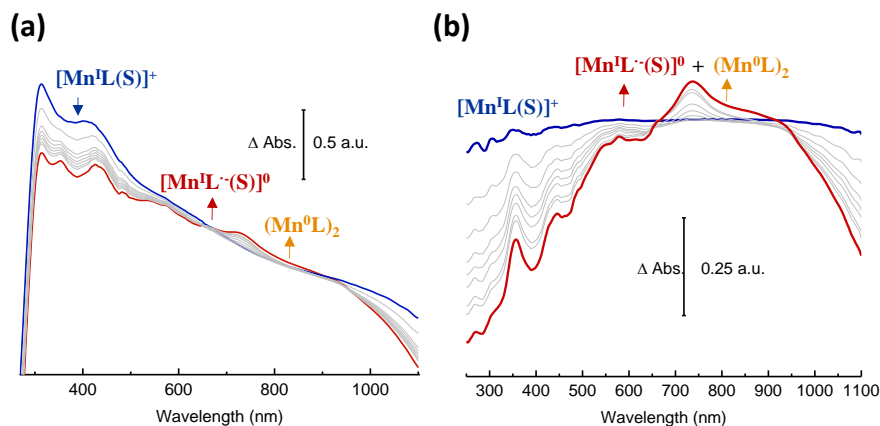


Figure V.17. UV-vis potential dependent spectra of $\text{COF}_{\text{bpyMn}}|\text{FTO}$. (a) Absolute and (b) differential UV-vis spectra of the reduction of the $\text{COF}_{\text{bpyMn}}|\text{FTO}$ at different potentials ($R_0 = \text{OCP}$, $R_1 = -1.25 \text{ V vs SCE}$). Proposed intermediates of $\text{COF}_{\text{bpyMn}}$ at R_1 : $[\text{Mn}^{\text{I}}\text{L}^{\cdot-}(\text{S})]^0$. All the experiments were performed in 0.5 M NaHCO_3 saturated with Ar at room temperature. The blue curve is the starting $\text{COF}_{\text{bpyMn}}|\text{FTO}$ (R_0 , $[\text{Mn}^{\text{I}}\text{L}(\text{S})]^+$). The reference spectra were recorded at the open circuit potential (R_0).

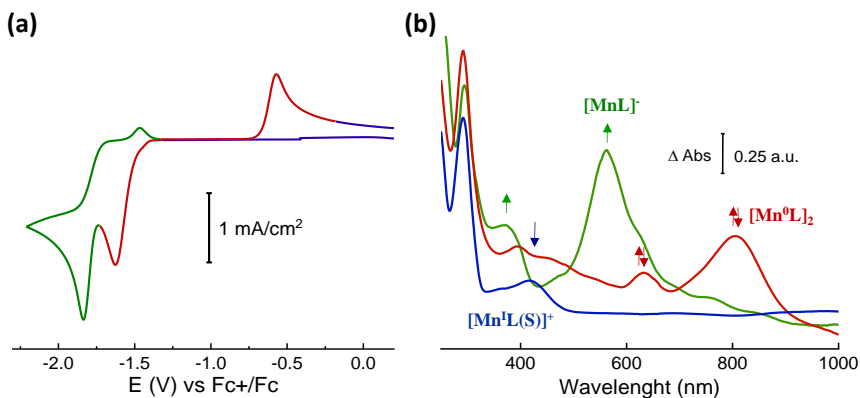


Figure V.18. (a) Cyclic voltammogram of $\text{Mn}(\text{bpy})(\text{CO})_3\text{Br}$ ($\sim 5 \text{ mM}$) at scan rate of $100 \text{ mV} \cdot \text{s}^{-1}$ (b) UV-vis-SEC changes observed during reduction at -1.70 V (red line) ($R_1 = [\text{Mn}^0\text{L}]_2$) and -2.10 V (green line) ($R_2 = [\text{MnL}]^-$) vs Fc^+/Fc of $\text{Mn}(\text{bpy})(\text{CO})_3\text{Br}$ ($\sim 5 \text{ mM}$) in $0.2 \text{ M TBAPF}_6/\text{CH}_3\text{CN}$ under Ar. The blue curve is the starting complex at the open circuit potential (R_0).

The comparison of the UV-vis-SEC spectra of $\text{COF}_{\text{bpyMn}}$ (Figure V.16) and $\text{Mn}(\text{bpy})(\text{CO})_3\text{Br}$ (Figure V.18) shows apparent differences in the intermediated generated upon the polarization of the electrode. Based on these observations, we hypothesized that after the first electron reduction

CHAPTER V Dynamic rearrangement of 2D-COF by electric field

of **COF_{bpyMn}** we have a mixture of two different intermediates, the dimer and the radical species. These observations agree with the previous intermediates detected by SEIRA-SEC, EPR-SEC and ATR-SEC, where the intermediates generated are dependent on the distance of the working electrode as an effect of the electric field in the first nm of the COFs layers. In the bulk of the film, we have the formation of the radical intermediate, while at the COF-electrode interface a dimeric intermediate is generated.

Table V. 1. Redox potentials and UV-Vis data of manganese carbonyl catalyts.

Catalyts	Proposed intermediated	E (V)	λ (nm)
COF_{bpyMn}FTO^a	[Mn ^I L(S)]	OCP	317, 408, 538, 576, 607
COF_{bpyMn}FTO^a	[Mn ^I L ⁻ (S)] ⁰ + [Mn ⁰ L] ₂	-1.55	314, 424, 562, 654, 730, 880 (sh)
COF_{bpyMn}FTO^a	[MnL] ⁻	-1.85	424, 654, 730, 1000
COF_{bpyMn}FTO^b	[Mn ^I L(S)] ⁰ + [Mn ⁰ L] ₂	-1.25	355, 430, 579, 657, 737, 878 (sh)
Mn(bpy)(CO)₃Br^{ad}	[Mn ^I L(S)]	OCP	292, 361, 417
Mn(bpy)(CO)₃Br^{ad}	[Mn ⁰ L] ₂	-1.70	394, 454, 632, 805
Mn(bpy)(CO)₃Br^{ad}	[MnL] ⁻	-2.10	370, 562, 626 (sh)

^a Performed in CH₃CN (0.2 M TBAPF₆) under Ar, E (V) vs Fc⁺/Fc. ^b Performed in water (0.5 M NaHCO₃) under Ar, E (V) vs SCE.

V.2.1.6. Dynamic rearrangement of **COF_{bpyMn}** with the electric field

By combining advanced *in situ* / *in operando* spectroelectrochemical techniques, we have obtained information on the dynamic rearrangement of **COF_{bpyMn}** triggered by the electric field.

Interestingly, different intermediates were detected depending on where the redox potential was applied, indicating a dependence of the generated intermediates with the distance to the working electrode (Figure V.19). After the first e⁻ reduction of **COF_{bpyMn}**, a [Mn^IL⁻(S)]⁰ radical species was observed in the material at the bulk and at the liquid-COF junction interface. In contrast, a dimeric [Mn⁰L]₂ intermediate was detected at the COF-electrode interface. Therefore, the *in situ* SEC techniques suggest that while the intralayer organization within **COF_{bpyMn}** bulk can still be described reasonably well by an eclipsed structure model after the first electron reduction to form the [Mn^IL⁻(S)]⁰ radical species, a lost in the layer stacking with a reorganization of the framework is induced over short

and intermediate distances to the working electrode, favoring the formation of the $[\text{Mn}^0\text{L}]_2$ intermediate (Figure V.19a, b).

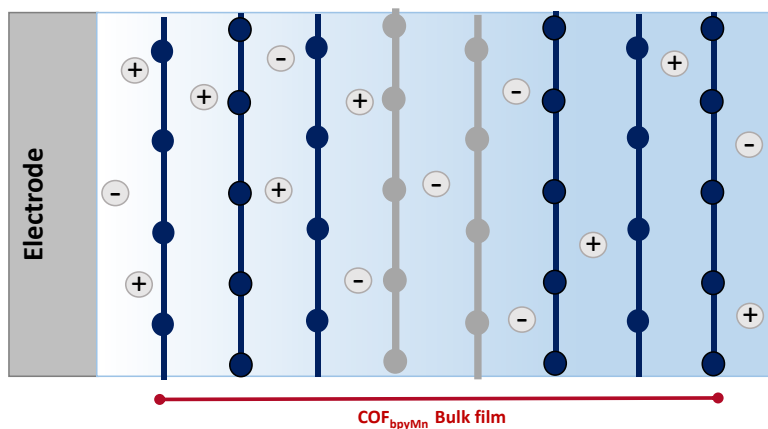
This phenomenon can be explained from a structural perspective. At E_{OCP} , the structure of $\text{COF}_{\text{bpyMn}}$ is well described by an eclipsed π - π stacking motif of the 2D layers with periodic order in all three dimensions and with the nitrogen atoms of bipyridines of consecutive stacked layers in alternated directions (Figure V.19a, c). These key features help to explain the radical formation in the bulk of the $\text{COF}_{\text{bpyMn}}$ and the absence of dimers upon the first reduction (see Chapter IV for details). Furthermore, by DFT calculations, the formation of a dimeric intermediate is uphill in energy by 0.62 eV. Such endothermicity comes from the unique environment of the $\text{COF}_{\text{bpyMn}}$, which leads to destabilization of the formation of dimeric species upon the first reduction (see Chapter IV for details). Based on the above observations, it can be concluded that the electric field generated at the COF-electrode interface is essential in determining structural changes within $\text{COF}_{\text{bpyMn}}$.

Under the influence of the electric field, attractive electrostatic forces between the adsorbed layers ($E_{\text{OCP}} = +0.450$ mV) and the negatively charged electrode interface drag the $\text{COF}_{\text{bpyMn}}|\text{NT}$ layers towards the Au electrode (Figure V.19b). This external stress over short and intermediate-range distances may simultaneously generate partial deformations within $\text{COF}_{\text{bpyMn}}$. The electric field can weaken the interactions between adjacent COF layers (van der Waals interactions), leading to instability in the COF stacking structure. Eventually, these perturbation may favor relatively unregulated mobility of COF layers in a random arrangement where the subnets can drift, relocate, or shift concerning each other, undermining its crystallinity and probably forming amorphous structures (Figure V.20).

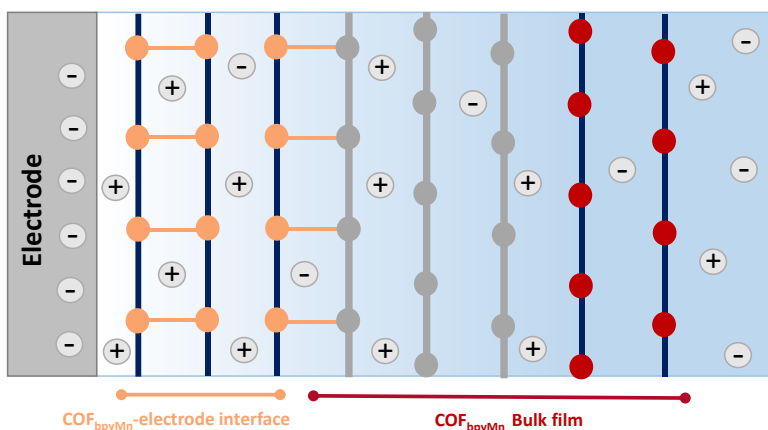
CHAPTER V

Dynamic rearrangement of 2D-COF by electric field

(a) Open circuit potential



(b) Reductive potential



(c) Dynamic rearrangement

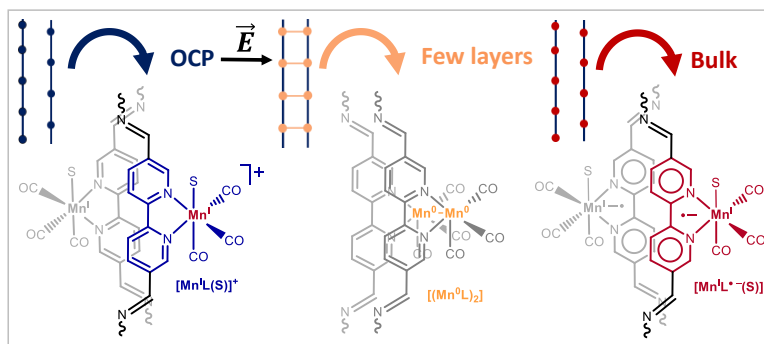


Figure V.19. Cartoon models for the possible intermediates of COF_{bpyMn} that may be generated after the first reduction within the COF. The relative placement concerning the working electrode leads to distinct intermediates generated in the mechanism.

All of these results suggest that the stronger electric field located at the COF-electrode interface could help to dynamically restructure by an expansion and translocation mechanism the layers of the 2D material. This dynamic motion of **COF_{bpyMn}** is a phenomenon restricted to COF-electrode interface. It can give rise to a drastic conformational change, probably modifying the pore environment and interlayer distances within the COF at the interface level and, accordingly, the generated intermediates upon the first electron reduction (Figure V.19b).

Equally important is the spatial arrangement of the bipyridine linkers within **COF_{bpyMn}**. Additional to the layer's mobility triggered by the electric field, the bpy units stacked in the π -columns of **COF_{bpyMn}** are also responsive to the electric field. Then, the formation of dimeric species at the interface level probably is also influenced by the spatial alignment of the bpy linkers. Although the spatial alignment of the linker can change by turning around the rotational axis, this rotational linker movement could induce interlayer contractions and conformational changes of the π -columns, triggering structural transformations of the layers and the pore environment.

Different scenarios can trigger the structural modification of **COF_{bpyMn}** under an electric field to favor the dimeric formation. We propose candidate structures that could explain experimental data by gradually tuning the relative position of adjacent COF layers and the spatial arrangement of the bipyridine linkers (Figure V.20). For example, under the effect of the electric field, the **COF_{bpyMn}** could suffer significant interlayer shifting, such that their stacking structures change from the AA mode at E_{OCP} to the mode close to the AB stacking. In consequence, after the interlayer shifting and the rotation of the bpy linkers, the distance between neighboring $\{Mn(bpy)(CO)_3S\}$ units could be reduced, favoring the dimer formation after the first electron reduction (Figure V.20).

In addition, the interlayers of the stressed COFs could also shift in different directions. For example, the adjacent layers of the **COF_{bpyMn}** could shift along the X direction over the next open pore (Figure V.20, scenario 1), while they can also shift along the Y direction, maintaining the AA-stacking mode. Besides, other stacking modes may be present in the COFs

due to the nonuniform reorganization of the layers (Figure V.20, scenario 2, 3). Eventually, the coexistence of different stacking styles could also bring disorder into the stressed COF crystal phase, decreasing the crystallinity and stacked disposition of the layers. The above reasoning implies that **COF_{bpyMn}** structure at the interface level may not be the contribution of the COF with a single stacking style but instead may contain the information on that COF with different stacking modes under the presence of the electric field.⁷⁶ It is highly possible that the reorganization of **COF_{bpyMn}** could also be a result of more complex slip-stacking transitions and/or distortions between the layers. For example, it may also be considered the formation of dimeric intermediates between one of the {Mn(bpy)(CO)₃S} of one pore with the stacked {Mn(bpy)(CO)₃S} unit of the consecutive layer (Figure V.20, scenario 4). In this case, a partial contraction of the distance between the Mn centers may occur under the presence of the electric field. While the distance between the rest of the framework is maintained, the staking mode between the two layers can be disrupted due to the interlayer distortion.

Likely, this interlayer reorganization phenomenon could also be observed in other 2D COFs. But, on the other hand, enormous new potential applications could be developed based on this electric field responsive structural flexibility.

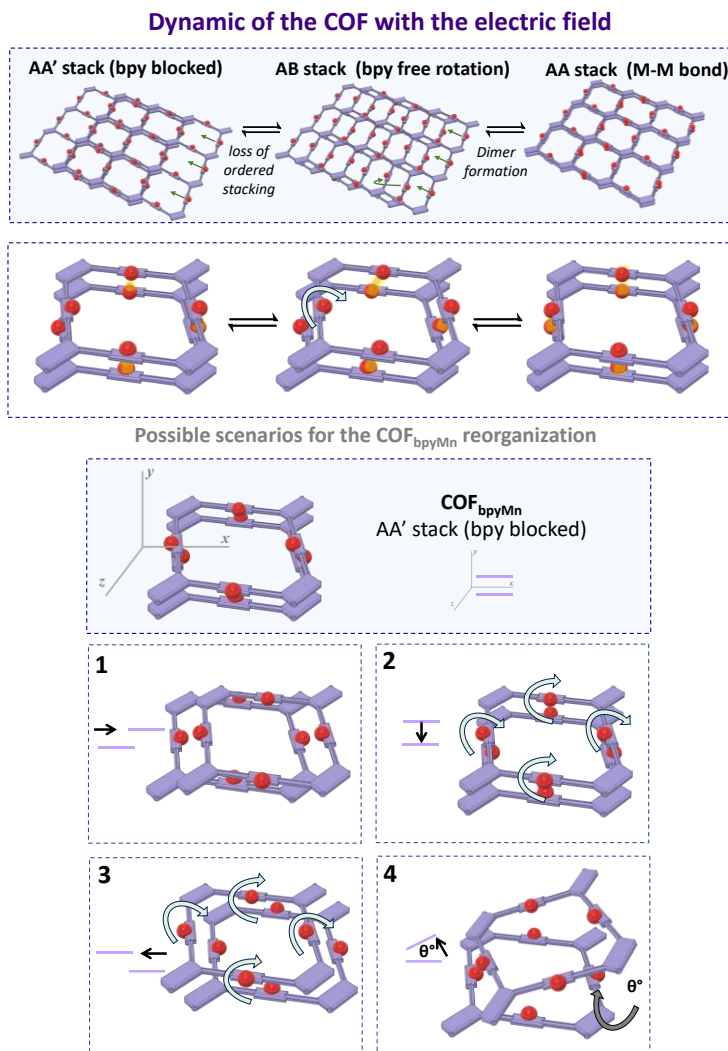


Figure V.20. COFs simulated structures showing possible interlayer transitions and reorganizations triggered by the electric field. The $\text{COF}_{\text{bpyMn}}$ structure at the interface level may not be the contribution of the COF with a single stacking style but instead may contain different stacking modes under the presence of the electric field.

V.3. Conclusions

In this chapter, the dynamic response of **COF_{bpyMn}** triggered by the electric field has been comprehensively proven by *in situ* / *in operando* spectroelectrochemical techniques.

After the first e⁻ reduction, the electric field induces structural transformations within **COF_{bpyMn}**, resulting in profound changes in the electrocatalytic mechanism. A $[\text{Mn}^{\text{I}}\text{L}^{\cdot\cdot}(\text{S})]^0$ radical is the main intermediated generated within **COF_{bpyMn}**, while a $[\text{Mn}^0\text{L}]_2$ species is generated over short and intermediate distances to the working electrode. This modification of the generated intermediates after the first reduction results from the weakness of the interlayer interactions induced by the electric field. The external stimulus disrupts the interlayer positional order and induces a dynamic interlayer reorganization within the **COF_{bpyMn}**.

Our results demonstrate the first example of electric field structurally dynamic COFs for CO₂ reduction. Since there is no precedent for such an experimentally characterized key dynamic flexibility of COFs, our work is a step forward in defining and understanding these catalysts' switching processes under electrocatalytic conditions.

Despite such progress, further studies are required to elucidate the exact mechanism of this unique structural flexibility in the **COF_{bpyMn}**.

V.4. Experimental section

V.4.1. Materials and reagents

All chemicals used in this study were purchased from commercial sources and used as received, without further purification. Solvents were purchased from SDS and Scharlab. Water (18.2 M Ω ·cm) was purified with a Milli-Q Millipore Gradient AIS system. NaHCO₃ (99.999% trace metals basis), TBAPF₆ (electrochemical grade), MWCNTs, and Nafion (5 % in water) were purchased from Sigma-Aldrich®.

V.4.2. Physical methods and experimental procedures.

V.4.2.1. Spectroelectrochemistry

V.4.2.1.1. SEIRA-SEC

Gold film deposits on silicon.

The reflecting plane of the prism (on which gold is deposited) was polished for one minute with successively finer grade alumina slurries down to 0.03 μ m. Then, after carefully rinsing milli-Q water, the prism was immersed in 40% NH₄F solution for two minutes. After removing the oxide layer on the Si surface, the prism was cleaned, dried and deposited in a water bath at 60 °C, leaving the reflecting plane in the air. Once the prism was at 60 °C and the surface was completely dry, a drop of 200 μ L of the plating solution: 0.015 M NaAuCl₄, 2H₂O + 0.15 M Na₂SO₃ + 0.05 M Na₂S₂O₃ \rightarrow 5H₂O + 0.05 M NH₄Cl mixed with 2% HF (2:1 in volume) was deposited on the surface. The reaction on the surface was stopped by adding water one minute after. In order to modify the surface of the gold, 20 μ L of a catalytic ink of COF_{bpyMn}|NT (cat : NT: CH₃CN: Nafion, 1 mg : 1 mg : 100 μ L : 100 μ L) was dropped on the surface and was dried under dark and N₂ atmosphere.

Electrochemical measurements.

The electrochemical measurements were run in three-electrode glass cells. A Ag/AgCl electrode and a Pt wire were used as reference and counter electrode, respectively. All the measurements were performed using an Autolab PGSTAT30 potentiostat/galvanostat, a μ -Autolab III

electrochemical analyzer controlled by GPES 4.9 software (Eco Chemie), or a VersaStat 4-400 potentiostat (Princeton Applied Research). The experiments were performed inside an anaerobic chamber (MBraun Unilab) filled with N₂. Different types of electrochemical measurements were carried out to obtain the different types of information needed in each experiment:

SEIRA was performed with a Kretschmann-ATR configuration under an angle of incidence of 60 °. All spectra were recorded in a spectral window of 2100 to 1700 cm⁻¹ and with a resolution of 4 cm⁻¹ using a Bruker 27 or a Bruker IFS66v/s spectrometer with a photoconductive MCT detector. For each spectrum, 150 scans were accumulated.

The spectroelectrochemical measurements were performed using a trapezium-shaped silicon ATR-IR element (W × L × H: 20 × 25 × 10 mm³) covered with a nanostructured SEIRA Au film formed by electroless deposition (described before). This prism was located in the SEIRA cell, as shown in Figure V.21.

Two different strategies were followed to achieve SEC characterization of the COF_{bpyMn}:

1. Configuration 1: To achieve supported COF_{bpyMn} on the electrode (Figure V. 21), 50 μL of ink with a catalyst dispersion was deposited over gold and let dry in the dark at room temperature.

2. Configuration 2: A different strategy was developed to deposit the catalyst on gold. The immobilization was carried out by depositing the catalyst directly on the silicon prism, and the electric contact was done by using a CP on the top of the film (Figure V.22).

CHAPTER V

Dynamic rearrangement of 2D-COF by electric field

Configuration 1.

Spectroelectrochemical cell SEIRA-SEC

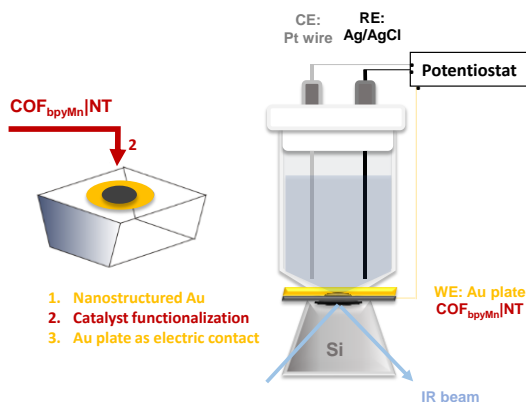


Figure V.21. Schematic representation of a typical Electrochemical-SEIRA setup. An IR-transparent silicon prism is used as support for the gold thin, which is the working electrode (WE) and the responsible SEIRA effect. A Pt wire is used as a counter electrode (CE) and a Ag/AgCl as a reference electrode (RE).

Configuration 2.

Spectroelectrochemical cell ATR-SEC

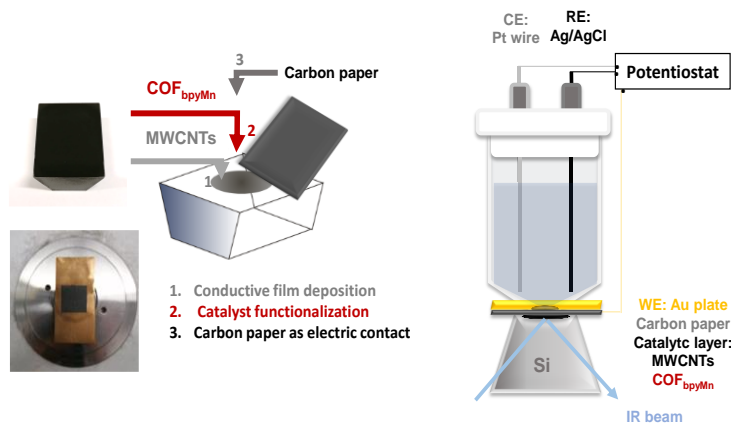


Figure V.22. Schematic representation of a typical Electrochemical-SEIRA setup. An IR-transparent silicon prism is used as support for the gold thin, which is the working electrode (WE) and the responsible SEIRA effect. A Pt wire is used as a counter electrode (CE) and a Ag/AgCl as a reference electrode (RE).

CHAPTER V Dynamic rearrangement of 2D-COF by electric field

In our approach, we probed the effect of the potential in the local reorganization of the COF. The dynamic of the COF was clear using SEIRA-SEC. From cyclic voltammetry, we can obtain information on the phase transitions in self-organized layers through sensitive changes in the double-layer capacitance as these transitions are fast on the time scale of the measurement. In our case for slower supramolecular changes, featureless voltammograms do not always imply the absence of supramolecular phase transitions

Absorbance (A) spectra were generated according to Lambert–Beer’s equation. Then, the normalized band intensities as a function of applied electrode potential E were fitted using a transformed Nernst equation. Finally, the following equations were used to analyze the Nernstian behavior assuming the Beer’s law and considering the apparent excess of chemical potential.

Oxidized

$$E = E^0 - \frac{RT}{nF} \log \frac{1 - I_{ox}}{I_{ox}} + \frac{\Delta\mu}{F}$$

Reduced

$$E = E^0 - \frac{RT}{nF} \log \frac{I_{red}}{1 - I_{red}} + \frac{\Delta\mu}{F}$$

Where:

E is the measured equilibrium potential at each point

R is the gas constant (8.314 J·mol⁻¹·K⁻¹)

T is the experimental temperature in Kelvin

n is the number of electrons in the half-reaction

F is the Faraday constant (96485 C·mol⁻¹)

Δμ/F is the apparent excess of chemical potential

V.4.2.1.2. UV-vis-SEC

Homogeneous conditions

Spectroelectrochemical experiments with the molecular catalyst in solution were carried out in dry 0.2 M TBAPF₆/ CH₃CN electrolyte within an optically transparent thin-layer electrode (OTTLE) cell, equipped with a Pt mini-grid working and auxiliary electrodes, an Ag microwire pseudoreference electrode and a CaF₂ window. FTIR spectra were recorded on a Nicolet iS50 FT-IR spectrometer.

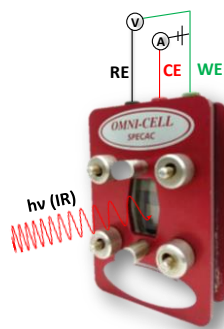


Figure V. 23. OTTLE cell for FT-IR-SEC experiments.

Heterogeneous conditions

The **COF_{bpy}Mn** was dispersed in CH₃CN (1mg : 100μL) and the ink was deposited over a FTO glass (0.7 cm²). The reference electrode used in water (0.5 M NaHCO₃) was SCE (3.5 M KCl solution), while in CH₃CN (0.2 M TBAPF₆) was Ag wire, a pseudo reference calibrated with Fc⁺/Fc vs a freshly clean glassy carbon electrode before and after experiments. The counter electrode was a Pt wire (Figure V. 24). To saturation the solution with Ar, a constant gas flow was continuously passed over the solution. All measurements were carried out at room temperature. UV-vis spectra were measured with an Agilent 8453 diode array spectrophotometer ($\lambda = 190\text{--}1100\text{ nm}$)

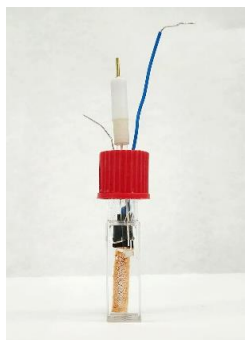


Figure V. 24. UV-vis SEC cell.

V.4.2.1.3. EPR-SEC

All electrochemical experiments were carried out inside an Ar glovebox at ambient temperature using a PARSTAT MC potentiostat/galvanostat from Princeton Applied Research. Electrolyte solutions were prepared using purified water (18 M Ω ·cm resistivity) obtained from the Milli-Q system. MWCNTS, NaHCO₃ (99.9%) and glycerol were used as received from Sigma-Aldrich. Carbon Paper (CP, Freudenberg H23C6) was used as a working electrode (approximately: 2 mm \times 0.2 mm \times 50 mm), which could easily fit within an X-band EPR tube. The design of a spectroelectrochemical cell used for the potential-dependent EPR of COF_{bpyMn}|NTs films is shown in Figure V.25. It consists of a Pt counter electrode parallel to the CP working electrode. An Ag wire is used as a reference electrode. Cyclic Voltammetry (CV) and Chronoamperometry (CA) measurements were performed inside the EPR spectroelectrochemical cell.

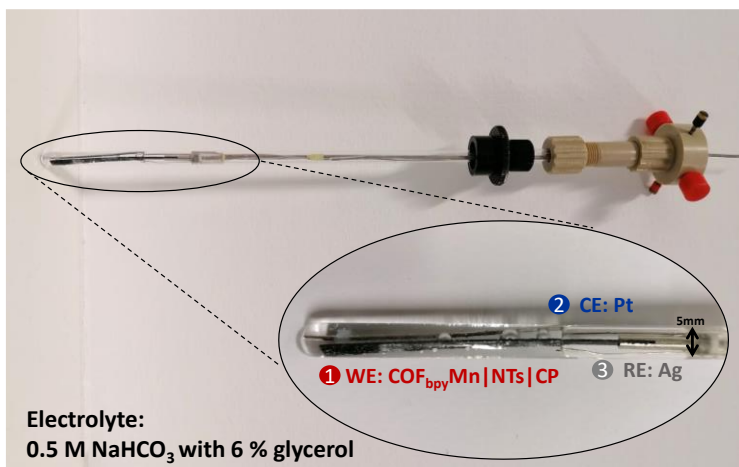


Figure V.25. EPR-SEC cell (top) used in this study with a zoomed view of the electrodes (bottom). The cell was filled until the electrolyte reached the reference electrode. A Carbon paper with the COF_{bpyMn}|NT film was used as a working electrode (WE: COF_{bpyMn}|NT); Platinum as a counter electrode (CE: Pt) and silver as a reference electrode RE: Ag. The bubbles are formed during catalysis and correspond to H₂ evolution.

Performance of the Spectroelectrochemical Cell

EPR measurements are conducted in EPR resonators that separate the magnetic field component (B_1), inducing the EPR signal, from the electric component (E_1) of the electromagnetic radiation. The conductive electrode with the electrodeposited film has to be positioned in the maximum of B_1 but should be separated in space from E_1 . In addition, the solvent (water) also strongly dampens microwaves (MW) in the liquid phase. Both these issues are typically solved by using very small electrodes/sample geometries, which inevitably lead to a reduction of the EPR signal. Our solution to this problem was a Carbon Paper (CP) electrode within a standard X-band EPR tube frozen under operating conditions (applied bias) and measured at low temperature. The presence of a large conducting electrode did not dramatically change the performance of the EPR resonator, i.e., did not lead to a loss in sensitivity.

Potential Dependence

CVs were recorded at 20 mV/s, for CA potentials were applied by steps in the range of 0 to -1.2 V vs Ag during 10 minutes. The EPR

spectroelectrochemical cell was frozen in liquid nitrogen, with the potential still applied during freezing to preserve the catalyst reduction state. Upon conclusion of the low-temperature EPR measurement, the spectroelectrochemical cell was slowly thawed and immediately connected to the potentiostat for the next step in the potential dependence.

EPR Spectroscopy

X-Band CW EPR measurements were performed using a Bruker E500 spectrometer equipped with a Bruker ER 4116DM resonator (Bruker BioSpin, Rheinstetten, BW, Germany), Oxford Instruments ESR 935 cryostat and ITC503 temperature controller (Oxford Instruments, Abingdon, Eng., UK). Microwave power P_{MW} was in the range of 6 to 65 mW. Magnetic field modulation was 7.5 G and temperature 10 K, 30. K, 60 K, respectively.

V.5 References

1. Wang, S.; Huang, P.; Chen, X., Stimuli-Responsive Programmed Specific Targeting in Nanomedicine. *ACS Nano* **2016**, *10* (3), 2991-2994.
2. Liu, Z.; Wang, H. I.; Narita, A.; Chen, Q.; Mics, Z.; Turchinovich, D.; Kläui, M.; Bonn, M.; Müllen, K., Photoswitchable Micro-Supercapacitor Based on a Diarylethene-Graphene Composite Film. *Journal of the American Chemical Society* **2017**, *139* (28), 9443-9446.
3. Kang, S.; Hong, S. Y.; Kim, N.; Oh, J.; Park, M.; Chung, K. Y.; Lee, S.-S.; Lee, J.; Son, J. G., Stretchable Lithium-Ion Battery Based on Re-entrant Micro-honeycomb Electrodes and Cross-Linked Gel Electrolyte. *ACS Nano* **2020**, *14* (3), 3660-3668.
4. McConnell, A. J.; Wood, C. S.; Neelakandan, P. P.; Nitschke, J. R., Stimuli-Responsive Metal–Ligand Assemblies. *Chemical Reviews* **2015**, *115* (15), 7729-7793.
5. Zhang, K. Y.; Liu, S.; Zhao, Q.; Huang, W., Stimuli-responsive metallopolymers. *Coordination Chemistry Reviews* **2016**, *319*, 180-195.
6. Mackanic, D. G.; Kao, M.; Bao, Z., Enabling Deformable and Stretchable Batteries. *Advanced Energy Materials* **2020**, *10* (29), 2001424.
7. McCune, J. A.; Mommer, S.; Parkins, C. C.; Scherman, O. A., Design Principles for Aqueous Interactive Materials: Lessons from Small Molecules and Stimuli-Responsive Systems. *Advanced Materials* **2020**, *32* (20), 1906890.
8. Rice, A. M.; Martin, C. R.; Galitskiy, V. A.; Berseneva, A. A.; Leith, G. A.; Shustova, N. B., Photophysics Modulation in Photoswitchable Metal–Organic Frameworks. *Chemical Reviews* **2020**, *120* (16), 8790-8813.
9. Wang, H.; Yao, C.-J.; Nie, H.-J.; Yang, L.; Mei, S.; Zhang, Q., Recent progress in integrated functional electrochromic energy storage devices. *Journal of Materials Chemistry C* **2020**, *8* (44), 15507-15525.
10. Liu, X.; Huang, D.; Lai, C.; Zeng, G.; Qin, L.; Wang, H.; Yi, H.; Li, B.; Liu, S.; Zhang, M.; Deng, R.; Fu, Y.; Li, L.; Xue, W.; Chen, S., Recent advances in covalent organic frameworks (COFs) as a smart sensing material. *Chemical Society Reviews* **2019**, *48* (20), 5266-5302.
11. Li, C.; Wang, K.; Li, J.; Zhang, Q., Recent Progress in Stimulus-Responsive Two-Dimensional Metal–Organic Frameworks. *ACS Materials Letters* **2020**, *2* (7), 779-797.
12. Férey, G.; Serre, C., Large breathing effects in three-dimensional porous hybrid matter: facts, analyses, rules and consequences. *Chemical Society Reviews* **2009**, *38* (5), 1380-1399.
13. Liu, Y.; Ma, Y.; Yang, J.; Diercks, C. S.; Tamura, N.; Jin, F.; Yaghi, O. M., Molecular Weaving of Covalent Organic Frameworks for Adaptive Guest Inclusion. *Journal of the American Chemical Society* **2018**, *140* (47), 16015-16019.
14. Chen, K.; Wu, C.-D., Transformation of Metal-Organic Frameworks into Stable Organic Frameworks with Inherited Skeletons and Catalytic Properties. *Angewandte Chemie International Edition* **2019**, *58* (24), 8119-8123.
15. Dissegna, S.; Epp, K.; Heinz, W. R.; Kieslich, G.; Fischer, R. A., Defective Metal-Organic Frameworks. *Advanced Materials* **2018**, *30* (37), 1704501.

16. Bigdeli, F.; Lollar, C. T.; Morsali, A.; Zhou, H.-C., Switching in Metal–Organic Frameworks. *Angewandte Chemie International Edition* **2020**, *59* (12), 4652-4669.
17. Xu, S.; Zhang, Q., Recent progress in covalent organic frameworks as light-emitting materials. *Materials Today Energy* **2021**, *20*, 100635.
18. Medina, D. D.; Sick, T.; Bein, T., Photoactive and Conducting Covalent Organic Frameworks. *Advanced Energy Materials* **2017**, *7* (16), 1700387.
19. Li, K.; Wong, N. K.; Strauss, M. J.; Evans, A. M.; Matsumoto, M.; Dichtel, W. R.; Adronov, A., Postsynthetic Modification of a Covalent Organic Framework Achieved via Strain-Promoted Cycloaddition. *Journal of the American Chemical Society* **2021**, *143* (2), 649-656.
20. She, P.; Qin, Y.; Wang, X.; Zhang, Q., Recent Progress in External-Stimulus-Responsive 2D Covalent Organic Frameworks. *Advanced Materials* **2021**, *n/a* (n/a), 2101175.
21. Zhang, Y.; Shen, X.; Feng, X.; Xia, H.; Mu, Y.; Liu, X., Covalent organic frameworks as pH responsive signaling scaffolds. *Chemical Communications* **2016**, *52* (74), 11088-11091.
22. Ning, G.-H.; Chen, Z.; Gao, Q.; Tang, W.; Chen, Z.; Liu, C.; Tian, B.; Li, X.; Loh, K. P., Salicylideneanilines-Based Covalent Organic Frameworks as Chemoselective Molecular Sieves. *Journal of the American Chemical Society* **2017**, *139* (26), 8897-8904.
23. Hao, Q.; Li, Z.-J.; Lu, C.; Sun, B.; Zhong, Y.-W.; Wan, L.-J.; Wang, D., Oriented Two-Dimensional Covalent Organic Framework Films for Near-Infrared Electrochromic Application. *Journal of the American Chemical Society* **2019**, *141* (50), 19831-19838.
24. Wang, S.; Ma, L.; Wang, Q.; Shao, P.; Ma, D.; Yuan, S.; Lei, P.; Li, P.; Feng, X.; Wang, B., Covalent organic frameworks: a platform for the experimental establishment of the influence of intermolecular distance on phosphorescence. *Journal of Materials Chemistry C* **2018**, *6* (20), 5369-5374.
25. Beaujuge, P. M.; Reynolds, J. R., Color Control in π -Conjugated Organic Polymers for Use in Electrochromic Devices. *Chemical Reviews* **2010**, *110* (1), 268-320.
26. Ma, Y.-X.; Li, Z.-J.; Wei, L.; Ding, S.-Y.; Zhang, Y.-B.; Wang, W., A Dynamic Three-Dimensional Covalent Organic Framework. *Journal of the American Chemical Society* **2017**, *139* (14), 4995-4998.
27. Huang, N.; Ding, X.; Kim, J.; Ihee, H.; Jiang, D., A Photoresponsive Smart Covalent Organic Framework. *Angewandte Chemie International Edition* **2015**, *54* (30), 8704-8707.
28. Zhang, J.; Wang, L.; Li, N.; Liu, J.; Zhang, W.; Zhang, Z.; Zhou, N.; Zhu, X., A novel azobenzene covalent organic framework. *CrystEngComm* **2014**, *16* (29), 6547-6551.
29. She, P.; Qin, Y.; Wang, X.; Zhang, Q., Recent Progress in External-Stimulus-Responsive 2D Covalent Organic Frameworks. *Advanced Materials* **2022**, *34* (22), 2101175.
30. Kornienko, N., Operando spectroscopy of nanoscopic metal/covalent organic framework electrocatalysts. *Nanoscale* **2021**, *13* (3), 1507-1514.
31. Uosaki, K., In situ real-time monitoring of geometric, electronic, and molecular structures at solid/liquid interfaces. *Japanese Journal of Applied Physics* **2015**, *54* (3), 030102.

32. Horányi, G., Chapter 4 Studies of electrified solid/liquid interfaces. In *Interface Science and Technology*, Horányi, G., Ed. Elsevier: 2004; Vol. 3, pp 39-97.
33. Wieckowski, A., *Interfacial electrochemistry : theory, experiment, and applications*. Marcel Dekker: New York, 1999.
34. Ye, S., Electrochemical Infrared Spectroscopy. In *Compendium of Surface and Interface Analysis*, The Surface Science Society of, J., Ed. Springer Singapore: Singapore, 2018; pp 79-85.
35. Pons, S., In situ vibrational spectroelectrochemistry. *Journal of Electron Spectroscopy and Related Phenomena* **1987**, *45*, 303-322.
36. Reuillard, B.; Ly, K. H.; Rosser, T. E.; Kuehnel, M. F.; Zebger, I.; Reisner, E., Tuning Product Selectivity for Aqueous CO₂ Reduction with a Mn(bipyridine)-pyrene Catalyst Immobilized on a Carbon Nanotube Electrode. *Journal of the American Chemical Society* **2017**, *139* (41), 14425-14435.
37. Dubed Bandomo, G. C.; Mondal, S. S.; Franco, F.; Bucci, A.; Martin-Diaconescu, V.; Ortuño, M. A.; van Langevelde, P. H.; Shafir, A.; López, N.; Lloret-Fillol, J., Mechanically Constrained Catalytic Mn(CO)₃Br Single Sites in a Two-Dimensional Covalent Organic Framework for CO₂ Electroreduction in H₂O. *ACS Catalysis* **2021**, *11* (12), 7210-7222.
38. Wang, L.-X.; Jiang, X.-E., Bioanalytical Applications of Surface-enhanced Infrared Absorption Spectroscopy. *Chinese Journal of Analytical Chemistry* **2012**, *40* (7), 975-982.
39. Nishikawa, Y.; Fujiwara, K.; Ataka, K.; Osawa, M., Surface-enhanced infrared external reflection spectroscopy at low reflective surfaces and its application to surface analysis of semiconductors, glasses, and polymers. *Analytical Chemistry* **1993**, *65* (5), 556-562.
40. Osawa, M., Surface-Enhanced Infrared Absorption. In *Near-Field Optics and Surface Plasmon Polaritons*, Kawata, S., Ed. Springer Berlin Heidelberg: Berlin, Heidelberg, 2001; pp 163-187.
41. Ye, S.; Fang, L.; Lu, Y., Contribution of charge-transfer effect to surface-enhanced IR for Ag@PPy nanoparticles. *Physical Chemistry Chemical Physics* **2009**, *11* (14), 2480-2484.
42. Ataka, K.; Heberle, J., Use of surface enhanced infrared absorption spectroscopy (SEIRA) to probe the functionality of a protein monolayer. *Biopolymers* **2006**, *82* (4), 415-9.
43. Ataka, K.; Giess, F.; Knoll, W.; Naumann, R.; Haber-Pohlmeier, S.; Richter, B.; Heberle, J., Oriented Attachment and Membrane Reconstitution of His-Tagged Cytochrome c Oxidase to a Gold Electrode: In Situ Monitoring by Surface-Enhanced Infrared Absorption Spectroscopy. *Journal of the American Chemical Society* **2004**, *126* (49), 16199-16206.
44. Ataka, K.; Stripp, S. T.; Heberle, J., Surface-enhanced infrared absorption spectroscopy (SEIRAS) to probe monolayers of membrane proteins. *Biochim Biophys Acta* **2013**, *1828* (10), 2283-93.
45. Metiu, H., Surface enhanced spectroscopy. *Progress in Surface Science* **1984**, *17* (3), 153-320.
46. Gersten, J. I.; Nitzan, A., Photophysics and photochemistry near surfaces and small particles. *Surface Science* **1985**, *158* (1), 165-189.
47. Kozuch, J.; Weichbrodt, C.; Millo, D.; Giller, K.; Becker, S.; Hildebrandt, P.; Steinem, C., Voltage-dependent structural changes of the

membrane-bound anion channel hVDAC1 probed by SEIRA and electrochemical impedance spectroscopy. *Physical Chemistry Chemical Physics* **2014**, *16* (20), 9546-9555.

48. Osawa, M.; Ataka, K.-I.; Yoshii, K.; Nishikawa, Y., Surface-Enhanced Infrared Spectroscopy: The Origin of the Absorption Enhancement and Band Selection Rule in the Infrared Spectra of Molecules Adsorbed on Fine Metal Particles. *Appl. Spectrosc.* **1993**, *47* (9), 1497-1502.

49. Ataka, K.; Nishina, G.; Cai, W.-B.; Sun, S.-G.; Osawa, M., Dynamics of the dissolution of an underpotentially deposited Cu layer on Au(111): a combined time-resolved surface-enhanced infrared and chronoamperometric study. *Electrochemistry Communications* **2000**, *2* (6), 417-421.

50. Murgida, D. H., In Situ Spectroelectrochemical Investigations of Electrode-Confined Electron-Transferring Proteins and Redox Enzymes. *ACS Omega* **2021**, *6* (5), 3435-3446.

51. Murgida, D.; Hildebrandt, P., Surface-Enhanced Vibrational Spectroelectrochemistry: Electric-Field Effects on Redox and Redox-Coupled Processes of Heme Proteins. In *Surface-Enhanced Raman Scattering: Physics and Applications*, Kneipp, K.; Moskovits, M.; Kneipp, H., Eds. Springer Berlin Heidelberg: Berlin, Heidelberg, 2006; pp 313-334.

52. Sezer, M.; Millo, D.; Weidinger, I. M.; Zebger, I.; Hildebrandt, P., Analyzing the catalytic processes of immobilized redox enzymes by vibrational spectroscopies. *IUBMB Life* **2012**, *64* (6), 455-64.

53. Harris, T. G. A. A.; Heidary, N.; Kozuch, J.; Frielingsdorf, S.; Lenz, O.; Mroginski, M.-A.; Hildebrandt, P.; Zebger, I.; Fischer, A., In Situ Spectroelectrochemical Studies into the Formation and Stability of Robust Diazonium-Derived Interfaces on Gold Electrodes for the Immobilization of an Oxygen-Tolerant Hydrogenase. *ACS Applied Materials & Interfaces* **2018**, *10* (27), 23380-23391.

54. Millo, D., Spectroelectrochemical analyses of electroactive microbial biofilms. *Biochemical Society Transactions* **2012**, *40* (6), 1284-1290.

55. Alkire, R. C.; Kolb, D. M.; Lipkowsky, J.; Ross, P. N., *Diffraction and Spectroscopic Methods in Electrochemistry: Quantitative SNIPTIRS and PM IRRAS of organic molecules at electrode surfaces*. Wiley-Vch: Weinheim, 2008; Vol. 9.

56. Cai, W.-B.; Wan, L.-J.; Noda, H.; Hibino, Y.; Ataka, K.; Osawa, M., Orientational Phase Transition in a Pyridine Adlayer on Gold(111) in Aqueous Solution Studied by in Situ Infrared Spectroscopy and Scanning Tunneling Microscopy. *Langmuir* **1998**, *14* (24), 6992-6998.

57. Cui, K.; Dorner, I.; Mertens, S. F. L., Interfacial supramolecular electrochemistry. *Current Opinion in Electrochemistry* **2018**, *8*, 156-163.

58. Otto, A. In *Surface-Enhanced Raman Scattering*, Dynamics of Gas-Surface Interaction, Berlin, Heidelberg, 1982//; Benedek, G.; Valbusa, U., Eds. Springer Berlin Heidelberg: Berlin, Heidelberg, 1982; pp 186-195.

59. LaFreniere, J. M. J.; Roberge, E. J.; Halpern, J. M., Review—Reorientation of Polymers in an Applied Electric Field for Electrochemical Sensors. *Journal of The Electrochemical Society* **2020**, *167* (3), 037556.

60. Bhadra, P.; Siu, S. W. I., Effect of Concentration, Chain Length, Hydrophobicity, and an External Electric Field on the Growth of Mixed

Alkanethiol Self-Assembled Monolayers: A Molecular Dynamics Study. *Langmuir* **2021**, *37* (5), 1913-1924.

61. Jeuken, L. J. C., AFM Study on the Electric-Field Effects on Supported Bilayer Lipid Membranes. *Biophysical Journal* **2008**, *94* (12), 4711-4717.

62. Cui, K.; Mali, K. S.; Ivasenko, O.; Wu, D.; Feng, X.; Walter, M.; Müllen, K.; De Feyter, S.; Mertens, S. F. L., Squeezing, Then Stacking: From Breathing Pores to Three-Dimensional Ionic Self-Assembly under Electrochemical Control. *Angewandte Chemie International Edition* **2014**, *53* (47), 12951-12954.

63. Yoshimoto, S.; Yokoo, N.; Fukuda, T.; Kobayashi, N.; Itaya, K., Formation of highly ordered porphyrin adlayers induced by electrochemical potential modulation. *Chemical Communications* **2006**, (5), 500-502.

64. Suto, K.; Yoshimoto, S.; Itaya, K., Electrochemical Control of the Structure of Two-Dimensional Supramolecular Organization Consisting of Phthalocyanine and Porphyrin on a Gold Single-Crystal Surface. *Langmuir* **2006**, *22* (25), 10766-10776.

65. Yang, D.; Bizzotto, D.; Lipkowski, J.; Pettinger, B.; Mirwald, S., Electrochemical and Second Harmonic Generation Studies of 2,2'-Bipyridine Adsorption at the Au(111) Electrode Surface. *The Journal of Physical Chemistry* **1994**, *98* (28), 7083-7089.

66. Sung, S.; Li, X.; Wolf, L. M.; Meeder, J. R.; Bhuvanesh, N. S.; Grice, K. A.; Panetier, J. A.; Nippe, M., Synergistic Effects of Imidazolium-Functionalization on fac-Mn(CO)(3) Bipyridine Catalyst Platforms for Electrocatalytic Carbon Dioxide Reduction. *J Am Chem Soc* **2019**, *141* (16), 6569-6582.

67. Rosser, T. E.; Windle, C. D.; Reisner, E., Electrocatalytic and Solar-Driven CO₂ Reduction to CO with a Molecular Manganese Catalyst Immobilized on Mesoporous TiO₂. *Angewandte Chemie International Edition* **2016**, *55* (26), 7388-7392.

68. Walsh, J. J.; Forster, M.; Smith, C. L.; Neri, G.; Potter, R. J.; Cowan, A. J., Directing the mechanism of CO₂ reduction by a Mn catalyst through surface immobilization. *Physical Chemistry Chemical Physics* **2018**, *20* (10), 6811-6816.

69. Šimėnas, M.; Ciupa, A.; Mączka, M.; Völkel, G.; Pöppel, A.; Banys, J. r., EPR of Structural Phase Transition in Manganese- and Copper-Doped Formate Framework of [NH₃(CH₂)₄NH₃][Zn(HCOO)₃]₂. *The Journal of Physical Chemistry C* **2016**, *120* (35), 19751-19758.

70. Bourrez, M.; Orio, M.; Molton, F.; Vezin, H.; Duboc, C.; Deronzier, A.; Chardon-Noblat, S., Pulsed-EPR Evidence of a Manganese(II) Hydroxycarbonyl Intermediate in the Electrocatalytic Reduction of Carbon Dioxide by a Manganese Bipyridyl Derivative. *Angewandte Chemie International Edition* **2014**, *53* (1), 240-243.

71. Roessler, M. M.; Salvadori, E., Principles and applications of EPR spectroscopy in the chemical sciences. *Chemical Society Reviews* **2018**, *47* (8), 2534-2553.

72. Hartl, F.; Rossenaar, B. D.; Stor, G. J.; Stufkens, D. J., Role of an electron-transfer chain reaction in the unusual photochemical formation of five-coordinated anions [Mn(CO)₃(α -diimine)]⁻ from fac-[Mn(X)(CO)₃(α -diimine)] (X = halide) at low temperatures. *Recueil des Travaux Chimiques des Pays-Bas* **1995**, *114* (11-12), 565-570.

CHAPTER V

Dynamic rearrangement of 2D-COF by electric field

73. Bourrez, M.; Molton, F.; Chardon-Noblat, S.; Deronzier, A., [Mn(bipyridyl)(CO)₃Br]: An Abundant Metal Carbonyl Complex as Efficient Electrocatalyst for CO₂ Reduction. *Angewandte Chemie International Edition* **2011**, *50* (42), 9903-9906.
74. Stor, G. J.; Morrison, S. L.; Stufkens, D. J.; Oskam, A., The Remarkable Photochemistry of fac-XMn(CO)₃(.alpha.-diimine) (X =Halide): Formation of Mn₂(CO)₆(.alpha.-diimine)₂ via the mer Isomer and Photocatalytic Substitution of X- in the Presence of PR₃. *Organometallics* **1994**, *13* (7), 2641-2650.
75. Franco, F.; Cometto, C.; Nencini, L.; Barolo, C.; Sordello, F.; Minero, C.; Fiedler, J.; Robert, M.; Gobetto, R.; Nervi, C., Local Proton Source in Electrocatalytic CO₂ Reduction with [Mn(bpy-R)(CO)₃Br] Complexes. *Chemistry – A European Journal* **2017**, *23* (20), 4782-4793.
76. Kang, C.; Zhang, Z.; Wee, V.; Usadi, A. K.; Calabro, D. C.; Baugh, L. S.; Wang, S.; Wang, Y.; Zhao, D., Interlayer Shifting in Two-Dimensional Covalent Organic Frameworks. *Journal of the American Chemical Society* **2020**, *142* (30), 12995-13002.

CHAPTER VI.

Novel Covalent Organic Framework with embedded Phenanthroline Mn(CO)₃Br Single Sites as CO₂ reduction electrocatalyst in aqueous media

Chapter VI: Novel Covalent Organic Framework with embedded Phenanthroline Mn(CO)₃Br Single Sites as CO₂ reduction electrocatalyst in aqueous media

VI.1. General insight

As seen in the previous chapters, incorporating catalytic units into reticular frameworks is an attractive strategy to maximize the number of active sites supported on an electrode^{1, 2} and enhance the electrocatalytic activity, compared with solution-based molecular electrocatalysts and other monolayer immobilization strategies.³⁻⁹

In addition, the molecular design of COFs makes possible an outstanding control over the chemical environment of the catalytic sites in confined spaces and their functional development. Several efforts have been oriented to the rational design of COFs by varying the size, shape, connectivity and electronic structures of their molecular building blocks.^{2, 4, 7, 10-29} In particular, tuning the electronic structure of the building blocks can strongly influence the COF's performance, mimicking the crucial role of the ligands on tuning the catalytic activity of molecular complexes. For example, the extensive work on metalloporphyrin systems and manganese tricarbonyl polypyridyl catalysts for CO₂ reduction illustrate how ligand tuning can improve catalytic performance.³⁰⁻³²

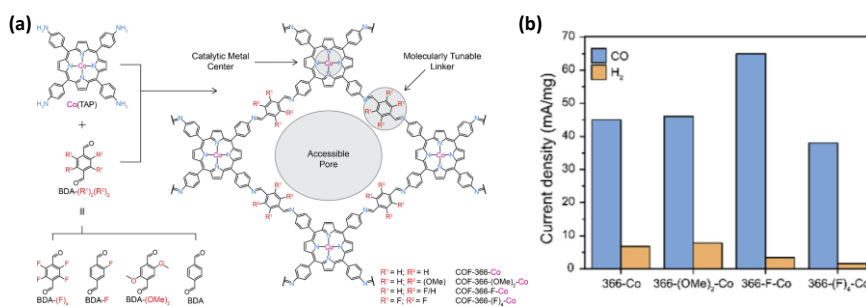


Figure VI.1. (a) Design of Co-porphyrin-based COFs by modifying the electronic properties of the linkers. (b) Current densities per mg of Co in the different COF catalysts: COF-366-Co, COF-366-(OMe)₂-Co, COF-366-F-Co, and COF-366-(F)₂-Co under an applied potential of -0.67 V vs RHE in 0.5 M KHCO₃ under CO₂. Reproduced with permission from [6] Copyright 2017 American Chemical Society

In particular, Yaghi and co-workers, afforded to tune the CO₂ reduction properties of the catalytic sites located in the corners of a COF by modifying the electronic properties of the linkers (Figure VI.1).⁶ These results indicate that a long-range electronic effect could be efficiently promoted between the COF backbone and a functional group remote from the active site to tune the catalytic properties.⁶

Similar to porphyrins, bipyridines have proven to be functional building blocks for COFs in electrocatalysis.³³⁻³⁵ For example, Marinescu and co-workers evaluated a COF with both metalloporphyrin (Co and Fe) and metal bipyridine (Re) moieties for electrocatalytic CO₂ reduction (Figure VI.2).³⁵ However, the incorporation of two distinct metal sites led to a low selectivity for CO₂ reduction. They rationalized the poor electrocatalytic activity with the presence of the two different metal centers in the linkers and corners of the COFs, respectively, which inhibit the generation of the doubly reduced species required for CO₂ reduction.

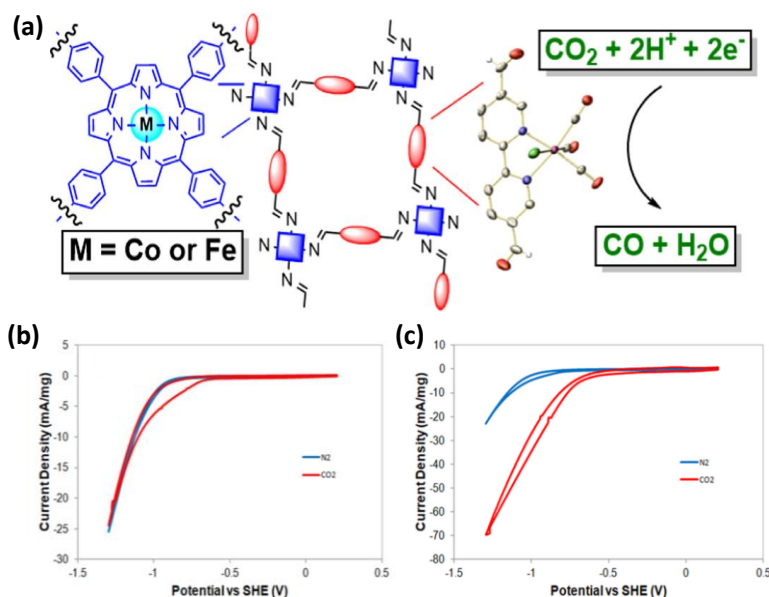


Figure VI.2. (a) COF-Re, COF-Re_Co, and COF-Re_Fe. CV of COF-Re_Co (b) and COF-Re_Fe (c) in aqueous phosphate buffer solutions (pH 7.2) under N₂ (blue) and CO₂ (red) atmospheres at 100 mV·s⁻¹. Reproduced with permission from [35] Copyright 2018 American Chemical Society.

These examples highlight the effect of the building blocks on the electrocatalytic properties of COFs and the importance of studying the catalytic activity-structure relationships of these reticular materials. Unfortunately, these fundamental correlations are underexplored and need further investigation. In this context, we became interested in understanding the electrocatalytic CO₂ reduction mechanism with COFs to design more efficient catalytic materials.

As mentioned in Chapter I, the *fac*-Mn(bpy)(CO)₃Br precatalyst represents one of the most widely studied prototypical molecular systems for electrocatalytic CO₂ reduction and several Mn derivatives with polypyridyl ligands have been reported as efficient and selective catalysts for the CO₂-to-CO reduction.^{30, 36} Rational modification of their main structure helped to understand the effect of the ligand and through-space interactions, which are crucial to tune the reaction kinetics and CO₂ reduction efficiency. Indeed, these catalysts have provided access to new insights into the CO₂ reduction mechanisms by combining them with spectroelectrochemical techniques like IR-SEC.³⁷ More recently, it has been shown that the CO₂ electroreduction selectivity can be shifted from CO towards HCO₂H.³⁸ These results led to a growth in the electrocatalytic CO₂RR studies using Mn-carbonyl complexes.^{7b,c, 30, 36, 39, 40}

In addition, the *fac*-Mn(PT)(CO)₃Br (PT: 1,10-phenanthroline) complex has been reported to exhibit similar electrochemical performance to the [Mn(α -diimine)(CO)₃L] complexes (see Chapter I, Section I.3 for details).^{41,42} Upon one-electron reduction of Mn^I, rapid CH₃CN dissociation occurs, and this metastable Mn⁰ complex, in the absence of any steric hindrance, rapidly forms the Mn⁰-Mn⁰ bound 18-valence electron, [Mn(PT)(CO)₃]₂. The second reduction event is attributed to an irreversible two-electron EC event whereby the dimer is reductively cleaved to generate two equivalents of [*fac*-Mn⁰(PT⁻)(CO)₃]⁻ anion, which is proposed to be the main active catalyst for CO₂ activation.⁴²

In Chapter III, we reported the coordination of the {*fac*-Mn(CO)₃Br} moiety in the bipyridine of the imine-linked 2D pyrene-bipyridine COF (COF_{bpyMn}) for the electrochemical CO₂ reduction in water. We hypothesized that a variation of the polypyridyl linker could tune the

structural and electronic properties of the reticular COF_{bpyMn}. This approach could give insights into the effect of the linker on the electrocatalytic CO₂ reduction mechanism. With this new system, we aim to investigate how the structural properties of the reticular framework influence the catalytic CO₂ reduction activity.

Rational design: Structure-activity relationship

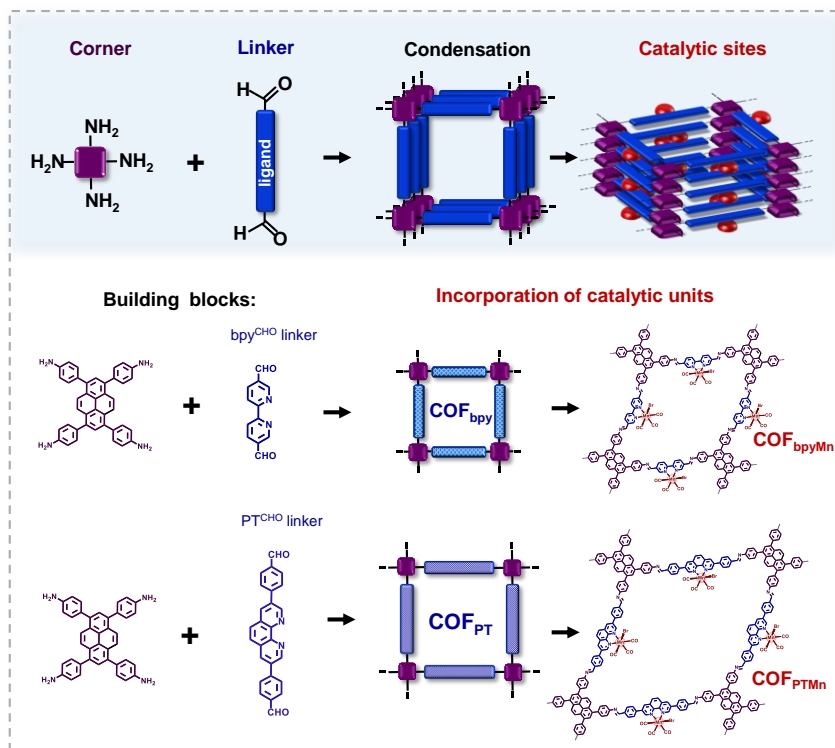


Figure VI. 3. Modular reticular design of COFs by modification of the polypyridyl linkers.

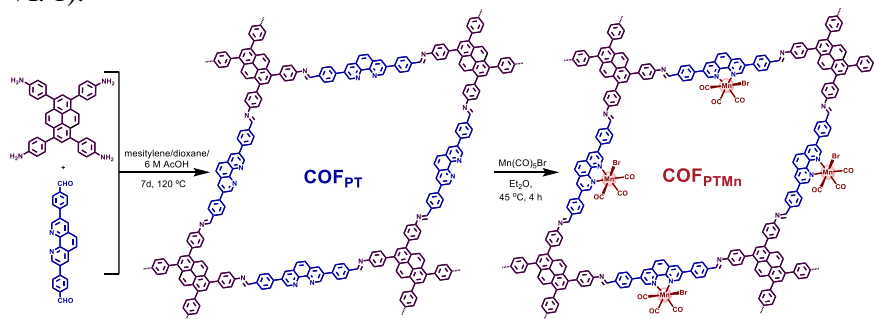
Therefore, in this chapter, we introduce a new polypyridyl moiety into a COF (Figure VI. 3). We have modified the COF_{bpyMn} by introducing the 1,10-phenanthroline ligand as a linker in the COF (COF_{PT}). However, we have also increased the size of the linker by adding phenyl rings to the 1,10-phenanthroline at the 3,8 positions (4,4'-(1,10-phenanthroline-3,8-diyl)dibenzaldehyde, PT^{CHO} for simplification) instead of bipyridine (COF_{bpy}, see Chapter III for details). The new COF_{PT} was post-synthetic modified by introducing {*fac*-Mn(CO)₃Br} single sites into the phenanthroline motif (COF_{PTMn}). Then, we studied the effect of the

sterically and electronically expanded phenanthroline derivate ligand into the reticular framework and compared it with the COF_{bpyMn}. We thoroughly characterized the new COFs and electrochemically evaluated their catalytic activity for CO₂ reduction in near-neutral pH aqueous media. In addition, the active species participating in the catalytic cycle for the CO₂ reduction was proposed based on ATR-IR-SEC. Altogether, the results suggest a correlation between the crystallinity and the activity of the resulting COF, where the structural properties of the COF_{PTMn} influence the intermediates generated in the catalytic cycle.

VI.2. Results and discussion

VI.2.1 Synthesis and characterization of COF_{PT} and COF_{PTMn}

COF_{PT} was synthesized by a similar procedure to our published work (see Chapter III and Experimental Section for details),⁴³ allowing the conventional two-component condensation reaction of amine unit (4,4',4'',4'''-(pyrene-1,3,6,8-tetrayl)tetraaniline (PyTTA)) and aldehyde unit 4,4'-(1,10-phenanthroline-3,8-diyl)dibenzaldehyde (PT^{CHO}, see the Experimental Section for details),⁴⁴ which leads to a 2D-COF_{PT} (Scheme VI. 1).



Scheme VI. 1. Synthetic procedure of COF_{PT} and COF_{PTMn}.

As shown in Figure VI.4a, the PXRD pattern of the COF_{PT} is poorly defined and considerably lower in intensity compared to COF_{bpy} (See Chapter III for details), suggesting less crystalline character of the former. Such difference in crystallinity could be related to the rate of COF formation and growth, which decreases with the reduction of Van der Waals surface and the non-planarity of the linkers, as the stacking of the 2D-

polymers influences the rate of COF formation.^{45, 46} In the case of COF_{PT}, the PT^{CHO} linker planarity is disrupted due to the free rotation of the phenyl ring.⁴⁵

The targeted Mn single sites were introduced into the strut of the COF_{PT} by using a post-synthetic approach. The solvent-free COF_{PT} reacted with Mn(CO)₅Br at 45 °C for 4 hours in diethyl ether (Et₂O) and the metalated COF_{PT} (COF_{PTMn}) was isolated as a dark orange microcrystalline powder. The color change during metalation from orange to dark orange can be ascribed to metal to ligand charge transfer due to the coordination of Mn^I to the framework. After metalation, the PXRD pattern of COF_{PTMn} exhibits similar diffraction peaks to the as-synthesized COF_{PT}, suggesting that the framework maintains its crystalline integrity even after metalation (Figure VI.4a).

To demonstrate the incorporation of {Mn(CO)₃Br} within the COF_{PT}, the ATR spectrum of COF_{PTMn} exhibits two prominent stretching frequencies at 2027 and 1922 cm⁻¹ (Figure VI.4b), which are absent in the parent COF_{PT} material. Moreover, the position of these characteristic CO stretching frequencies was identical to those of the molecular Mn(PT)(CO)₃Br (MnPT) (PT: 1,10-phenanthroline) complex (Figure VI.4b) and similar to the previously reported values for COF_{bpyMn} (See Chapter III for details),⁴³ suggesting successful incorporation of the {*fac*-Mn(CO)₃Br} moiety within the COF_{PT} structure.

In addition, the Thermo Gravimetric Analysis (TGA) trace of COF_{PTMn} exhibits two decomposition steps at ~70–180 and ~200–900 °C, unlike parent COF_{PT}, which displayed only one continuous decomposition step (Figure VI.4c). The first decomposition step for COF_{PTMn} is likely due to thermal liberation of the CO ligands bound to the Mn centers. The remaining loss is assigned to the organic ligand decomposition.

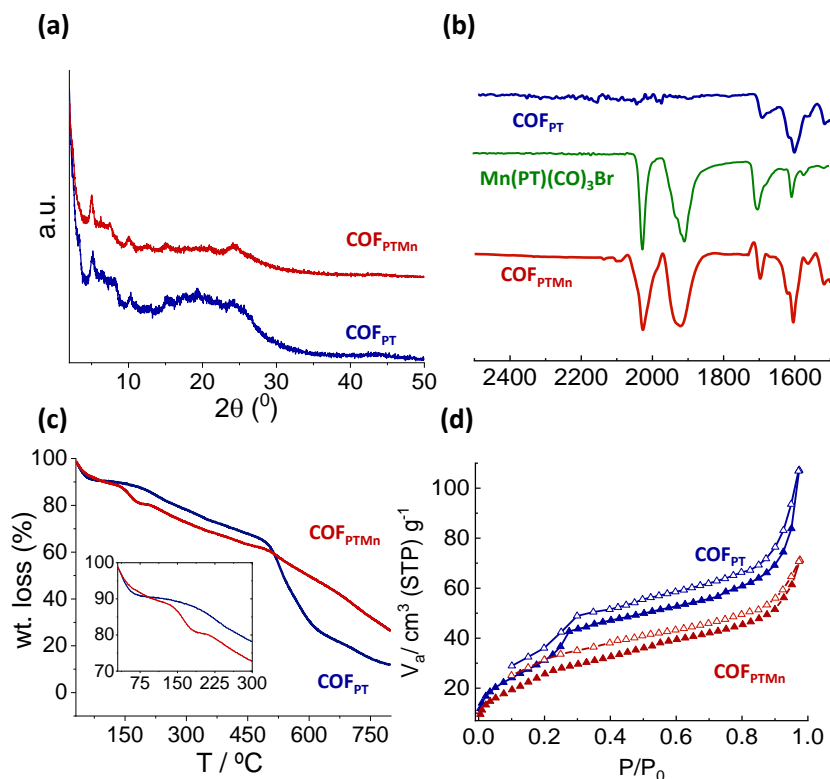


Figure VI.4. (a) PXRD, (b) ATR spectra, (c) TGA analysis and (d) N₂ isotherms of COF_{PT} and COF_{PTMn}

Dinitrogen (N₂) absorption/desorption isotherms (77 K) of COF_{PT} and COF_{PTMn} (Figure VI.4d), indicate that the materials present low porosity with Brunauer-Emmett-Teller (BET) surface areas determined to be 130 and 94 m²/g, respectively. The considerable difference between the surface areas of COF_{PT} (130 m²/g) and the previously evaluated COF_{bpy} (2127 m²/g) represents a clear indicator of the modification of the structural properties of the COF as a result of the ligand modification. We attribute these differences to two main reasons: i) the size of the linker that could disrupt the formation of the reticular framework, favoring the formation of the amorphous kinetic product, and ii) the non-planarity of the resulted COF_{PT} which may have a significant spatial effect on the crystallinity by controlling the π - π stacking interaction between interlayers.⁴⁷

The amount of Mn within COF_{PTMn} was found to be 38 mg/g *via* ICP-OES, which proposes that ~36% of PT^{CHO} sites were metalated. The low

incorporation of Mn could also be a consequence of irregular channels, which reduce the accessibility of binding sites within the pores. In this sense, high crystallinity helps to increase the accessible surface area and pore volume of the COFs, exposing more well-ordered binding sites.⁴⁸

Additionally, FESEM and TEM images of COF_{PT} and COF_{PTMn} reveal that the materials tend to form tubular morphologies of μm sizes (Figure VI. 5). This also represents another difference between the COF_{PT} and COF_{bpy}, where the latter showed a globular morphology (See Chapter III for details).

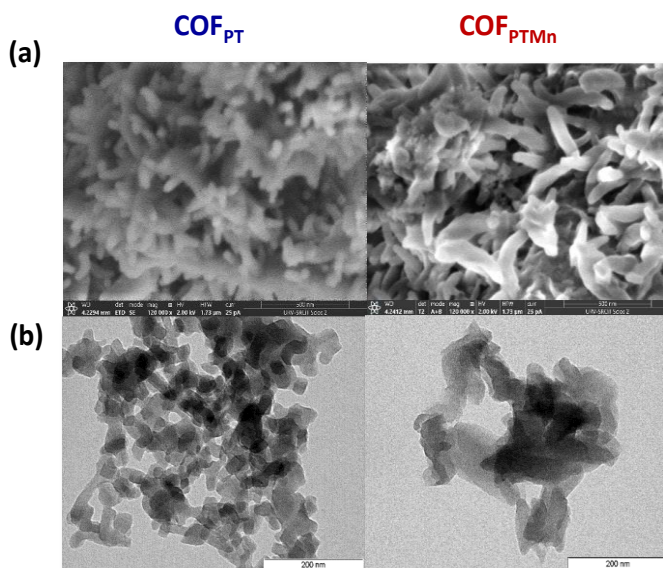


Figure VI. 5. FESEM (a) and TEM (b) of COF_{PT} and COF_{PTMn}.

VI.2.2 Electrocatalytic CO₂ reduction in water with COF_{PTMn}

In order to evaluate the electrochemical behavior and the catalytic CO₂ reduction performances of COF_{PTMn}, cyclic voltammetry (CV) and controlled-potential electrolysis (CPE) measurements were carried out in 0.5 M NaHCO₃ electrolyte under Ar (pH 8.4) and CO₂ (pH 7.4) atmosphere, respectively. For the electrode preparation, the COF_{PTMn} was supported on a GC electrode by drop-casting a dispersion of the catalyst's powder and MWCNTs (NT) in CH₃CN and Nafion (5% water) (COF_{PTMn}|NT) (Figure VI.6a, see Experimental Section for details).

The electrochemical results of COF_{PTMn}|NT were compared with the molecular counterpart Mn(PT)(CO)₃Br (MnPT|NT) and the COF_{bpyMn}|NT under identical reaction conditions.

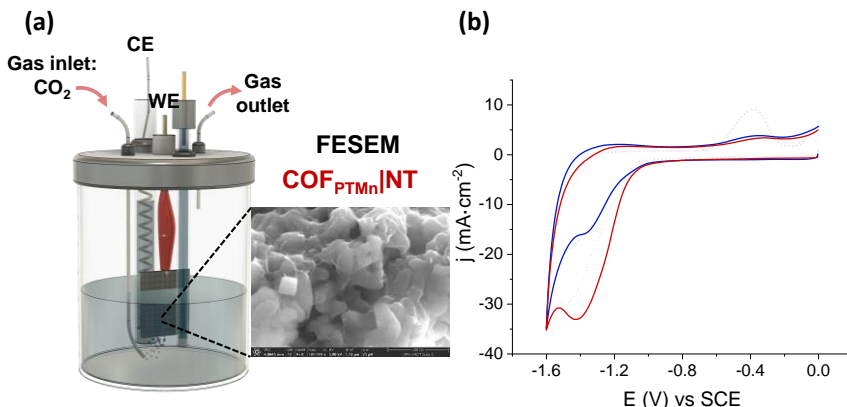


Figure VI.6. (a) Electrochemical setup and FESEM of COF_{PTMn}|NT, (b) CVs on GC of COF_{PTMn}|NT ($[Mn]_{total} = 900 \text{ nmol}\cdot\text{cm}^{-2}$, solid line) and MnPT|NT ($[Mn]_{total} = 900 \text{ nmol}\cdot\text{cm}^{-2}$, dotted line) in water (NaHCO₃ 0.5 M) under Ar (blue, pH 8.4) and CO₂ (red, pH 7.4) at $100 \text{ mV}\cdot\text{s}^{-1}$.

Under Ar, the CV of COF_{PTMn}|NT shows an intense irreversible cathodic wave for catalytic H₂ evolution reaction. When the solution was saturated with CO₂ (pH 7.4), a 2-fold increase of the catalytic current is observed (j_{CO_2}/j_{Ar} at -1.4 V vs SCE , Figure VI.6b), suggesting some activity towards CO₂ reduction.

Such current increase under CO₂ is slightly larger than that observed for the corresponding molecular counterpart Mn(PT)(CO)₃Br non-covalently supported on NTs (MnPT|NT). However, the strongly intense reoxidation peak at -0.38 V appearing for MnPT|NT on the backward scan, is only barely seen in the case of COF_{PTMn}|NT. The lower intensity of this redox feature, which is related to the oxidative cleavage of a Mn⁰-Mn⁰ dimer species formed upon the cathodic forward potential sweep,^{38, 49} was previously observed for the analogous COF_{bpyMn} and suggests a partial mechanical constraint of the Mn centers imposed by the framework hindering Mn-Mn dimerization (See Chapter III for details).

In order to explore the catalytic activity and selectivity, we supported COF_{PTMn}|NT on Carbon Paper (CP) (see Experimental Section for details). CPE of COF_{PTMn}|NT ($[Mn]_{total} = 900 \text{ nmol}\cdot\text{cm}^{-2}$) at -1.34 vs SCE ($\eta = 550$

CHAPTER VI

Mn based 2D-COF_{PT} for electrocatalytic CO₂RR

mV) under CO₂ atmosphere showed an average of -1.5 mA·cm⁻² for the steady-state current density (Figure VI. 7a). The gaseous and liquid products formed during the reaction were analyzed by gas chromatography and ¹H-NMR, respectively. The overall Faradaic Yield (FY) for CO₂ reduction products is 45% (FY_{CO}= 30%, FY_{HCOO}-= 15%), whereas the remaining FY accounts for H₂ production. (Figure VI. 7b).

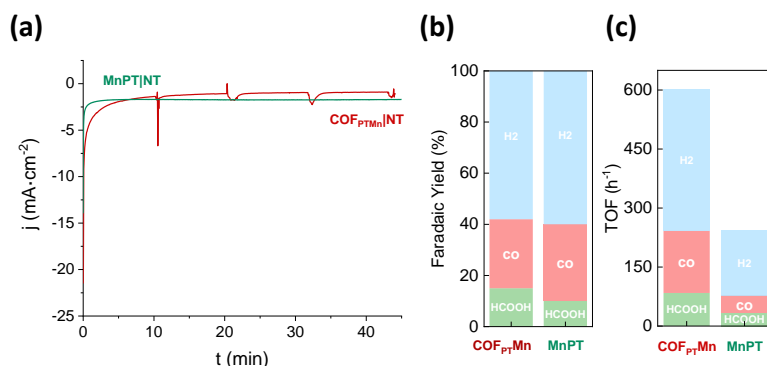


Figure VI. 7. CPE of COF_{PTMn}|NT (900 nmol·cm⁻²) and MnPT|NT ([Mn]_{total} = 900 nmol·cm⁻²) on Carbon Paper (1 cm²) at -1.34 V vs SCE under CO₂ in water (NaHCO₃ 0.5 M, pH 7.4). (a) Current density, (b) Faradaic yields and (c) TOF_F. Generated products: HCOO⁻ (green), CO (pink) and H₂ (blue).

Under similar conditions, MnPT|NT show similar current density (-1.7 mA·cm⁻², (Figure VI. 7a) and product distribution as COF_{PTMn}|NT, providing FY of 30% and 10% for CO and HCOO⁻, respectively (Figure VI. 7b). These results evidence that MnPT|NT presents similar catalytic activity to the COF_{PTMn}|NT.

However, in order to better compare the catalytic activity of COF_{PTMn}|NT with MnPT|NT, we estimated the electroactive surface concentration (Γ , see the Supporting Information for details). Γ values for COF_{PTMn}|NT and MnPT|NT were 4% and 10% of the total Mn deposited, respectively (Figure VI. 8). Normalizing the observed Turnover Frequency for Γ (TOF_F), the sum of the TOF_F values for CO and HCOO⁻ formation at -1.34 V vs SCE was found to be 3-fold higher for COF_{PTMn}|NT than for MnPT|NT (242 and 77 h⁻¹, respectively) (Figure VI. 7c), indicating that the Mn centers in the reticulated material are intrinsically more active than in the equivalent molecular complex.

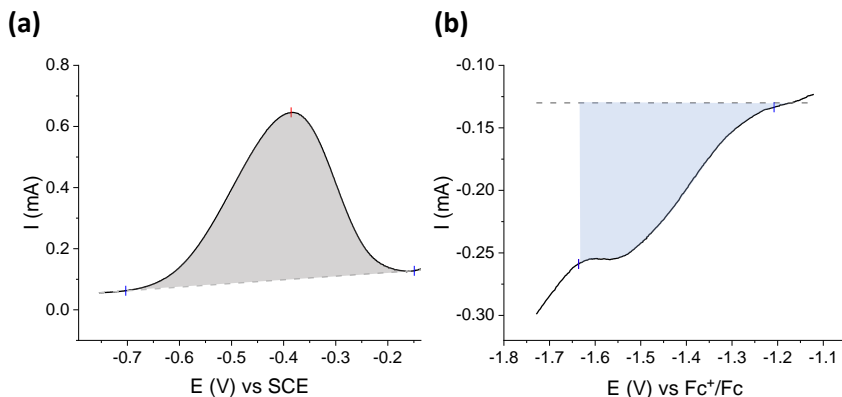


Figure VI. 8. CV of **COF_{PTMn}|NT** ($[Mn]_{total} = 900 \text{ nmol}\cdot\text{cm}^{-2}$) recorded in water (0.5 M NaHCO_3) (a) and **MnPT|NT** ($[Mn]_{total} = 900 \text{ nmol}\cdot\text{cm}^{-2}$) recorded in CH_3CN (0.1 M TBAPF_6) (b) under Ar at 100 mV/s.

After CPE, no significant changes were observed for **COF_{PTMn}|NT** in terms of morphology and elemental composition by FESEM and EDX analysis (Figure VI. 9a,b). The Mn coordination in **COF_{PTMn}|NT** is also preserved after CPE as confirmed by ATR-IR of the electrode after the catalytic test (Figure VI. 9c), showing the characteristic $\nu(\text{CO})$ of $\{fac\text{-Mn}(\text{CO})_3\text{S}\}$ ($\text{S} = \text{Br}, \text{CH}_3\text{CN}, \text{H}_2\text{O}$). However, ICP-OES of the electrolyte after CPE indicates that 18% of the total amount of Mn of the **COF_{PTMn}|NT** electrode leached out, which indicates a partial decomposition of the catalyst during CPE. It is worth noting that this amount is significantly higher

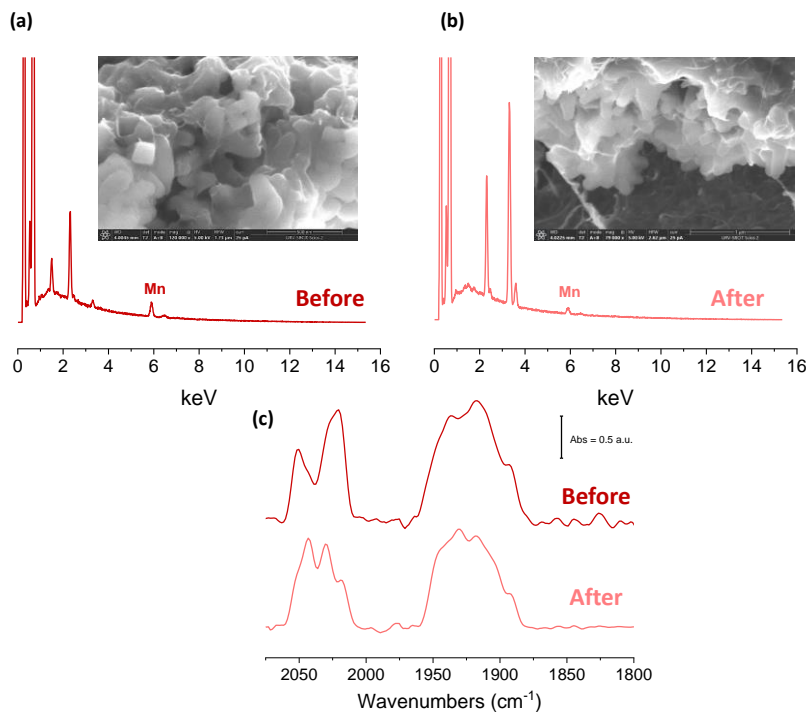


Figure VI. 9. Comparison before and after CPE of **COF_{PTMn}|NT** at -1.34 V vs SCE. (a, b) FESEM and EDX (c) ATR-IR.

To evaluate the effect of the modification of the Mn platform by the modification of the linker, we compared the catalytic activity of the **COF_{PTMn}|NT** with the analog **COF_{bpyMn}|NT**, using bpy in the strut in place of the longer PT linker (See Chapter III for details). First, CV of **COF_{bpyMn}|NT** and **COF_{PTMn}|NT** (Figure VI.10) under Ar showed similar profiles with an intense irreversible cathodic wave. Then, when the solution was saturated with CO₂ (pH 7.4), the catalytic current increased ~2-fold ($j_{\text{CO}_2}/j_{\text{Ar}}$ at -1.40 V vs SCE) in both cases. However, a clear difference between **COF_{bpyMn}|NT** and **COF_{PTMn}|NT** was observed in the backward scan features, where **COF_{PTMn}|NT** exhibits a higher peak at -0.35 V vs SCE, which according to the literature and our previous results, we assigned to the reoxidation of Mn⁰-Mn⁰ dimer formed during the forward scan. This difference in the formation of Mn dimers is attributed to the structural properties of the **COF_{PTMn}|NT**. The reticular introduction of a larger linker probably results in the collapse of the reticular framework and,

consequently, the decrease of the crystallinity and the mechanical constrain of the Mn single sites within the COF. Further discussion supported by *in situ* ATR-IR-SEC is presented in the next section.

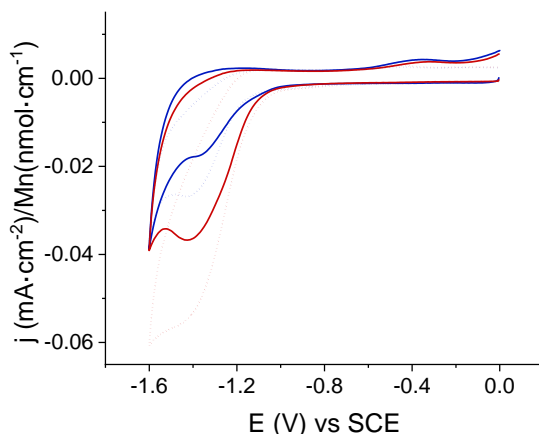


Figure VI.10. CVs on GC of **COF_{PTMn}|NT** ($[Mn]_{total} = 900 \text{ nmol}\cdot\text{cm}^{-2}$, solid line) and **COF_{bpyMn}|NT** ($[Mn]_{total} = 700 \text{ nmol}\cdot\text{cm}^{-2}$, dotted line) in water (NaHCO_3 0.5 M) under Ar (blue, pH 8.4) and CO_2 (red, pH 7.4) atm at $100 \text{ mV}\cdot\text{s}^{-1}$.

On the other hand, the comparison of the CPE experiments evidenced a substantial improvement of catalytic activity of **COF_{bpyMn}|NT** over **COF_{PTMn}|NT** (Figure VI.11). The current density of **COF_{bpyMn}|NT** was 5-fold higher than **COF_{PTMn}|NT**. Moreover, the introduction of the catalytic Mn centers within the **COF_{bpy}** showed greater than 30% enhancement in CO_2 products generation over the expanded **COF_{PTMn}|NT**, and as a result, the $\mu\text{mol}\cdot\text{cm}^{-2}$ of CO_2 reduction products were 8-fold higher in the case of the **COF_{bpyMn}|NT** than in the analog **COF_{PTMn}|NT**.

On the other hand, the minor TOFs differences between them (Figure VI.11d) are associated with the lower electrochemical active Mn in the case of the **COF_{PTMn}|NT**, around 4% versus 18% for the **COF_{bpyMn}|NT**. The decrease in Γ with the lattice expansion could again be attributed to differences in crystallinity and porosity ($1601 \text{ m}^2\cdot\text{g}^{-1}$ vs $94 \text{ m}^2\cdot\text{g}^{-1}$, respectively) between both platforms. In this sense, crystallinity reflects the porous structure regularity, which is vital for electrical and mass transport phenomena.⁵⁰ The self-assembled π -stacked columns formed in crystalline COFs enable electronic transport across the layers.⁵¹ Probably, in **COF_{PTMn}**

CHAPTER VI

Mn based 2D-COF_{PT} for electrocatalytic CO₂RR

the pores are block and not fully accessible due to the stacking faults or the amorphous regions.

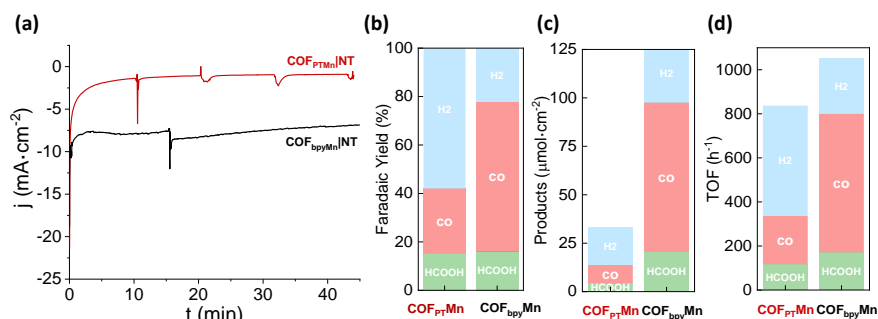


Figure VI.11. Comparison of the performance **COF_{PTMn}|NT** ($[Mn]_{total} = 900$ nmol·cm⁻²) and **COF_{bpyMn}|NT** ($[Mn]_{total} = 700$ nmol·cm⁻²) on Carbon Paper (1cm²) at -1.34 V vs SCE under CO₂ in water (NaHCO₃ 0.5 M, pH 7.4). (a) Current density, (b) Faradaic yields, (c) products formed and (d) TOF_r. Generated products: HCOO⁻ (green), CO (pink) and H₂ (blue).

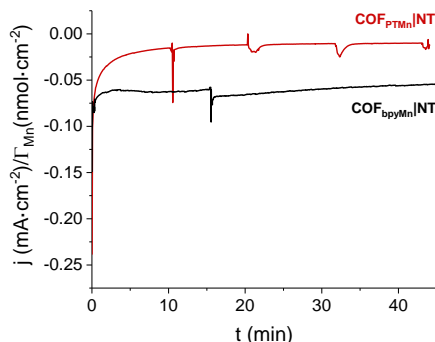


Figure VI.12. Comparison of the normalized current density by the active Mn (Γ_{Mn}) in the CPE of **COF_{PTMn}|NT** ($[Mn]_{total} = 900$ nmol·cm⁻²) and **COF_{bpyMn}|NT** ($[Mn]_{total} = 700$ nmol·cm⁻²). The data was taken from Figure VI.11.

To better compare the catalytic activity, the current density during the CPE of Figure VI.11 was normalized by the electroactive Mn (Γ_{Mn}) in each reticular catalyst (Figure VI.12). From the results, after considering the current density generated per electroactive Mn, the **COF_{bpyMn}|NT** still presents better relative performance (~4-fold higher) than the **COF_{PTMn}|NT**. In addition, the Mn centers in the bpy moieties are mechanically constrained by the reticular framework. However, in the **COF_{PTMn}** the COF steric effect is probably limited due to the loss of crystallinity. By reason, part of the {Mn(CO)₃} is not mechanically

constrained within the COF_{PTMn}, and the formation of the dimeric resting state intermediate is not avoided.

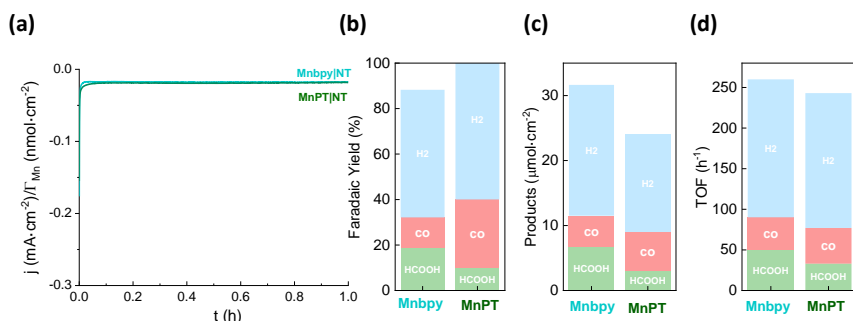


Figure VI.13. Comparison of the performance **MnPT|NT** ($[Mn]_{total} = 900$ nmol·cm⁻²) and **Mnppy|NT** ($[Mn]_{total} = 700$ nmol·cm⁻²) on Carbon Paper (1cm²) at -1.34 V vs SCE under CO₂ in water (NaHCO₃ 0.5 M, pH 7.4). (a) Current density, (b) Faradaic yields, (c) Products formed and (d) TOF_r. Generated products: HCOO⁻ (green), CO (pink) and H₂ (blue).

Additionally, the catalytic activity of the COFs' linkers was compared (Figure VI.13). From the electrochemical evaluation, **MnPT|NT** and **Mnppy|NT** present similar performance considering the j , FY, moles of generated products and TOFs, respectively. These results confirm that the differences observed in the catalytic activity of COF_{PTMn} and COF_{bpyMn} are due to the COFs structure.

VI.2.3 Spectroelectrochemistry of the COF_{PTMn}|NT in CH₃CN.

SEC experiments provide further evidence of the intermediates that can be formed at different potentials in catalysis. In particular, ATR-IR-SEC is a powerful technique that takes advantage of the structural specificity of IR spectroscopy for transition metal carbonyl moieties and the ability to generate *in situ* catalytic intermediates by gradually stepping the potential of the working electrode. Indeed, ATR-IR-SEC (Figure VI.14a) has been previously employed to obtain structural information on the catalytically relevant species of the COF_{bpyMn}|NT (See Chapter IV for details).⁴³ Considering these advantages, ATR-IR-SEC of COF_{PTMn}|NT was performed in CH₃CN (0.2 M TBAPF₆) by a stepwise decrease of the potential from 0 V to -2.3 V vs Fc⁺/Fc under Ar to monitor the reduction of the precatalyst.

Before performing ATR-IR-SEC, we performed CV of **COF_{PTMn}|NT** in dry CH₃CN (0.2 M TBAPF₆) under Ar (Figure VI.14b). The CV shows two irreversible cathodic waves at -1.50 V and -1.90 V vs Fc⁺/Fc, respectively. Besides, during the forward scan, two reoxidation processes were observed at -1.25 and -0.60 V vs Fc⁺/Fc, respectively. These redox transformations are similar to those observed for **COF_{bpymn}|NT** (See Chapter IV for details), suggesting an electronic similarity between **COF_{bpymn}** and **COF_{PT}** as ligands for the {*fac*-Mn(CO)₃S} centers.

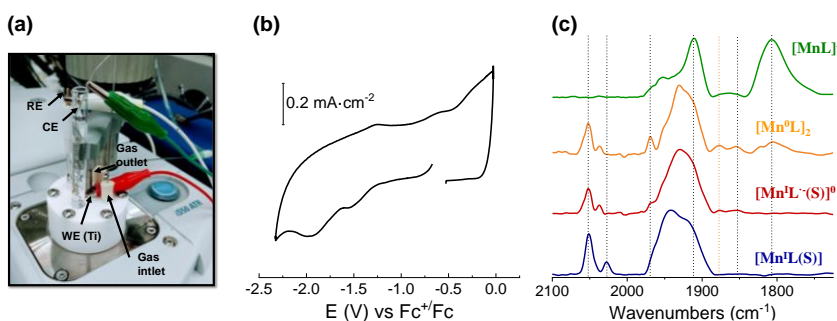


Figure VI.14. (a) Schematic representation of the ATR-IR-SEC cell, (b) CV of **COF_{PTMn}|NT** at a scan rate of 100 mV·s⁻¹ in CH₃CN (0.2 M TBAPF₆) and (c) ATR-SEC of **COF_{PTMn}|NT** showing the precatalyst (blue), the first reduction process to form a contribution of the radical intermediate [Mn^IL⁻(S)]⁰ (red) and the dimer [Mn⁰L]₂ (orange) and the second reduction process to form the anion five-coordinate intermediate [MnL]⁻ (green). All spectra were recorded in CH₃CN (0.2 M TBAPF₆) under Ar.

Similar behavior was observed in the CV of the **MnPT** complex in dry CH₃CN (0.2 M TBAPF₆) under Ar (Figure VI.15a). **MnPT** exhibits a first one-electron irreversible reduction at -1.4 and -1.5 V vs. Fc⁺/Fc, the two waves correspond to the reduction of two facial tricarbonyls Mn environments as a result of the partial Br⁻ solvolysis. The further reduction process was observed at -1.8 V vs. Fc⁺/Fc, and it is associated with the generation of the anionic intermediate.^{41, 52}

With these considerations, ATR-IR-SEC was carried out to gain structural insights into the electrochemical activation of the **COF_{PTMn}|NT** precatalyst. At open-circuit potential (E_{OCP}), the ATR-FT-IR of **COF_{PTMn}|NT** (Figure VI.14c) showed the *fac* arrangement

of the {Mn(CO)₃} within the core structure of COF_{PT}, with two $\nu(\text{CO})$ bands at 2053 and 2028 cm⁻¹ and a broad feature at 1937 cm⁻¹, respectively. The IR pattern corresponds to a combination of two facial tricarbonyl metal environments that also match well with the pattern observed for the complex MnPT|NT (Figure VI.15b). This profile agrees with the $\nu(\text{CO})$ bands of several reported immobilized facial tricarbonyl manganese polypyridine complexes^{38, 49, 53} (Table VI.1) and with the previously observed for the COF_{bpyMn}|NT (See Chapter IV for details).⁴³ The similarities in $\nu(\text{CO})$ stretching modes between COF_{PTMn}|NT and COF_{bpyMn}|NT illustrate the negligible electronic influence of the π -extended PT ligand within the framework. When the potential was biased beyond -1.8 V (*vs* Fc⁺/Fc), $\nu(\text{CO})$ bands at 2053 and 2028 cm⁻¹ diminished, while a peak at 2037 cm⁻¹ appeared. In addition, a broadening and a slight shift to lower energies of the peak at 1943 cm⁻¹ was also noticed. Similar behavior was detected for the COF_{bpyMn}|NT after the first reduction event (See Chapter IV for details). Based on this observation and the electronic similarity of both COFs we attributed this pattern to the formation of a radical intermediate [Mn^IL⁻(S)]⁰ (Figure VI.14c, Figure VI.16, Table VI.1).

The stepwise potential between -1.8 and -2.0 V *vs* Fc⁺/Fc produced the formation of four new $\nu(\text{CO})$ stretching modes that grew at 1968, 1931, 1876 and 1854 cm⁻¹ (Figure VI.14c). These new bands overlapped the previous radical intermediate, consistent with the bands expected for a Mn⁰-Mn⁰ dimer.⁴¹ We propose that after the first electron reduction of the COF_{PTMn}|NT, two different intermediates contributed to the spectra, the radical and dimeric species (Figure VI.16). As a result of the low crystallinity of COF_{PTMn}, the formation of the dimer can be more favored than in the case of the COF_{bpyMn} where the framework mechanically constrains the Mn centers.

Upon biasing the working electrode potential further negative, at -2.3 V *vs* Fc⁺/Fc a decrease of the dimer stretching intensities was observed (Figure VI.14c) with concurrent growth of two new $\nu(\text{CO})$ stretching modes at lower wavenumbers, 1910 and 1807 cm⁻¹,

respectively, corresponding to the five-coordinate two-electron reduced $[\text{MnL}]^-$ active catalyst (Figure VI.14c, Figure VI.16, Table VI.1).

Additionally, we performed the ATR-SEC of **MnPT|NT**. Similar to the **Mnbp|NT**, the first reduction event was associated with the formation of the $\text{Mn}^0\text{-Mn}^0$ dimeric species,⁵⁴ with no evidence of radical formation (Figure VI.15b). At the second reductive wave (-2.3 V vs Fc^+/Fc) the increase of the bands at 1906 cm^{-1} and 1802 cm^{-1} in the IR spectra is also rationalized with the generation of the five-coordinate anion intermediate of **MnPT|NT**.

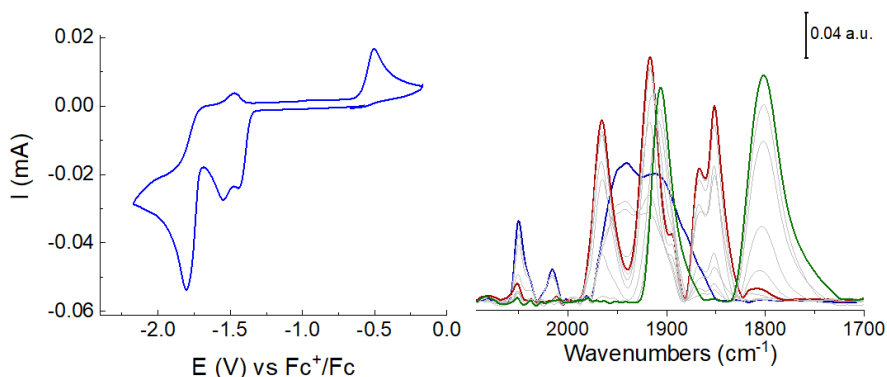


Figure VI.15. (a) CV of **MnPT** (~5 mM) in homogeneous conditions at scan rate of $100 \text{ mV}\cdot\text{s}^{-1}$. (b) ATR-IR-SEC of the model **MnPT|NT** in CH_3CN (0.2 M TBAPF_6) under Ar at room temperature. Potential causes changes in the immobilized **MnPT|NT** with the $\text{Mn}^0\text{-Mn}^0$ dimer formation after the first reduction at vibrations at 1860 and 1836 cm^{-1} (in red) and the generation of the five-coordinate anion intermediate $[\text{MnL}]^-$ after the second reduction (green). The blue curve is the starting complex at R0.

ATR-IR-SEC of **COF_{PTMn}|NT** indicates the formation of one-electron Mn species upon the first redox event. While the $1e^-$ reduction of **MnPT|NT** leads to the formation of a $\text{Mn}^0\text{-Mn}^0$ dimer, analogous to the observed for homogeneous $[\text{Mn}^{\text{I}}(\text{bpy})(\text{CO})_3(\text{X})]$ complexes (See Chapter IV), the $\{\text{Mn}(\text{PT})(\text{CO})_3\}$ moieties into the COF platform led to the radical $[\text{Mn}^{\text{I}}\text{L}^-(\text{S})]^0$ formations after the first reduction and limited the dimer formation. However, the reduced crystallinity of **COF_{PTMn}|NT** led to the formation of the dimeric species in a small quantity.

Table VI.1. Summary of the $\nu(\text{CO})$ frequencies under different conditions and respective assignment to different Mn-carbonyl species based on literature values.

Catalyst	$\nu(\text{CO})/\text{cm}^{-1}$				Reference
	$[\text{Mn}^{\text{I}}\text{L}(\text{S})]^+$	$[\text{Mn}^{\text{I}}\text{L}^{\cdot-}(\text{S})]^0$	$(\text{Mn}^0\text{L})_2$	$[\text{MnL}]^{\cdot-}$	
$\text{COF}_{\text{PTMn}} \text{NT}^b$	2051, 2027, 1943 (sh)	2050, 1921	1968, 1931, 1876, 1854	1910, 1807	This work
$\text{Mn}(\text{PT})(\text{CO})_3\text{Br} \text{NT}^a$	2050, 2028, 1942, 1917		1954, 1915, 1867, 1850	1906, 1802	
$\text{COF}_{\text{bpyMn}} \text{NT}^a$	2053, 2028, 1939 (sh)	2026, 1937		-	This work
$\text{COF}_{\text{bpyMn}} \text{NT}^b$	2050, 2025, 1941, 1915	2023, 1930		1915, 1808	This work
$\text{Mn}(\text{bpy})(\text{CO})_3\text{Br} \text{NT}^a$	2042, 2021, 1933 (sh)		1960, 1919, 1860, 1836	-	This work
$\text{Mn}(\text{bpy})(\text{CO})_3\text{Br} \text{NT}^b$	2050, 2025, 1935 (sh)		1971, 1930, 1876, 1853	1910, 1808	This work
$\text{Mn}(\text{bpy})(\text{CO})_3\text{Br}^b$	2027, 1936, 1923		1975, 1932, 1877, 1855	1910, 1809	Inorg. Chem. 2013, 52, 5, 2484–2491
MnBy-pyrene^a	2022, 1930, 1912		1968, 1921, 1870, 1844	-	J. Am. Chem. Soc. 2017, 139, 41, 14425–14435
$\text{MnBy-pyrene_H}_2\text{O}^a$	2025, 1938, 1903		1968, 1921, 1870, 1844	-	J. Am. Chem. Soc. 2017, 139, 41, 14425–14435

All the experiments were performed under Ar at room temperature. ^a 0.5 M NaHCO₃, ^b 0.2 M TBAPF₆/CH₃CN.

VI.2.4 Mechanistic proposal

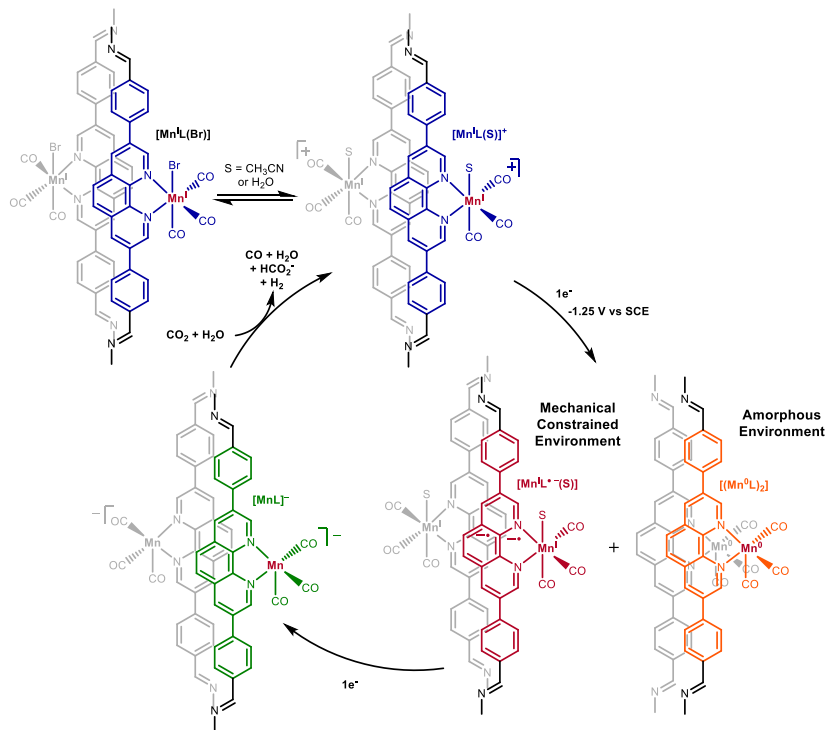


Figure VI.16. Proposed catalytic cycle for COF_{PTMn} based on spectroelectrochemical evidence.

Figure VI.16 presents a proposal for the CO₂ electroreduction mechanism obtained from the most relevant information gathered in this study. First, the manganese centers of the initial COF_{PTMn} suffer from a ligand exchange with the solvent followed by a reduction event. The monoreduced COF_{PTMn} species are critical in the catalytic cycle. First, there is a small contribution of the electronic effect of the COF. We hypothesized that, similar to COF_{bpyMn}, the COF partially facilitates the first reduction event *via* the electron delocalization in the COF. However, the reduced crystallinity of the COF_{PTMn} also allows the formation of the detrimental Mn⁰-Mn⁰ dimer typically found in molecular catalysts. Therefore, upon the first reduction, a contribution of the radical and the dimeric species are observed, negatively impacting other catalytic events. Following the reduction events, IR studies in CH₃CN point toward the formal Mn⁻¹ detected as the intermediate that reacts with CO₂ and water to form the CO₂ reduced products.

VI.3. Conclusions

To study the structure-activity relationships of COFs, we have followed a modular reticular approach to synthesize a new polypyridyl based-COF (COF_{PT}) and compare it with the COF_{bpyMn} previously evaluated. We introduced the analog PT moiety at the linker position and expanded the dimensions of the framework by increasing the size of the ligand (PT^{CHO}: 4,4'-(1,10-phenanthroline-3,8-diyl)dibenzaldehyde) in the strut in place of bpy (bpy^{CHO}: 2,2'-bipyridyl-5,5'-dialdehyde). COF_{PT} was post-synthetic modified with Mn(CO)₅Br and the resulted COF (COF_{PTMn}) was evaluated for the electrocatalytic CO₂ reduction in water. The spectroscopic characterization of COF_{PTMn} by IR shows that the Mn center has an equivalent coordination environment to the homologous molecular complex MnPT and the COF_{bpyMn}. However, the expansion of the linker resulted in a crystallinity loss, lowered CO₂ adsorption capacity inside the framework, and lower Mn incorporation (COF_{PTMn} 36% vs COF_{bpyMn} 85%). These physical properties direct affect catalysis, reducing the electrochemical accessibility of the catalytic {Mn(CO)₃}single sites. Besides, the extended COF_{PTMn} performed similar catalytic activity to the MnPT in water, with 45% selectivity for CO₂ reduction products. However, when the COF_{PTMn} was compared with the COF_{bpyMn} analog, the crystalline COF_{bpyMn} presented higher catalytic activity (~4-fold higher).

Additionally, by ATR-SEC two different intermediates were detected upon the first reduction of the COF_{PTMn} precatalyst, the [Mn^IL⁻(S)]⁰ radical and the (Mn⁰L)₂ dimeric species. These results suggest a direct effect of the mechanical properties of the reticular platform on the mechanism for CO₂ reduction. Therefore, the disorder between the layers of COF_{PTMn} reduces the mechanical constraint effect imposed by a crystalline framework (effect previously observed on COF_{bpyMn}), resulting in the formation of the dimeric resting state intermediate.

In addition, the reticular approach did not improve the catalytic activity with respect to the molecular MnPT. Therefore, we hypothesized that part of the Mn catalytic centers in COF_{PTMn} present similar spatial arrangement to the adsorbed molecular MnPT.

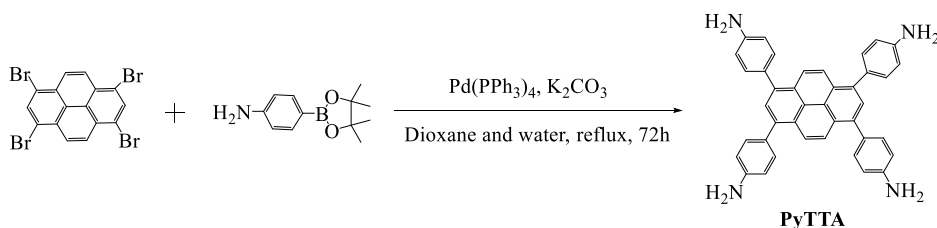
This study represents an important step in understanding the effects of the structure and physical parameters of the COFs on catalytic activity. Furthermore, it will guide the rational design of these reticular materials to promote further opportunities for a broad array of catalytic transformations and related applications.

VI.4 Experimental section

VI.4.1. Materials and reagents

All chemicals used in this study were purchased from commercial sources and used as received without further purification. Solvents were purchased from SDS and Scharlab. Water (18.2 MΩ·cm) was purified with a Milli-Q Millipore Gradient AIS system. NaHCO₃ (99.999% trace metals basis), TBAPF₆ (electrochemical grade), MWCNTs, and Nafion (5 % in water) were purchased from Sigma-Aldrich®.

VI.4.2. Synthesis and characterization



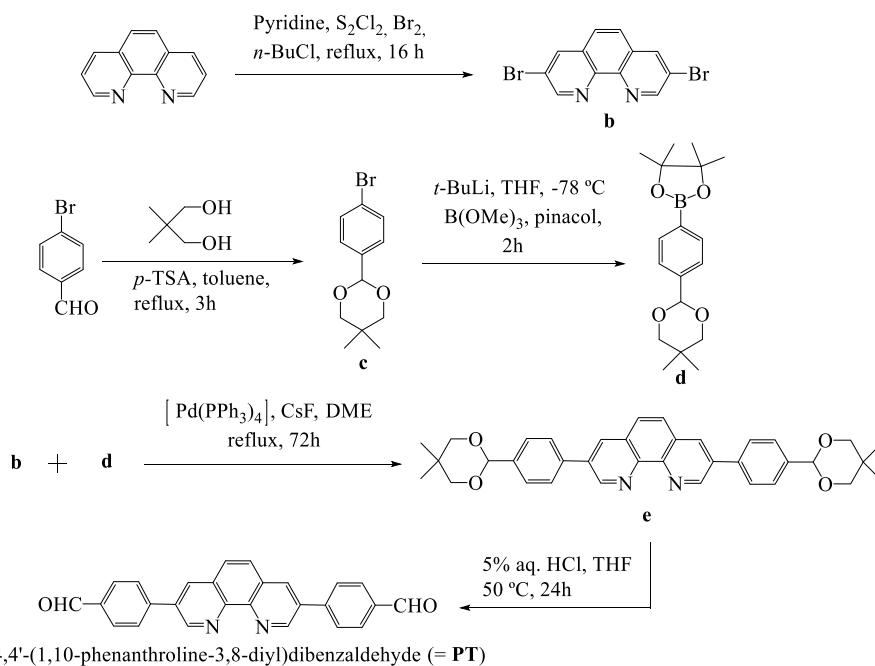
4,4',4'',4'''-(pyrene-1,3,6,8-tetrayl)tetraaniline (PyTTA): PyTTA is synthesized according to the published procedure.¹ A reaction mixture containing 1,3,6,8-tetrabromopyrene (0.74 g, 1.43 mmol, 1.0 eq.), 4-aminophenylboronic acid pinacol ester (1.50 mg, 6.85 mmol, 4.8 eq.), K₂CO₃ (1.08 g, 7.85 mmol, 5.5 eq.) and Pd(PPh₃)₄ (0.16 mg, 0.14 mmol, 10 mol%) in 20 mL 1,4-dioxane and 4 mL H₂O was heated to reflux (115 °C) for 3 d under N₂ atmosphere. After cooling to room temperature (r.t.), H₂O was added. The resulting yellow precipitate was collected via filtration and was washed with H₂O (3 × 10 mL), and MeOH (2 × 20 mL). Recrystallization from hot 1,4-dioxane, followed by drying under vacuum, furnished the title compound, co-crystallized with approximately 1.5 dioxane molecules per formula unit (0.90 g, 91%). ¹H NMR (DMSO-*d*₆, 400 MHz) δ, (ppm): 8.14 (s, 4H), 7.80 (s, 2H), 7.36 (d, *J* = 7.94 Hz, 8H), 6.77 (d, *J* = 8.00 Hz, 8H), 5.30 (s, 8H), 3.56 (s, 13H, dioxane); ¹³C NMR (DMSO-*d*₆, 400 MHz): 148.3, 137.3, 131.2, 129.2, 127.7, 126.8, 126.3, 124.6, 113.7, 66.5 (dioxane).

1E, 1'E)-2,2'-([2,2'-Bipyridine]-5,5'-diyl)bis(*N,N*-dimethylethenamine (a): a is synthesized following to the published

CHAPTER VI

Mn based 2D-COF_{PT} for electrocatalytic CO₂RR

procedure.² Pyrex tube was charged with 5,5'-dimethyl-2,2'-bipyridine (1.00 g, 5.4 mmol), DMF (10 mL), and *t*-butoxybis(dimethylamino)methane (10 mL); the reaction mixture was degassed by three freeze pump- thaw cycles. The tube was sealed and kept in the oven at 120 °C for 4 days. On cooling to r.t., yellow crystals were deposited in the bottom of the tube. The crystals were collected, washed with ether (3 × 20 mL), and dried to obtain the target compound in 32 % yield. ¹H NMR (CDCl₃, 400 MHz) δ, (ppm): 8.41 (s, 2H), 8.12-8.09 (d, 2H), 7.55-7.52 (d, 2H), 6.87-6.84 (d, 2H), 5.12-5.09 (s, 2H), 2.85 (s, 12H).



Scheme VI. 2. Synthesis of PT linker.

3,8-dibromophenanthroline (b):³ Phenanthroline monohydrate (4.97 g, 27.6 mmol) was dissolved in 220 mL of *n*-butyl chloride and degassed. Pyridine (7.2 mL, 90 mmol, 3.3 equiv.), S₂Cl₂ (7.5 mL, 94 mmol, 3.4 equiv.) and bromine (3 mL, 58 mmol, 2.1 equiv.) were then added sequentially to the solution. The resulting mixture was then heated to reflux for 16 h under a nitrogen atmosphere and cooled to r.t. The supernatant was decanted, and the solid was suspended in a mixture of equal volume (150 mL each) of 2 M NaOH (aq) and CHCl₃. The aqueous

layer was separated and extracted with CHCl₃ twice. The organic layer was then combined, dried over Na₂SO₄ and concentrated to give the crude product. The crude product was purified *via* column chromatography (silica gel, ethyl acetate: hexane = 1:4 v/v) to give a yellow solid as the pure 3,8-dibromophenanthroline (3.01 g, 32%). ¹H NMR (CDCl₃, 500 MHz) δ (ppm): 9.19 (d, *J* = 2.33 Hz, 2H), 8.42 (d, *J* = 2.28 Hz, 2H), 7.76 (s, 2H).

2-(4-Bromophenyl)-5,5-dimethyl-1,3-dioxane (c): 4-Bromobenzaldehyde (3.00 g, 16.2 mmol), neopentyl glycol (1.86 g, 17.9 mmol), and p-toluenesulfonic acid (0.05 g, 0.3 mmol) were dissolved in toluene (30 mL), and the solution was refluxed for 3 h. Then the solution was cooled to r.t. and washed with aqueous NaHCO₃ (10%) and water, and dried (Na₂SO₄). The solvent was evaporated, and the oily residue was crystallized from hexanes, affording colorless needles (2.81 g, 64%): ¹H NMR (CDCl₃, 500 MHz) δ, (ppm): 7.50 (d, *J* = 8.33 Hz, 2H), 7.38 (d, *J* = 8.29 Hz, 2H), 5.34 (s, 1H), 3.77-3.74 (d, *J* = 11.16 Hz, 2H), 3.65-3.62 (d, *J* = 10.55 Hz, 2H), 1.27 (s, 3H), 0.80 (s, 3H); ¹³C NMR (500 MHz, CDCl₃): 137.7, 131.5, 128.1, 123.0, 101.1, 77.8, 30.3, 23.1, 22.0; ¹³C NMR (APT): 22.0 (-), 23.1 (-), 30.3 (+), 77.7 (+), 101.0 (-), 123.0 (+), 128.0 (-), 131.5 (-), 137.7 (+). Analytical data were consistent with the literature.⁴

2-(4-(5,5-dimethyl-1,3-dioxan-2-yl)phenyl)-4,4,5,5-tetramethyl-1,3,2-dioxaborolane (d): **d** is synthesized following to the published procedure.⁵ To a cold solution of **c** (1.00 g, 3.68 mmol) in THF (40 mL) at -78 °C under argon, a solution of *t*-BuLi (1.7 M in pentane, 5.0 mL) was slowly added, keeping the temperature below -78 °C. This was followed 30 min later by trimethyl borate (0.45 mL, 4.05 mmol). The temperature rose slowly up to r.t. over 2.5 h. Pinacol (0.982 g, 8.31 mmol) was added, and 1 h later, the reaction was quenched with acetic acid (0.215 mL, 3.77 mmol). The reaction mixture was filtered through Celite. The filter was washed with diethyl ether and the solvents were removed from the filtrate under reduced pressure. The yellow residue was dissolved in CHCl₃-H₂O (1:1 v/v, 40 mL). The organic phase was separated and washed with water (3 × 10 mL). It was dried over Na₂SO₄,

filtered and the chloroform removed under reduced pressure to leave a residue, which was recrystallized, from cyclohexane. Compound **d** was obtained as a white crystalline solid (0.98 g, 80%), ¹H (CDCl₃, 500 MHz), δ, (ppm): 7.82-7.80 (d, *J* = 8.13 Hz, 2H,), 7.50-7.48 (d, *J* = 7.78 Hz, 2H,), 5.39 (s, 1H), 3.78-3.75 (d, *J* = 11.18 Hz, 2H), 3.65-3.63 (d, *J* = 11.22 Hz, 2H), 1.34 (s, 12H), 1.28 (s, 3H), 0.80 (3H, s).

3,8-di[*p*-(5,5-dimethyl-1,3-dioxan-2-yl)]phenyl-1,10-phenanthroline (e): **e** is synthesized with slight modification of the published procedure.⁶ 3,8-dibromo-1,10-phenanthroline (**b**) (0.80 g, 2.36 mmol), boronic ester (**d**) (1.69 g, 5.32 mmol), and Pd(PPh₃)₄ (0.191 g, 0.16 mmol) and CsF (2.01 g, 13.23 mmol) were mixed under argon in anhydrous dimethoxy ethane (70 mL). The resulting mixture was refluxed under argon for 72h. The reaction mixture was allowed to cool to r.t. The suspension obtained was filtered and washed with hexane (20 mL), and subject to Soxhlet extraction with CHCl₃ for 48h. The solvent was evaporated and dried in vacuum, afforded **e** (1.22 g, 81% yield) as a pale yellow solid. ¹H NMR (CDCl₃, 500 MHz), δ (ppm): 9.42 (s, *J* = 2.30 Hz, 2H, phen), 8.38 (d, *J* = 2.28 Hz, 2H, phen), 7.87 (s, 2H, phen), 7.80-7.78 (d, *J* = 8.29 Hz, 4H, Ar), 7.70-7.68 (d, *J* = 8.22 Hz, 4H, Ar), 5.49 (s, 2H, CH), 3.83-3.80 (d, *J* = 11.23 Hz, 4H, CH₂), 3.71-3.68 (d, *J* = 10.90 Hz, 4H, CH₂), 1.32 (s, 6H, CH₃), 0.83 (s, 6H, CH₃).

4,4'-(1,10-phenanthroline-3,8-diyl)dibenzaldehyde (abbreviated as PT): To a solution of (0.477 g, 0.810 mmol) in THF (90 mL) was added 5% aqueous HCl (18 mL) under argon. The reaction mixture was heated at 50°C for 24 h. After removal of the solvents, the residue was washed with a saturated aqueous solution of NaHCO₃ (150 mL) and extracted with CHCl₃ (2 × 125 ml). The organic layer was washed with H₂O (2 × 100 mL). The combined organic layers were washed with brine and dried over Na₂SO₄. The solvent was evaporated and the resulting residue purified by chromatography (silica gel, CHCl₃/MeOH (9:1 v/v)) to afford 0.301 g of **PT** ligand (80% yield) as a pale yellow solid; m.p.: 327-329 °C; ¹H NMR (CDCl₃, 500 MHz), δ (ppm) 10.13 (s, 2H, CHO), 9.50 (s, 2H, phen), 8.51 (d, 4H, Ar), 8.10-8.08 (s, *J* = 8.42 Hz, 2H, phen), 7.99 (s, 2H, phen), 7.97-7.96 (d, *J* = 4.28 Hz, 4H, Ar), ¹³C NMR (CDCl₃,

500 MHz), δ (ppm): 191.5, 149.2, 145.5, 143.2, 135.9, 134.5, 133.9, 130.5, 128.5, 128.1, 127.3; ESI-MS (positive mode): m/z 389 (M+H⁺).

Synthesis of Mn(PT^{CHO})(CO)₃Br complex: Mn(CO)₅Br (0.176 g, 0.64 mmol) was added to a N₂ sparged round-bottom flask containing 25 mL of THF. The flask was covered in Al-foil to shield it from ambient light. The PT ligand (0.250 mg, 0.64 mmol) was added to the mixture, and the reaction was heated to reflux. After 3 h, the reaction mixture was allowed to cool to r.t., and then, the reaction flask was placed in a freezer for 2 h. A red solid was collected and washed with THF and Et₂O and finally, dried under vacuum overnight. Yield: 0.21 g (45 %). ¹H NMR (DMSO-*d*₆, 400 MHz), δ (ppm): 10.16 (s, 2H), 9.84 (s, 2H), 9.30 (s, 2H), 8.37-8.17 (m, 10H); ¹³C NMR (CDCl₃, 500 MHz); Elemental analysis (%) calcd. for Mn(PT)(CO)₃Br complex, [C₂₉H₁₆BrN₂O₅Mn]: C (57.3), H (2.6), and N (4.6), found C (57.1), H (2.2), and N (4.3);

Synthesis of Mn(PT)(CO)₃Br complex: This was prepared by a published procedure.⁷ Manganese pentacarbonyl bromide Mn(CO)₅Br (0.371 g, 1.35 mmol) was stirred with 1,10-phenanthroline (0.267 g, 1.48 mmol) in dichloromethane (10 mL) under ambient temperature for overnight under an argon atmosphere. Then the reaction solution was cooled to -40 °C (acetonitrile/dry ice bath), resulting in an orange precipitate with a yield of 0.35 g (65 %). ¹H NMR spectrum agreed with reported values⁷: ¹H NMR (Acetone-*d*₆, 400 MHz), δ (ppm): δ = 9.68 (d, 2H), 8.81 (d, 2H), 8.25 (s, 2H), 8.08 (dd, 2H).

Synthesis of COF_{PT}: PyTTA (0.02 mmol, 11.3 mg) and PT linkers (0.04 mmol, 8.5 mg) were placed in a Pyrex tube (20 mL), followed by adding a solution of mesitylene/dioxane/6 M AcOH (5/5/1 by vol.; 1.1 mL). The mixture was sonicated for 10 min and then degassed by three freeze-pump-thaw cycles. The reaction was heated at the optimized conditions of 120 °C for 7 days yielding a yellow precipitate, which was isolated by filtration. The wet sample was then transferred to a Soxhlet extractor and thoroughly washed with THF (24 h) and acetone (24 h). The powder was dried at 120 °C under vacuum overnight to give an isolated

yield of 81%. Elemental analysis (%) calcd. for COF_{PT}, [(C₉₂H₅₄N₈)_n]: C (86.9), H (4.3), and N (8.8), found C (78.2), H (4.8), and N (7.6).

Synthesis of COF_{PT}Mn: COF_{PT} (0.035 mmol; 1 eq. of PT) was suspended in 10 mL of Et₂O. Mn(CO)₅Br (0.038 mmol; 1.1 PT eq.) was added to the suspension under N₂ atmosphere. The material was heated to reflux for 4 h. Then, the solid was isolated by filtration and washed profusely with Et₂O (3 × 10 mL) until the supernatant was colorless. The resulting material was dried under vacuum at room temperature and kept in inert atmosphere (Isolated yield ca. 90 %). Due to the potential light-sensitive nature of the resulting {Mn(CO)₃}-COF, the reaction, washing, and drying were performed, minimizing the exposure to light. ICP OES in COF_{PTMn} (mg Mn/g) = 39. IR, $\nu(\text{CO})$; 2026 cm⁻¹, 1941 2026 cm⁻¹ (sh), 1917 cm⁻¹ (sh)

VI.4.3. Physical methods and experimental procedures.

VI.4.2.1. Electrochemistry.

Working electrode: Glassy carbon (GC) electrodes (99.9995% trace metal basis, purchased from Bio-Logic) were polished with diamond paste and alumina (3 and 1 μm for 60 seconds each), thoroughly rinsed and sonicated in water and acetone, and dried before functionalization.

Working electrodes (GC, 0.0717 cm²) were prepared by drop casting 10 μL of ink containing the catalyst and MWCNTs (NT) (1 mg) dispersed in CH₃CN and Nafion 5% in water (1:1, 200 μL) and let dry under dark. Catalyst deposited [Mn]_{total} = 900 nmol·cm⁻² of Mn(PT)(CO)₃Br|NT and COF_{bpyMn}|NT (Figure VI. 17)

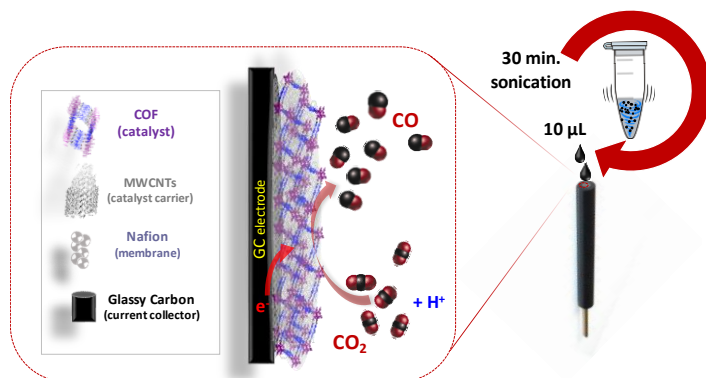


Figure VI. 17. Schematic representation of the hybrid catalyst immobilization (cat|NT).

Electrochemical measurements were performed using a Biologic potentiostat/galvanostat with a glass cell in the dark. The three-electrodes setup consisted of a working electrode, a Pt wire counter electrode, and a reference electrode. The working electrode was glassy carbon (99.9995% trace metal basis) and purchased from Bio-Logic. The reference electrode used in water was SCE (3.5 M KCl solution), while in CH₃CN was Ag wire, a pseudo reference calibrated with Fc⁺/Fc *vs* a freshly clean glassy carbon electrode before and after experiments.

All experiments were performed in water (0.5 M NaHCO₃) or CH₃CN (0.2 M TBAPF₆) electrolyte under Ar or CO₂ atmosphere at 25 °C. The cell was purged for 10 minutes before each experiment. The pH was measured using a CyberScan pH510. Ohmic drop was compensated using the positive feedback compensation implemented in the instrument.

Controlled Potential Electrolysis (CPE)

For CPE experiments, an H-type electrochemical cell was used, in which the counter electrode was a Pt wire immersed in a bridge tube containing electrolyte solution and separated from the cathodic compartment by a ceramic frit. As a working electrode, we employed a glassy carbon plate (GC) or carbon paper (CP, Freudenberg H23C6), and SCE electrode as reference. To saturate with Ar or CO₂, a constant gas flow (30 ml·min⁻¹, fixed with a mass-flow controller, Alicat®) was continuously passed over the solution and on-line analyzed with a gas chromatography every 10 minutes. An Agilent 490 micro

gas chromatograph equipped with a thermal conductivity detector and a Molesieve 5Å column was calibrated with different H₂/He/CO/CH₄ mixtures of known composition. The products formed during the reaction in liquid phases were analyzed by ¹H-NMR recorded on Bruker AV400 and AV500 spectrometers using standard conditions (300 K) and maleic acid as analytical standard. Catalyst deposited [Mn]_{total}= 900 nmol·cm⁻² of **Mn(PT)(CO)₃Br|NT** and **COF_{PTMn}|NT**.

The Faradaic Yield has been calculated by the following equation

$$FY(\%) = n_e \frac{mol_{product}}{mol_e} \cdot 100$$

Where:

n_e is the number of electrons of the redox transformation (2 for H₂, CO and HCO₂⁻) and $mol_{product}$ and mol_e are the moles of product generated and moles of electrons consumed in the CPE at a given time. $mol_{product}$ was determined by integrating the chromatogram areas, considering the flow of gas and Δt between each measurement. mol_e was determined by integrating the charge.

Electroactive surface coverage

The amount of electroactive material was calculated using the following equation:

$$\Gamma = \frac{Q}{n \cdot F \cdot S}$$

Where Γ is the electroactive surface coverage, Q the charge, n the number of electrons (in our case, we have considered 1 electron for **COF_{PTMn}|NT** and 2 electrons for **Mn(PT)(CO)₃Br|NT**), F the Faraday constant and S the geometric area of the working electrode (GC, 0.0717 cm²). The Q for **COF_{PTMn}|NT** was obtained by integration of the first redox wave of CV of **COF_{PTMn}|NT** in anhydrous CH₃CN (0.1 M TBAPF₆) under Ar at 100 mV/s, where the system is not catalytic, and the integral of the redox feature can be associated to the number of redox-active species. (Electrochemical Methods: Fundamentals and Applications, 2nd Edition Allen J. Bard, Larry R. Faulkner ISBN: 978-0-471-04372-0).

VI.4.2.2. Spectroelectrochemistry

VI.4.3.2.1 . ATR-IR-SEC.

The cat|NT ink was deposited over the Si prism and was electrically connected and pressed by a titanium electrode (tip d = 0.25 cm) (working electrode) into a homemade ATR-IR spectroelectrochemical cell (ATR-IR-SEC, fill volume of 4 mL). The reference electrode used in water (0.5 M NaHCO₃) was SCE (3.5 M KCl solution), while in CH₃CN (0.2 M TBAPF₆) was Ag wire, a pseudo reference calibrated with Fc⁺/Fc vs a freshly clean glassy carbon electrode before and after experiments. The counter electrode was a Pt wire immersed in a bridge tube containing electrolyte solution and separated from the cathodic compartment by a ceramic frit. To saturation the solution with Ar, a constant gas flow was continuously passed over the solution. All measurements were carried out at room temperature. The spectral region was set to a range from 2100 to 1700 cm⁻¹. A total of 128 scans were co-added for a spectrum with a resolution of 4 cm⁻¹. ATR-IR spectra were recorded on a Nicolet iS50 spectrometer using ATR accessory. See Experimental Section in Chapter IV for more details.

VI.4.3.2.2 . FT-IR-SEC

Spectroelectrochemical experiments with the molecular catalyst in solution were carried out in dry 0.2 M TBAPF₆/ CH₃CN electrolyte within an optically transparent thin-layer electrode (OTTLE) cell, equipped with a Pt mini-grid working and auxiliary electrodes, an Ag microwire pseudo-reference electrode and a CaF₂ window. FTIR spectra were recorded on a Nicolet iS50 FT-IR spectrometer.

VI.5 References

1. Li, C.; Yu, G., Controllable Synthesis and Performance Modulation of 2D Covalent–Organic Frameworks. *Small* **2021**, *17* (47), 2100918.
2. El-Kaderi, H. M.; Hunt, J. R.; Mendoza-Cortés, J. L.; Côté, A. P.; Taylor, R. E.; O'Keeffe, M.; Yaghi, O. M., Designed synthesis of 3D covalent organic frameworks. *Science* **2007**, *316* (5822), 268-72.
3. Cheung, P. L.; Lee, S. K.; Kubiak, C. P., Facile Solvent-Free Synthesis of Thin Iron Porphyrin COFs on Carbon Cloth Electrodes for CO₂ Reduction. *Chemistry of Materials* **2019**, *31* (6), 1908-1919.
4. Hod, I.; Sampson, M. D.; Deria, P.; Kubiak, C. P.; Farha, O. K.; Hupp, J. T., Fe-Porphyrin-Based Metal–Organic Framework Films as High-Surface Concentration, Heterogeneous Catalysts for Electrochemical Reduction of CO₂. *ACS Catalysis* **2015**, *5* (11), 6302-6309.
5. Waller, P. J.; Gándara, F.; Yaghi, O. M., Chemistry of Covalent Organic Frameworks. *Acc. Chem. Res.* **2015**, *48* (12), 3053-3063.
6. Diercks, C. S.; Lin, S.; Kornienko, N.; Kapustin, E. A.; Nichols, E. M.; Zhu, C.; Zhao, Y.; Chang, C. J.; Yaghi, O. M., Reticular Electronic Tuning of Porphyrin Active Sites in Covalent Organic Frameworks for Electrocatalytic Carbon Dioxide Reduction. *Journal of the American Chemical Society* **2018**, *140* (3), 1116-1122.
7. Lin, S.; Diercks Christian, S.; Zhang, Y.-B.; Kornienko, N.; Nichols Eva, M.; Zhao, Y.; Paris Aubrey, R.; Kim, D.; Yang, P.; Yaghi Omar, M.; Chang Christopher, J., Covalent organic frameworks comprising cobalt porphyrins for catalytic CO₂ reduction in water. *Science* **2015**, *349* (6253), 1208-1213.
8. Lin, S.; Diercks, C. S.; Zhang, Y. B.; Kornienko, N.; Nichols, E. M.; Zhao, Y.; Paris, A. R.; Kim, D.; Yang, P.; Yaghi, O. M.; Chang, C. J., Covalent organic frameworks comprising cobalt porphyrins for catalytic CO₂ reduction in water. *Science* **2015**, *349* (6253), 1208-13.
9. Kornienko, N.; Zhao, Y.; Kley, C. S.; Zhu, C.; Kim, D.; Lin, S.; Chang, C. J.; Yaghi, O. M.; Yang, P., Metal-organic frameworks for electrocatalytic reduction of carbon dioxide. *J Am Chem Soc* **2015**, *137* (44), 14129-35.
10. Baldwin, L. A.; Crowe, J. W.; Pyles, D. A.; McGrier, P. L., Metalation of a Mesoporous Three-Dimensional Covalent Organic Framework. *J Am Chem Soc* **2016**, *138* (46), 15134-15137.
11. Ascherl, L.; Sick, T.; Margraf, J. T.; Lapidus, S. H.; Calik, M.; Hettstedt, C.; Karaghiosoff, K.; Döblinger, M.; Clark, T.; Chapman, K. W.; Auras, F.; Bein, T., Molecular docking sites designed for the generation of highly crystalline covalent organic frameworks. *Nature Chemistry* **2016**, *8* (4), 310-316.
12. Ding, S.-Y.; Gao, J.; Wang, Q.; Zhang, Y.; Song, W.-G.; Su, C.-Y.; Wang, W., Construction of Covalent Organic Framework for Catalysis: Pd/COF-LZU1 in Suzuki–Miyaura Coupling Reaction. *Journal of the American Chemical Society* **2011**, *133* (49), 19816-19822.
13. Doonan, C. J.; Tranchemontagne, D. J.; Glover, T. G.; Hunt, J. R.; Yaghi, O. M., Exceptional ammonia uptake by a covalent organic framework. *Nature Chemistry* **2010**, *2* (3), 235-238.
14. Ngo, K. T.; McKinnon, M.; Mahanti, B.; Narayanan, R.; Grills, D. C.; Ertem, M. Z.; Rochford, J., Turning on the Protonation-First Pathway for Electrocatalytic CO₂ Reduction by Manganese Bipyridyl Tricarbonyl Complexes. *Journal of the American Chemical Society* **2017**, *139* (7), 2604-2618.

15. Sampson, M. D.; Nguyen, A. D.; Grice, K. A.; Moore, C. E.; Rheingold, A. L.; Kubiak, C. P., Manganese Catalysts with Bulky Bipyridine Ligands for the Electrocatalytic Reduction of Carbon Dioxide: Eliminating Dimerization and Altering Catalysis. *J. Am. Chem. Soc.* **2014**, *136* (14), 5460-5471.
16. Pakhira, S., Rotational dynamics of the organic bridging linkers in metal-organic frameworks and their substituent effects on the rotational energy barrier. *RSC Advances* **2019**, *9* (65), 38137-38147.
17. Pakhira, S.; Mendoza-Cortes, J. L., Quantum Nature in the Interaction of Molecular Hydrogen with Porous Materials: Implications for Practical Hydrogen Storage. *The Journal of Physical Chemistry C* **2020**, *124* (11), 6454-6460.
18. Pakhira, S.; Mendoza-Cortes, J. L., Tuning the Dirac Cone of Bilayer and Bulk Structure Graphene by Intercalating First Row Transition Metals Using First-Principles Calculations. *The Journal of Physical Chemistry C* **2018**, *122* (9), 4768-4782.
19. Pakhira, S.; Lucht, K. P.; Mendoza-Cortes, J. L., Dirac cone in two dimensional bilayer graphene by intercalation with V, Nb, and Ta transition metals. *The Journal of Chemical Physics* **2018**, *148* (6), 064707.
20. Nguyen, H. L., Reticular design and crystal structure determination of covalent organic frameworks. *Chemical Science* **2021**, *12* (25), 8632-8647.
21. Zhang, B.; Mao, H.; Matheu, R.; Reimer, J. A.; Alshimiri, S. A.; Alshihri, S.; Yaghi, O. M., Reticular Synthesis of Multinary Covalent Organic Frameworks. *Journal of the American Chemical Society* **2019**, *141* (29), 11420-11424.
22. Liu, X.; Li, J.; Gui, B.; Lin, G.; Fu, Q.; Yin, S.; Liu, X.; Sun, J.; Wang, C., A Crystalline Three-Dimensional Covalent Organic Framework with Flexible Building Blocks. *Journal of the American Chemical Society* **2021**, *143* (4), 2123-2129.
23. Hu, J.; Gupta, S. K.; Ozdemir, J.; Beyzavi, H., Applications of Dynamic Covalent Chemistry Concept toward Tailored Covalent Organic Framework Nanomaterials: A Review. *ACS Applied Nano Materials* **2020**, *3* (7), 6239-6269.
24. Jiang, H.; Alezi, D.; Eddaoudi, M., A reticular chemistry guide for the design of periodic solids. *Nature Reviews Materials* **2021**, *6* (6), 466-487.
25. Biswal, B. P.; Chandra, S.; Kandambeth, S.; Lukose, B.; Heine, T.; Banerjee, R., Mechanochemical Synthesis of Chemically Stable Isoreticular Covalent Organic Frameworks. *Journal of the American Chemical Society* **2013**, *135* (14), 5328-5331.
26. Dong, J.; Wang, Y.; Liu, G.; Cheng, Y.; Zhao, D., Isoreticular covalent organic frameworks for hydrocarbon uptake and separation: the important role of monomer planarity. *CrystEngComm* **2017**, *19* (33), 4899-4904.
27. Cui, X.; Lei, S.; Wang, A. C.; Gao, L.; Zhang, Q.; Yang, Y.; Lin, Z., Emerging covalent organic frameworks tailored materials for electrocatalysis. *Nano Energy* **2020**, *70*, 104525.
28. Lin, C.-Y.; Zhang, D.; Zhao, Z.; Xia, Z., Covalent Organic Framework Electrocatalysts for Clean Energy Conversion. *Advanced Materials* **2018**, *30* (5), 1703646.
29. Lyle, S. J.; Waller, P. J.; Yaghi, O. M., Covalent Organic Frameworks: Organic Chemistry Extended into Two and Three Dimensions. *Trends in Chemistry* **2019**, *1* (2), 172-184.
30. Fernández, S.; Dubed Bandomo, G. C.; Lloret-Fillol, J., Recent advances in electrocatalytic CO₂ reduction with molecular complexes. In *Advances in Inorganic Chemistry*, Academic Press: 2022.
31. Takeda, H.; Cometto, C.; Ishitani, O.; Robert, M., Electrons, Photons, Protons and Earth-Abundant Metal Complexes for Molecular Catalysis of CO₂ Reduction. *ACS Catalysis* **2017**, *7* (1), 70-88.

32. Costentin, C.; Robert, M.; Savéant, J.-M., Catalysis of the electrochemical reduction of carbon dioxide. *Chemical Society Reviews* **2013**, *42* (6), 2423-2436.
33. Popov, D. A.; Luna, J. M.; Orchanian, N. M.; Haiges, R.; Downes, C. A.; Marinescu, S. C., A 2,2'-bipyridine-containing covalent organic framework bearing rhenium(i) tricarbonyl moieties for CO₂ reduction. *Dalton Transactions* **2018**, *47* (48), 17450-17460.
34. Aiyappa, H. B.; Thote, J.; Shinde, D. B.; Banerjee, R.; Kurungot, S., Cobalt-Modified Covalent Organic Framework as a Robust Water Oxidation Electrocatalyst. *Chemistry of Materials* **2016**, *28* (12), 4375-4379.
35. Johnson, E. M.; Haiges, R.; Marinescu, S. C., Covalent-Organic Frameworks Composed of Rhenium Bipyridine and Metal Porphyrins: Designing Heterobimetallic Frameworks with Two Distinct Metal Sites. *ACS Applied Materials & Interfaces* **2018**, *10* (44), 37919-37927.
36. Fernandez, S.; Dubed Bandomo, G. C.; Lloret-Fillol, J., Manganese Complexes for Electro- and Photocatalytic Transformations. In *Manganese Catalysis in Organic Synthesis*, 2021; pp 137-181.
37. Rønne, M. H.; Cho, D.; Madsen, M. R.; Jakobsen, J. B.; Eom, S.; Escoudé, É.; Hammershøj, H. C. D.; Nielsen, D. U.; Pedersen, S. U.; Baik, M.-H.; Skrydstrup, T.; Daasbjerg, K., Ligand-Controlled Product Selectivity in Electrochemical Carbon Dioxide Reduction Using Manganese Bipyridine Catalysts. *Journal of the American Chemical Society* **2020**, *142* (9), 4265-4275.
38. Reuillard, B.; Ly, K. H.; Rosser, T. E.; Kuehnel, M. F.; Zebger, I.; Reisner, E., Tuning Product Selectivity for Aqueous CO₂ Reduction with a Mn(bipyridine)-pyrene Catalyst Immobilized on a Carbon Nanotube Electrode. *Journal of the American Chemical Society* **2017**, *139* (41), 14425-14435.
39. Bourrez, M.; Molton, F.; Chardon-Noblat, S.; Deronzier, A., [Mn(bipyridyl)(CO)₃Br]: An Abundant Metal Carbonyl Complex as Efficient Electrocatalyst for CO₂ Reduction. *Angewandte Chemie International Edition* **2011**, *50* (42), 9903-9906.
40. Riplinger, C.; Sampson, M. D.; Ritzmann, A. M.; Kubiak, C. P.; Carter, E. A., Mechanistic Contrasts between Manganese and Rhenium Bipyridine Electrocatalysts for the Reduction of Carbon Dioxide. *Journal of the American Chemical Society* **2014**, *136* (46), 16285-16298.
41. McKinnon, M.; Belkina, V.; Ngo, K. T.; Ertem, M. Z.; Grills, D. C.; Rochford, J., An Investigation of Electrocatalytic CO₂ Reduction Using a Manganese Tricarbonyl Biquinoline Complex. *Frontiers in Chemistry* **2019**, *7*.
42. Kurtz, D. A.; Dhakal, B.; Hulme, R. J.; Nichol, G. S.; Felton, G. A. N., Correlations between photophysical and electrochemical properties for a series of new Mn carbonyl complexes containing substituted phenanthroline ligands. *Inorganica Chimica Acta* **2015**, *427*, 22-26.
43. Dubed Bandomo, G. C.; Mondal, S. S.; Franco, F.; Bucci, A.; Martin-Diaconescu, V.; Ortuño, M. A.; van Langevelde, P. H.; Shafir, A.; López, N.; Lloret-Fillol, J., Mechanically Constrained Catalytic Mn(CO)₃Br Single Sites in a Two-Dimensional Covalent Organic Framework for CO₂ Electroreduction in H₂O. *ACS Catalysis* **2021**, *11* (12), 7210-7222.
44. Feng, X.; Ding, X.; Jiang, D., Covalent organic frameworks. *Chem. Soc. Rev.* **2012**, *41* (18), 6010-6022.
45. Auras, F.; Ascherl, L.; Hakimioun, A. H.; Margraf, J. T.; Hanusch, F. C.; Reuter, S.; Bessinger, D.; Döblinger, M.; Hettstedt, C.; Karaghiosoff, K.; Herbert, S.; Knochel, P.; Clark, T.; Bein, T., Synchronized Offset Stacking: A Concept for

Growing Large-Domain and Highly Crystalline 2D Covalent Organic Frameworks. *Journal of the American Chemical Society* **2016**, *138* (51), 16703-16710.

46. Bisbey, R. P.; Dichtel, W. R., Covalent Organic Frameworks as a Platform for Multidimensional Polymerization. *ACS Central Science* **2017**, *3* (6), 533-543.

47. Da, H.-J.; Yang, C.-X.; Qian, H.-L.; Yan, X.-P., A knot-linker planarity control strategy for constructing highly crystalline cationic covalent organic frameworks: decoding the effect of crystallinity on adsorption performance. *Journal of Materials Chemistry A* **2020**, *8* (25), 12657-12664.

48. Huang, X.; Sun, C.; Feng, X., Crystallinity and stability of covalent organic frameworks. *Science China Chemistry* **2020**, *63* (10), 1367-1390.

49. Walsh, J. J.; Forster, M.; Smith, C. L.; Neri, G.; Potter, R. J.; Cowan, A. J., Directing the mechanism of CO₂ reduction by a Mn catalyst through surface immobilization. *Physical Chemistry Chemical Physics* **2018**, *20* (10), 6811-6816.

50. Chen, X.; Addicoat, M.; Irle, S.; Nagai, A.; Jiang, D., Control of Crystallinity and Porosity of Covalent Organic Frameworks by Managing Interlayer Interactions Based on Self-Complementary π -Electronic Force. *Journal of the American Chemical Society* **2013**, *135* (2), 546-549.

51. Jin, S.; Ding, X.; Feng, X.; Supur, M.; Furukawa, K.; Takahashi, S.; Addicoat, M.; El-Khouly, M. E.; Nakamura, T.; Irle, S.; Fukuzumi, S.; Nagai, A.; Jiang, D., Charge dynamics in a donor-acceptor covalent organic framework with periodically ordered bicontinuous heterojunctions. *Angew Chem Int Ed Engl* **2013**, *52* (7), 2017-21.

52. Grills, D. C.; Ertem, M. Z.; McKinnon, M.; Ngo, K. T.; Rochford, J., Mechanistic aspects of CO₂ reduction catalysis with manganese-based molecular catalysts. *Coordination Chemistry Reviews* **2018**, *374*, 173-217.

53. Rosser, T. E.; Windle, C. D.; Reisner, E., Electrocatalytic and Solar-Driven CO₂ Reduction to CO with a Molecular Manganese Catalyst Immobilized on Mesoporous TiO₂. *Angewandte Chemie International Edition* **2016**, *55* (26), 7388-7392.

54. McKinnon, M.; Belkina, V.; Ngo, K. T.; Ertem, M. Z.; Grills, D. C.; Rochford, J., An Investigation of Electrocatalytic CO₂ Reduction Using a Manganese Tricarbonyl Biquinoline Complex. *Frontiers in Chemistry* **2019**, *7* (628).

CHAPTER VII.

General conclusions

Chapter VII: General conclusions

In this thesis, a new family of Single Atom Catalysts based on well-defined Mn-COFs with N-chelating ligands embedded on the structure was designed and studied for the electrocatalytic CO₂ reduction in water. This study allowed for critical insights into the fundamental reaction mechanism of COFs for the CO₂RR, showing the key role of the structure-activity relationship on these materials, where the confined space and the electronic delocalization in the framework affect the nature of the active sites and in consequence, the catalytic activity, selectivity and stability for the CO₂RR. In addition, the dynamic stimuli-responsive nature of these frameworks was probed under electrocatalytic conditions. The structural transformations within the framework induced by an external stimulus modify the pore environment and drastically change the nature of the generated intermediates. From this study, we strongly believe COFs can provide an ideal platform for the efficient tuning of the catalytic activity of molecular complexes by immobilizing them into reticular frameworks.

In **Chapter III**, we have studied the new Mn^I tricarbonyl aminopyridine based-2D covalent organic framework, **COF_{bpyMn}**. The catalyst was fully characterized by combining experimental and computational (DFT) techniques. Its spectroscopic characterization, along with correlation to theoretical calculations, confirmed that the Mn centers within the **COF_{bpyMn}** have an equivalent coordination environment to the homologous molecular complex *fac*-Mn(bpy)(CO)₃Br. Additionally, **COF_{bpyMn}** was found active for electrochemical CO₂ reduction in water at lower overpotential than the molecular counterpart. The encapsulation of the Mn centers into an ordered 3D porous framework outperforms the molecular *fac*-Mn(bpy)(CO)₃Br counterpart in current density, onset potential, turnover number (TON) and turnover frequency (TOF).

In **Chapter IV**, further investigations based on experimental and theoretical techniques provided insights into the catalytic cycle of **COF_{bpyMn}** for the CO₂ reduction. The encapsulation of the Mn molecular catalyst not only leads to a substantial improvement of the activity and

selectivity for CO₂RR but also induces a drastic change of the redox mechanism, allowing to stabilize different intermediate than those observed for the molecular counterpart. A $[\text{Mn}^{\text{I}}\text{L}^-(\text{S})]^0$ ligand centered radical intermediate was detected after the first electron reduction of **COF_{bpyMn}** instead of the dimeric resting state species. Unlike the classical approaches for the heterogenization of molecular catalysts, the reticular approach leads to a total suppression of a diffusional behavior which contributes to alter the redox pathway of a well-defined catalyst. In addition to steric hindrance, the increased electron-withdrawing character of the COF framework, compared to the bare bpy ligand, further contributes to delocalize the extra negative charge localized on the Mn⁰ center, thus disfavoring the formation of the dimeric resting state.

In **Chapter V**, the study of the mechanically constrain Mn centers within the COF was expanded and focused on the understanding of the mechanism and dynamic involve at the electrode interface. In this chapter, the dynamic response of **COF_{bpyMn}** triggered by the electric field was proven by *in situ* / *in operando* spectroelectrochemical techniques. Altogether points out that after the first e- reduction, the electric field induces structural transformations within **COF_{bpyMn}** resulting in profound changes in the electrocatalytic mechanism. A $[\text{Mn}^{\text{I}}\text{L}^-(\text{S})]^0$ radical is the main intermediate generated within **COF_{bpyMn}**, while a $[\text{Mn}^0\text{L}]_2$ specie is generated over short and intermediate distances to the working electrode as result of the dynamic interlayers reorganization within **COF_{bpyMn}**.

Additionally, in **Chapter VI**, we introduce a new polypyridyl moiety into a COF. We modified the **COF_{bpyMn}** by introducing as N-chelating building block a 1,10-phenanthroline ligand derivate (4,4'-(1,10-phenanthroline-3,8-diyl)dibenzaldehyde) in order to modify the size and electronic nature of the ligand. We studied the effect of the sterically and electronically expanded phenanthroline derivate ligand into the reticular framework and compared it with the **COF_{bpyMn}**. The clear differences in activity and stability of **COF_{bpyMn}** compare to **COF_{PTMn}**, evidenced a direct correlation between the structural properties of the COFs and the catalytic activity as well as with intermediates generated in the catalytic cycle.

Along the thesis, we have seen the power of mechanistic studies to improve catalysis by rational design with a dramatic impact in the robustness of the catalyst for the CO₂ reduction. Among all the studies with Mn-base COFs, it seems that the activity resides in the single active sites and the mechanical constrain imposed by the framework to access the active species under the catalytic conditions

We believe that this information will serve as the basis for creating a novel family of single sites catalysts active for CO₂ reduction and other electrochemical transformations.



UNIVERSITAT
ROVIRA i VIRGILI